Title
Laboratory Astrochemistry: Instrumentation for characterization and kinetics of low temperature small molecules.

Permalink
https://escholarship.org/uc/item/0991796z

Author
Buchanan, Zachary

Publication Date
2022

Peer reviewed|Thesis/dissertation

Laboratory Astrochemistry: Instrumentation for characterization and kinetics of low temperature small molecules.

By

ZACHARY SCOTT BUCHANAN
DISSERTATION

Submitted in partial satisfaction of the requirements for the degree of

DOCTOR OF PHILOSOPHY

in

Chemistry

in the

OFFICE OF GRADUATE STUDIES

of the

UNIVERSITY OF CALIFORNIA

DAVIS

Approved:

Kyle N. Crabtree, Chair

Davide Donadio

Matthew Augustine

Committee in Charge

2022

Acknowledgements

The sophomore year of my undergraduate degree, I took an analytical chemistry course taught by a senior graduate student. That class turned out to be highly influential in my life, as it not only sparked my interest in instrumentation and got me interested in scientific programming, but changed my career path towards becoming a scientist. 11 years later, I still remember Taylor telling me that in grad school learning was fun again, because he got to learn whatever he wanted. I came to grad school to get that experience.

At Davis I made the choice to join a brand new professors lab, which was a little risky, but it also was risky for Kyle bringing me on in his first group of graduate students. I hope that investment paid off for him, because it paid off for me. Kyle, thanks for giving me the opportunity to build the skills that I wanted, and for being patient as I learned them. I appreciate your support, your advice and your patience with me over the last seven years, and I'll be grateful for the time I spent learning about research and about teaching from you. The work I did here would have been impossible to do without your vision.

I've had many other great mentors in my time at Davis. The early years of my PhD, when our group was small, I got to meet often with Lee-Ping Wang and his group. Lee-Ping, I don't know if you remember, meeting with you when I had to reschedule my QE was a pivotal moment in my life. Thank you for telling me everything was going to be ok and your counsel on what to do to recover. My committee members, Davide Donadio and Matt Augustine have also been great mentors to me. Thank you for teaching me when I was your TA, and for your feedback in writing this dissertation. Matt, I appreciate all of the times you came up to me to tell me about Mormon's in the media you were consuming. It was always a bright spot in my day. I got to spend a wonderful 6 months in Saclay France learning from Marie-Aline Martin-Drumel and Olivier Pirali, who took me into their research group and guided me through a lot of fruitful projects, which gave me the opportunity to do science, and not just build instruments to make it possible. Thank you both for your support then and after I returned the the states.

I've been fortunate to work with a number of brilliant people, and I want to thank some of them specifically for their influence during grad school. Zhongxing and Sommer, both joined me from the beginning in Kyle's lab and I am extremely grateful for your friendship and the things you've taught me over the years. Sommer, I will always appreciate you pushing me to keep going even when times seemed dark, and your encouragement to finish my PhD. I've really missed working with you the last few years. Eric and Kelly, thanks for being willing to let me practice mentoring and training on you guys. I enjoyed working with you, and sharing the things I'd learned, and learning from you, and I appreciate the work you did for my projects. Anna, I'm glad you joined our lab, and I'm grateful for your genuine interest in my well-being over the last several years. Wes, it's been fun working around you. I genuinely think that you're a good person, even if we have vastly different opinions on what constitutes good music. Our crazy cross country road trip moving black widow is a highlight of grad school for me. Adam and Sophie, thank you for taking ownership of the kinetics experiment, and for pushing me to know more, and be better at research. Good luck, and I hope you get v2 up and running smoothly. I'm always happy to answer any questions you might have.

There are a number of other graduate students that have been large influences in getting this work done. Sommer, Dan, Marshall, Zachary and Shannon (The Physical Kids): Thank you guys for the great conversations, the friendship, the fun activities, and all of the help understanding math. I hope you forgive me for already knowing some programming when we got to grad school. I still miss getting to spend so much time complaining and working together in the basement of the library year one. Tyler, thanks for convincing me to come to Davis and join Kyle's lab. Thanks for always answering my questions, and I'll always be grateful that you and Tiffani adopted me when I got to Davis. I miss our weekly hangouts. Others I want to mention are Julia, Trish and Josh, you guys were a joy to TA with, and made the analytical lab so much fun.

This would have been impossible to accomplish without my family. Mom and Dad, thank you for the support you've given me my entire life. I bet you never thought that the kid who was constantly in trouble because he didn't do his homework would end up choosing to spend an extra 12 years in school after high school. Thank you for your encouragement and excitement for me and for my research. The phrase "standing on the shoulders of giants" I think appropriately describes my success relative to what you've done for me. Thanks to my siblings, Adam, Taylor, Jacob and Lucas who also been there to love and support me. Taylor, thanks for checking in on "Bruno" even though I told you that I didn't want to talk about my writing progress.

My best result that I got in grad school makes no appearance in the chapters to follow.

Three years ago, I started dating Sara, and one year ago we got married. That may seem short, but most of that time has been in COVID times, so it's more like a decade that we've known each other. Sara, I love you. Thank you for your support the last 3 years, especially the last year as I've struggled writing this and the last 2 months where I've basically done nothing else. You mean the world to me, and it feels like we've known each other forever, but that we're also still that cute new couple. I'm excited to get to support you now as you finish your own studies. There have been a lot of crazy life events in the last year and I don't think this could have happened without your support.

Abstract

Astrochemists seek to understand the rich chemical presence contained in the observable universe through detection and quantification of astronomical molecules and experimental and theoretical molecular physics. To date, around 270 unique molecules have been detected in the interstellar medium or in circumstellar shells. Chemical models are a tool used to understand the evolution of astronomical environments and they are improved with detections and laboratory studies. Thousands of molecular species and tens of thousands of reactions as well as molecular abundances, reaction rates and physical conditions form a network which models the composition of space over time. The accuracy of a model is dependent on the quality of data and the completeness of the network; imprecise and inaccurate data leads to significant uncertainty in the models. Understanding of the formation of complex organic molecules (COMs, defined as carbon containing species with 6 or more atoms) in cold, dense molecular clouds and prestellar cores has been challenged by recent detections, which highlights some deficiencies of chemical models. This work describes experimental and theoretical work increasing astrochemical knowledge through the study of chemical kinetics at low temperatures and through spectroscopic studies of molecules to facilitate their detection in space. A new instrument combining the CRESU method for producing cold, uniform environments with chirped-pulse Fourier transform microwave spectroscopy and laser induced fluorescence has been constructed to measure rate coefficients and branching ratios of neutral-radical reactions. Additionally, the pure rotational spectra of phenylpropiolonitrile (PhC_3N), 1-cyanoadamantane (CNAda), 1-isocyanoadamantane (NCAda), *o*-dibenzonitrile and *m*-dibenzonitrile were measured in the 75–110 and 120–220 GHz ranges, and the vibrational spectra of PhC_3N, CNAda and NCAda measured between 50–3200 cm^{-1}. Finally, a new instrument has been constructed to measure broadband (5 GHz), high resolution (<100 kHz) spectra in the THz region using heterodyne detection of synchrotron radiation mixed with a newly developed molecular laser. The instruments described here expand the tools available to laboratory astrochemists for producing data useful for chemical modeling and facilitating high resolution spectroscopic studies of molecules in support of astronomical detection. The spectroscopic measurements of 5 new molecules demonstrated here also provides high quality data useful for their detection by radio or IR telescopes.

Contents

Chapter 1

Introduction

Astrochemistry lies in the interface of chemistry, astronomy, and molecular physics. The observable universe contains a rich chemical presence which is still being catalogued as astronomers identify molecules based on their spectroscopic features observed by telescopes. Since the advent of radio telescopes, almost all of the detections of new molecules in space have been performed through the measurement of pure rotational transitions.[1,2] Around 270 unique molecules have been detected in the interstellar medium and circumstellar shells.[3] The complicated nature of rotational energy levels results in astronomers relying on precisely measured rotational transition frequencies to identify new molecules from radio observations. Molecules like benzene, which have no permanent dipole, have instead been detected through vibrational transitions,[4] which must be first measured in a laboratory. As more detections are made, astrochemists continue to refine chemical models of the universe which can be used to infer its past and future.

Chemical models are networks of thousands of species and tens of thousands of reactions that use molecular abundances, reaction rates, and physical conditions to model the composition of space and how it changes over time. They typically target a specific phase of stellar evolution, such as photon dominated regions,[5] interstellar clouds,[6] or cold dense clouds.[7] Chemical models are an essential tool towards addressing one of the key goals of astrochemistry, understanding the chemical evolution in various environments in the universe. However, models are inherently limited by the available knowledge and biases of the modelers. They tend to have a bias towards molecules that have already been detected in space, and species that are similar in structure.[8]

Progress towards understanding the origin of complex organic molecules (COMs) requires 1) development of chemical models, 2) detection and quantification of astronomical molecules, and 3) experimental and theoretical molecular physics.[9] This dissertation describes experimental and theoretical work aimed to push the boundary of knowledge in astrochemistry by experimentally studying chemical kinetics at low temperatures and by characterizing molecules to facilitate their detection in space through established and new techniques. Three projects are presented here:

1. Construction of an instrument to measure rate constants and branching ratios for radical-neutral reactions to inform chemical models.

2. Measurement of IR and mm-wave transition frequencies and spectroscopic constants to facilitate astronomical searches.

3. Construction of a new instrument to perform measurements in the THz gap with unprecedented broadband/resolution for studying molecules between 0.3-6 THz.

As dust and gas from exploded stars begin to coalesce into diffuse clouds, they experience typical temperatures of 30–100 K and densities of 10-10^2 cm^{-3}. Molecules in diffuse clouds are bombarded with UV radiation, destroying COMs that might form.[10] Diffuse clouds collapse into dense molecular clouds and dust causes shielding in the outer layers which cause them to become more opaque to UV and visible radiation creating a colder environment where molecules can survive. Temperatures in dense clouds typically are 10–30 K, with a density of $> 10^4$ cm^{-3}. Regions in clouds with higher mass continue to gravitationally collapse and become prestellar cores, cold ($\approx$ 10 K) regions that are considered the embryos of new stars. As these regions continue to collapse, they form hot molecular cores, which increase in temperature to greater than 100 K, with densities of greater than 10^6 cm^{-3}. Many complex species have been detected in hot cores[11] and are thought to form at this stage of stellar evolution. Eventually, these hot cores ignite, and proto-stars surrounded by circumstellar disks are formed.

It has been long thought that at the low temperatures in prestellar cores heavier atoms and molecules (like CO and H_2O), freeze onto icy grains, which results in little complex chemistry in either the gas or solid phase.[6,12] Below 30 K, only atomic hydrogen is mobile on the ice and so the only feasible reactions that can occur are simple hydrogen additions and subtractions. As the prestellar core evolves into a hot core, the surfaces of the icy grains are heated thermally and irradiated with UV light. Heavier radicals become more mobile, react, and form more complicated molecules. Heat generated from exothermic reactions[13] or the warmer environment cause the newly formed complex molecules to desorb. This mechanism requires temperatures exceeding 30 K to proceed,[14] and it implies that the presence of COMs, carbon containing species of 6 or more heavy atoms, in dark clouds and prestellar cores is unlikely.

However the detection of COMs in colder environments challenges the assumption that COMs are not formed prior to hot core formation. Examples of these detections include vinyl alcohol toward Sagittarius B2N,[15] methyl formate, dimethyl ether,[16] formaldehyde and ethylene oxide toward L1689B,[12,17] methanol and acetaldehyde towards 31 different starless and prestellar cores in TMC-1.[18] The variety of molecules and environments of these detections raise several important questions. What are the origins of COMs in prestellar cores, and what is their fate? To what extent do COMs from prestellar cores continue to play a role in chemistry as the cloud continues its collapse into stars?

Chemical models have struggled to explain the formation of COMs[19] and to accurately predict the abundance of newly detected molecules (i.e. benzonitrile[20]). The accuracy of models relies on the completeness of the network, as well as accurate reaction rate coefficients. Imprecise and inaccurate data leads to significant uncertainty in models,[5] for instance, a factor of 2 error in some rate coefficients significantly impacts predicted abundances. New models are continually under development to better represent measured observations of space. A recent chemical model developed by Balucani et al.[21] suggests that the formation of COMs in dark clouds/prestellar cores happens both on the surfaces of icy grains and in the gas phase. To fully understand the reaction mechanics of such environments, more data on rate coefficients and branching ratios is needed.

One goal of experimental molecular physics is to identify and measure reactions under astronomical conditions to improve models. An early class of targeted reactions were ion-neutral reactions, as it was assumed that neutral-neutral gas phase reactions in cold environments were unlikely to occur. It is proposed that the ionization of H_2 to H_2^+ initiates a chain of ion-neutral reactions[22,23] which result in the various unsaturated carbon chains found in the interstellar medium. To probe reactions at low temperatures and densities either ion traps or cold expansions/flows with ion injection were used.[24] However, many of these techniques (particularly the optical detection methods) provide no information on the products of the reactions, which limits their utility, as does the tendency of neutral reactants to freeze on reactor walls. CRESU was later developed to address the freezing issue at low temperatures.

CRESU, a French acronym that translates to reaction kinetics in a uniform flow,[25] is a technique that uses supersonic flow through a de Laval (or just Laval) nozzle to produce a cold, uniform molecular beam, free from shocks. The temperature, pressure and density are all well defined in a properly behaving flow.[26] The wall-less nature of these cold beams prevents condensation and enables measurement of cold gas phase reaction rates down to 6 K.[27] The CRESU method has been successfully applied over the last 40 years for studying reaction kinetics at low temperatures.[7,8,19,25,28–39]

As of 2019,[24] 65 ion-neutral and 160 neutral-neutral bi-molecular reactions had been studied using the CRESU technique at temperatures ranging from 11–200 K. The first neutral-neutral reaction to be measured below 100 K was between CN and O_2.[40] This study found an increased rate of reaction at lower temperatures and provided evidence that radical chemisty, like ion-neutral chemistry, can be feasible under interstellar conditions.

Recent experimental measurements have even shown that certain neutral-neutral reactions with barriers proceed much faster at low temperatures than predicted by Arrhenius theory.[7,19,29,30,32–34] The cause of this deviation is still under investigation. Some examples include $OH + HCOOCH_3$,[19] $OH + CH_3OH$,[29,30,32] $OH + CH_3CH_2OH$,[33] $OH^{\cdot} + CH_3OCH_3$.[31] This data provides evidence of gas-phase reaction pathways under the conditions found in dark clouds and prestellar cores. The full list of bimolecular reactions involving OH that have been studied (as of 2019[24]) can be found in Table 1.1. Reaction rates have been measured through observing the loss of OH radical, with products not observed. The mechanism for this reaction has been proposed to be hydrogen abstraction by the radical, accelerated by tunneling through the activation energy barrier. If these reactions do have enhanced rate constants at low temperature they have the potential to play an important role in astrochemical models. To verify these findings, it is important to perform similar measurements using a detection method that is capable of simultaneously observing reactants and product concentrations.

Many instruments employing a CRESU apparatus use LIF detection schemes, though it has also successfully been coupled with mass spectrometry.[41] The primary advantage of LIF is its high sensitivity (down to ≈10 ppm) and a high spatial resolution (limited by the linewidth of the laser). Recently,[36,42] development is underway on CRESU instruments using chirped-pulse Fourier transform microwave (CP-FTMW) spectroscopy as the detection method. Chapters 2 and 3 cover the work performed in the construction of a new instrument that couples the wall-less reactor of CRESU[25] with laser induced fluorescence (LIF) and chirped-pulse Fourier transform microwave (CP-FTMW) spectroscopy.[43] The

Table 1.1: List of bimolecular reactions with $OH^{\cdot}$ that have been studied below 100 K, and their minimum temperatures.

Minimum temperature / K	Reactant
12	CH_3OH
12	CH_3COCH_3
21	CH_3CH_2OH
22	$HC(O)OCH_3$
22	H_2CO
23	HBr
23	C_4H_8
39	O
58	CH_3CHO
58	$CH_3CH(NH_2)COOC_2H_5$
58	C_2H_5CHO
63	CH_3OCH_3
86	$(CH_3)_3COOH$
88	$CH_3CH(OH)CH_3$
93	$CH_3C(O)CH_2CH_3$
96	H_2O_2

goal of project 1 is to measure rate coefficients and branching ratios between 10–200 K for two- and three-body reactions, so as to improve chemical models. CP-FTMW has the advantage of measuring the entirety of its available spectrum (≈10.5 GHz) simultaneously. It is capable of spectroscopically resolving a complex mixture of gases, enabling monitoring of all molecules in the reaction at once. This includes detecting unanticipated molecules in the mixture, such as clusters, complexes, or secondary chemical reaction products.

The development of CP-FTMW as a detection method for CRESU type instruments creates a more robust instrument that can measure reactants, products, and unintended species. CP-FTMW provides the means to measure branching ratios, something that CRESU-LIF instruments lack. By coupling LIF and CP-FTMW together, rate constants can be measured for molecules accessible to both techniques, giving more confidence than the results measured only by CP-FTMW. LIF can also detect molecules that cannot be observed by the microwave spectrometer.

Chapter 3 describes the process for designing and profiling new Laval nozzles. It covers the relevant derivations from fluid dynamics for the method of characteristics, and describes the algorithm used in a home built python script to design nozzles with the desired final temperature, pressure and density. A series of uniform molecular beams have been produced at temperatures ranging between 19–65 K, with a goal of extending the range to 10–200 K. Included are the results of several beam profiles for these nozzles. The expected outcomes of the work described in these two chapters is a database of low temperature kinetics data, including rate constants and branching ratios, for a series of reactions involving $OH^{\cdot}$ with various COMs.

In addition to improving chemical models by measuring reaction rates, identification and quantification of new molecules is important for expanding the catalog of known astronomical molecules. The work presented in chapter 4 was heavily influenced by the recent detection of benzonitrile towards TMC-1.[4] Benzonitrile is the first interstellar detection of an aromatic molecule by rotational spectroscopy. Since the detection of benzonitrile, several other nitrile substituted carbon rings – cyanocyclopentadiene,[44] 2-cyanocyclopentadiene,[45] 1- and 2-cyanonapththaline[20] – have been detected in space. The detection of each new molecule relies on high accuracy experimental rotational measurements. Carbon rings are thought to be precursors of larger polycyclic aromatic hydrocarbons (PAHs), which are suspected of containing a large portion of the carbon in the universe.[46] The so-called unidentified infrared bands prevalent throughout the ISM are attributed to the vibrational fluorescence of PAHs,[34] but the similarity in IR spectra makes it difficult to assign specific bands to a particular PAH. Nevertheless, they remain of strong interest for astrochemistry and inspire the search for precursor molecules to their formation.

Diamondoids, like PAHs, are mostly non-polar or only weakly polar and therefore cannot be directly measured by rotational spectroscopy. Diamondoids have been proposed as potential constituents of the dust and gas in space[47] and have been extracted from meteorites, providing evidence of their presence in some astronomical conditions.[48,49] Recently new synthetic diamondoid production techniques[50] have been developed making studies of the vibrational bands of this class of molecule possible.[51–54] Remarkably little work has been performed on adamantane and its derivatives; only adamantane and hexamethylenetetramine have been studied in the mid- and far-IR.[51–53]

The detection of benzonitrile has renewed interest in benzene and its derivatives, and opened the possibility of using other nitrile substituted hydrocarbons as tracers for their parent species,[55,56] as the nitrile group typically induces a large dipole when functionalized onto non-polar molecules like aromatic rings or diamondoids. Nitriles comprise roughly 30% of the molecules detected in space, motivating accurate spectroscopic studies of new nitriles to facilitate future detection.

In light of this, chapter 4 covers rotational and vibrational spectroscopy for five nitrile-labeled ring molecules. The pure rotational spectra of phenylpropiolonitrile (PhC_3N), 1-cyanoadamantane (CNAda), 1-isocyanoadamantane (NCAda), *o*-dibenzonitrile (*o*-DCB) and *m*-dibenzonitrile (*m*-DCB) were measured using mm-wave absorption spectroscopy in the 75–110 and 120–220 GHz ranges. The vibrational spectra of PhC_3N, CNAda and NCAda were also measured between 50–3200 cm^{-1}.

Between the mm-wave and IR lies the THz region (0.3–7 THz)[57] where many rotational transitions of small molecules and vibrational transitions of large molecules lie. Chapter 5 focuses on improving technology for performing experimental work in the THz regime. It is often referred to as the THz gap, as the technology for detection in this region has lagged behind that of other regions. However, due to recent advances in telecommunications and astronomical observatories, this region has become increasingly accessible for astrochemistry. As telescopes like the Atacama large millimeter array (ALMA; 40–950 GHz), the Stratospheric Observatory for Infrared Astronomy (SOFIA; 3-1884 GHz), and the high elevation Antarctic terahertz (HEAT; 500-2000 GHz) telescope measure new data, laboratory studies are falling behind in providing high resolution spectra to assist in interpretation.[58]

The FTIR spectrometer described in Chapter 4 reaches as low as 3 THz, with a minimum resolution of 30 MHz, which is typically insufficient to resolve the rotational structure of large molecules at room temperature. On the lower-frequency side, absorption spectrometers employing multiplication chains are capable of performing absorption measurements up to 2.7 THz[59] with a sufficiently narrow linewidth to resolve rotations (order of 50 kHz), but their limited instantaneous bandwidth necessitates hours to days of scanning to measure their full range. To address the limitations of existing instruments, significant effort is underway to push the boundaries of THz technology.[60] New stable, high power sources are being developed to produce THz light,[59] while improvements in photoconductive antenna have expanded broadband detection of THz light up to measured frequencies of 2.759 THz.[61]

Chapter 5 describes construction of a new THz instrument capable of <100 kHz resolution spectra with 5 GHz of instantaneous bandwidth in the 0.3–6 THz range. This instrument takes advantage of synchrotron radiation and uses a heterodyne receiver to mix a single frequency source (produced by a molecular laser) to down-convert the THz synchrotron radiation into radio frequencies which can be measured quickly with high precision.[62,63] A database of suitable molecular laser frequencies and proof of concept measurements of methanol (CH_3OH) and hydrogen sulfide (H_2S) are reported.

Chapter 2

Development of a new instrument for study of reaction kinetics, rate coefficients and branching ratios

The instrument described in this chapter is intended to address the growing need of high quality laboratory data to inform reaction kinetics for astronomical models. The lack of this data is a cause for dissonance between astronomical observation and chemical models.[27] Data obtained by measuring branching ratios and reaction rates between species detected in the ISM can be used to improve existing models.[4]

Since the 1980s,[28] Laval nozzles have been used to produce wall-less reactors to study gas phase kinetics at low (<20 K) temperatures in a uniform environment. CRESU, a french acronym that translates to reaction kinetics in uniform supersonic flow, takes advantage of this technique which cools gas rotationally and vibrationally through supersonic expansion to perform kinetics experiments. Coupled with laser induced fluorescence (LIF) spectroscopy[27,30,35,40] or mass spectrometry,[64] researchers have probed low temperature reactions to extract rate coefficients and branching ratios. Many target reactions have products that are poor fluorophores however which precludes measurement of branching ratios with LIF..

Broadband chirped pulse Fourier transform microwave (CP-FTMW) spectroscopy has inspired the design of a new instrument for performing reaction kinetics. By combining the CRESU method with CP-FTMW spectroscopy and LIF spectroscopy, this instrument benefits from the low temperature wall-less reactor, the specificity of CP-FTMW to simultaneously measure all polar molecules in the flow by means of their rotational spectra, and the proven method of LIF to augment and verify findings from rotational measurements. Care must be taken designing the LIF part of the experiment to probe single species participating in the reaction, and that the target species is a good fluorophore. Similar instruments are being developed in other laboratories.[36,39]

This new instrument uses the CRESU method to probe a class of reactions involving $OH^{\cdot}$, with the goal to produce a comprehensive data set of rate constants and branching ratios for each reaction under a variety of temperatures ranging from 10–200 K. This chapter will outline the theory for extracting rate coefficients and branching ratios relevant to astrochemical models, describe the details of the instrument and give an overview of its operation.

2.1 CRESU kinetics

The majority of reactions involving $OH^{\cdot}$ have never been measured at temperatures below 200 K.[19] Chemical models instead use the Arrhenius behavior of these reactions extrapolated down to the temperatures relevant to the ISM. This class of reactions have barriers, and upon extrapolation, it is expected that the rate coefficient, k, will decrease exponentially with temperature. Recent studies[7,29,30,32] have shown the reaction of $OH^{\cdot}$ with methanol to proceed much faster at low temperatures than predicted. Reactions with $OH^{\cdot}$ with other hydrogen bonding hydrocarbons have also been measured with increased rates of reaction at low temperatures.[19,31,33] If these enhanced rates of reaction are due to the formation of products and not another, non-astronomically relevant, mechanism for $OH^{\cdot}$ loss, they would greatly impact current chemical models.

Relevant reactions to astrochemistry involving $OH^{\cdot}$ are second order reactions. For example, the abstraction of methanol (CH_3OH) by $OH^{\cdot}$ is:

$$\begin{gathered} \mathrm{CH_3OH + OH^{\cdot} \xrightarrow{k_1} H_2O + CH_3O^{\cdot}} \\ \mathrm{CH_3OH + OH^{\cdot} \xrightarrow{k_2} H_2O + CH_2OH^{\cdot}} \end{gathered} \tag{2.1}$$

where the differential rate law can be written as:

$$\frac{-\mathrm{d}[\mathrm{OH^{\cdot}}]}{\mathrm{d}t} = k[\mathrm{OH^{\cdot}}][\mathrm{CH_3OH}] \tag{2.2}$$

where k is the 2nd order rate constant, and [X] are in units of number density (cm^{-3}). Equation 2.2 can be integrated from $t = 0$ to $t = \bar{t}$, to obtain an equation relating time and the rate equation to $[OH^{\cdot}]$, $[CH_3OH]$, $[OH^{\cdot}]_0$, $[CH_3OH]_0$, where the 0 subscript indicates initial number densities.

However, if the experimental conditions are such that $[CH_3OH] >> [OH^{\cdot}]$, the approximation $[CH_3OH] \equiv [CH_3OH]_0$ can be made. Equation 2.2 can be rewritten and integrated:

$$\int_{[\mathrm{OH}^\cdot]_0}^{[\mathrm{OH}^\cdot]} \frac{-d[\mathrm{OH}^\cdot]}{[\mathrm{OH}^\cdot]} = \int_0^{\bar{t}} k_p \, \mathrm{d}t \tag{2.3}$$

where:

$$k_p = k_{2\mathrm{nd}}[\mathrm{CH_3OH}]_0 \tag{2.4}$$

Integrating results in the equation describing $[\mathrm{OH}^\cdot]$ over time, where $[\mathrm{OH}^\cdot]_0$ is the concentration of $\mathrm{OH}^\cdot$ at $t = 0$:

$$[\mathrm{OH}^\cdot] = [\mathrm{OH}^\cdot]_0 e^{-k_p \bar{t}} \tag{2.5}$$

Equations 2.4 and 2.5 provide everything needed to measure the total rate constant of loss of reactants in a bimolecular reaction. However, in the case of methanol with $\mathrm{OH}^\cdot$, two parallel reactions contribute to the loss of $\mathrm{OH}^\cdot$ (see Equation 2.1). The set of differential equations that describe the rates for these parallel reactions are:

$$\frac{\mathrm{d}[\mathrm{OH}^\cdot]}{\mathrm{d}t} = -k_1[\mathrm{OH}^\cdot][\mathrm{CH_3OH}] - k_2[\mathrm{OH}^\cdot][\mathrm{CH_3OH}] \tag{2.6a}$$

$$\frac{\mathrm{d}[\mathrm{CH_3O}^\cdot]}{\mathrm{d}t} = k_1[\mathrm{OH}^\cdot][\mathrm{CH_3OH}] \tag{2.6b}$$

$$\frac{\mathrm{d}[\mathrm{CH_2OH}^\cdot]}{\mathrm{d}t} = k_2[\mathrm{OH}^\cdot][\mathrm{CH_3OH}] \tag{2.6c}$$

Equation 2.6a simplified to pseudo first-order conditions and rearranged becomes:

$$\int_{[\mathrm{OH}^\cdot]_0}^{[\mathrm{OH}^\cdot]} \frac{d[\mathrm{OH}^\cdot]}{[\mathrm{OH}^\cdot]} = \int_0^{\bar{t}} -(k_{p1} + k_{p2}) \, \mathrm{d}t \tag{2.7}$$

Comparing Equation 2.7 to Equation 2.3, it is seen that $k_p \bar{t} = (k_{p1} + k_{p2})\bar{t}$.

Solving for the Equation 2.6b, and 2.6c gives the system of equations:

$$[\mathrm{OH}^{\cdot}] = [\mathrm{OH}^{\cdot}]_0 e^{-(k_{p1}+k_{p2})\bar{t}} \tag{2.8a}$$

$$[\mathrm{CH_3O}^{\cdot}] = \frac{k_{p1}}{k_{p1}+k_{p2}}[\mathrm{OH}^{\cdot}]_0\left(1 - e^{-(k_{p1}+k_{p2})\bar{t}}\right) \tag{2.8b}$$

$$[\mathrm{CH_2OH}^{\cdot}] = \frac{k_{p2}}{k_{p1}+k_{p2}}[\mathrm{OH}^{\cdot}]_0\left(1 - e^{-(k_{p1}+k_{p2})\bar{t}}\right) \tag{2.8c}$$

Equation 2.8 implies that both $[\mathrm{CH_3O}^{\cdot}]$ and $[\mathrm{CH_2OH}^{\cdot}]$ have the same exponential rise rate, $1 - e^{-(k_{p1}+k_{p2})\bar{t}}$, but reach different concentrations at $\bar{t}$. The ratio between the different products is equal to the ratio between the pseudo first-order rate coefficients: $[\mathrm{CH_3O}^{\cdot}]/[\mathrm{CH_2OH}^{\cdot}] = k_{p1}/k_{p2}$. The fit of the concentration of the products or reactants vs time for a particular temperature and density to Equation 2.8 results in the rate coefficients (and thus branching ratios) for those conditions. This concept can be extended to bigger systems with n product channels (P_n) by the following:

$$[\mathrm{OH}^{\cdot}] = [\mathrm{OH}^{\cdot}]_0 e^{-\sum_n k_{pn}\bar{t}} \tag{2.9a}$$

$$[\mathrm{P}_n] = \frac{k_{pn}}{\sum_n k_{pn}}[\mathrm{OH}^{\cdot}]_0\left(1 - e^{-\sum_n k_{pn}\bar{t}}\right) \tag{2.9b}$$

The intensity of the LIF signal is proportional to $[\mathrm{OH}^{\cdot}]$, so by plotting the intensity of the LIF vs time, it is expected that the intensity will follow Equation 2.5, which can be seen in the simulated data in the left panel of Figure 2.1.

The results from this fit give a value of the pseudo first-order rate coefficient for the specific concentration of the excess reactant. Repeating these measurements for multiple concentrations of the excess reactant, the plot in the right panel of Figure 2.1 is constructed

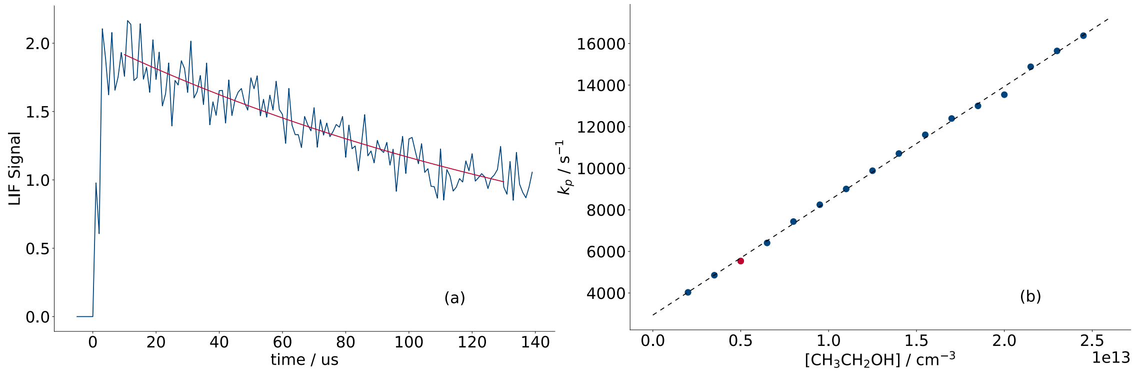

Figure 2.1: Simulated data for an expected LIF decay. Panel a shows a decay of $OH^{\cdot}$ observed by LIF for a constant value of [CH_3CH_2OH]. These data are fit to Equation 2.5 to find a value of k_p. This data point is shown in red in panel b. Panel b shows a series of k_p measurements. By fitting these measurements linearly, k_{2nd} is extracted for a single temperature.

and the slope related through Equation 2.4 is the 2nd order rate coefficient for that temperature. These measurements are then repeated for multiple temperatures and densities. In the case there are three-body involved in reaction, the pseudo first-order rate coefficient will be dependent on density, or have a non-linear dependence on the concentration of the excess reagent. When this arises, the density dependence can be extrapolated to zero density to extract the bimolecular rate coefficients.

2.2 Instrument overview

A block diagram of this instrument is shown in Figure 2.2. Section 2.2.1 describes the process for creating the desired reaction conditions, and section 2.2.2 describes the detection methods.

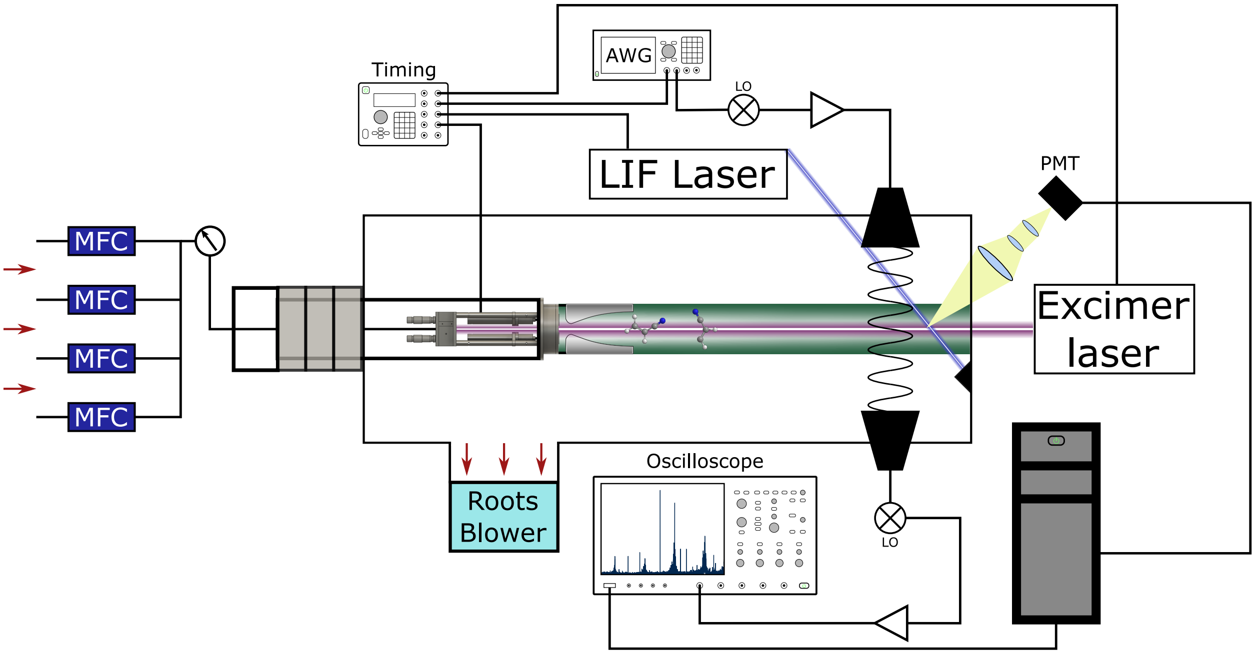

Figure 2.2: Schematic of CRESU/PLP CP-FTMW LIF instrument constructed in the Crabtree lab.

2.2.1 Reaction setup

To achieve meaningful results from kinetics experiments, some care must be taken when preparing the reaction to produce a uniform environment with well known temperature, pressure and density. Laval nozzles designed using a home built python script are used to produce a wall-less reactor. Several nozzles have been designed to produce flows at specific temperatures that fall into the 10–200 K range. More details about the nozzle design and performance are discussed in chapter 3.

This instrument employs a 250 L, 16 inch diameter, 2 meter long aluminum vacuum chamber, typically operating at pressures between 200–1600 mTorr. The pressure in the chamber is maintained by a dry compressing vacuum (Leybold DV 650) and roots booster (Leybold RUVAC WHU2500) capable of a maximum pumping speed of 675 L/s. The effective pumping speed at the chamber is approximately 511 L/s when accounting for the conductance of the connection between the chamber and pumps, which has proven effective for pulsed beam experiments in this instrument. The chamber pressure is controlled through choking the flow with a Nor-Cal Intellisys pendulum valve (TPV-QPA-ISO160) coupled with a capacitance diaphragm gauge (CDG025) which act to match the pumping speed with the gas flowing in through the nozzle.

A Physik Instrumente piezo actuator (212.80) is used to drive a t-valve which produces a pulsed beam with short rise and fall times. The PI piezo actuator has a push force of 500 N and a pull force of 10N, a stroke of 120 µm and a minimum response time of approximately 10 ns. Due to dynamic forces placed on the piezo during operation by the valve, to prevent damage to the crystal, it must be operated slower with rise and fall times of approximately 100–200 µs. The driver for this instrument is set to produce rise and falls times of approximately to 4 ms (see Figure 2.3).

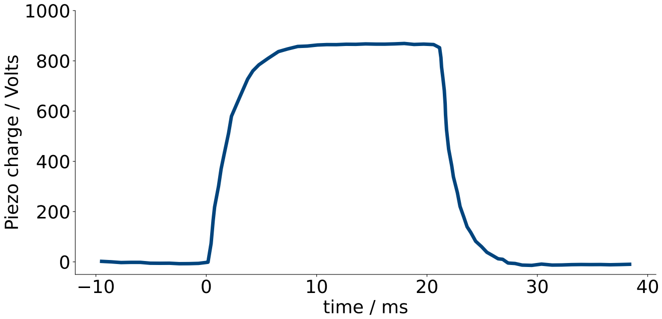

Figure 2.3: Voltage over time for the piezo actuator. 10/90% rise and fall times are 3.9791/3.9891 ms for a pulse of 928V.

When the valve is open, gas at a pressure between 5–50 Torr flows from a reservoir of 0.01 L to a stagnation region of 0.02 L. The source reservoir is fed by a gas flow manifold equipped with 2 MKS GE50A series mass flow controllers (MFCs) with ranges adjustable up to 500 sccm and 1000 sccm controlled by a MKS 946 vacuum system controller. Gas can be introduced into the manifold through pure gas tanks, small premix tanks, or by flowing a carrier gas through a bubbler of liquid reactant. The bubbler can be equipped with a cooling reservoir to reduce vapor pressure of solvents and decrease the concentration. The manifold uses the MFCs to dynamically mix the input gases into the main line leading to the source, and can control both the total pressure of the flow to the source, and the ratio of gases. This control is crucial for accurately controlling the concentration of the excess reactant, facilitating rate constant measurement under pseudo first-order reaction conditions.

To study reactions involving radical reactants, a stable precursor molecule is chosen and introduced into the gas flow. Radicals are produced in the flow through pulsed laser photolysis, which is often coupled with CRESU flows[27,64,65] (CRESU/PLP). $OH^{\cdot}$ for target reactions on this instrument are produced from a H_2O_2 precursor. The beam is irradiated with a 193 nm Lambda-Physik excimer laser with pulse width of 20 ns, a pulse energy of 400 mJ operating at 10 Hz (synced to the piezo valve). Time 0 for a reaction in the beam corresponds to the excimer laser pulse.

2.2.2 Reaction measurement

This instrument combines laser induced fluorescence (LIF) with chirped-pulse Fourier transform microwave (CP-FTMW) spectroscopy for monitoring reaction progress.

CP-FTMW spectroscopy has a much higher instantaneous bandwidth compared with previous microwave techniques (10+ GHz bandwidth vs 0.5 MHz). Cavity enhanced Fourier transform microwave spectroscopy is a narrow-band technique with greater sensitivity, but when scanning a broad frequency range only measures rotational transitions half of the time.[66] The CP-FTMW spectrometer developed for the kinetics experiments was designed using the same principles originally described by the Pate group,[43] but for the Ka band: 26.5–40 GHz.

A short, high-power, frequency-ramped signal ("chirp") is generated and broadcast towards molecules of interest. Any polar molecules with rotational transitions in the chirp's frequency are coherently excited. As they dephase, they emit a free induction decay (FID) which is a superposition of the FIDs for each excited transition. By Fourier transforming this FID the individual transition frequencies are extracted, resulting in the pure rotational spectrum. This is broadband (<10 GHz) and is typically sufficient to resolve complex gas mixtures spectroscopically. The FIDs are coherently averaged to improve the signal to noise ratio (SNR) for the transformed spectrum. The flat intensity of the chirp facilitates the calculation of partition functions, relative concentrations in a mixture, and rotational temperatures, especially compared to cavity-FT MW measurements where the relative intensity of the transitions can vary with frequency.

The Ka band was chosen for this instrument as most molecules with 3 or more heavy atoms have at least one transition between 26.5–40 GHz. $OH^{\cdot}$ also has a several well characterized transitions in this range[67,68] which can be used to calculate relative concentrations for determining rate constants. However, these transitions are for high *J* states, which may not be sufficiently populated at the temperatures measured. LIF detection is retained partly to ensure the capabilities to measure concentrations if the rotational spectrum is insufficient.

The CP-FTMW detection scheme begins with a chirp produced with a Tektronix AWG70002A arbitrary waveform generator (AWG) from 1.52–4.895 GHz. The chirp is then filtered and mixed with a 11.52 GHz waveform (ValonTech synthesizer) to produce a chirp ranging from 6.625-10 GHz, which is quadrupled to produce a chirp spanning the 26.5–40 GHz (Ka) frequency band. This is amplified by an Applied Systems Engineering 187Ka-H 170W traveling wave tube amplifier. The chirp is then broadcast through a microwave antenna horn inside the vacuum chamber.

Opposite to the transmit horn is a matching receiving horn to collect the FID and convert it back into an electronic signal. The receiver electronics are protected from the high power chirp by a diode limiter and switch, which nevertheless pass enough of the chirp signal through the open switch to permit observation of the chirp. The FID signal is amplified using a low noise amplifier and mixed with 40.96 GHz to produce an output signal from 0.96–14.46 GHz. This signal is recorded using a Tektronix DPO72004 oscilloscope which records 16 GHz of analog bandwidth and digitizes at 50 GSa/s, which then transmits to a computer.

The second method for measuring the reaction is an LIF spectrometer with a tunable excitation laser and photo multiplier tube (PMT) detector. LIF is widely used as an analytical technique in large part owing to the strong linear dependence of signal intensity on density. For analytical purposes, deriving an absolute concentration typically requires calibration; however, measuring the exponential decay rate requires only relative concentrations, which are measured by LIF spectroscopy without need for calibration. This makes it an ideal measurement tool for kinetics studies, and it has been used successfully for many years coupled with CRESU/PLP experiments.[27,28,35,69]

LIF is initiated by irradiating a molecule of interest with a laser tuned to a frequency resonant with an electronic, vibronic or rovibronic transition. For OH$^{\cdot}$ the $A\,^2\Sigma^+$-$X\,^2\Pi_i$ (1-0) vibronic transition at 281 nm is chosen. This absorption is represented in Figure 2.4 as a blue arrow. The molecule then undergoes a spontaneous radiative emission from the excited state to a lower energy state. This is shown in the figure by a red arrow, dropping in energy from the $A\,^2\Sigma^+$ $\nu = 1$ state to $X\,^2\Pi_i$ $\nu = 1$ state, which has a transition frequency of 314 nm.

Care must be taken when targeting a specific LIF measurement in a mixture. Often, molecules have overlapping absorption features, which complicate extraction of rate coefficients if both concentrations are changing. Ideally, the desired fluorescence is acquired through selective excitation. For OH$^{\cdot}$, we pump the 1-0 transition, and measure the fluorescence signal primarily from the 1-1 transition.

The LIF system for this instrument was designed to initially observe OH$^{\cdot}$, but is easily reconfigurable. The excitation laser is a OPOTek Opolette HE 355, with UV modules 1 and 2, extending the tuneable range to 210–2400 nm. The laser light is introduced to the chamber at a maximum repetition rate of 20 Hz though a fiber optic cable (200 μm diameter, NA: 0.22) and collimator mounted on a kinematic mount . This beam intersects

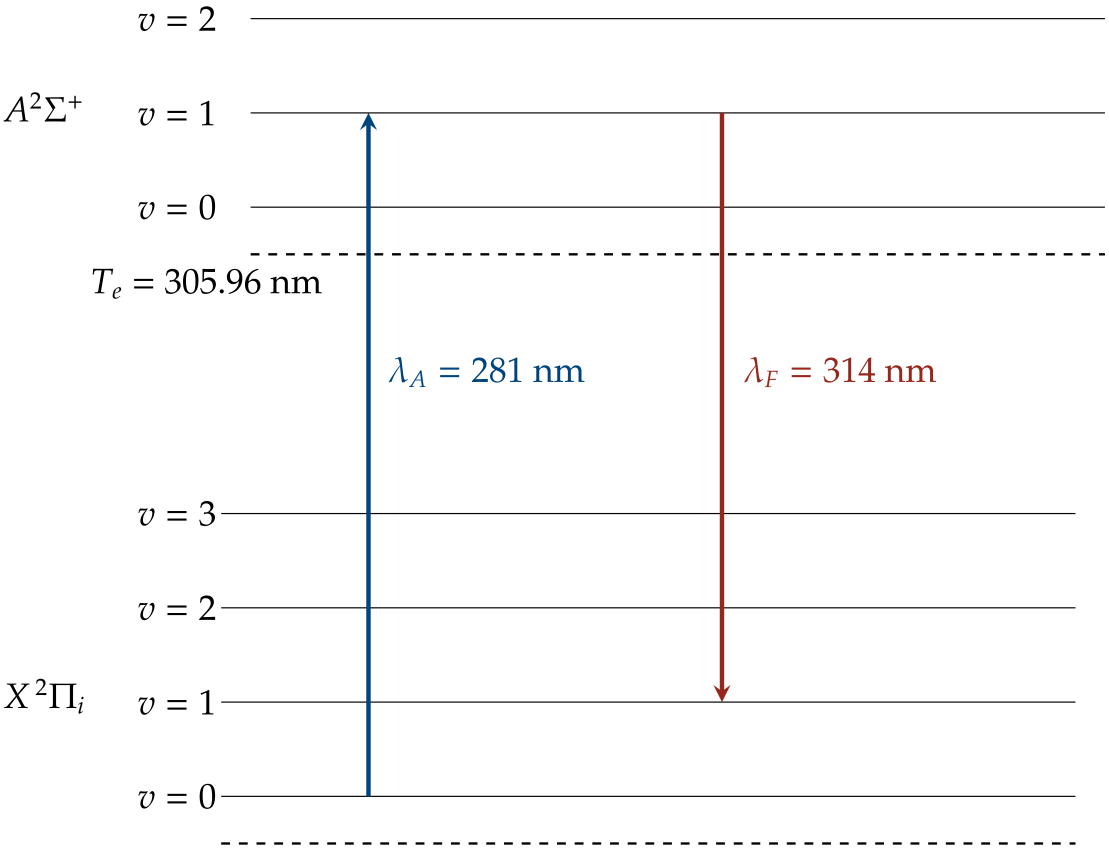

Figure 2.4: Jablonski diagram for the $X\,^2\Pi_i$ and $A\,^2\Sigma^+$ vibronic transitions of OH$^{\cdot}$. Vibrational levels are drawn to scale, electronic energies are not. Fluorescence is shown as a red arrow and absorption is shown with a blue arrow. The 1-1 transition is the target fluorescence frequency for this instrument. λ_F is calculated from the fundamental vibrational frequencies and electronic energies for both states.

the molecular beam, and terminates in a beam dump to minimize interference from reflections inside of the chamber. Emitted fluorescent light is collected via a telescope and filtered to remove light with wavelengths below 304 nm. Filtering minimizes detector response from Rayleigh scattering or reflections from chamber walls. Fluorescence is focused onto a Hamamatsu PMT (H9305-01), with a spectral response of 185–750 nm, which is powered by a Hamamatsu C7169 power supply. The signal is passed through a pre-amplifier (Hamamatsu C11184) which has a bandwidth of 300 MHz and a rise time of 1.2 ns, and the signal is recorded using a Spectrum Instruments M4i2211-x8 PCI express digital oscilloscope which has a max sampling rate of 1.25 GS/s and a bandwidth of 500 MHz. A Thorlabs silicon photodiode (Thorlabs DET10A2; rise time of 1 ns, 200–1100 nm detection range) measures the power and normalizes the fluorescence signal of each pulse. The signal is averaged and gate integrated to produce a final intensity measurement of the fluorescence.

2.3 Kinetics measurement

A complete kinetics measurement consists of a series of temperature dependent second-order rate coefficient determinations. Figure 2.5 is a graphical representation for the process of acquiring the raw data for a kinetics experiment. Reactions are set up to proceed under pseudo first-order conditions, with H_2O_2 seeded into the flow of a carrier gas with an excess of the other reactant. This gas mixture flows into the reservoir of the piezo source from the MFC manifold, then through the nozzle as the piezo valve pulses, expanding supersonically into the chamber to the final temperature, pressure and density determined

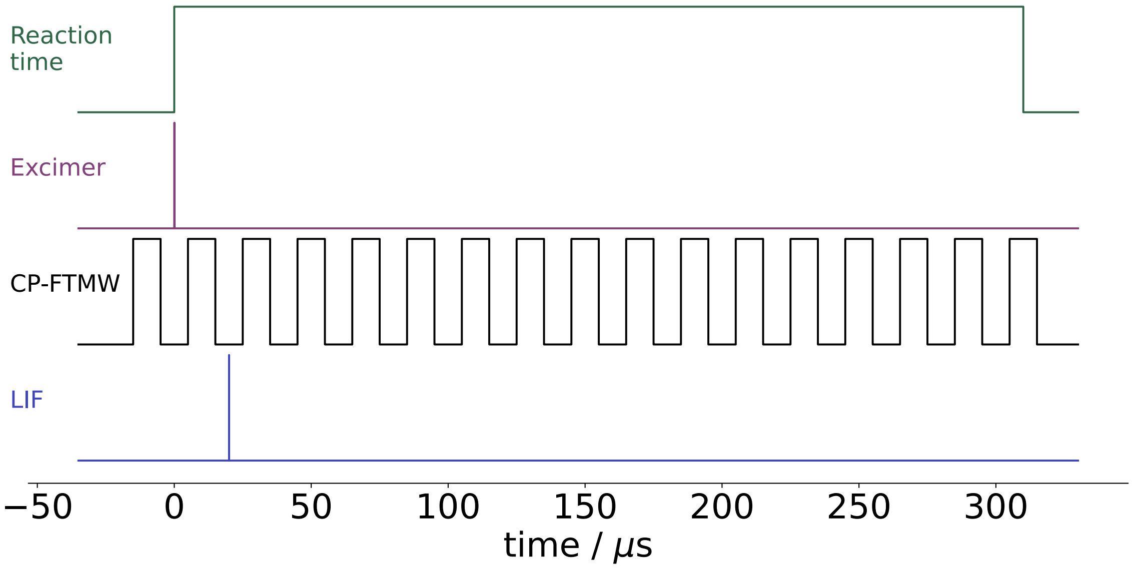

Figure 2.5: Timing diagram example of a pulse train for a kinetics experiment. Green: Reaction time. Only gas that was in the uniform flow at the time of the excimer firing will give meaningful results. Its length is dependent on the Mach number of the flow and the length of its stability. For a 55 K Ar nozzle the duration is about 313 μs long. Purple: Excimer laser pulse, which initiates the start of chemistry through dissociation of the precursor. Black: CP-FTMW measurement, which is about 5 μs in length, and is taking multiple measurements per gas pulse, starting prior to the exicmer pulse to measure the beam composition before the reaction. Blue: LIF excitation pulse, which is set at a delay from the excimer laser. This delay is adjusted as the experiment proceeds to sample the entirety of the gas pulse.

by the nozzle. At some point after uniform flow has been established, an excimer pulse is fired to initiate the reaction. Prior to the excimer pulse, CP-FTMW measurements begin in a sequence, which provides a series of snapshots before and during the reaction, monitoring concentrations throughout. Each CP-FTMW measurement takes between 5-10 μs, so for a typical gas pulse, 10-15 snapshots are performed. LIF measurements are performed by varying the timing compared to the excimer, probing the entirety of reaction time. This is shown in the left panel of Figure 2.1, where each data point represents a different delay of the LIF laser from the excimer laser.

LIF and CP-FTMW are both integrated into this instrument due to their complementary natures. LIF has high sensitivity and selectivity, and has been proven to work for measuring rates of reaction by many groups. CP-FTMW spectroscopy has the ability to resolve complex mixtures of gases spectroscopically, which gives it the advantage of being able to measure reactants and products simultaneously. Running these two detection measurements simultaneously allows the derivation of low temperature rate coefficients accurately, using two techniques in the same reaction. In addition to these advantages of using both measurement techniques, CP-FTMW probes the entirety of its bandwidth for each measurement and will detect unexpected molecules in the flow including cluster complexes, unpredicted products, or secondary products formed using initial products as reactants.

Each reaction studied with this instrument will undergo a series of measurements. First, the reactants will be measured in the flow with no photolysis laser, to detect any clusters that form between reactant molecules. Second, only the excess reactant will be seeded into the beam with the excimer. Third, the radical precursor with the excimer will be measured. Both the second and third measurements will look for any contaminants, secondary products, or clusters that form in the beam. Fourth, both reactants with the excimer will be studied for set densities of reactants. Next, steps 1–4 will be repeated, varying the density of the excess reactant, then varying the total number density. Finally, all of these steps will be repeated using multiple nozzles to vary the temperature of the flow, which will be used to extract the temperature dependent rate coefficients and branching ratios.

Chapter 3

Laval nozzle design and testing

Central to the reaction environment established for the instrument described in chapter 2 is the production of a cold molecular beam with the desired temperature, pressure and density. The objective of studies using this instrument is to probe the kinetics of reactions at temperatures between 20–200 K where $OH^{\cdot}$ has been shown to exhibit non-Arrhenius behavior when reacting with hydrogen-bonding species.[31]

To achieve these lower temperatures, a supersonic expansion of a high pressure gas into a low pressure environment converts rotational and vibrational energy into kinetic energy, leaving the molecules much colder in their relative frame of reference. Supersonic expansion is a well known technique for molecular cooling[28] and has been used to produce cold molecular environments in many experiments.[35,39–42,70–79] The production of a uniform beam of known parameters is achieved through the use of a Laval nozzle.

Named after the Swedish engineer who pioneered them,[71] a Laval nozzle is a type of converging/diverging nozzle used to supersonically expand gas into a uniform beam. These nozzles have been used for a variety of purposes, such as producing useful conditions in wind tunnels for aeronautic research, the expansion of rocket fuel for spaceships, depositing charged nano-particles onto a surface,[80] and others. In general, the design for converging/diverging nozzles results from the application of the partial differential equations for continuity, momentum and energy, discussed below (Equations 3.3, 3.6, and 3.9).[81]

This chapter first describes the mathematical background to calculate nozzles capable of creating molecular beams of desired temperature, pressure and density. These nozzles are designed in two parts: An "ideal" isentropic core and a boundary layer correction. The ideal core ignores any interaction with the wall of the nozzle and produces a shock free uniform flow. The boundary layer correction adjusts the physical wall to account for friction and heat transfer propagating into the flow from the nozzle so that an isentropic core is still produced. Next, the calculation of the isentropic core is presented, using the method of characteristics, followed by the calculation for the boundary layer. Finally, data gathered on 2 argon and 1 helium nozzles produced using the code described in this chapter are presented. Section 3.3 describes the procedure for measuring the Mach number in this flow and shows the results of these measurements.

3.1 Isentropic expansion

The continuity equation is a result of applying the law of conservation of mass to a fluid system.

$$\frac{\partial}{\partial t} \oiiint_V \rho \, \mathrm{d}V + \oiint_S \rho \vec{v} \cdot \mathrm{d}S = 0 \tag{3.1}$$

where dV is the elemental volume, $\vec{v}$ is the flow velocity, ρ is the density, dS is the vector elemental surface area. Reducing to a partial differential equation by applying the divergence theorem describes the relationship of the flow field variables at a point rather than in an arbitrary area, assuming that the flow is continuous:

$$\frac{\partial \rho}{\partial t} + \nabla \cdot (\rho \vec{v}) = 0 \tag{3.2}$$

Assuming a steady, inviscid flow, this equation becomes

$$\nabla \cdot (\rho \vec{v}) = 0 \tag{3.3}$$

The momentum equation is a result of applying Newton's second law to a flow, expressed in integral form as:

$$\frac{\partial}{\partial t} \oiiint_V \rho \vec{v}\, \mathrm{d}V + \oiint_S (\rho \vec{v} \cdot dS)\vec{v} = -\oiint_S \mathrm{P}\, \mathrm{d}S + \oiiint_V \rho \vec{f}\, \mathrm{d}V + \vec{F}_{\text{viscous}} \tag{3.4}$$

where $\vec{f}$ is the net body force per unit mass exerted on the fluid inside of V, $\vec{F}_{\text{viscous}}$ is the total viscous force on the surface and P is the pressure. A body force is defined as a force which acts at a distance (such as gravity, electromagnetic forces, etc) on the fluid. Using the gradient theorem, this can be broken into x, y, and z components of the equation, and expressed as a set of partial differential equations.

$$\frac{\partial(\rho v_x)}{\partial t} + \nabla \cdot (\rho v_x \vec{v}) = -\frac{\partial \mathrm{P}}{\partial x} + \rho f_x + (F_x)_{\text{viscous}} \tag{3.5a}$$

$$\frac{\partial(\rho v_y)}{\partial t} + \nabla \cdot (\rho v_y \vec{v}) = -\frac{\partial \mathrm{P}}{\partial y} + \rho f_y + (F_y)_{\text{viscous}} \tag{3.5b}$$

$$\frac{\partial(\rho v_z)}{\partial t} + \nabla \cdot (\rho v_z \vec{v}) = -\frac{\partial \mathrm{P}}{\partial z} + \rho f_z + (F_z)_{\text{viscous}} \tag{3.5c}$$

where v_x, v_y and v_z are the velocity of the flow in the x, y and z dimensions. These equations are known as the Navier-Stokes equations, and are important for solving the boundary layer, discussed later in the chapter. They apply to unsteady, three dimensional flows of fluids.

For the ideal core calculation of the nozzle, these equations can be simplified by assuming a steady flow ($\mathrm{d}/\mathrm{d}t = 0$) and by assuming that $\vec{F}_{\text{viscous}} = 0$ and $\vec{f} = 0$.

$$\nabla \cdot (\rho v_x \vec{v}) = \frac{\partial P}{\partial x} \tag{3.6a}$$

$$\nabla \cdot (\rho v_y \vec{v}) = \frac{\partial P}{\partial y} \tag{3.6b}$$

$$\nabla \cdot (\rho v_z \vec{v}) = \frac{\partial P}{\partial z} \tag{3.6c}$$

These equations are known as the Euler equations, and are used for the isentropic core calculations.

The energy equation becomes important for compressible flows, as ρ is no longer a constant, and another equation is needed to solve for the unknowns in this system: P, $\vec{v}$ and ρ. This equation is an application of the first law of thermodynamics to a fluid. The integral form is:

$$\oiiint_V \dot{q}\rho \,\mathrm{d}V + \dot{Q}_{\text{viscous}} - \oiint_S PV \cdot dS + \oiiint_V \rho(\vec{f} \cdot V) \,\mathrm{d}V + \dot{W}_{\text{viscous}}$$
$$= \frac{\partial}{\partial t} \oiiint_V \rho \left(e + \frac{V^2}{2} \,\mathrm{d}V \right) + \oiint_S \rho \left(e + \frac{V^2}{2} \,\mathrm{d}V \right) V \cdot dS \quad (3.7)$$

where e is the internal energy, T is the temperature, $\dot{q}$ is the volumetric rate of heat addition per unit mass in $\mathrm{J} \cdot \mathrm{kg/s}$, $\dot{Q}_{\text{viscous}}$ is the rate of volumetric heating from viscous effects, $\dot{W}_{\text{viscous}}$ is the shear stress on the surface.

Using the divergence theorem, the differential equation form of the energy equation is written:

$$\frac{\partial}{\partial t} \left[\rho \left(e + \frac{V^2}{2} \right) \right] + \nabla \cdot \left[\rho \left(e + \frac{V^2}{2} \right) \vec{v} \right] = \rho\dot{q} - \nabla \cdot (P\vec{v}) + \rho(\vec{f} \cdot V) + \dot{Q}_{\text{viscous}} + \dot{W}_{\text{viscous}} \quad (3.8)$$

This can be simplified by assuming a steady, inviscid, adiabatic flow without external forces, which reduces the differential form to:

$$\nabla \cdot \left[\rho \left(e + \frac{V^2}{2} \right) \vec{v} \right] = -\nabla \cdot (P\vec{v}) \quad (3.9)$$

Applying the differential forms of the momentum, continuity and enegry equations to a cylindrically symmetric nozzle, the area-velocity relation can be derived for a quasi-one dimensional flow through a variable area three dimensional nozzle, which shows how the velocity of the flow in a direction changes with the change of the area of the cross section of the duct (see Chapter 10 of Anderson):[81]

$$\frac{\mathrm{d}A}{A} = \left(M^2 - 1 \right) \frac{\mathrm{d}\vec{v}}{\vec{v}} \quad (3.10)$$

where A is the area of the cross section of the nozzle, M is the Mach number, and $\mathrm{d}\vec{v}$ is the change in velocity of the flow. M is a unifying variable for many flow properties and it is defined as the ratio between the velocity of the gas and the velocity of the local speed of sound:

$$M = \frac{|\vec{v}_{\text{gas}}|}{|\vec{v}_{\text{sound}}|} \tag{3.11}$$

When M is less than 1, decreasing the area of the cross-section ($\mathrm{d}A < 0$) requires the change in velocity be positive, resulting in acceleration of the flow. Likewise, when M is greater than 1, increasing A ($\mathrm{d}A > 0$) leads to an acceleration of the flow. Flow begins in the stagnation region before being accelerated subsonically through a converging region of the nozzle. At the throat of the nozzle (narrowest point) the flow is sonic (M=1), and then the nozzle diverges to continue to accelerate the flow supersonically.

Laminar flow is achieved by controlling the shape of the walls which rapidly accelerate and expand the flow, creating parallel streamlines after the nozzle exit.[82] Following the measurement of M after the nozzle exit, the temperature, pressure and density of the beam can be calculated using the relations in Equation 3.12[72,83]:

$$\frac{T}{T_0} = \left(1 + \frac{\gamma - 1}{2} M^2\right)^{-1} \tag{3.12a}$$

$$\frac{P}{P_0} = \left(1 + \frac{\gamma - 1}{2} M^2\right)^{-\gamma/(\gamma-1)} \tag{3.12b}$$

$$\frac{\rho}{\rho_0} = \left(1 + \frac{\gamma - 1}{2} M^2\right)^{-1/(\gamma-1)} \tag{3.12c}$$

In these equations, the subscript $_0$ indicates the conditions in the stagnation region, T

is the temperature in Kelvin, P is the pressure, ρ is the density, and the heat capacity ratio is defined as $\gamma = \frac{C_p}{C_v}$.

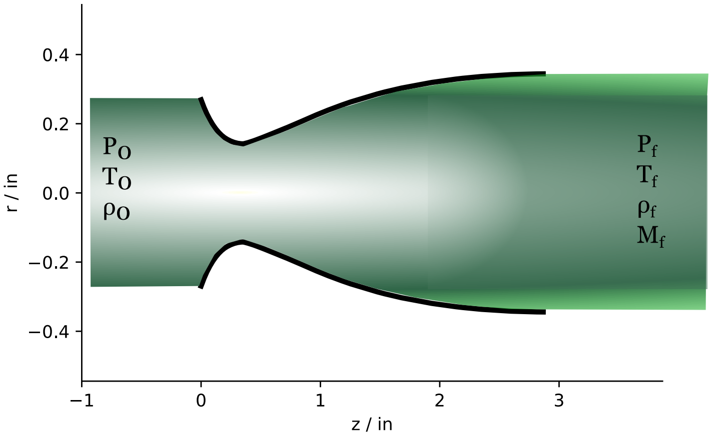

Figure 3.1: Calculated contour (black) for a Laval nozzle designed for argon at 54K. To the left of the nozzle is the stagnation region, where the properties of the gas are at their initial values of T_0, P_0 and ρ_0. After exiting the nozzle on the right, the flow is shock free and uniform with known values of T, P, and ρ.

3.2 Axisymmetric nozzle design

Laval nozzles require a contour similar to that shown above in Fig 3.1, and typically come in one of two configurations: 2 dimensional (2D: 4 wall rectangle with 2 walls that are the Laval contour and 2 that are parallel) or axisymmetric. Axisymmetric nozzles are simpler to design, and agnostic with regard to orientation of the nozzle, which is most suitable for the design considerations of the instrument. They also don't suffer from the same boundary layer issues that are caused by the corners with the parallel walls in 2D nozzles. For axisymmetric nozzles, the wall contour is first calculated in terms of radius, r and the distance along the flow-axis, z. The resulting contour is then rotated around the z-axis to produce a 3 dimensional nozzle that can be produced through 3D printing[78] or with a

CNC lathe.

The nozzle designs were calculated using a custom python script which is available on GitHub.[†] Designing a nozzle that produces a flow with desirable conditions is a difficult problem to solve analytically, but is much simpler to do numerically. This is accomplished through the method of characteristics (MoC), an approach to solve the momentum, continuity and energy equations by transforming the partial differential equations into ordinary differential equations. The MoC is used to produce a core contour for the ideal isentropic flow, and will be discussed in detail in section 3.2.1. This contour is then corrected for the effect of heat transfer and friction with the nozzle wall by iteratively solving the Navier-Stokes equations, creating the real world nozzle contour. The following sections describe how the basic equations of fluid dynamics are leveraged to numerically calculate these contours with the desired flow parameters.

3.2.1 The Isentropic Core

Characteristics

The discussion in this section follows derivations in Refs 72, 81, and 84.

The method of characteristics uses a bottom up approach to producing nozzles with an exit flow of the desired parameters, beginning with a target flow, and finding the wall contour that will produce it. A streamline is defined as a curve whose tangent at any point along the curve corresponds to the direction of the flow velocity at that point. The equations in this section are for axisymmetric nozzles in cylindrical coordinates. The

---

[†] https://github.com/zsb1010/LavalProject

streamlines for a supersonic, steady, inviscid flow such as in a Laval nozzle are described by the following equation:

$$\left(1-\frac{u^2}{a^2}\right)\frac{\partial^2\phi}{\partial z^2}+\left(1-\frac{v^2}{a^2}\right)\frac{\partial^2\phi}{\partial r^2}-\frac{2uv}{a^2}\frac{\partial^2\phi}{\partial z\partial r}=0 \tag{3.13}$$

where a is the acceleration, $u=\frac{\partial\phi}{\partial z}$, and $v=\frac{\partial\phi}{\partial r}$, ϕ is the full velocity potential defined by: $\nabla\phi=\vec{v}$, and is a function of z and r such that $\frac{\partial\phi}{\partial z}=f(z,r)$. This relationship and the definition of an exact differential produces the following equations:

$$\mathrm{d}\left(\frac{\partial\phi}{\partial z}\right)=du=\frac{\partial^2\phi}{\partial z^2}dz+\frac{\partial^2\phi}{\partial z\partial r}dr \tag{3.14a}$$

$$\mathrm{d}\left(\frac{\partial\phi}{\partial r}\right)=dv=\frac{\partial^2\phi}{\partial z\partial r}dz+\frac{\partial^2\phi}{\partial r^2}dr \tag{3.14b}$$

Equations 3.13 and 3.14 form a system of equations with 3 unknowns: the second derivatives $\frac{\partial^2\phi}{\partial r^2}$, $\frac{\partial^2\phi}{\partial z^2}$ and $\frac{\partial^2\phi}{\partial z\partial r}$. This system can be solved using Cramer's rule, shown below for $\frac{\partial^2\phi}{\partial z\partial r}$:

$$\frac{\partial^2\phi}{\partial z\partial r}=\frac{\begin{vmatrix}1-\frac{u^2}{a^2} & 0 & 1-\frac{v^2}{a^2}\\ \mathrm{d}z & \mathrm{d}u & 0\\ 0 & \mathrm{d}v & \mathrm{d}r\end{vmatrix}}{\begin{vmatrix}1-\frac{u^2}{a^2} & -\frac{2uv}{a^2} & 1-\frac{v^2}{a^2}\\ \mathrm{d}z & \mathrm{d}r & 0\\ 0 & \mathrm{d}z & \mathrm{d}r\end{vmatrix}} \tag{3.15}$$

Given the value of $\frac{\partial^2\phi}{\partial z\partial r}$, this equation can be solved for any arbitrary choice of dz and dr with corresponding values of du and dv constrained by that choice. There is an exception however that leads to the denominator of Equation 3.15 being 0. In order for the value of $\frac{\partial^2\phi}{\partial z\partial r}$ to be finite, the the numerator must also be zero, which leads to an indeterminate form of the equation. The line coming off an arbitrary point on the streamline is a characteristic line along which the derivatives of the flow field variables (ρ, T, P) are indeterminate, and the slope is dr/dz. Along these lines, the partial differential equations that describe the flow become ordinary differential equations (ODEs), which can be readily solved by numerical integration.

The slope of the characteristic can can be determined by setting the denominator in Equation 3.15 to 0 and solving for dr/dz using the quadratic formula.

$$\left(\frac{dr}{dz}\right) = \tan(\theta \mp \mu) \tag{3.16}$$

where $\mu = \arcsin(1/M)$ and θ is the angle of the flow velocity with respect to the z axis.

Equation 3.16 indicates that any given point on a streamline lies at the intersection of 2 characteristics as shown in Figure 3.2.

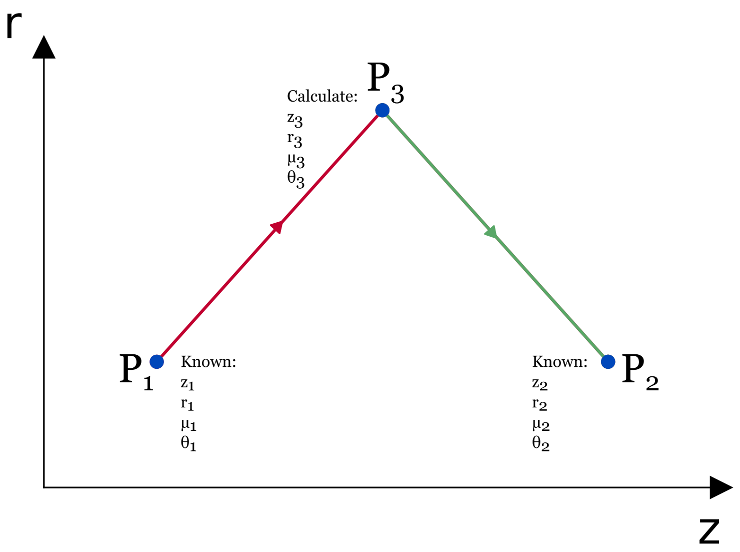

Figure 3.2: Characteristic lines from points 1 and 2 intersecting at point 3. The red line represents the positively sloped characteristic running through point 1, and green line the negatively sloped characteristic running through point 2.

Setting the numerator of Equation 3.15 to 0, which is necessary for the characteristic lines to be indeterminate and finite, and rearranging gives the following relationship:

$$\frac{1}{v}\frac{\mathrm{d}v}{\mathrm{d}\theta} = \mp\tan\mu + \frac{\sin\mu\tan\mu\sin\theta}{\sin(\theta\mp\mu)}\frac{1}{r}\frac{\mathrm{d}r}{\mathrm{d}\theta} \tag{3.17}$$

Equation 3.17 is a set of ODEs called the compatibility relations, which describe the Mach number and the flow angle for a point on the characteristic. They will be used with Equation 3.16 to calculate the mesh of characteristics used for designing an axisymmetric nozzle.

Method of characteristics

Beginning with point 1 (P_1) and point 2 (P_2) where the coordinates, flow angle and Mach angle are all known, it is possible to calculate those same properties for point 3 (P_3) using Equations 3.16 and 3.17. P_3 occurs at the intersection of a positive characteristic from P_1, and the negative characteristic from P_2, demonstrated in Figure 3.2.

For the characteristic with a positive slope originating from P_1, Equation 3.16 is solved by finite differences.

$$\frac{r_3 - r_1}{z_3 - z_1} = \tan(\theta_1 - \mu_1) = \frac{\sin(\theta_1 - \mu_1)}{\cos(\theta_1 - \mu_1)} \tag{3.18}$$

which can be rearranged to:

$$r_3\cos(\theta_1 - \mu_1) - z_3\sin(\theta_1 - \mu_1) = r_1\cos(\theta_1 - \mu_1) - z_1\sin(\theta_1 - \mu_1) \tag{3.19}$$

dividing both sides by $\cos(\theta_1 - \mu_1)$ results in:

$$r_3 - z_3\tan(\theta_1 - \mu_1) = r_1 - z_1\tan(\theta_1 - \mu_1) \tag{3.20}$$

Through the same steps, the negatively slopped line from P_2 can be written:

$$r_3 - z_3 \tan(\theta_2 + \mu_2) = r_2 - z_2 \tan(\theta_2 + \mu_2) \tag{3.21}$$

because the values of z, r, θ and μ are known for both P_1 and P_2, the system of two equations created by Equations 3.19 and 3.21 can be solved for z_3 and r_3.

Solving for θ_3 and μ_3 requires solving a similar system of equations derived from equation 3.17. Rewriting it:

$$\mathrm{d}\theta \pm \frac{\mathrm{d}v}{v\tan(\mu)} \mp \frac{\sin(\theta)\sin(\mu)}{sin(\theta \mp \mu)}\frac{\mathrm{d}r}{r} = 0 \tag{3.22}$$

The finite difference form for the positive characteristic originating at P_1 becomes:

$$\theta_3 + \frac{v_3}{v_1\tan(\mu_1)} = \theta_1 + \frac{1}{\tan(\mu_1)} + \frac{\sin(\theta_1)\sin(\mu_1)}{\sin(\theta_1 - \mu_1)}\frac{(r_3 - r_1)}{r_1} \tag{3.23}$$

For the negatively sloped characteristic, the finite difference form of Equation 3.17 is:

$$\theta_3 - \frac{\vec{v}_3}{v_2\tan(\mu_2)} = \theta_2 - \frac{1}{\tan(\mu_2)} - \frac{\sin(\theta_2)\sin(\mu_2)}{\sin(\theta_2 + \mu_2)}\frac{(r_3 - r_2)}{r_2} \tag{3.24}$$

Equations 3.23 and 3.24 form a system of equations that can be solved for θ_3 and v_3 using known values (v can be converted to M and μ as previously noted).

If P_1 and P_2 are on the axis ($r = 0$, $\theta = 0$) then a modified version of the system of equations should be used, as $\frac{\sin(\theta_1)\sin(\mu_1)}{\sin(\theta_1-\mu_1)r_1}$ becomes indeterminate. In the limit that r and θ go to zero, this term becomes approximately equal to $\frac{\theta}{r}$, and the following system of equations is used instead:

$$\theta_3 - \frac{r_3 - r_1}{r_3}\theta_3 + \frac{v_3}{\tan(v_1\mu_1)} = \theta_1 + \frac{1}{\tan(\mu_1)} \tag{3.25a}$$

$$\theta_3 + \frac{r_3 - r_2}{r_3}\theta_3 - \frac{v_3}{\tan(v_2\mu_2)} = \theta_2 - \frac{1}{\tan(\mu_2)} \tag{3.25b}$$

Calculating the properties of P_3 then allows calculation of two new characteristics originating from that point that can be used in subsequent calculations. From an initial set of data points on the axis of the flow (which will be described later), an entire mesh of character points can be built to describe the entirety of the flow at discrete points in the nozzle. An example is shown in Figure 3.3, where points are calculated on the mesh at every intersection of characteristics. The black wall contour will be discussed in the next section.

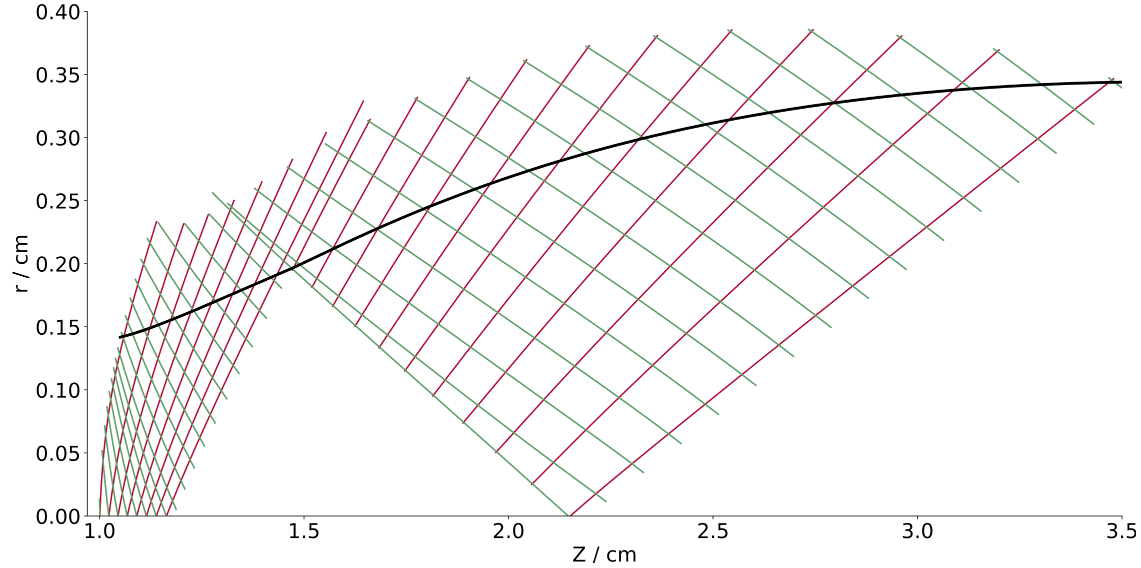

Figure 3.3: Mesh for a 54 K Argon nozzle with positively sloped characteristic lines shown in red and negatively sloped characteristic lines shown in green. Less than 5 percent of the lines calculated for the mesh are shown as the true mesh is too fine to be shown as distinct lines.

Calculating the core boundary

Once the mesh describing the flow is calculated, the last step is determining the isentropic core's "wall". Crucial to this step is the concept of mass flux, defined as the mass flow per unit area, which plays an important role in the continuity equation (Eq 3.3). Mass flux is conserved throughout the nozzle and is used to identify the points in the flow representing the wall, as the mass flux through each characteristic is equal.

To find the wall points, the dimensionless mass flux is calculated for one characteristic, using the following equation:

$$\mathrm{d}m = rW(1 - W)^{1/(\gamma-1)} \sin(\mu)\, \mathrm{d}\ell \tag{3.26}$$

where m is the mass flux, l is the length along the characteristic, and W is defined by:

$$W = \sqrt{\frac{\gamma - 1}{2} M^2 \left(1 + \frac{\gamma - 1}{2} M^2\right)^{-1}} \tag{3.27}$$

The characteristic used to calibrate the wall is the right running characteristic originating on the axis, and ending at the inflection point in the wall. To find the edge of the isentropic core, each characteristic is then integrated using Equation 3.26 point by point until the mass flux matches that of the first characteristic.

3.2.2 Algorithms for calculating nozzle contours

The code performs the following calculations in order to design a new nozzle.

1. The input parameters are the identity of the carrier gas, the desired temperature, and the wall inflection angle (∠COB). Directly related to the choice of temperature are the final pressure and density, which are related through the Mach number by Equation 3.12. The angle of inflection choice is important. If a poor angle is chosen, the calculation for the nozzle will not converge and the characteristic curves will cross. In general, this angle is selected to be as large as possible to minimize the overall length of the nozzle.

2. The calculation for the nozzle is divided into 3 regions, designated I, II, and III. See Fig 3.4. Region I is the initial acceleration into a supersonic flow. Region II is called the "source flow" region,[72,85] and it is assumed that the streamlines all originate at some point O. No characteristics are calculated for this region, except between BC and CD. In region III the flow reaches its final Mach number along line EF, and the shock waves are removed from the flow.

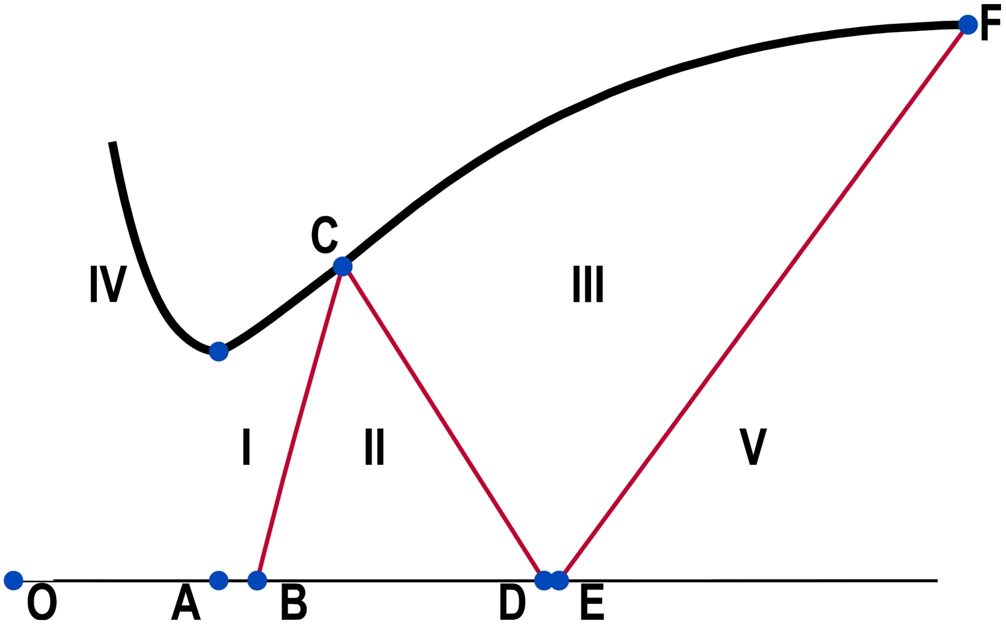

Figure 3.4: Regions of nozzle design. Region I represents the region where the flow is quickly accelerated to 2/5 of the terminal Mach number. In region II flow is assumed to originate from the origin O, and in region III the flow is accelerated to the final Mach number. Region IV is the converging section of the nozzle, with point A the axial location of the throat of the nozzle where the Mach number of the flow is equal to 1. Line BC is the first characteristic calculated, and the characteristic used to calibrate the mass flux through all characteristics. Line EF represents the last characteristic, after which the flow is uniform with the desired Mach number in region V.

3. The equations described in Section 3.2.1 are used to calculate points in the characteristic mesh from an initial set of points with known properties. The initial set of points for the isentropic core are located along lines AB, BC, CD, DE and EF.

4. For the line AB, the flow is accelerated from $M = 1$ at point A to 2/5 of the terminal Mach number at point B using $M = z^3$ from $1 \leq M \leq 0.4M_f$.

5. The points on the characteristic BC are calculated by picking a point P that is dθ above the axis so that $\angle$COP= $n * d\theta \equiv \theta_P$ where n is incremented for each successive point. A streamline of the expansion fan that originates at point O (the origin) and passes though point P is described using the Prandtl-Meyer angle (ψ),[86] related to θ_P by:

$$\psi_P = \psi_B + 2\theta_P = \sqrt{\frac{\gamma+1}{\gamma-1}} \arctan\left(\sqrt{\frac{\gamma-1}{\gamma+1}(M_P^2 - 1)}\right) - \arctan\left(\sqrt{(M_P^2 - 1)}\right) \tag{3.28}$$

   Solving this equation for M provides the Mach number, which can be used to calculate the distance d from O using:

$$d = \sqrt{\frac{1}{M}\frac{2}{(\gamma+1)}\left(1 + \left(\frac{\gamma-1}{2}M^2\right)\right)^{\frac{\gamma+1}{2(\gamma-1)}}} \tag{3.29}$$

   which is used to calculate the values for z and r of point P.

$$z = d \sin\theta \tag{3.30a}$$

$$y = d \cos\theta \tag{3.30b}$$

   A new angle θ_P is calculated, and process is repeated until θ_P reaches the value of the inflection angle.

6. Characteristic CD is calculated similarly to BC, starting with $\theta_P = \theta_C - n * d\theta$ with a slight change to Equation 3.28:

$$\psi_P = \psi_C + 2(\theta_C - \theta_P) \tag{3.31}$$

7. The flow along line DE is accelerated from M_D at point D (found when calculating CD) to the final Mach number at point E. The acceleration along the axis from D to E is defined as $M = z^4$ from $M_D \leq M \leq M_f$.

8. EF is defined as the right running characteristic for which the flow properties (including M) for every point in the flow are uniform. Additionally, the streamlines through EF are parallel to each other ($\theta = 0$) reducing Equation 3.16 to:

   $$\left(\frac{dr}{dz}\right) = \tan(\mu) \tag{3.32}$$

   The mass flux through EF needs to match the mass flux through BC, which is accomplished by using the slope in Equations 3.26 and 3.32 to find point F. The line is then divided into the same number of points as BC and CD.

9. The mesh for Region I and Region III are calculated separately using the same method based on Section 3.2.1. The characteristic points on the axis from A to B are used with Equations 3.19, 3.21, 3.23 and 3.24 to calculate a row of characteristic points just above the axis, which includes the second point on the BC characteristic. This is illustrated in Figure 3.5. This process is continued for as many rows as there are points in the BC characteristic.

   The mesh in Region III is calculated similarly, including the characteristic points from both CD and EF on either side of each row as the mesh is calculated. At this point, the mesh extends beyond the location of the wall of the isentropic core.

10. The total mass flux through each characteristic for the nozzle is calculated by integrating Equation 3.26 for the BC characteristic line.

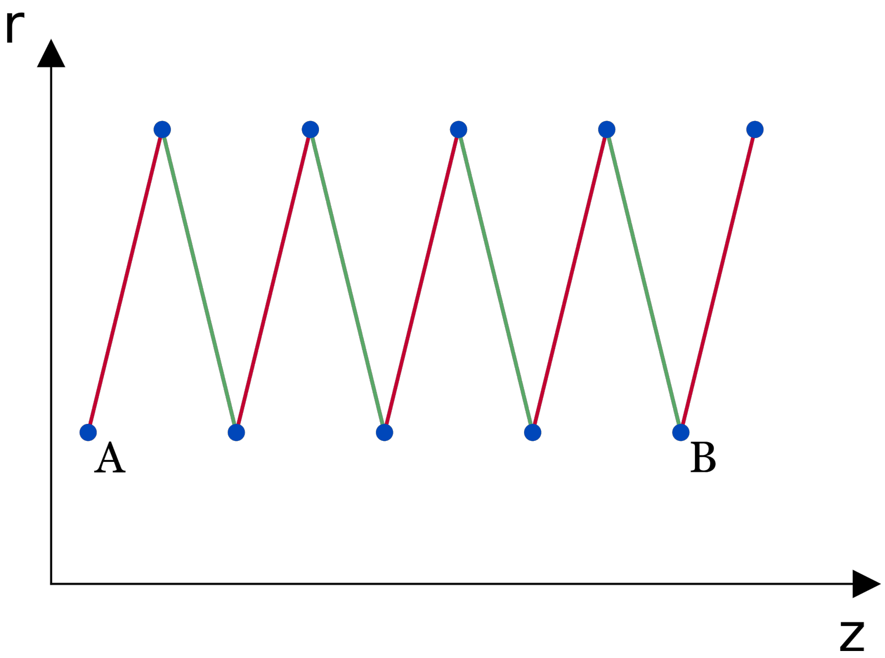

Figure 3.5: After a single iteration of the Method of Characteristics, the characteristic points along the flow axis, and a row above the axis are both known.

11. The wall of the nozzle is located using Equation 3.26. Each characteristic is integrated until the mass flux matches the value for BC. To achieve this match, the wall coordinate is found by interpolating between calculated characteristic points, assuming the characteristics are linear between points. The final wall points for the isentropic core are recorded as a set of (z, r) coordinates.

12. The nozzles have been scaled preserving the dA relationship of the nozzle so the value of r (radius) at the throat for argon nozzles is equal to 0.5 cm, and for the helium nozzles so that the throat radius is 0.25 cm.

3.2.3 Boundary Layer

The calculations in the previous sections assume that the flow does not interact with the wall of the nozzle. For a real flow, it is assumed that the effects of interacting with the wall only penetrates a finite distance from the wall. These wall effects are represented as a "momentum thickness" Θ. The boundary of the isentropic core is corrected to account for the momentum thickness, resulting in a nozzle which produces a flow consisting of the calculated isentropic core surrounded by a boundary layer.[28]

The calculation for the boundary layer is based on the momentum equation (Equation 3.6) the solution of which in cylindrical coordinates is:

$$n = -\frac{1}{r^2 u_e}\frac{\mathrm{d}u_e}{\mathrm{d}s}\frac{A}{M_e^{B-1}}\left(\frac{T_0}{T_e}\right)^{K+1}\int_0^s \left(\frac{T_e}{T_0}\right)^K r^2 M_e^{B-1}\,\mathrm{d}s \tag{3.33}$$

where s is the distance along the wall from the throat, the subscript $_0$ refers to the stagnation region before the nozzle, the subscript $_e$ refers to the edge of the isentropic core and A and B are constants from the work by Cohen and Reshotko.[87] They are measured parameters related to the momentum equation (N) by:

$$N = A + Bn \tag{3.34}$$

A and B for the calculation of nozzles using this code are set to $A = 0.44$ and $B = 5.1$.[72]

An estimate for the momentum thickeness (Θ_1) can be calculated for the isentropic core using:

$$\Theta_1 = \frac{T_e}{T_w}\left(-\frac{1}{Re_w}\frac{T_e}{T_0}\frac{n\,s\,u_e}{\mathrm{d}u_e/\mathrm{d}s}\right)^{1/2} \tag{3.35}$$

where the subscript w refers to the value at the wall, and the Reynolds number $Re_w = \rho_w u_e s/\mu_w$ where ρ is density and μ is the dynamic viscosity of the fluid.

This momentum thickness is related to displacement thickness $\delta^*(z,r)$, which will be applied to the wall points to correct them for the momentum thickeness. $\delta^*(z,r)$ is calculated:

$$\frac{\delta^*}{\Theta} = H_{tr} + \frac{\gamma - 1}{2} M_e^2 (H_{tr} + 1) \tag{3.36}$$

where H_{tr} is a physical form factor taken from a table in Cohen and Reshotko.[88]

The corrected wall points are calculated using the displacement thickenss:

$$z_w = z_e \tag{3.37a}$$

$$r_w = r_e + \delta^* \cos\beta \tag{3.37b}$$

where β is the angle of the wall with respect to the nozzle axis.

The true value for the momentum thickness of this new wall can then be calculated using:

$$\Theta = \frac{1 - \sqrt{1 - 2\left(\frac{\Theta_1}{r_w}\right)\cos\beta}}{\cos\left(\frac{\beta}{r_w}\right)} \tag{3.38}$$

where β is the angle with respect to the nozzle axis, and Θ_1 is the value of the momentum thickness estimated using Equation 3.35.

Algorithm for boundary layer

In practice, calculating the boundary layer works best as an iterative process. Starting with the coordinates and Mach numbers calculated for the isentropic core, the following process is performed.

1. The solution for the momentum equation (n) is calculated for each point along the isentropic core using Equation 3.33.

2. The values of n are used to calculate an estimate for the momentum thickness (Θ_1) using Equation 3.35.

3. Θ_1 is used in Equation 3.36 to find a value for the displacement thickness δ^*, which is used in Equation 3.37 with the core nozzle radius to predict a new radius for the wall that will produce the desired isentropic core surrounded by a boundary layer.

4. The wall coordinates are used with the estimate for momentum thickness in Equation 3.38 to calculate the true momentum thickness.

5. The true momentum thickness is then used with Equation 3.36 to calculate δ^*. This value is then used with Equation 3.37 to find a new set of wall coordinates.

6. These steps are iterated until the value of n converges.

7. After n converges, steps 2–5 are repeated until Θ converges. z_w and r_w following this process are output from the code as a .csv file for nozzle production.

3.3 Beam Profiles

Following the design of a nozzle it is produced on a computer numeric controlled (CNC) lathe from aluminum with a resolution of 0.004 inches. In the design of nozzles, assumptions in derivations as well as machining imperfections can cause the physical nozzle to deviate from theory. To correct for this, each nozzle is profiled to experimentally determine the final Mach number available for that nozzle. For the three nozzles designed and tested, the measured temperature is within 21 K of the design temperature. This process includes optimizing the conditions (backing pressure, chamber pressure) for nozzle operation for each nozzle produced.

Figure 3.6: Simple schematic of a Pitot tube. The Pitot tube is inserted in the flow to collect a sample. The output from the pressure transducer is recorded by an oscilloscope. The entire assembly is mounted on to a 3D stage controlled by stepper motors to probe the entirety of the beam.

The testing apparatus to perform beam profiling experiments relies on a Pitot tube equiped with a pressure transducer. Pitot tubes were invented in 1732 to measure the velocity of fluids, and have remained an important tool for aerodynamics.[81] By placing a Pitot tube in the path of the uniform beam from the nozzle, a shock wave forms inside the tube. This impact pressure is measured by a Kulite XCL-093-50A pressure transducer, see Figure 3.6. This process is illustrated by Figure 3.7 which is a 3D representation of a beam profile for a 54 K argon nozzle.

The measured impact pressure (P_i) can be related to the Mach number, and therefore the free stream pressure in the flow, by using the initial pressure from the reservoir (P_0) and the Rayleigh-Pitot formula:[76]

$$\frac{P_i}{P_0} = \left[\frac{(\gamma+1)M^2}{(\gamma-1)M^2+2}\right]^{\gamma/(\gamma-1)} \left[\frac{\gamma+1}{2\gamma M^2-(\gamma-1)}\right]^{1/(\gamma-1)} \tag{3.39}$$

The stagnation region of the nozzle includes a second pressure transducer that is used to measure P_0. Solving this formula for M provides all relevant parameters for the nozzle using Equation 3.12.

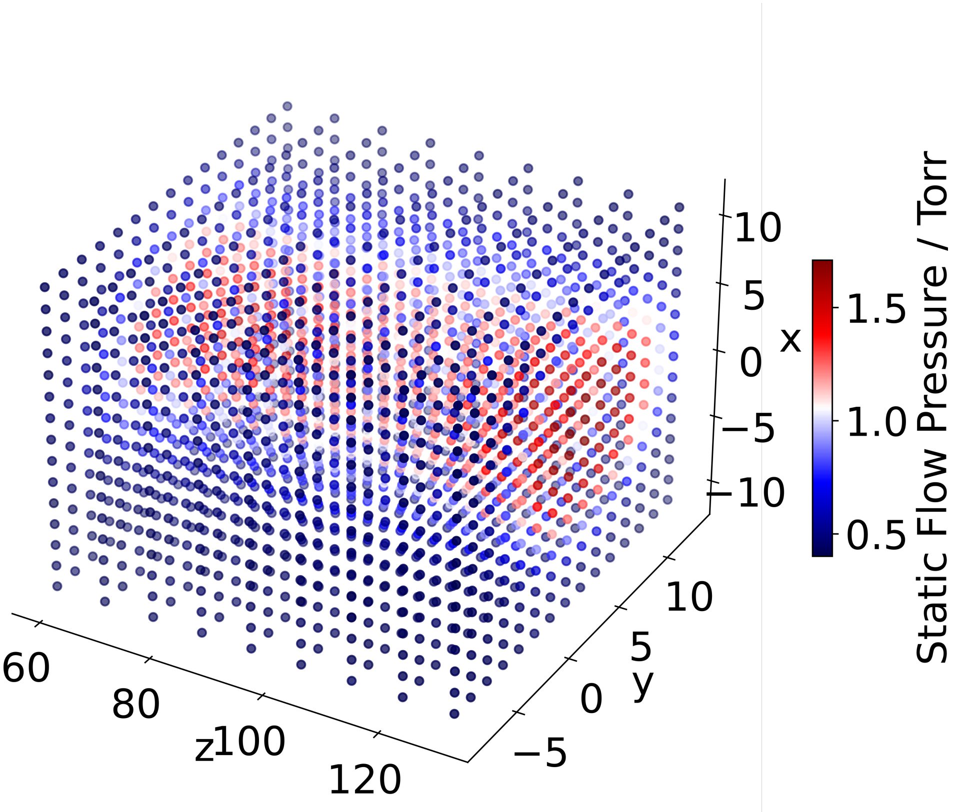

Figure 3.7: An example of how a beam profile is constructed. Each point represents a x, y, and z position that the Pitot tube is placed, with the color representing the static flow pressure of the beam at those coordinates. The exit diameter of the nozzles is typically less than 5 cm, so a 10x10 cm grid is sufficient to measure the XY plane of the beam. The beam length is dependent on the nozzle and backing pressures, typically on order of 10-30 cm.

It is also of note that the beam profiles measured are for a pulsed valve system. An example of the time evolution of a pressure trace is shown in Figure 3.8, where the impact pressure was measured for approximately 40 ms. The pressure for t=0 to t≈10000 μs is the baseline chamber pressure. Around t=10000, the piezo valve opens, and stays open for 9990 μs, with a target rise time of about 3200 μs. Steady state is achieved at about 16 ms (see inset panel). The stability over time and the length of beam determines the timescale for kinetics experiments. The goal during beam profiling is to maximize the distance from the nozzle, with a uniform/shock free flow in the beam through adjustments to the

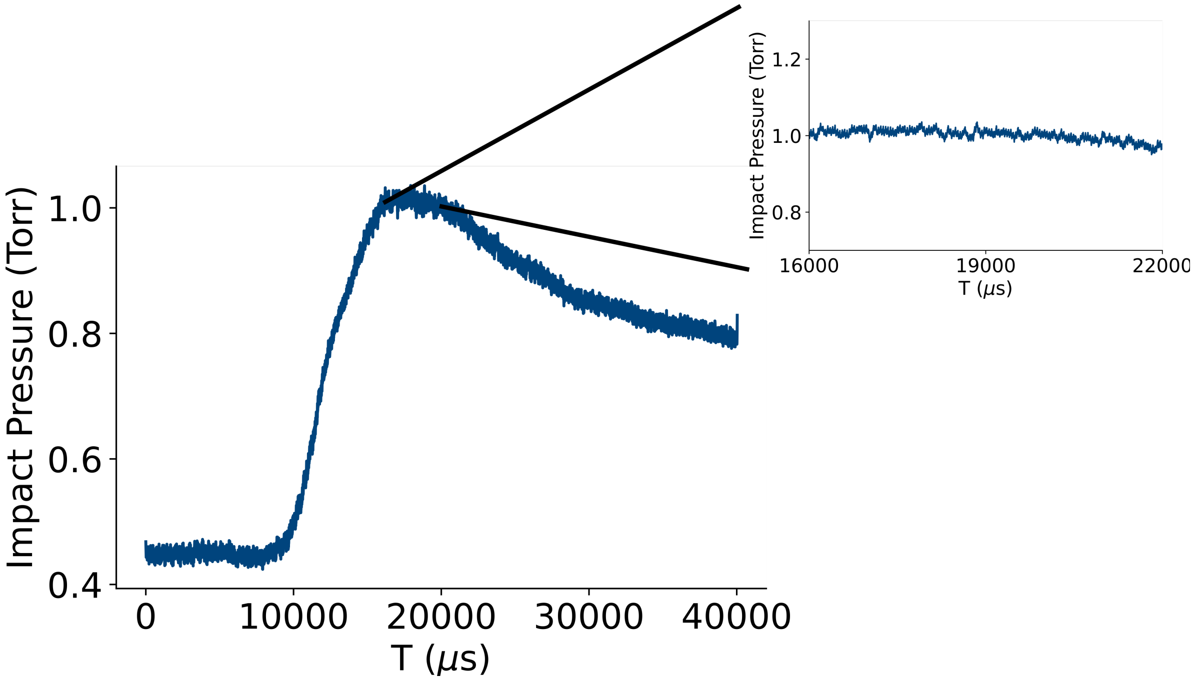

Figure 3.8: The averaged measurement of impact pressure vs time for a point in the uniform flow. This figure shows the base pressure of the chamber, a rise after the valve is open, about 6 ms of uniform flow, followed by a decrease in pressure after the valve closes.

backing pressure behind the valve, the chamber pressure and the open time for the valve.

When performing experiments to profile the beams, an iterative approach is taken to find the chamber pressure that works with each nozzle at different backing pressures until a uniform beam is achieved. Figures 3.9 and 3.10 show two measurements of non-ideal conditions for an argon nozzle designed for 55 K. For a nozzle to produce a uniform flow, the pressure of the chamber must match the pressure of the beam at the nozzle exit.[81] When the chamber pressure is higher than the flow pressure, a shock wave is formed at the nozzle exit that compresses the flow to a pressure that is equal to the chamber pressure. An example of a collapsing beam is shown in Figure 3.9, with an initial collapse of the beam, followed by a more diffuse and lower pressure beam. Profiles like this one indicate that a lower chamber pressure/backing pressure ratio (P_c/P_0) is needed for uniform flow.

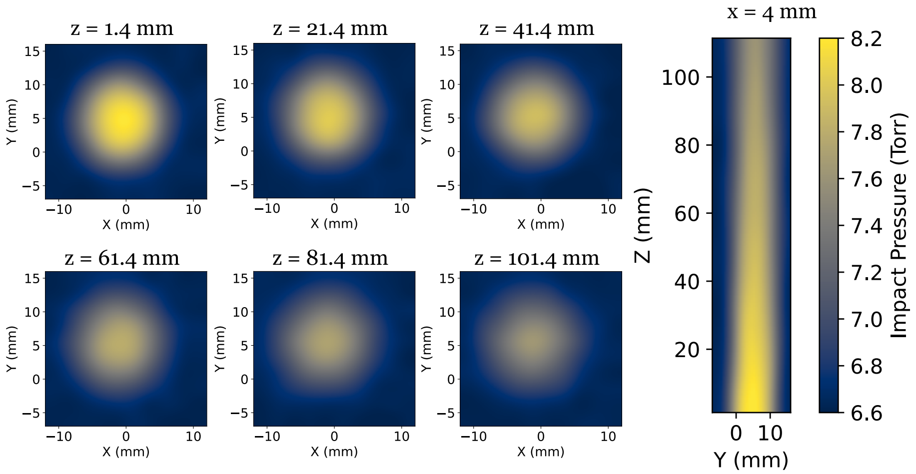

Figure 3.9: Experimental measurement of a collapsing beam. Chamber pressure is too high in this experiment, resulting in flow collapse after the nozzle exit.

When the chamber pressure is lower than the exit pressure of the nozzle, the flow must expand after exiting the nozzle. This results in shock waves that cause the flow to expand, decreasing pressure on the edge of the expansion to match the chamber pressure. This expansion results in further shock waves that continue to impact the flow, creating non-uniform conditions. This can be clearly seen in Figure 3.10, which has a much larger beam diameter compared to Figure 3.11. There is also evidence of shock waves in the disks and the side view of the profile, which exhibit a donut shaped low pressure region surrounding a barrel of higher pressure. Profiles like this one indicate that a higher P_c/P_0 ratio is needed for uniform flow.

Figures 3.11, 3.13, and 3.14 show the best impact pressure profiles for the three nozzles that have been produced and tested: An argon nozzle designed for 55 K, an argon nozzle designed for 30K, and a helium nozzle designed for 55 K.

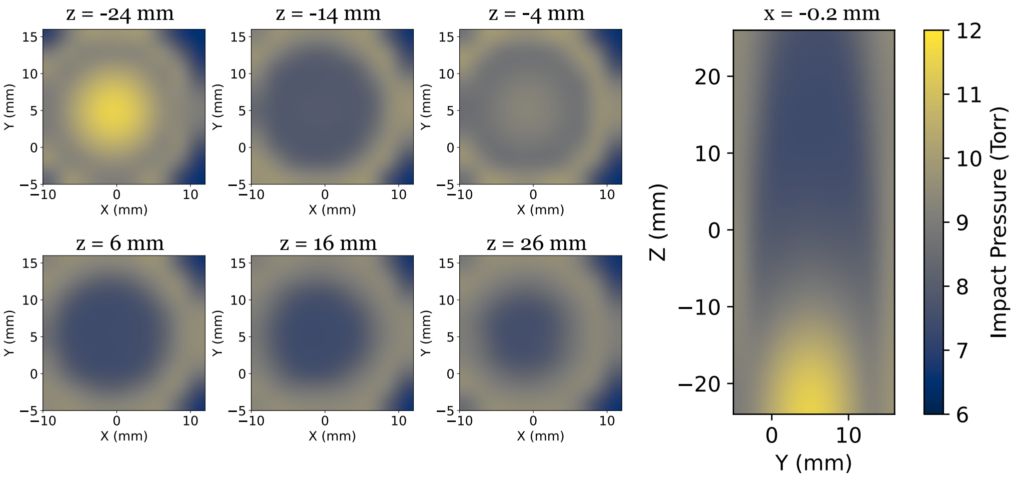

Figure 3.10: Experimental measurement of a diverging beam. The chamber pressure was too low in this experiment, leading to continued expansion of the flow outside of the nozzle.

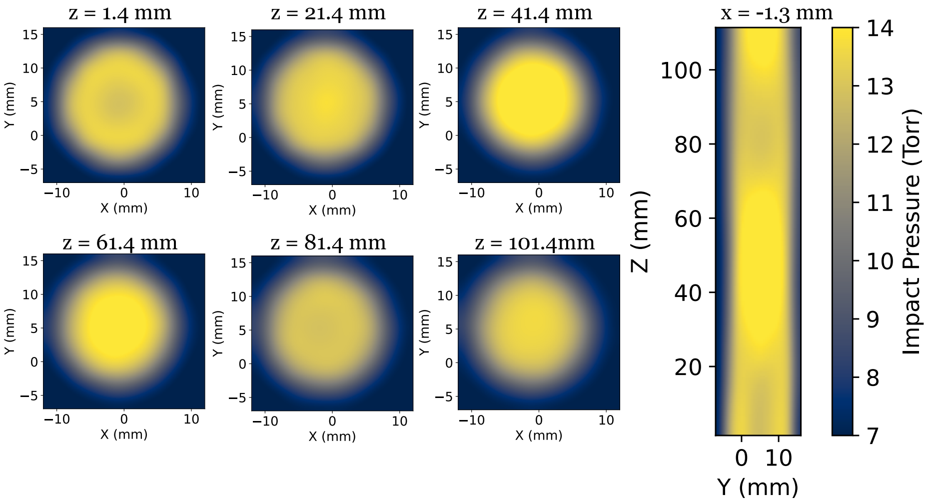

Figure 3.11: Experimental measurement of an uniform argon beam from a nozzle designed for 55 K. The measured temperature is 61.3 ± 0.8 K.

Figure 3.11 shows an example of uniform flow through a nozzle designed for argon. The throat of the nozzle is 1 cm in diameter and the exit is approximately 2.5 cm, of which about 2 cm represents the isentropic core. This matches well to the diameter measured using impact pressures. There are some slight pressure fluctuations in the flow axis, which can be seen as Mach diamonds in Figure 3.11. While these lead to some variation in the uniformity of the flow, they are comparable to nozzles used in prior kinetics studies.[76,89] This nozzle was able to achieve uniform flow for at least 10 cm. This is further demonstrated in Figure 3.12, which shows close to identical diameters and impact pressure profiles through the whole beam.

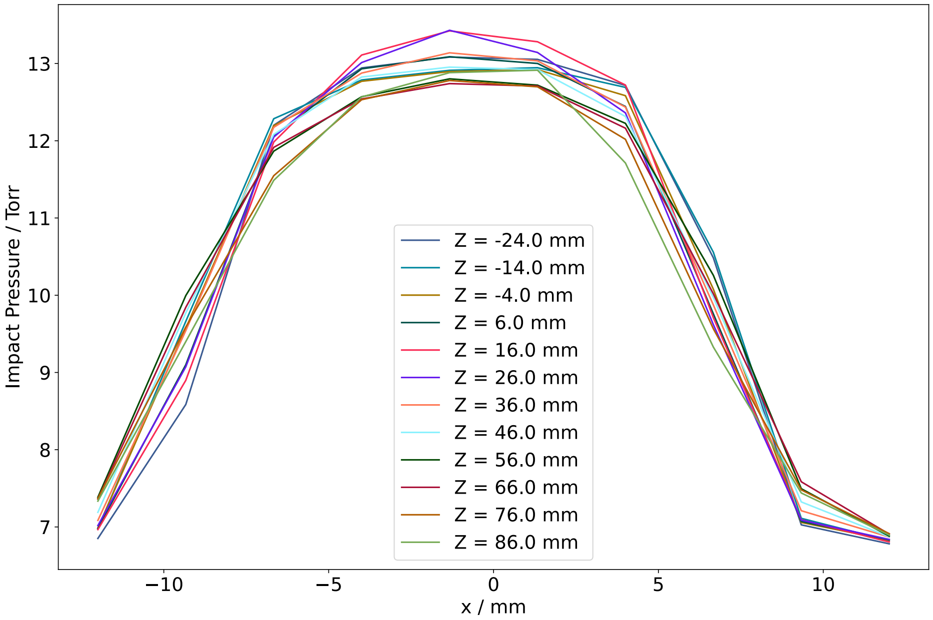

Figure 3.12: Uniform argon beam from a nozzle designed for 55 K. The ideal nozzle each slice would be identical as z increases.

Using Equation 3.39, the final temperature for this beam is measured as 61.3 ± 0.8 K. While this is 6 K warmer than originally designed, it is more important for the kinetics measurements to have a variety of nozzles at different well defined temperatures, so this departure from design is not critical.

Figure 3.13 shows the profile for another argon nozzle, designed to be 30 K. The stable region for this nozzle is shorter than the 55 K nozzle, only extending about 3.5 cm from the nozzle exit. The pressure and density for this test however were much lower than for the other nozzle (1.3 Torr vs 14 Torr). Experiments with the 55 K nozzle showed a similar shortening of the stable region of the beam when decreasing P_0 while maintaining the same P_c/P_0 ratio. The converted temperature in the flow was measured as 19.8 ± 0.4 K, which is significantly different than the design temperature, but still a useful operating temperature for kinetics experiments.

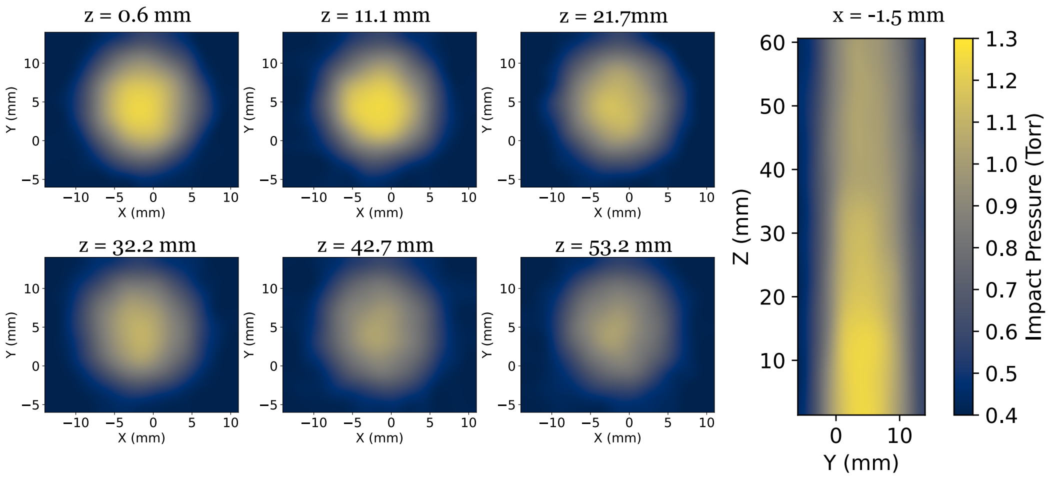

Figure 3.13: Example of a uniform beam for an argon nozzle designed for 30 K. The actual temperature measured here is 19.8 K

The helium nozzle profile was the most sensitive to P_c/P_0 when producing a uniform flow. To prevent the nozzle from becoming prohibitively long, the helium design was scaled to a throat diameter of 0.5 cm with an exit diameter of 0.95 cm, which translates to an isentropic core diameter of order 0.5 cm at the nozzle exit. It was also desirable to find a beam profile that was low density for the spectroscopy part of the experiment, which lead to very short stable regions from the helium nozzle.

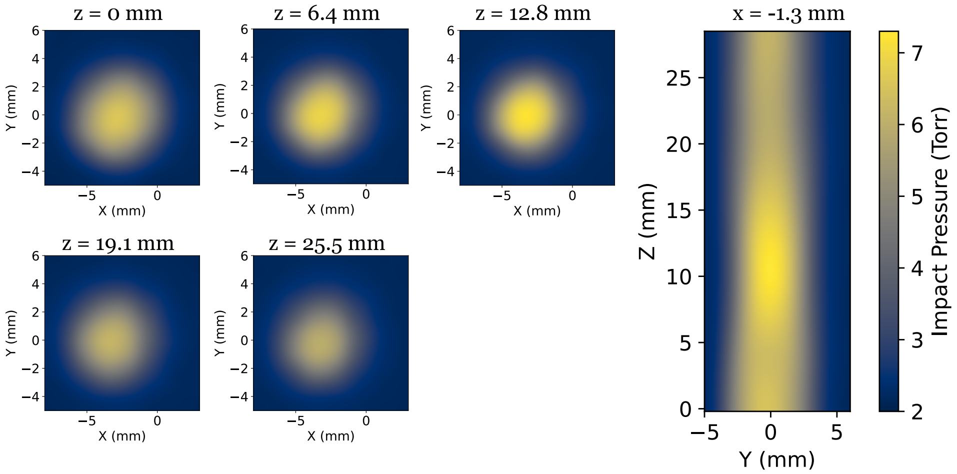

Figure 3.14: Example of a uniform beam for an helium nozzle designed for 55 K. The actual temperature measured here is 34.6 K.

Figure 3.14 shows an example of a uniform flow through a helium nozzle designed for 55 K. The actual temperature measured for this flow is 34.6 ± 1.5 K. Shocks are apparent in the flow just after the nozzle exit, and it can be seen that the beam is much higher pressure at the nozzle exit (-25.6 mm) than further in the flow (0 mm), but the relative stability of the flow in the first 1.5 cm indicates that with a higher P_0, the P_c/P_0 ratio could produce an uniform beam.

The nozzles produced and characterized here are a start towards the planned full coverage of 10–200 K. The next steps with these nozzles is to use spectroscopy to verify the flow temperature for a gas seeded into the uniform flow. Additional nozzles will also need to be produced and profiled to adequately cover the desired temperature range.

Chapter 4

Rotational and vibrational spectroscopy of CN-labeled ring molecules: Potential tracers of nonpolar carbon rings in space

The contents of this chapter are adapted, focusing on the contributions of the author, from the following publications:

Buchanan, Z., Lee, K. L. K., Chitarra, O., McCarthy, M. C., Pirali, O., Martin-Drumel, M. A. **A rotational and vibrational investigation of phenylpropiolonitrile ($C_6H_5C_3N$),** *Journal of Molecular Spectroscopy, 377, (2021), 111425.*

Chitarra, O., Martin-Drumel, M.-A., Buchanan, Z. S., Pirali, O. **Rotational and vibrational spectroscopy of 1-cyanoadamantane and 1-isocyanoadamantane**. *Journal of Molecular Spectroscopy, 378, (2021), 111468*

Chitarra, O., Lee, K. L. K., Buchanan, Z., Melosso, M., McGuire, B. A., Goubet, M., Pirali, O., Martin-Drumel, M. A. **Hunting the relatives of benzonitrile: Rotational spectroscopy of dicyanobenzenes.** *Astronomy and Astrophysics, 652 (2021) A163*

In the last 100 years, about 270 molecules have been detected in the interstellar medium (ISM) or circumstellar shells.[3] Of those detections, roughly 30% contain nitrile groups. The identification of these molecules has been facilitated by high quality laboratory spectroscopic characterization. As the amount of data from astronomical observations continues to grow, there is a pressing need for more molecules to be studied through rotational and vibrational spectroscopy.[90]

Due to their high prevalence in the ISM, nitrile containing molecules have been proposed as a potential tracer[20] for astronomical detection of nonpolar carbon rings. Molecules like benzene and adamantane have no permanent dipole, which makes them difficult to detect in space. The presence of a nitrile group on the molecule often creates a large dipole moment and a strong rotational spectrum. For example, adding a nitrile group to benzene makes benzonitrile with a dipole of 4.5 D,[91] making detection much more feasible. This chapter reports the work performed to characterize five nitrile substituted carbon rings: phenylpropiolonitrile (PhC_3N), 1-cyanoadamantane (CNAda), 1-isocyanoadamantane (NCAda), *m*-dicyanobenzene (*m*-DCB) and *o*-dicyanobenzene (*o*-DCB). These spectra have been measured and assigned in the cm-, mm-, far- and mid-IR bands of the electromagnetic spectrum with accuracy sufficient to facilitate astronomical searches. The structures for these compounds are shown in Figure 4.1.

PhC_3N is a benzonitrile derivative with an additional C_2 inserted between the ring and the nitrile group. It has been identified as a potential product in the reaction of phenylacetylene with cyano radical,[92] and its vibronic structure has been measured[93] but its pure rotational spectrum has not been previously studied. Also unreported is its

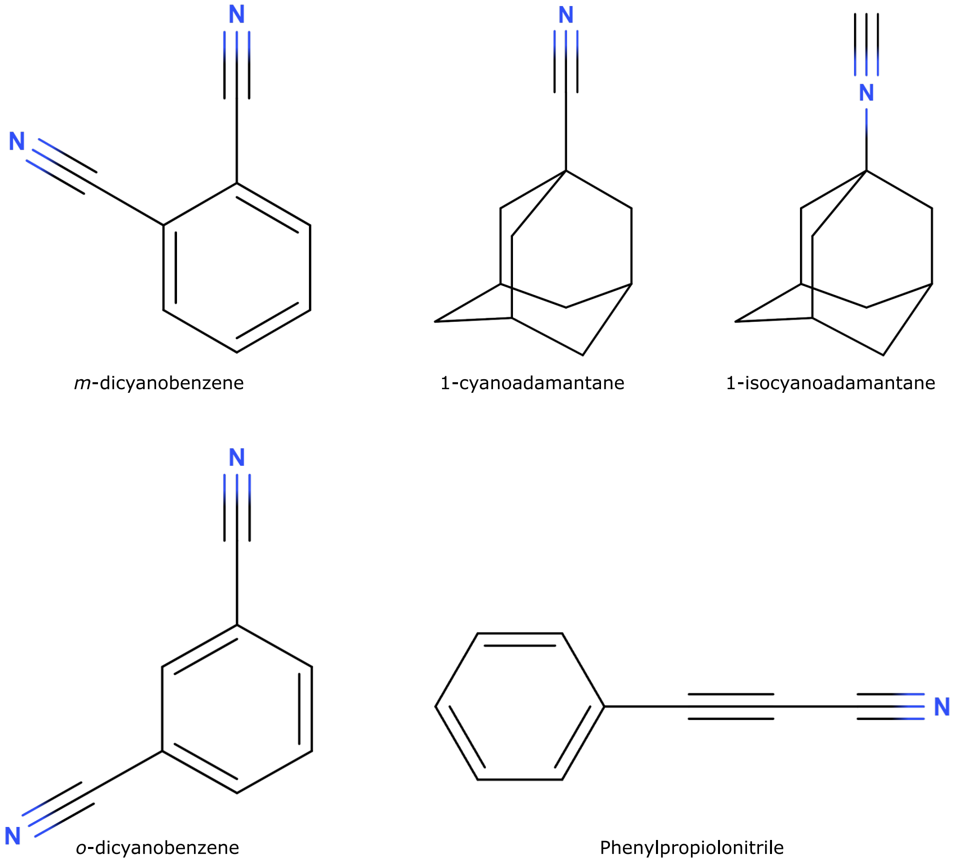

Figure 4.1: Molecular structure of *m*-dicyanobenzene, *o*-dicyanobenzene, 1-cyanoadamantane, 1-isocyanoadamantane, and Phenylpropiolonitrile.

infrared spectrum, which is relevant for comparison to other benzene derivatives, which often have perturbations and resonances that are problematic for assigning frequencies..

Dicyanobenzene has three isomers, *p*-dicyanobenzene (*p*-DCB), *o*-dicyanobenzene (*o*-DCB), *m*-dicyanobenzene (*m*-DCB). These DCBs have been of interest to researchers as they are relatively simple and facilitate research on the affect of nitrile substitution on aromatic rings.[94–97] The low vapor pressure and low solubility of DCBs make them difficult to study. Of the three, only the *p*-DCB isomer has had rotationally resolved spectra reported (as part of robribronic measurements).[98] A single vibrational transition for each of *o*-DCB and *m*-DCB was recorded for a solid[99] sample in the 1950s, and more recently IR spectra were recorded at low resolution in the 1–5 THz band.[100,101]

Diamondoids are a class of molecules that have long been suspected to be present in the ISM.[47–49] Bands observed at 3.43 µm and 3.53 µm bear a strong resemblance to the absorption features of thin-film nanodiamonds.[102,103] Recent developments in the synthesis of nanodiamonds and their derivatives[50] have provided the means for a more thorough characterization of these molecules. 1-cyanoadamantane and 1-isocyanoadamantane are nitrile substituted derivatives of adamantane. Previously[104] 3 transitions between 30–33 GHz have been measured for each, and rough rotational constants reported, which proved insufficient to assign the full spectrum.

The instruments used for mm-wave and IR measurements are described in Section 4.1. Section 4.3.1 shows the results for pure rotational and vibrational measurements of PhC_3N, Section 4.3.2 shows the results for the pure rotational and vibrational measurements of 1-cyanoadamantane and 1-isocyanoadamantane and Section 4.3.3 shows the results from the pure rotational measuresments of *o*-DCB and *m*-DCB.

4.1 Instrumentation

The measurements for this work were taken in two different labs: Infrared measurements were performed at the AILES beamline at the synchrotron SOLEIL in Saclay France, and the mm-wave spectroscopy was performed at the Institut des Sciences Moléculaires d'Orsay (ISMO).

4.1.1 ISMO mm-wave absorption spectrometer

Two experimental setups have been constructed at ISMO for mm-wave spectroscopy: a microwave plasma flow cell used for studies involving ions and radicals, and a gas flow cell used for studies of stable molecules. Figure 4.2 shows the schematic for the plasma cell, which is the same as the stable setup with the addition of a radio frequency plasma generator.

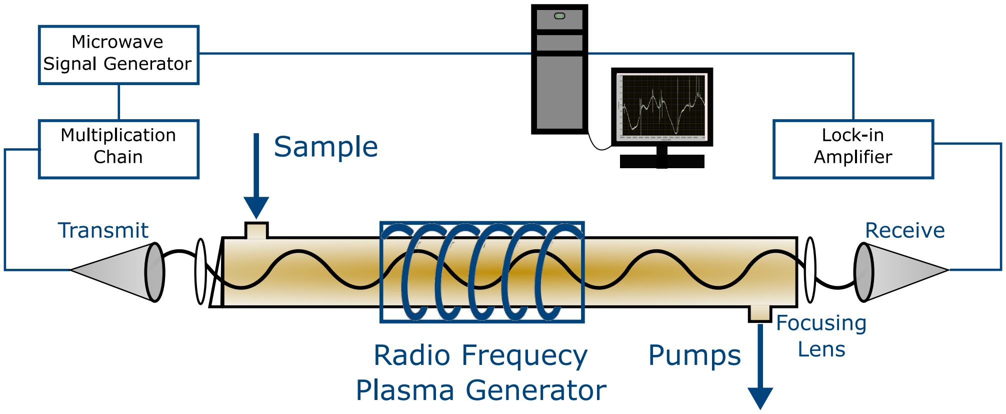

Figure 4.2: Schematic of the microwave plasma flow cell at ISMO. The vapor pressure of the sample is introduced into the Pyrex cell through a needle valve and is removed from the cell through another needle valve connecting to pumps to create a constant, low pressure flow through the cell. A 1000 W radio frequency generator is wrapped around the cell, which produces a plasma discharge approximately 1 m long. Detection is performed with one of two multiplication chain mm-wave absorption spectrometers, which can be easily swapped and a lock-in amplifier. The stable molecule experimental setup is similar, omitting the RF plasma generator.

The analyte is placed in a reservoir attached at one end of a 2 m long Pyrex cell connected by a needle valve set to provide a constant flow through the tube, with constant pressure inside the tube of the order of 1 μbar. The flow is maintained through the use of a choked flow to a turbo pump system. The cell is sealed with Teflon windows on either side placed at Brewster angles.

A radio frequency synthesizer (Rhodes & Schwarz, SMF100A) feeds one of two multiplication chains to produce mm-wave radiation: one ranging from 75-110 GHz, and one from 120-220 GHz. The output from the multiplication chains is broadcast through antenna horns and collimated through the cell using a 10 mm focal length Teflon lens, then focused onto a Schottky diode detector with a matching lens. The radiation is frequency modulated at 48.2 kHz, which produces a $2f$ modulation in the detector output, which is monitored with a lock-in amplifier. The frequency modulated light interacts with the molecular line shape to produce a 2nd derivative line shape. The accuracy for these measurements is in the 30-50 kHz range, limited by the linewidth of the transition and the signal to noise ratio (SNR) of the transitions. The 120-220 GHz spectrometer tends to have a lower SNR than the 75-110 GHz spectrometer.

4.1.2 Synchrotron SOLEIL AILES beamline Fourier-transform infrared spectroscopy with White-type cell

The IR spectra for these studies were measured using the AILES A beamline at the synchrotron SOLEIL (called AILES from here on).[105] AILES (see Figure 4.3) is equipped with a Bruker IFS125 Fourier transform interferometer and is capable of using as its light source either synchrotron radiation or an internal silicon carbide globar, attenuated with an adjustable entrance iris. For far-IR measurements, a mylar-silicon beamsplitter and a helium cooled hot electron bolometer (HEB) are used, while for the mid-IR a KBr beamsplitter and a Mercury-Cadmium-Telluride detector (MCT) is used.

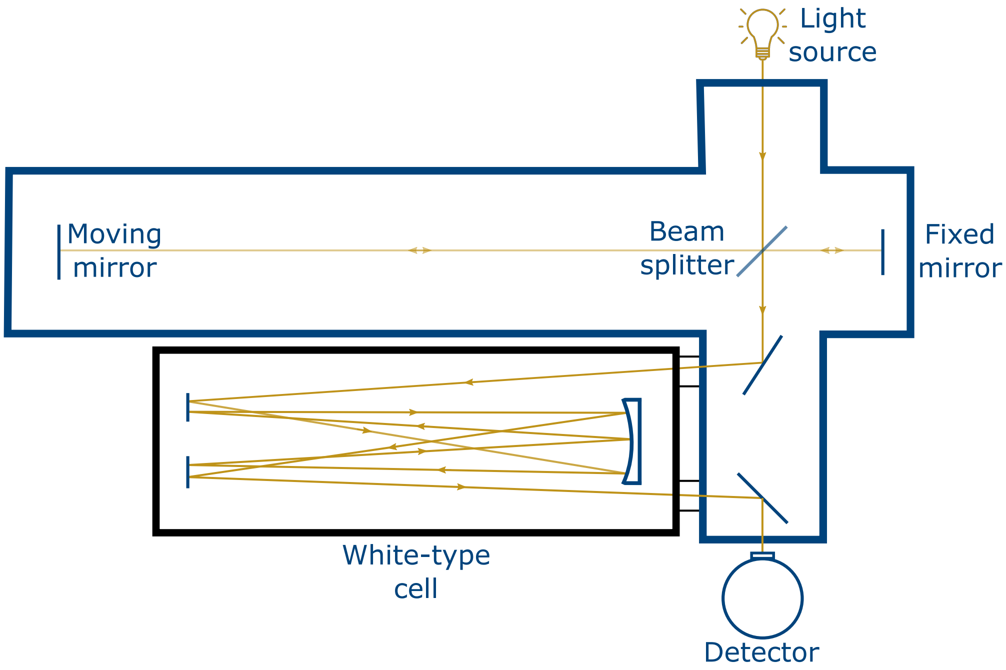

Figure 4.3: Schematic of the gas phase spectroscopy setup at the AILES A beamline. The light source for this instrument can be an internal globar, or radiation from the synchrotron. The light goes through a Michelson interferometer (Bruker IF125), then is passed into a White-type multipass cell. Vapor from the analyte is held static in this chamber at a few μbar. The light is then collected on a detector (HEB for far-IR, MCT for mid-IR).

The sample cell for this setup is a 3 m aluminum chamber equipped with a White-type multipass cell,[51,106] which extends the optical path length to approximately 150 m. The long path achieves high signal-to-noise with a small amount of sample in a relatively short amount of time. The far-IR spectra were recorded from 50-650 cm^{-1}, and the mid-IR spectra from 500-3200 cm^{-1} with a maximum resolution of <0.0009 cm^{-1}, limited by the mirror path of 5 meters.

4.2 Methods

Samples were purchased from commercial sources and used without further purification for mm-wave and IR measurements.

4.2.1 Computational predictions

For PhC_3N Gaussian16[107] was used with second order vibrational perturbation theory (VPT2) using ωB97X-D[108]/cc-pVQZ[109] to calculate: optimized geometry, harmonic and anharmonic vibrational frequencies and relative intensities for each vibrational mode. For CNAda, NCAda, *o*-DCB, and *m*-DCB, Gaussian09[110] was used to calculate at a MP2/cc-pVTZ[109] level geometry optimizations and harmonic vibrational frequencies. Harmonic frequency analysis was performed to predict distortion constants except for PhC_3N, which used the anharmonic calculations. The results of these calculations are reported with the experimental results in the appropriate sections of this chapter.

4.2.2 Vibrational spectroscopy

PhC3N

Mid-IR and far-IR spectra were measured at AILES for PhC_3N, CNAda, and NCAda from 50–3200 cm^{-1}. The chamber was evacuated and 5 μbar of the sample introduced to the chamber following several iterations of a freeze-pump-thaw cycle. The relevant light source, resolution, and number of co-averages are given in Table 4.1.

Table 4.1: Parameters for FTIR experiments.

	PhC_3N	CNAda	NCAda
Light source	globar	synchrotron	synchrotron
Resolution / cm^{-1}	0.5	1	1
# of co-averaged scans (FIR/MIR)	100/500	500/500	500/500

4.2.3 Rotational spectroscopy

The mm-wave spectra for all five molecules were measured using the stable molecule cell as ISMO and a $2f$ harmonic modulation scheme. The relevant experimental parameters for each molecule are reported in Table 4.2.

Table 4.2: Parameters for mm-wave experiments.

	PhC_3N		CNAda		NCAda		*o*-DCB		*m*-DCB	
Frequcy range / GHz	75-97	120-214	75-97	120-214	75-97	120-214	75-110	120-220	75-110	120-220
pressure / μbar	2.	2.	3.3	1.7	1.7	0.7	1-2	1-2	1-2	1-2
modulation frequency / kHz	48.2	48.2	48.2	48.2	48.2	48.2	48.2	48.2	48.2	48.2
frequency step / kHz	50	50	30	30	30	50	50	50	50	50
FM deviation / kHz	200	250	130	260	130	260	180	360	180	360
time constant / ms	50	100	100	20	100	50	100	100	100	100
Dwell time / ms	200	400	400	80	400	200	400	400	400	400
Line accuracy / kHz	50	50	30	50	50	50	50	50	50	50

The parameters for each molecule were optimized using a strong transition, balancing linewidth with SNR.

4.3 Results

4.3.1 Phenylpropiolonitrile

Vibrational spectroscopy

Figure 4.4 shows the experimental spectrum for PhC_3N and the simulated spectrum produced using the ωB97X-D[108]/cc-pVQZ[109] anharmonic frequencies.

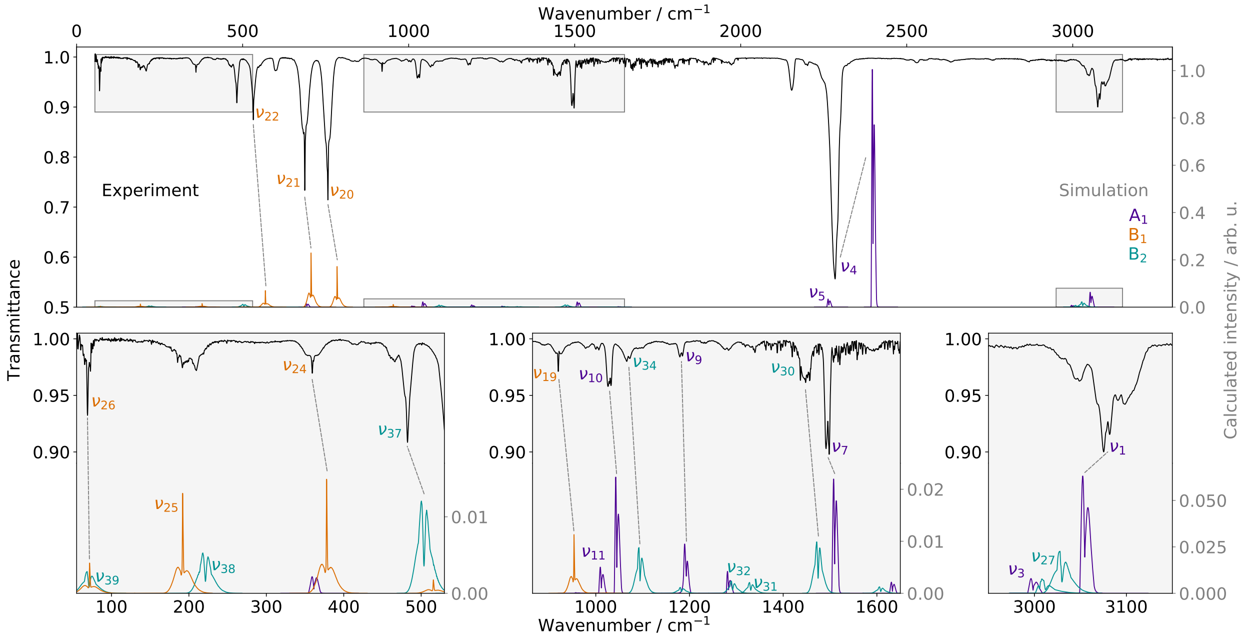

Figure 4.4: The top panel shows the experimental vibrational spectrum in black. The bottom spectrum is a simulation produced with PGOPHER[111] and the anharmonic vibrational frequencies. Three panels show zoomed in regions of the spectrum, with the assignments from Table 4.3 shown as dashed lines, and proposed assignments labeled, but not connected. Bands that have no assignment are not labeled.

PhC_3N belongs to the C_{2v} point group and its vibrational modes have the following symmetry: $\Gamma = 14\,A_1 \oplus 3\,A_2 \oplus 9\,B_1 \oplus 13\,B_2$. IR active symmetries for C_{2v} are A_1, B_1, B_2. These modes can be seen in Table 4.3 with their corresponding frequencies and intensities. All predicted fundamental vibrational frequencies for PhC_3N lie within the range of frequencies covered by AILES, 50-3200 cm^{-1}.

Predicted vibrational frequencies and measured rotational constants were used in PGOPHER to produce a simulated spectrum. In the simulation, modes with A_1 symmetry tended to be narrower than B_1 or B_2 symmetries, and B_1 modes were the only bands with a strong Q branch. Of the 36 IR active bands in this molecule, 14 have been assigned with confidence (indicated by Assign. in Table 4.3) with an additional 9 modes tentatively

Table 4.3: Fundamental harmonic and anharmonic vibrational frequencies and intensities for PhC$_3$N calculated at a ωB97X-D[108]/cc-pVQZ[109] level. The experimental results were assigned using these calculations. Frequencies for unambiguous assignments are reported in the Assign. column, while more uncertain assignments are reported in Tentative.[112] The δ values for tentative assignments are reported in italics.

Mode		Harm. Calc.		Anharm. Calc.		Experimental			
ν	Sym.	Frequency [cm^{-1}]	Int. [km/mol]	Frequency [cm^{-1}]	Int. [km/mol]	Assign. [cm^{-1}]	Tentative [cm^{-1}]	Relative intensity	δ^a [%]
1	A_1	3214	6.7	3055	13.5	3078		0.15	0.8
2	A_1	3226	5.6	3026	0.0				
3	A_1	3197	0.0	2999	1.7		3047	0.06	*1.6*
4	A_1	2431	242.3	2399	220.1	2284		0.77	-4.8
5	A_1	2292	10.7	2265	7.5		2154/2198	0.10	*-4.9/-3.0*
6	A_1	1675	1.0	1633	0.5				
7	A_1	1545	7.7	1510	4.9	1495		0.19	-1.0
8	A_1	1306	1.6	1284	0.8				
9	A_1	1214	2.1	1193	2.0	1182		0.03	-0.9
10	A_1	1064	4.6	1045	4.5	1029		0.07	-1.5
11	A_1	1027	1.3	1012	1.0		1004/981	0.02	*-0.8/-3.1*
12	A_1	981	0.1	960	0.0				
13	A_1	706	3.4	693	3.5				
14	A_1	371	0.8	362	0.5				
15	A_2	1019	0.0	1000	0.0				
16	A_2	876	0.0	862	0.0				
17	A_2	413	0.0	412	0.0				
18	B_1	1042	0.0	1023	0.0				
19	B_1	967	2.8	953	2.4	920		0.07	-3.5
20	B_1	792	38.7	784	32.7	757		0.54	-3.4
21	B_1	716	36.7	706	42.7	687		0.61	-2.6
22	B_1	576	13.2	568	12.4	532		1.00	-6.3
23	B_1	523	0.2	515	0.3				
24	B_1	384	2.8	377	2.8	359		0.19	-4.9
25	B_1	195	2.6	192	2.5		185	0.13	*-3.4*
26	B_1	74	0.6	71	0.7	69		0.44	-3.3
27	B_2	3206	1.9	3030	9.5		3095	0.09	*2.1*
28	B_2	3222	8.4	3012	2.6				
29	B_2	1646	0.7	1608	0.5				
30	B_2	1493	8.6	1475	4.5	1448		0.06	-1.8
31	B_2	1364	1.2	1331	0.9		1336	0.02	*0.4*
32	B_2	1320	1.3	1292	1.0		1280	0.02	*-0.9*
33	B_2	1193	0.4	1183	0.5				
34	B_2	1117	4.4	1094	3.8	1069		0.04	-2.3
35	B_2	644	0.0	635	0.0				
36	B_2	584	0.5	574	0.4				
37	B_2	511	5.3	504	5.6	482		0.63	-4.3
38	B_2	226	2.3	221	2.4		209	0.16	*-5.6*
39	B_2	71	1.1	71	1.2		69	0.44	*-2.7*

[a] δ = (Exp. − Anharm.Calc.)/Anharm.Calc. × 100

proposed (indicated as Tentative in Table 4.3). Frequencies are within 5% of the calculated values in each case, and for those assigned were enough removed from neighboring transitions that there was no confusion in the assignment. Relative intensities were also used to match predictions, though the difference in relative magnitudes for measurement and simulation were $> 10\%$. While the relative intensity patterns for the measured spectrum mostly followed the simulation, a few exceptions are outlined below.

The tentative assignments for 9 of the vibrational modes were difficult to resolve because the regions around the predicted frequencies were too congested (obvious band overlap) or the signal was not strong enough to be distinguished from noise.

Either the frequency of the Q-branch or the frequency equidistant between the P and R branches was used as the fundamental frequency, due to the inability to resolve the rotational structure for a more accurate measurement. The estimated error for these values is ± 5 cm^{-1} for the transitions without a Q-branch and ± 2 cm^{-1} for the transitions containing a Q-branch.

There are a few irregularities with the assignments that merit mention. The ν_{26} band is much stronger relative to other bands than the calculations would suggest it should be (see Figure 4.4). One possibility is overlap with the ν_{39} band, which is unassigned and predicted to be near the same frequency, increasing the overall absorption. The proposed assignment for these bands is 69 cm^{-1}. Similarly, ν_{25} and ν_{38} are predicted to overlap around 200 cm^{-1}, with a corresponding complex feature in the spectrum in that window.

The hardest region to assign is around 3000 cm^{-1}, with many predicted transitions

State 1	State 2	Type	Coupling / cm^{-1}
$\nu_1 = 1$	$\nu_3 = 1$	DD	−6.6
$\nu_2 = 1$	$\nu_3 = 1$	DD	14.5
$\nu_3 = 1$	$\nu_6 = 1 + \nu_7 = 1$	FR	−23.2
$\nu_3 = 1$	$\nu_{29} = 1 + \nu_{30} = 1$	FR	−29.3
$\nu_{27} = 1$	$\nu_{28} = 1$	DD	9.4

Table 4.4: Anharmonic resonances and their corresponding off-diagonal matrix elements in the 3000–3200 cm^{-1} region. Darling-Dennison (DD) and Fermi (FR) resonances are indicated as Type.

seen in the combination structure of the rovibrational envelope. Anharmonic calculations for PhC_3N show resonances, which complicate the assignment. These complications have also caused issues with the assignment of other other cyclic compounds such as phenylacetylene[113] and naphthalene.[114] PhC_3N contains 5 IR active modes within 15 cm^{-1} of each other, and we expect the complication of the spectrum here is both due to competing bands absorbing, as well as a suspected mixing of the states. The values of the coupling for these states is given in Table 4.4. It is possible that further studies at lower temperatures or with isotopically substituted compounds could confirm and tighten the proposed assignments.

Rotational spectroscopy

Low *J* measurements were performed in the cm-band by collaborators at the Harvard Smithsonian Center for Astrophysics (CfA) from 8-18 GHz with a CP-FTMW spectrometer, and from 6-40 GHz using a cavity-enhanced Fourier transform microwave (CE-FTMW) spectrometer. CP-FTMW data is shown with the simulated data in Figure 4.5

PGOPHER software[111] was used to assign the 65 strong transitions identified in the

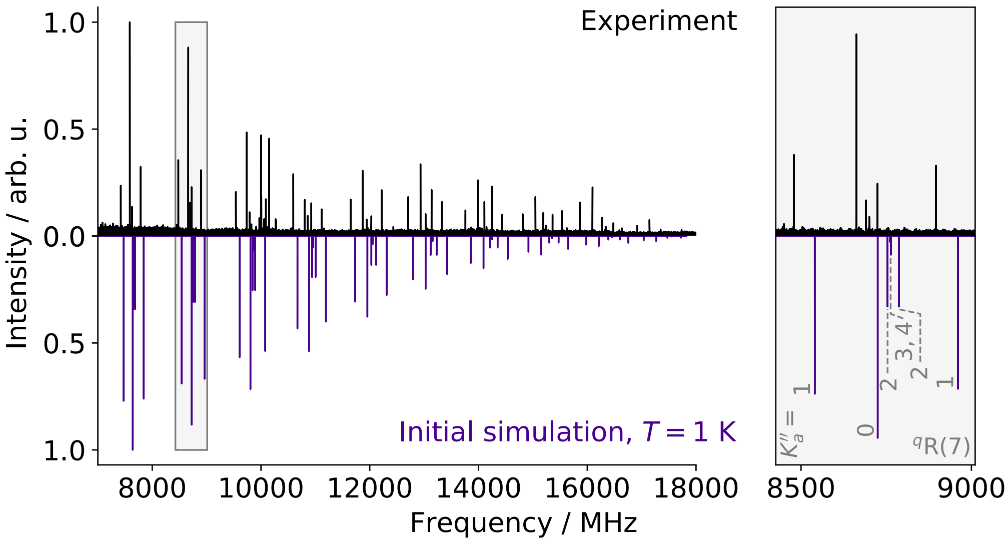

Figure 4.5: Comparison of CP-FTMW rotational spectrum with ωB97X-D/cc-pVQZ theoretical spectrum.

cm-band and fit the A_0, B_0 and C_0 constants. Initial estimates of these rotational constants from the geometry optimization were within 1% of the measured values in the cm-band. The fitted constants were used in conjunction with Pickett's SPCAT program[115] to predict higher J transitions in the 75-220 GHz frequency range which were subsequently assigned with the assistance of Lodyga's LWWa software.[116] A portion of the experimental and theoretical spectra are shown in Figure 4.6

6151 a-type transitions were assigned from the mm-wave spectra up to values of $K_a'' = 42$ and $J'' = 199$, corresponding to 3780 different frequencies. These assignments were used with SPFIT[115] to refine A, B and C, and to fit distortion constants to the octic terms.

The difference in number of assignments vs frequencies is due to *a*-type transitions appearing as doublets in the spectrum. The resolving power of the spectrometer, and the relative magnitudes of A with B and C dictate the ability to distinguish individual

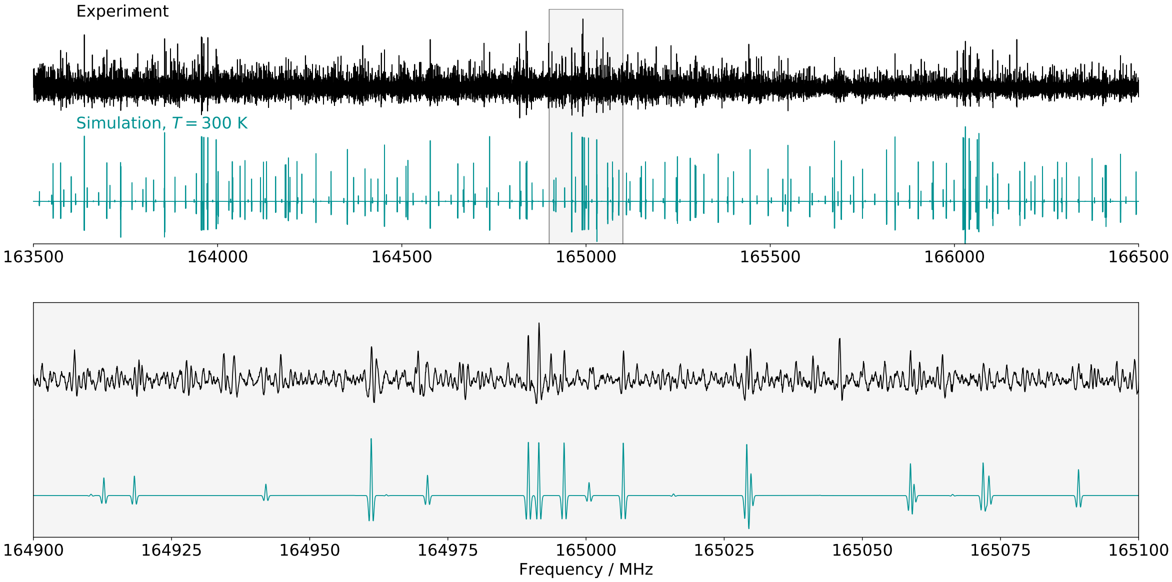

Figure 4.6: Comparison of experimental and theoretical mm-wave rotational spectra. The theoretical spectrum was calculated using the best fits for the rotational constants. The line density of the experimental spectrum is much more dense than the theoretical spectrum, likely due to lines from vibrational satellites.

transitions.[117] These doublets collapse at higher values of K_a, becoming more difficult to resolve.

The addition of hyperfine-resolved measurements from CE-FTMW spectroscopy performed by collaborators at the CfA enabled the assignment of 57 transitions between 8-20 GHz, and the fit of nuclear hyperfine coupling terms. χ_{aa} and χ_{bb} were fit from these assignments, with χ_{cc} reported as the calculated value, see Table 4.5. The hyperfine splitting is not resolvable in the mm-wave measurements, as it collapses as J increases. All fitted constants can be found in Table 4.5, and the transitions and their assignments are contained in the supplementary information for the paper.[112]

Table 4.5: Spectroscopic constants (rotational, centrifugal distortion, and nuclear quadruple constants) of PhC_3N in its vibrational ground state (in MHz) and relevant fit parameters using a Watson S-reduced effective Hamiltonian. Numbers in parenthesis are 1σ uncertainties expressed in the unit of the last digit.[112]

Constant	Calculated[a]	Experimental	δ[b]
A_0	5656.9	5659.722 (15)	0.05
B_0	567.0	569.582206 (39)	0.46
C_0	515.4	517.404488 (37)	0.39
$D_J \times 10^6$	3.6	3.85110 (77)	7.0
$D_{JK} \times 10^3$	0.78	0.827177 (85)	6.1
$D_K \times 10^3$	0.42	0.400 (68)	-4.8
$d_1 \times 10^6$	−0.50	−0.55191 (24)	10
$d_2 \times 10^6$	−0.52	−0.57101 (79)	9.8
$H_J \times 10^{12}$		−0.957 (11)	
$H_{JK} \times 10^9$		0.7916 (18)	
$H_{KJ} \times 10^6$		−0.03051 (10)	
$h_2 \times 10^{12}$		0.575 (15)	
$h_3 \times 10^{12}$		0.10329 (55)	
$L_{JJK} \times 10^{15}$		−1.295 (20)	
$L_{JK} \times 10^{12}$		0.06954 (86)	
$L_{KKJ} \times 10^{12}$		−3.512 (36)	
χ_{aa}	−4.96	−4.219 (77)	-14.9
χ_{bb}	2.39	2.114 (68)	-11.5
χ_{cc}	2.57	[2.143]	-16.6
# assigned transitions		6256	
# assigned frequencies		3877	
# hyperfine resolved transitions		57	
$J''_{\max}$, $K''_{a\,\max}$		199, 42	
rms /kHz		0.049	
σ[c]		1.00	

[a] ωB97XD/cc-pVQZ level of theory, Bayesian corrected[118] for A, B, and C, and centrifugal distortion constants derived from anharmonic force constants.

[b] $\delta = (B_{\text{exp.}} - B_{\text{calc.}})/B_{\text{calc.}} \times 100$

[c] Reduced standard deviation, unitless

Astronomical Considerations

The calculated dipole moment at ωB97XD/cc-pVQZ of PhC_3N is 5.9 D, much higher than the previous Stark-shift measurement of 4.5 D.[119] Based on the typical performance of ωB97XD/cc-pVQZ, it is expected the uncertainty of this calculation is ± 0.25 D.[118] The temperatures of dark clouds such as TMC-1, near 10-20 K, the strongest transition for PhC_3N is near 23 GHz, and it is expected that hyperfine splitting would be resolvable in observations of these regions. The linewidths in these clouds are comparable with those measured by the CE-FTMW, so it is expected that the rotational constants presented here are sufficient to enable detection in dark molecular clouds.

Collaborators searched the GOTHAM[120] survey using this fit, but did not detect PhC_3N towards TMC-1. Despite the lack of detection, PhC_3N remains strong candidate for astronomical searches in dark molecular clouds similar to TMC-1, owing to PhC_3N's strong dipole moment and its similarity to benzonitrile, which has been detected in these environments.

4.3.2 1-cyanoadamantane and 1-isocyanoadamantane

Vibrational Spectroscopy

Figure 4.7 shows the experimental spectrum for CNAda, and Figure 4.8 shows the experimental spectrum for NCAda. The far-IR regions of the spectra have been scaled so the peaks measured in the overlap between mid- and far-IR (near 600 cm^{-1}) are equivalent intensities, so that relative intensity comparisons can be performed between mid- and far-IR transitions.

1-cyanoadamantane and 1-isocyanoadamantane belong to the C_{3v} point group and their vibrational modes have the following symmetry: $\Gamma = 17\,A_1 \oplus 8\,A_2 \oplus 25\,E$. IR active symmetries for the C_{3v} point group are A_1 and E, and any vibrational modes sharing this

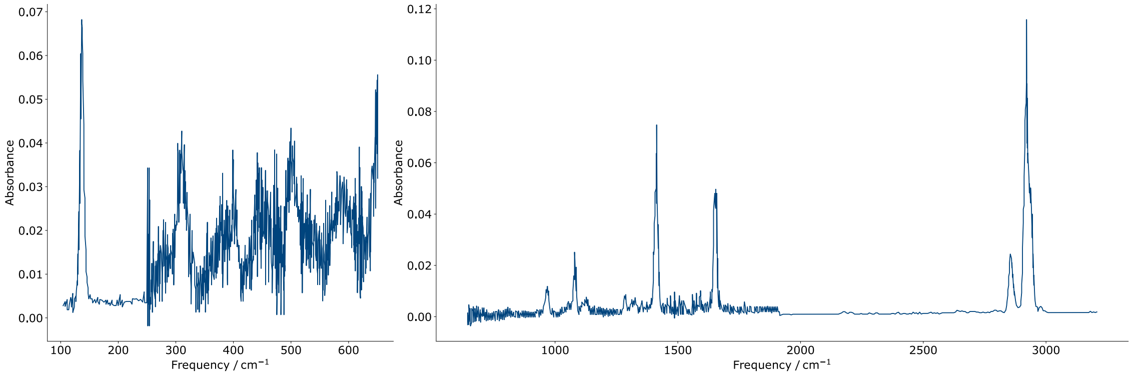

Figure 4.7: IR spectrum of 1-cyanoadamantane

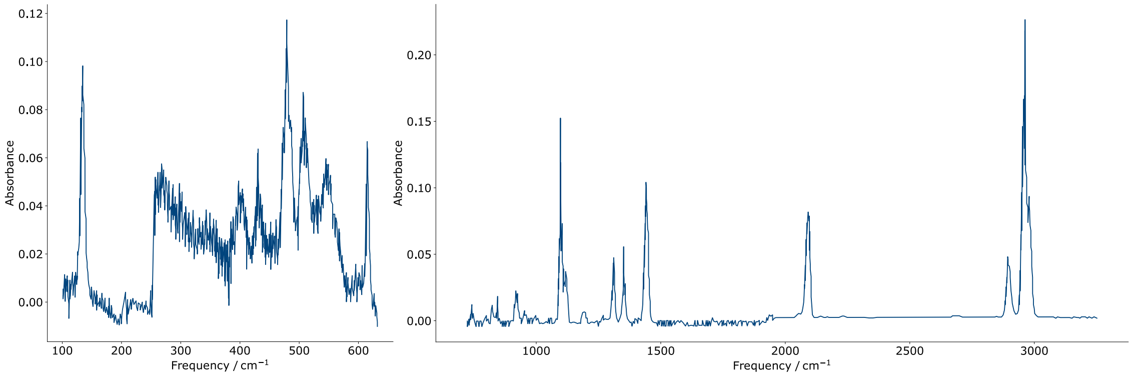

Figure 4.8: IR spectrum of 1-isocyanoadamantane

symmetry are expected to have have pure vibrational transitions. The IR active modes for both 1-cyanoadamantane and 1-isocyanoadamantane are reported in Table 4.6 (8 inactive A_2 modes omitted).

The experimental IR spectra of CNAda and NCAda share several features with their parent molecule adamantane. They each have strong transitions close to 3100 cm^{-1} associated with the C-H stretching modes in their cages. Their other bands are much weaker, with the exception of a scissoring motion that appears strongly near 1500 cm^{-1}. The ν_5 band of 1-isocyanoadamantane (CCN asymmetric stretch) is predicted to be much more intense than the corresponding band for 1-cyanoadamantane. This has been assigned to the band from the experimental spectrum at 2133 cm^{-1}. There are also several weaker bands in the 800–1500 cm^{-1} range. The congestion in this region for both molecules and the relatively low intensity of these bands make definitive assignments here difficult, but they have been assigned or proposed based on the calculated frequencies.

The lowest frequency mode for both molecules, ν_{50}, is at 137/134 cm^{-1}. This mode is related to the wagging motion of the CN group and is the most intense band in the far-IR. ν_{50}, ν_{17}, ν_{48} and ν_{49} are all expected to be significantly populated at room temperature, and the spectra show congested regions in the 250–800 cm^{-1} range from a mixture of hot and combination bands which make assignment of vibrational bands here difficult.

Overall, 17 modes of CNAda and 24 modes of NCAda were definitively assigned to the experimental spectrum. Additionally, 8 modes for CNAda and 4 modes of NCAda are proposed as possible assignments. Further experiments are required to assign these spectra with more confidence. The calculated and experimental data are summarized in Table 4.6.

In the absence of anharmonic calculations, NIST recommends the frequencies calculated using MP2/cc-pVTZ be scaled by a factor of 0.95,[121] which matches well with the ratios of assigned frequencies compared to theory (0.94 for far-IR and 0.98 in the mid-IR). Figure 4.8 shows contamination of the sample as an intense peak at 1718 cm^{-1} which does not correspond to any calculated value for 1-cyanoadamantane, but likely is the result of C-O stretching, which typically gives rise to an intense peak near 1700 cm^{-1}. There are no other unambiguous peaks however from which to deduce the identity of this contaminant.

Table 4.6: Vibrational modes of 1-cyanoadamantane and 1-isocyanoadamantane calculated at MP2/cc-pVTZ and comparison with experimental assignments. Experimental bands are separated into two columns: confident assignments are presented in the column "Assigned" and tentative ones in the column "Proposed".

		1-cyanoadamantane						**1-isocyanoadamantane**					
Mode		Calculated		Experimental				Calculated		Experimental			
ν	Sym.	Frequency	Intensity [a]	Assigned	Proposed	Rel Int	δ [b]	Frequency	Intensity [a]	Assigned	Proposed	Rel Int	δ [b]
ν_1	A_1	3110	59.5	2927		1.00	−5.9	3113	58.7	2928		1.00	−5.9
ν_2	A_1	3088	17.3	2927		1.00	−5.2	3091	27.0	2928		1.00	−5.3
ν_3	A_1	3062	25.7	2866		1.00	−6.4	3067	21.4	2869		0.20	−6.5
ν_4	A_1	3054	21.2	2866		0.29	−6.2	3056	21.4	2869		0.20	−6.1
ν_5	A_1	2179	0.7		2254	0.29	3.4	2108	78.1	2133		0.35	1.2
ν_6	A_1	1517	0.1					1518	0.1				
ν_7	A_1	1495	14.5	1458		0.56	−2.5	1496	11.4	1459		0.44	−2.5
ν_8	A_1	1391	1.0		1358	0.11	−2.4	1388	5.2	1361		0.24	−2.0
ν_9	A_1	1352	2.6		1320	0.12	−2.4	1345	10.1	1316		0.20	−2.1
ν_{10}	A_1	1157	0.2					1141	5.9	1111		0.16	−2.6
ν_{11}	A_1	1120	2.6	1099		0.10	−1.8	1110	17.8	1089		0.65	−1.9
ν_{12}	A_1	1003	2.8	979		0.14	−2.4	1001	0.1				
ν_{13}	A_1	924	0.1					927	3.4	900		0.10	−2.9
ν_{14}	A_1	791	0.3					793	0.6				
ν_{15}	A_1	712	1.2		700	0.06	−1.7	722	1.9	709		0.05	−1.8
ν_{16}	A_1	498	0.3		501	0.45	0.6	507	1.4	507		0.37	0.0
ν_{17}	A_1	384	0.01					393	0.2		400	0.22	1.6
ν_{26}	E	3118	63.7	2927		1.00	−6.1	3125	57.5	2928		1.00	−6.3
ν_{27}	E	3107	15.7	2927		1.00	−5.8	3109	17.0	2928		1.00	−5.8
ν_{28}	E	3086	134.1	2927		1.00	−5.2	3089	126.1	2928		1.00	−5.2
ν_{29}	E	3060	21.4	2866		0.29	−6.3	3064	18.3	2869		0.20	−6.4
ν_{30}	E	3054	48.3	2866		0.29	−6.2	3056	48.6	2869		0.20	−6.1
ν_{31}	E	1493	24.3	1458		0.56	−2.3	1493	24.5	1459		0.44	−2.3
ν_{32}	E	1480	0.1					1481	0.04				
ν_{33}	E	1403	0.1					1404	0.5				
ν_{34}	E	1378	2.2		1358	0.11	−1.4	1378	1.8				
ν_{35}	E	1345	0.1					1345	0.9				
ν_{36}	E	1328	0.04					1328	0.2				
ν_{37}	E	1288	0.1					1298	0.3				
ν_{38}	E	1212	0.69					1215	2.3	1189		0.03	−2.1
ν_{39}	E	1124	4.2	1104		0.10	−1.8	1124	6.0	1111		0.16	−1.2
ν_{40}	E	1077	0.007					1078	0.5				
ν_{41}	E	1000	3.6	979		0.14	−2.1	1006	1.2				
ν_{42}	E	963	0.6					964	2.4	936			−3.0
ν_{43}	E	898	0.03					899	0.003				
ν_{44}	E	834	1.6					835	3.1		793	0.05	−5.1
ν_{45}	E	652	0.3					650	0.2		614	0.28	−5.5
ν_{46}	E	541	0.003					486	2.5	478			−1.6
ν_{47}	E	437	0.2		442	0.37	1.1	432	0.1				
ν_{48}	E	399	0.3		397	0.40	−0.6	399	0.3		400	0.22	0.3
ν_{49}	E	307	0.5	309		0.44	0.5	300	0.1				
ν_{50}	E	134	9.1	137		0.70	2.4	135	11.2	134			−1.0

[a] For vibrational bands with an E symmetry, the reported intensity corresponds to the sum of the two equivalent band intensities calculated by Gaussian

[b] $\delta = (\tilde{\nu}_{\text{exp.}} - \tilde{\nu}_{\text{calc.}})/\tilde{\nu}_{\text{calc.}} \times 100$

Rotational Spectroscopy

The full spectrum for 1-isocyanoadamantane can be seen in Figure 4.9. The density of lines necessitated an iterative approach to assigning transitions and fitting constants for 1-cyanoadamantane and 1-isocyanoadamantane.

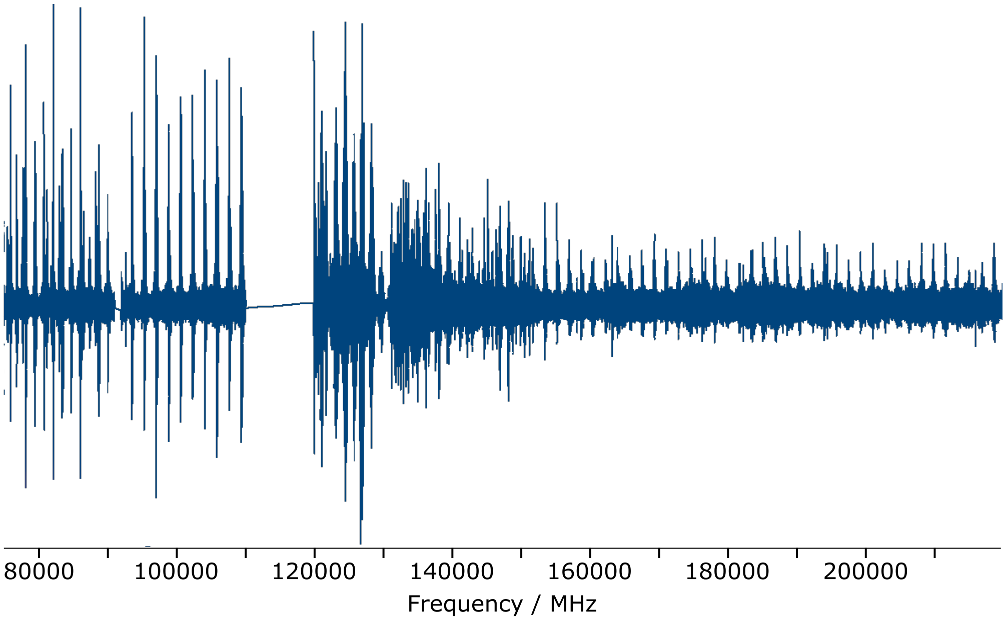

Figure 4.9: Full range rotational spectrum for 1-isocyanoadamantane.

(1) An initial assignment of several clusters of *a*-type transitions using PGOPHER provided a rough fit of the B_0 rotational constant. This fit was used with the calculated values for A_0, D_J, D_{JK} and D_K and SPCAT[115] to predict rotational energies for the adamantanes. (2) These predictions were plotted with LWWs[116] to assign branches of the same value of K. (3) After making assignments, SPFIT/SPCAT were used to fit rotational constants and predict new rotational energies. Steps 2 and 3 were repeated to continue to assign more transitions from the spectra.

Following this general fitting procedure, 4929 transitions in the ground state (A_1

symmetry) for 1-cyanoadamantane and 3968 transitions of 1-isocyanoadamantane in the ground state, were used to fit B, D_J, D_{JK}, H_{JK}, and H_{KJ}. As only a-type transitions were observed, it was not possible to calculate A or D_K, and these are left fixed at the calculated values. The reduced standard deviation for both fits was near 1 assuming experimental line accuracies reported in Table 4.2. All constants are reported in Table 4.7. Both molecules exhibit strong rigid-rotor character as the distortion constants are 6 orders of magnitude smaller than B, which is similar to other adamantane-like species.[51,104]

The energy of $\nu_{50} = 1$ vibrational state is 67.5 cm^{-1}, which has close to half the population of the ground state at room temperature, which was sufficient to enable assignment of pure rotational transitions within this state. To account for ℓ-type doubling (E symmetry) and the vibration-rotation interaction, q, η_J and ζ terms were included in the fit. Many lines in the spectra remain unassigned, and it is likely that more hotbands are present. However, the energy of the $\nu_{50} = 2$ band is similar to that of the $\nu_{49} = 1$ band, and we had no success fitting either.

4.3.3 *m*-DCB and *o*-DCB

Figure 4.10 shows the a portion of the pure rotational spectrum for *o*-DCB and the theoretical spectrum predicted by the calculated rotational constants prior to assignment.

To fit the mm-band spectra for the two DCB molecules, first hyperfine structure resolved CE-FTMW cm-band data obtained by collaborators at PhLAM[122,123] were used for an initial fit of the A, B, and C constants using PGOPHER software,[111] initially ignoring the hyperfine structure and focusing on the center of the clusters. The resulting constants

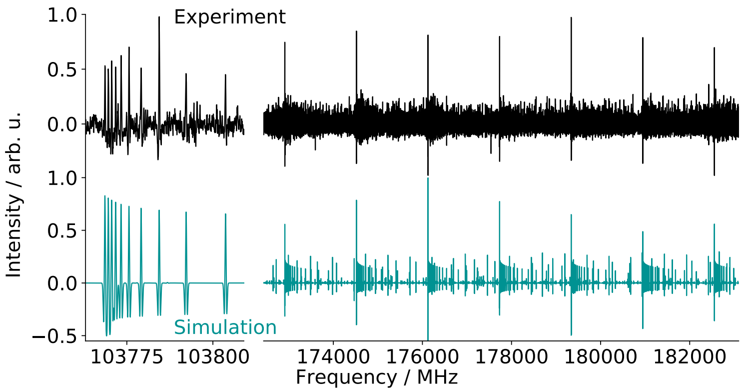

Figure 4.10: Example of a portion of the mm-wave spectrum of o-DCB with the simulated spectrum based on fitted rotational constants (see Table 4.8).

were then used with the SPCAT[115] program to predict transitions in the mm-band. For *o*-DCB/*m*-DCB, 5767/7561 transitions assigned to 4071/5695 frequencies were used to fit the rotational constants to a reduced standard deviation of 0.84/0.92 assuming line accuracies of 50 kHz (see Table 4.2). The parameters from the fit can be found in Table 4.8. The cm-band data were then revisited and the hyperfine structure assigned and nuclear quadrupole coupling constants fit.

Astronomical Considerations

The constants resulting from these fits facilitated a search in the interstellar medium for these molecules. Collaborators at MIT used the simulations resulting from these measurements to search data from the GOTHAM project[120] for *o*-DCB and *m*-DCB. Stacking 1522 lines from *o*-DCB and 2115 lines for *m*-DCB, they were not successful at detecting either towards TMC-1. They were able to establish upper limits on the column densities: $< 5 \times 10^{12}$ cm^{-2} for *o*-DCB and $< 7 \times 10^{11}$ cm^{-2} for *m*-DCB. Based on recent experimental work,[34] it is assumed that the efficiency of substituting 2 nitrile groups onto a benzene leads to an approximate 1:100 benzene:DCB ratio. This would result in an approximate expected column density of 2×10^{10} cm^{2}, which is well below the calculated maximum densities found.

Table 4.7: Spectroscopic constants (rotational, centrifugal distortion and l−doubling) for the ground state and first excited state (ν_{50} = 1) for 1-cyanoadamantane and 1-isocyanoadamantane using a Watson S-reduced effective Hamiltonian. Calculations were performed using Gaussian09 at MP2/cc-pVTZ. All frequencies are reported in MHz. Numbers in parenthesis are 1σ uncertainties expressed in the unit of the last digit.

1-cyanoadamantane

	Equilibrium	Ground State		Excited state ν_{50} = 1
Constant	Calculated	Experimental	δ^a	Experimental
A_0	1698.76	[1698.76]^b		[1698.76]^b
B_0	858.47	852.218045 (11)	-0.73	852.771240 (13)
$D_J \times 10^5$	1.22	1.231404 (47)	0.93	1.241490 (51)
$D_{JK} \times 10^4$	1.23	1.166870 (32)	-5.13	1.157348 (63)
$D_K \times 10^5$	-9.01	[-9.01]^b		[-9.01]^b
$H_{JK} \times 10^{11}$		4.443 (13)		4.068 (23)
$H_{KJ} \times 10^{11}$		-6.048 (18)		-5.811 (64)
$-2A\zeta$				-2700.90 (35)
$\eta_J \times 10^3$				0.823705 (61)
q^c	0.36			0.386501 (53)
# assigned transitions		4929		4375
$J''_{\max}/ K''_{\max}$		128/119		128/91
rms			0.033	
σ^d			1.11	

1-isocyanoadamantane

	Equilibrium	Ground State		Excited state ν_{50} = 1
Constant	Calculated	Experimental	δ^a	Experimental
A_0	1701.93	[1701.93]^b		[1701.93]^b
B_0	889.95	882.475497 (16)	-0.84	883.199299 (20)
$D_J \times 10^5$	1.27	1.286431 (76)	1.29	1.301015 (92)
$D_{JK} \times 10^4$	1.10	1.099262 (81)	-0.07	1.08068 (13)
$D_K \times 10^5$	-7.78	[-7.78]^b		[-7.78]^b
$H_{JK} \times 10^{11}$		4.698 (30)		3.763 (43)
$H_{KJ} \times 10^{11}$		-6.834 (88)		-6.39 (23)
$-2A\zeta$				-2850.2 (10)
$\eta_J \times 10^3$				1.11643 (12)
q^c	0.39			0.41759 (14)
# assigned transitions		3968		3703
$J''_{\max}/ K''_{\max}$		123/91		123/77
rms			0.048	
σ^d			1.01	

[a] $\delta = (B_{0\,\text{exp.}} - B_{\text{e calc.}})/B_{\text{e calc.}} \times 100$

[b] Fixed to the calculated value

[c] Calculated value of q in v_{50} = 1

[d] Reduced standard deviation, unitless

Table 4.8: Spectroscopic constants for *o*- and *m*- dicyanobenzene. Included are the calculated values from Gaussian09 at MP2/cc-pVTZ level of theory. All frequencies are given in MHz. The two nitrogen atoms in each molecule are equivalent to each other, and χ_{aa}(N), χ_{bb}(N), and χ_{cc}(N) are equal for both N atoms while χ_{ab}(N) takes opposite values.

	o-DCB			*m*-DCB		
	Calculated	Experimental	δ	Calculated	Experimental	δ
A_0	2012.43	2000.710452(98)	-0.58	2723.66	2723.018609(46)	-0.02
B_0	1341.09	1346.325041(27)	0.39	905.57	906.419893(21)	0.09
C_0	804.78	804.503123(25)	-0.03	679.61	679.859840(15)	0.04
$\Delta_J \times 10^5$	7.48	7.45641 (54)	-0.28	4.14	4.10739 (15)	−0.69
$\Delta_{JK} \times 10^4$	−4.19	−4.02541 (27)	−3.87	−4.32	−4.16931 (11)	−3.45
$\Delta_K \times 10^3$	1.82	1.718768 (75)	−5.79	2.63	2.565775 (28)	−2.56
$\delta_J \times 10^5$	3.14	3.132056 (31)	−0.40	1.68	1.657443 (78)	−1.40
$\delta_K \times 10^5$	−7.20	−6.54041 (11)	−9.15	5.85	6.12211 (64)	4.68
$\Phi_J \times 10^{11}$		5.523 (57)			2.1712 (50)	
$\Phi_{JK} \times 10^{10}$		−5.737 (20)			−2.663 (10)	
$\Phi_{KJ} \times 10^9$		1.1015 (59)			0.4702 (37)	
$\Phi_K \times 10^9$		1.911 (18)			4.7834 (65)	
$\phi_J \times 10^{11}$		2.703 (29)			1.0707 (27)	
$\phi_{JK} \times 10^{10}$		−1.645 (15)				
$\phi_K \times 10^9$		1.1220 (24)			2.0409 (88)	
χ_{aa}(N)	−2.36	−2.5243 (17)	6.69	−2.53	−26816(39)	6.60
χ_{bb}(N)	0.42			0.50		
χ_{cc}(N)	1.94			2.03		
χ_{bb}(N)$-\chi_{cc}$(N)	−1.52	−1.6256(52)	6.35	−1.54	−1.3408 (52)	−12.06
χ_{ab}(N)	−2.70	[−2.70][a]		−2.57	[−2.57][a]	
# assigned transitions		5767			7561	
# assigned frequencies		4071			5695	
$J''_{\max}/K''_{a\max}$		152/77			173/58	
rms		0.041			0.045	
σ[b]		0.84			0.92	

[a] Fixed to the calculated value. The removal of this parameter does not affect the present fit, however, considering its large value for both isomers, it has been kept in the model.

[b] Reduced standard deviation, unitless

Chapter 5

Development of new THz spectrometer coupled to synchrotron radiation

The contents of this chapter are adapted, focusing on the contributions of the author, from the following publications:

Lampin, J.-F., Pirali, O., Buchanan, Z. S., Eliet, S., Martin-Drumel, M.-A., Turut, J., Roy, P., Hindle, F., Mouret, G. **Broadband terahertz heterodyne spectrometer exploiting synchrotron radiation at megahertz resolution.** *Optics Letters, 44(20), (2019). 4985.*

Mammez, M.-H., Buchanan, Z., Pirali, O., Martin-Drumel, M.-A., Turut, J., Ducournau, G., Eliet, S., Hindle, F., Barbieri, S., Roy, P., Mouret, G., Lampin, J.-F. **Optically pumped terahertz molecular laser: Gain factor and validation up to 5.5 THz.** *Advanced Photonics Research, 3(4), (2022). 2100263.*

The THz region of electromagnetic spectrum spans from approximately 0.3–7 THz between microwave and infrared radiation.[57] This region in spectroscopy is often referred to as the THz gap, named because of the few components (sources, optics, detectors and electronics) that were availiable for this region. As a result of this lagging technology, it has traditionally been difficult to have simultaneous broadband and high resolution measurements in this region. The THz region is important to astrochemistry as most molecules as well as interstellar dust emit radiation in this range. THz spectroscopy can play an important role in searching for reaction intermediates and transient species in the ISM. The launch of the Herschel telescope in 2009 provided high quality THz measurements outside of the interference of Earth's atmosphere, SOFIA/GREAT is capable of measuring up to 4.59 THz, the Atacama large millimeter array (ALMA) from 0.04–0.95 THz and the High Elevation Antarctic THz (HEAT) telescope currently capable of probing the lower (0.5-2 THz) portion of the spectrum.

Improvements in THz technology will open interesting opportunities for studying rotational spectra of small molecules, and empower rotationally resolved rovibrational spectroscopy in studies performed on heavy molecules (greater than 20 atoms) which current technology struggles with. Multiplication chains have advanced sufficiently in recent years to allow for inexpensive narrow band high resolution THz spectroscopy up to 2.7 THz,[59] while photoconductive antennae breakthroughs have expanded broadband detection of THz light up to 2.759 THz.[61] Instruments capable of broadband measurements with resolution comparable to laser or multiplication chain measurements have not yet materialized, particularly in the regions between 2.7-9 THz.[124]

The HEROES consortium (HEterodyne Receivers OptimizEd for Synchrotron sources) is attempting to design and construct new instruments operating in the THz region. The work in this chapter will describe the construction of a new instrument, called THzSOLEIL, capable of 5 GHz of instantaneous bandwidth with a resolution of <100 kHz between 0.3–6

THz. The high spectral resolution is achieved through heterodyne mixing of light from SOLEIL with a local oscillator centered on the targeted frequency window. Conventional Fourier transform far-IR instruments operating in the 3 THz range at best can achieve around 30 MHz resolution.

Heterodyne detection in this case involves multiplying a local oscillator (f_{LO}) frequency with the synchrotron frequencies (f_s) to produce an intermediate frequency (f_{IF}).

$$f_{IF} = |f_{LO} - f_s| \tag{5.1}$$

The hot electron bolometer (HEB) used as a heterodyne mixer and detector records the absolute values of the difference intermediate frequencies, overlapping the regions where $f_{LO} > f_s$ and $f_{LO} < f_s$ into a single measurement between 0.1-2.5 GHz.[124] An example of a simulated spectrum recorded by the HEB is shown in Figure 5.1.

The light source for THzSOLEIL is the AILES beamline at the synchrotron SOLEIL, a bright, broadband continuum ideal for these measurements. The synchrotron provides 3.4 mW mean-power at a repetition rate of 353 MHz. Prior to irradiating the sample cell, the light is optically filtered to attenuate its power to about 1.6 μW.

The local oscillator used by THzSOLEIL is a quantum cascade laser (QCL)-pumped ammonia molecular laser developed by collaborators at the IEMN institute.[125] Molecular lasers have been used since the 1970s.[126] These original THz molecular lasers used a CO_2 laser to excite a molecular gas (such as NH_3), producing lasing. The CO_2 laser near 988 cm^{-1} excite a vibrational transition in the molecular gas, which then emits radiation from pure rotational transitions in the excited vibrational state. A cavity tuned to the frequency

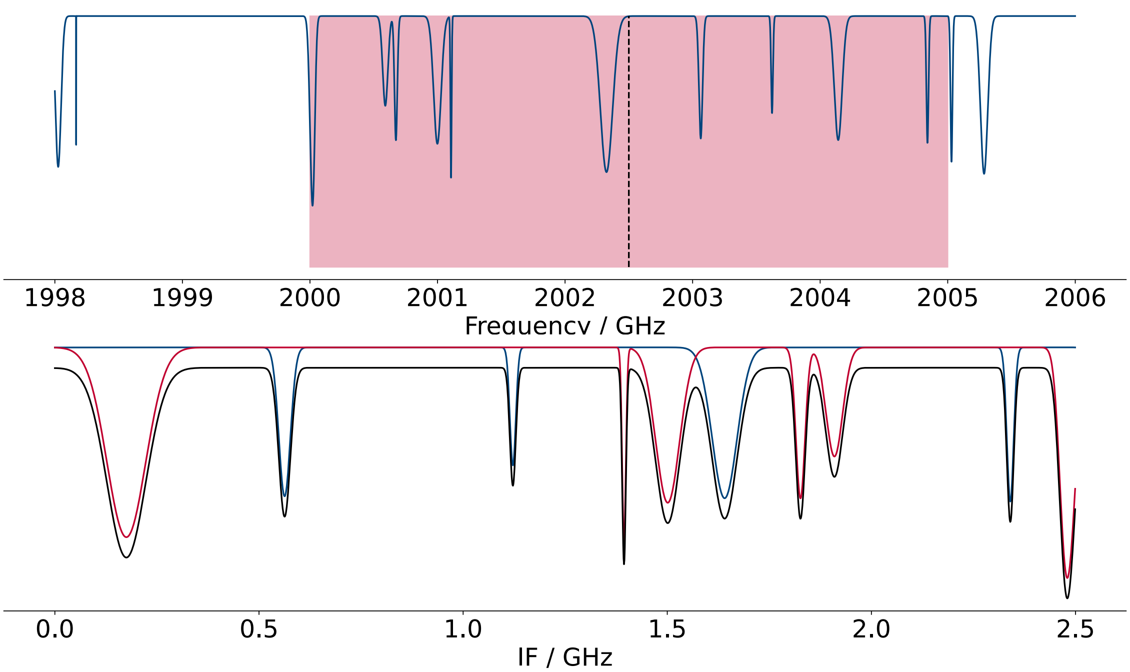

Figure 5.1: Example of heterodyne mixing. The upper plot shows a simulated experimental spectrum in blue. The black line indicates the frequency of the local oscillator. The red box is the instantaneous bandwidth of 5 GHz. The bottom plot shows the folded spectrum detected by heterodyne mixing. The red trace is the lower frequency side band, the blue trace is the higher frequency side band, and the black is the sum of the two, as seen on the detector. The IF is the absolute distance of the peak from the LO frequency.

difference of the excited rotational states amplifies the light to produce lasing.

Molecular lasers pumped using CO_2 lasers were bulky and were limited to relatively few lasing lines.[127] Advances[128] in quantum cascade lasers (QCLs) have opened possible avenues for easy to operate, portable, laser-pumped molecular lasers with a wider range of tuneable frequencies.[125] The continuous tuneability of the QCL lasers creates flexibility in the pumping frequency making THz lasers using a broader selection of gain media possible.

This work involves the development of a database of pump/lasing frequencies which can be used with a THz laser previously developed by the consortium.[125] Figure 5.2

demonstrates the 3-level system typical for these lasers. The pump frequency is shown by the blue ν_{02} transition, and the lasing frequency is the red ν_{12} transition.

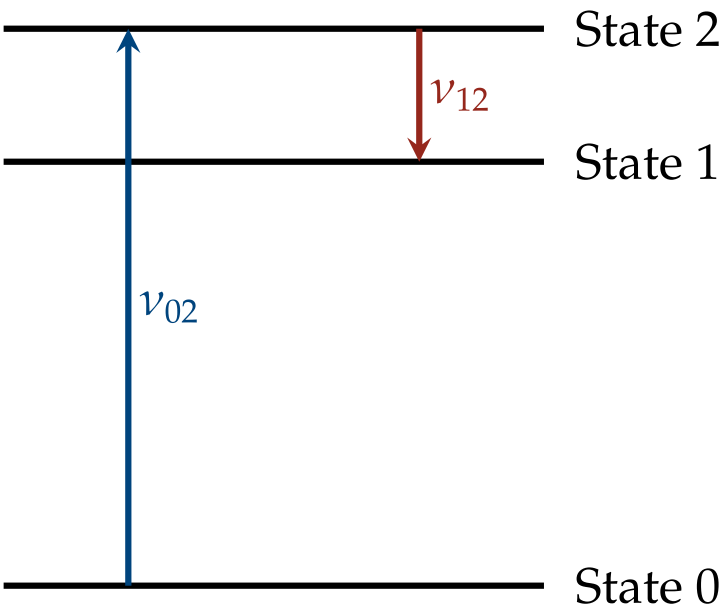

Figure 5.2: Diagram of a 3 level molecular laser system.

This database has been developed in two phases.[129] First spectroscopic line databases, such as HITRAN[130] and ExoMol,[131] were used to calculate a list of molecules and transitions that would produce lasing frequencies in the target 0.3–6 THz range, with corresponding pump transitions arising from the ground vibrational state to build a database of pump/lasing frequencies. Second, using the instrument located at Lille, these pairs were tested, and the frequencies converged to experimental values which provided maximum lasing.

To facilitate finding new lasing lines for all sorts of molecules, the consortium developed a figure of merit called the "Gain Factor" to predict the relative expected lasing for each transition. It is calculated in the following equation:

$$G_m = \frac{I_a S_{02} A_{12}}{\nu_{02}^2 \nu_{12}^3} \frac{10^{-15} M}{16\pi^2 h N_A k_B T} \tag{5.2}$$

where G_m is the molecular gain factor, S_{02} is the spectral line intensity as defined by HITRAN (shown in Equation 5.3) of the 0-2 pump transition (units of cm^2 molecule^{-1}), ν_{02} is the frequency of the pump transition (in Hz), ν_{12} is the frequency of the lasing transition (in Hz), I_a is the isotopic abundance, A_{21} is the Einstein A coefficient for the 1-2 transition in s^{-1} and M is molecular weight of the gain medium in g/mol.

S_{ij} is defined as the spectral line intensity given by:

$$S_{ij} = I_a \frac{A_{ij}}{8\pi c \nu_{ij}^2} \frac{g_j e^{hcE_i/k_B T}(1 - e^{hc\nu_{ij}/k_B T})}{Q(T)} \tag{5.3}$$

where g_j is degeneracy of state j, and E_i is the energy of state i.

The pump frequency, lasing frequency, gain factor, and the quantum numbers for participating states have been compiled into a database.† The measured frequencies for $^{14}NH_3$ and $^{15}NH_3$ are found in Appendix A.

5.1 Optically pumped THz laser using a molecular gain medium

5.1.1 Compiling a database using HITRAN and ExoMol

Both HITRAN and ExoMol are databases of line parameters designed to provide detailed information about the atmosphere of Earth (HITRAN) and exoplanet and cool-star atmospheres (ExoMol). They store information about the quantum states involved in these

---

†Available by request from the author: zsbuchanan@ucdavis.edu

transitions, but they have no network of linked transitions that share a common quantum state. To compile pump/lasing pairs for the molecular laser database, ExoMol and HITRAN were queried to find pairs of transitions that had a common excited state. These pairs were then filtered for pump frequencies accessible by the QCL and lasing frequencies in the 0.3–6 THz range.

ExoMol identifies the upper and lower states of the molecules by their energies, while HITRAN also stores the quantum numbers for each energy level, so the queries to produce the database for each were slightly different. The algorithm for producing the database is as follows:

1. The range of the QCL laser and the desired range for the THz lasing frequencies are required inputs for building the database.
2. The HITRAN and ExoMol are queried to produce lists of all transitions in the desired pumping and lasing frequency ranges.
3. To find potential pump/lasing pairs, for each molecule, each pump frequency is compared to each lasing frequency.
    - For HITRAN, the quantum numbers from the excited states of the pump and the lasing frequency transitions are compared. If there is a match, those lines are added to a list of pump/lasing pairs.
    - For ExoMol, the energies of the upper states are compared. Transitions for the ExoMol database are all from quantum chemical calculations and the upper state energies match each other in transitions that share an upper quantum

state. Matching transitions are added to the list of pump/lasing pairs.

4. Once all potential pump/lasing pairs are identified, the script then goes though each pair and calculates a gain factor, using Equation 5.2.

5. This list of pump/lasing pairs is output from the script as a .csv text file with all relevant information (eg. molecule, lasing frequency, pump frequency, lasing quantum numbers for both states, pump quantum numbers for both states, all relevant state's energies, which database the value originated from).

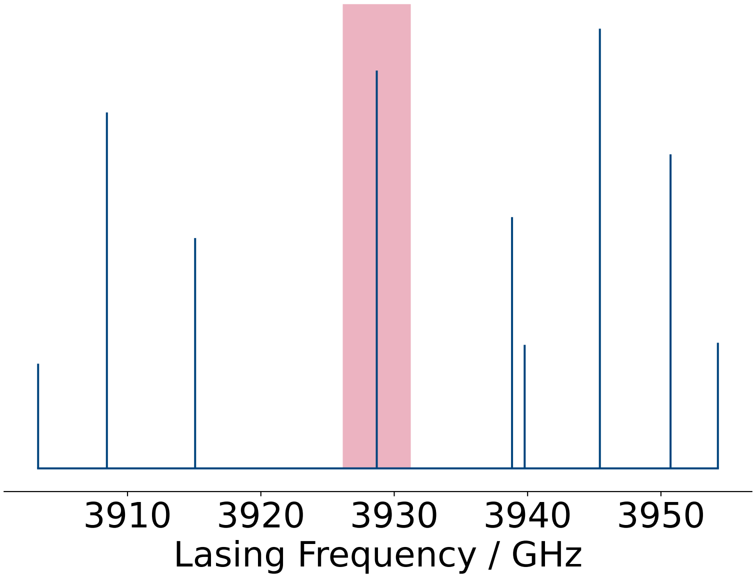

Figure 5.3: Example of the lasing lines from ammonia in a 30 GHz frequency range. The blue lines denote the frequency and relative strength (using our Gain factor, see Equation 5.2) of the line, while the red represents the frequency range accessible using this line as the local oscillator with the THzSOLEIL. The gain factors have been normalized in this figure so that the most intense transition for each molecule has a value of 1.

Figure 5.3 shows a portion of the predicted lasing lines produced by the database described above for $^{14}NH_3$, and an example of the expected spectral coverage available using them as the local oscillator (LO) for THzSOLEIL.

5.1.2 Experimental Setup

Ammonia was studied first for several reasons: it has a high vapor pressure at room temperature, it is available commercially, it is safe to work with, and it has a large permanent dipole moment (approximately 1.5 D). Inversion tunneling splittings in the ν_2 band gave rise to many transitions in the THz range.

Pairs of pump/lasing transitions have been tested at the IEMN institute in Lille, France.[129] Fig 5.4 shows a schematic of the instrument. A vacuum chamber with a ZnSe window on the input side and a TOPAS (cyclic olegin copolymer) window on the output side is filled with 10–30 μbar of ammonia. In future experiments, ammonia will be replaced by other molecular gases. A continuous wave QCL (Daylight Solutions MIRcat) that operates between 920–1330 cm^{-1} with a power of about 100 mW provides the pump radiation with a linewidth of < 1 cm^{-1}. The QCL light is focused into the chamber using a ZnSe lens. The laser cavity consists of a 10 mm diameter copper tube that is housed inside the larger vacuum chamber. On either end of the cavity are flat input and output couplers composed of gold-coated flat mirrors, and its length can be adjusted using a piezoelectric crystal. The THz output is focused with a Zeonex lens onto a pyroelectric detector (PD, Sensor und Lasertechnik GmbH, THZ 10 HS) coupled with a lock-in amplifier to improve the SNR of the PD output. The QCL beam passes through a beam splitter before being coupled into the cavity, and a Bristol wavemeter is used to measure the stability and frequency of the QCL.

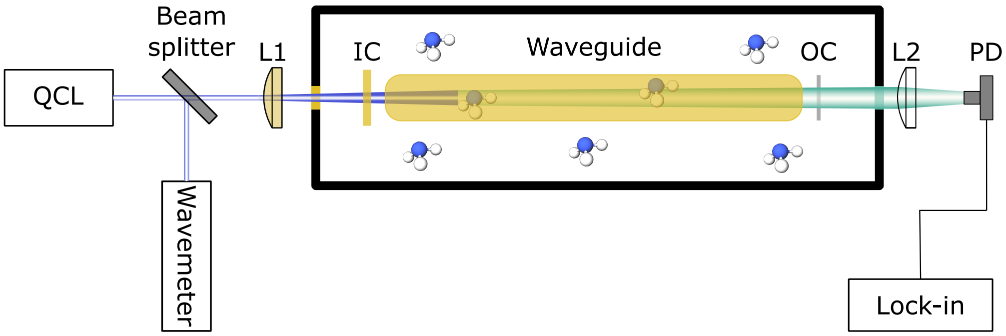

Figure 5.4: Schematic of the molecular laser setup. Tuneable QCL produces pump radiation, which is calibrated using a beamsplitter and a wavemeter. The light is expanded through L1: A ZnSe lens, then passed through the input coupler (IC). The black box is a vacuum chamber filled with vapor pressure of the molecular gain medium. Lasing occurs in the waveguide, and is passed through the output coupler (OC) and focused onto a pyroelectric detector (PD) by L2: Zeonex lens.

5.1.3 Results

Using the molecular lasing database calculated in Section 5.1.1 for $^{14}NH_3$ and $^{15}NH_3$, 37 pump/lasing pairs were measured. Of these, 30 lines were measured for $^{14}NH_3$ and 5 for $^{15}NH_3$. The pump and lasing frequencies for these measured transitions are in Tables 5.1 and 5.2.

For the lines measured, there is poor agreement between G_m and the measured intensity of the lines (see Figure 5.5). While the gain factor developed by collaborators was a poor predictor of overall line intensity, it was useful as a threshold. Of the lines tested, only those with a gain factor $> 1\times10^{-19}$ produced detectable laser light. For the purposes of searching for new pump/lasing pairs, the gain factor informs the search for a new lasing frequency.

Table 5.1: Observed laser transitions of $^{14}NH_3$ in the $\nu_2 = 1$ vibrational state and associated QCL pump frequencies, molecular gain factors (G_m) and observed lasing intensities.

THz laser [GHz]	QCL pump [cm^{-1}]	G_m [μG_m]	Measured Signal Intensity [mV]
Rotation-Inversion			
741.7881	991.6905	9.0×10^{-19}	3.1
762.8525	992.4503	2.2×10^{-18}	5.2
769.7102	992.6987	5.2×10^{-18}	7.5
1338.6790	1011.2036	1.2×10^{-18}	9.0
1978.1120	1032.1310	2.2×10^{-18}	8.5
2010.3707	1033.3158	1.8×10^{-18}	12.5
2029.2006	1034.0127	2.2×10^{-18}	20.0
2035.4532	1034.2448	4.6×10^{-18}	21.4
2244.4659	1007.5471	3.6×10^{-18}	4.7
2622.0015	1053.1304	2.3×10^{-18}	12.5
2669.4110	1054.9126	1.6×10^{-18}	14.0
2822.2564	1027.0470	1.9×10^{-18}	10.7
3101.5415	1067.9744	3.0×10^{-19}	0.6
3373.6128	1046.4055	4.6×10^{-18}	16.0
3915.0670	1095.1293	1.1×10^{-18}	9.4
3928.6856	1065.5943	1.9×10^{-18}	12.0
4458.8750	1084.6290	3.0×10^{-18}	3.8
5048.5821	1103.4412	1.5×10^{-18}	5.4
5505.9143	1122.1853	1.1×10^{-18}	4.0
Pure Inversion			
945.6048	966.4736	1.3×10^{-19}	0.3
979.6498	966.3799	1.4×10^{-18}	6.4
979.6498	1065.5654	2.0×10^{-18}	10.0
1032.3214	965.4994	2.4×10^{-18}	7.7
1035.8161	967.4067	1.2×10^{-18}	5.8
1045.3191	967.7747	2.7×10^{-19}	1.7
1050.5203	963.5585	1.5×10^{-18}	6.0
1067.6770	967.7384	4.6×10^{-18}	5.8
1073.0499	967.3463	1.3×10^{-17}	8.9
1082.5928	966.8147	7.5×10^{-18}	9.3
1096.5904	966.1511	7.2×10^{-18}	4.0
1115.0810	965.3539	1.2×10^{-17}	11.6
1138.2110	964.4240	4.7×10^{-18}	8.3

Table 5.2: Observed laser transitions of $^{15}NH_3$ in the $\nu_2 = 1$ vibrational state and associated QCL pump frequencies, molecular gain factors (G_m) and observed lasing intensities.

THz laser [GHz]	QCL pump [cm^{-1}]	G_m [μG_m]	Measured Signal Intensity [mV]
Rotation-Inversion			
2064.9399	1030.1412	4.9×10^{-18}	–
3332.3527	1041.0901	5.2×10^{-18}	3.5
5463.2430	1116.9334	1.2×10^{-18}	3.2
Pure Inversion			
1035.2013	962.1285	1.5×10^{-17}	5.0
1044.4973	961.6018	8.3×10^{-18}	7.4

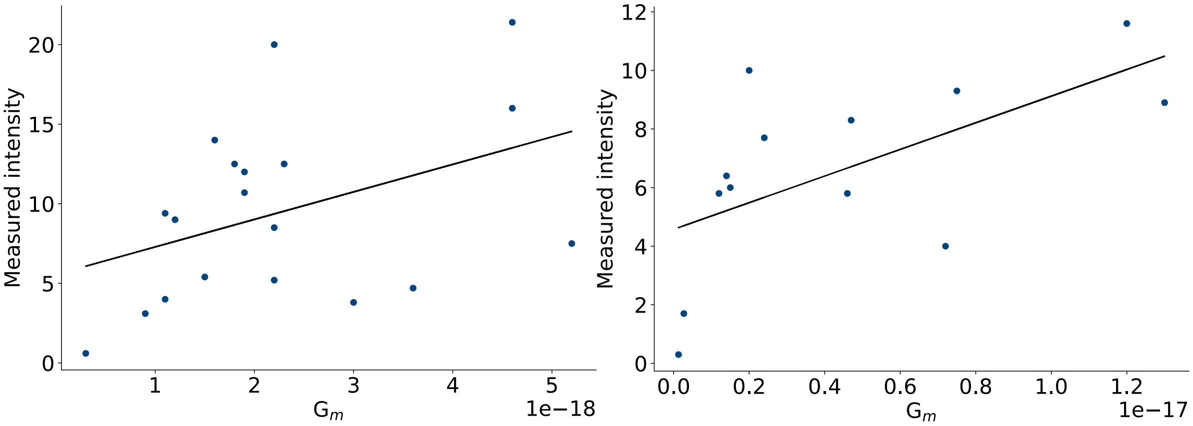

Figure 5.5: Measured intensities vs the calculated gain factor. The left panel shows the rotation-inversion transitions, while the right panel shows the pure rotation transitions.

5.2 Sub-MHz Broadband THz heterodyne spectrometer

5.2.1 Experimental setup

Figure 5.6 shows a schematic of THzSOLEIL. Light from 900–1100 GHz is picked off from the AILES beamline of the Synchrotron SOLEIL using a bandpass filter and attenuated to approximately 1.6 μW. This light is collimated by a plano-convex aspheric polymethylpentene lens through a 55 cm pyrex tube sealed by two polytetrafluoroethylene (PTFE) windows. The tube contains a few μbar of the gas to be studied, in this case CH_3OH and H_2S. The light exiting the sample cell is then focused using a PTFE lens through a wire grid polarizer onto a Hot Electron Bolometer (HEB, Scontel) which is cooled by liquid helium. The HEB is the mixer for this experiment, and is sensitive to frequencies between 0.3 and 4 THz.

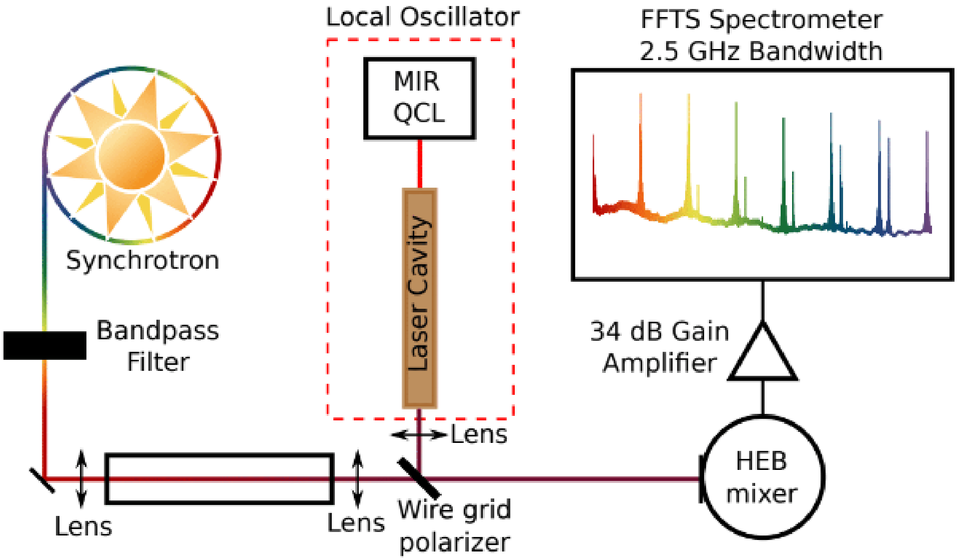

Figure 5.6: Instrument Schematic for broadband THz heterodyne spectrometer at the AILES beamline at SOLEIL.[63]) Synchrotron radiation on the AILES beamline is filtered and collimated through a sample cell, then mixed with a THz laser on the HEB. The output from the HEB is amplified and Fourier transformed to yield the final signal.

The $^{14}NH_3$ transition resulting from Q(3,3) a ← s pure inversion in the $\nu_2 = 1$ vibrationally excited state was selected as the LO for the THzSOLEIL proof of concept measurements using methanol (CH_3OH) and hydrogen sulfide (H_2S). It has an output frequency of 1.0730496 THz and a pump frequency of 967.346 cm^{-1}. The THz laser is focused with a TPX lens through the wire grid polarizer and onto the HEB mixer. The output from the HEB is then amplified and transmitted to a Fast-Fourier Transform Spectrometer (FFTS) from RPG-Radiometer Physics GmbH. The instantaneous bandwidth of this spectrometer is 0.1-2.5 GHz with a best resolution of 88.5 kHz at the full bandwidth. The 2.4 GHz wide side bands are overlapped on top of each other in the spectrum, leading to 4.8 GHz of effective bandwidth. As this is a prototype the data output from the spectrometer is not yet ideal for studying previously unknown lines, as this initial design did not include a way to discern sidebands in the final output.

5.2.2 Data processing and results

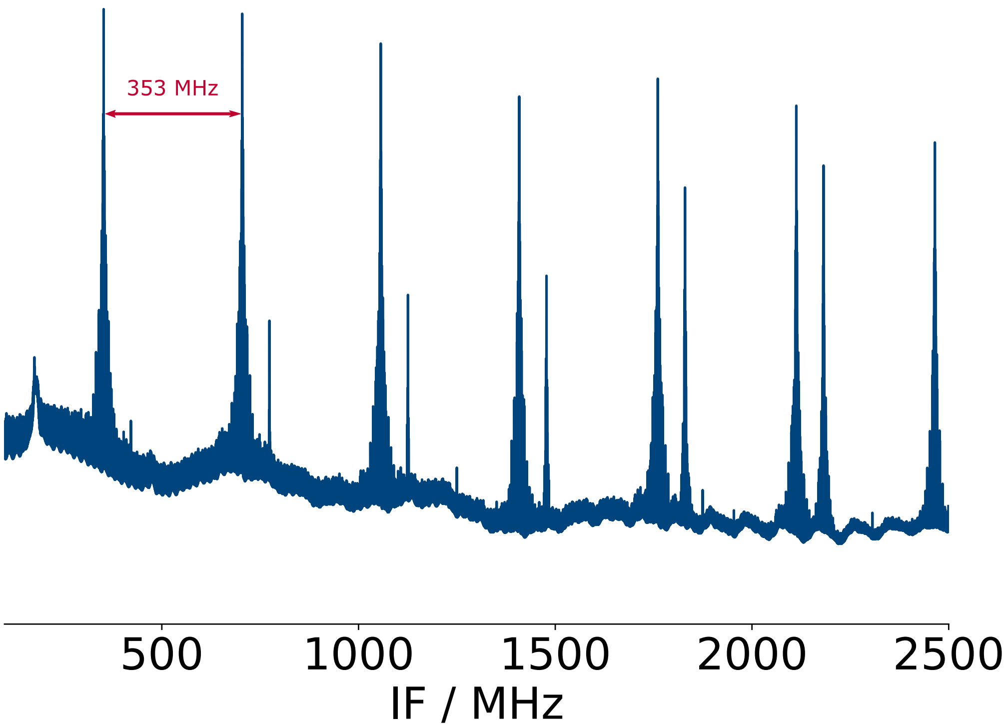

Figure 5.7: Raw data output. Large spikes originate from the repetition rate of the electron bunches spaced 2.8 ns apart.

Figure 5.7 shows the full 2.5 GHz output from the detector as a transmission spectrum. The large frequency comb like spikes in the data are a result of the discontinuous nature of the synchrotron radiation. The coherent synchrotron radiation (CSR) mode at SOLEIL is produced by discrete packets of electrons in the storage ring passing through undulators, and releasing a burst of radiation. The gap between these packets of electrons is about 2.8 ns, which corresponds to a frequency of 353 MHz.[62] The frequency comb character of the synchrotron radiation in this prototype experiment required extra processing of the data to extract the spectra. In addition, the storage ring is not completely full; about 1/4 of the ring is empty, and these missing packets of energy lead to the small, closely spaced frequency spikes that appear in the spectrum. Fortunately, the smaller spikes are easily smoothed away using a Savitzky–Golay filter, as they are only a data point or two wide. After processing a cleaner spectrum is obtained and the molecular peaks are extracted, see Figure 5.8.

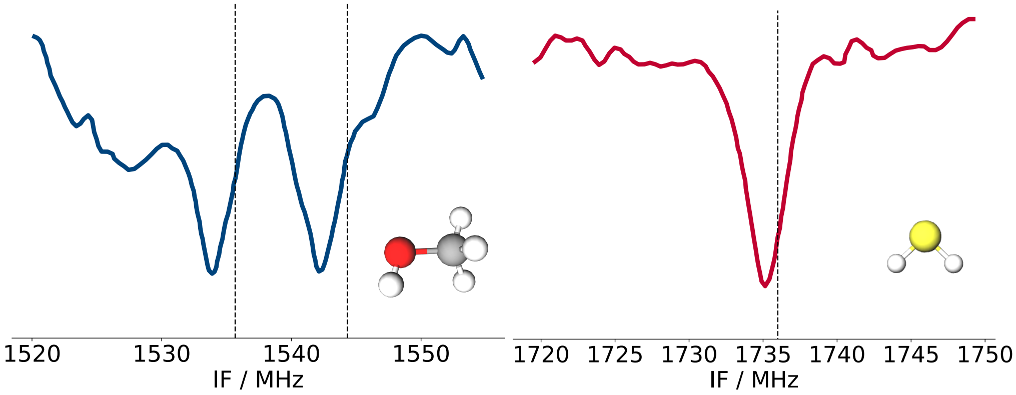

Figure 5.8: Proof of concept measurements of lines for both methanol (left) and H2S (right). The black lines indicate the expected line centers from literature.

Fig 5.8 shows example spectra of single scans performed for CH_3OH and H_2S with a sample length of 1 second for both background and measurement scans. The $9_{4,+,0} - 8_{3,+,0}$ transition and the $9_{4,-,0}8_{3,-,0}$ transitions for CH_3OH were measured, and the $8_{6,3} - 8_{5,4}$ for H_2S.

In addition to the artifacts caused by the synchrotron, artifacts in the data made processing the output from this spectrometer difficult. While measuring data for methanol and hydrogen sulfide, the local oscillator was fluctuating in both power and frequency. The fluctuations in the power output from the laser resulted in 0.4 dB shifts in the baseline power recorded by the HEB. In addition, jittering in the LO frequency resulted in broadened lines in the 1 second averaged measurements, which was amplified if multiple measurements were averaged together (see Figure 5.9).

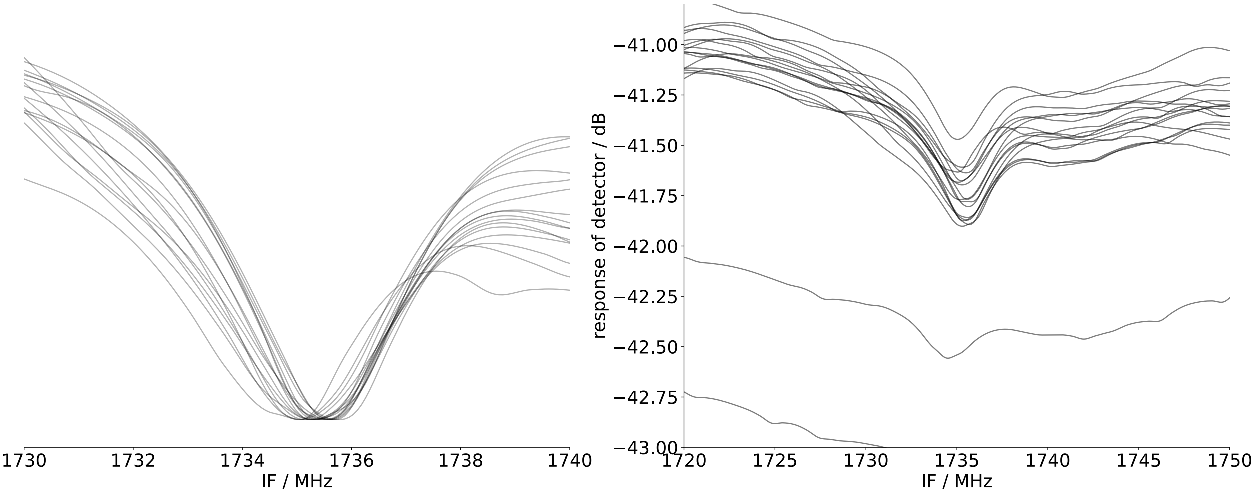

Figure 5.9: Series of measurements for H_2S. The measurements on the left have all been normalized so the peaks for each match, demonstrating jitter from the LO affecting the measured line center for the peak. The plot on the right shows obvious shifts in baseline between measurements due to fluctuating power output in the molecular laser.

Future work is needed to improve the stability of the LO. Improvements that can be made to the cavity include changing the copper cavity for a more thermally stable material, using spherical mirrors rather than flat, and adding active locking for the cavity modes. Methods also need to be developed to deconvolute the mixed sidebands from the HEB. This could potentially be accomplished by intentionally creating laser jitter, which would move the negative sidebands in the opposite direction as it does the positive sidebands.

The work shown here demonstrates the potential for a synchrotron/molecular THz instrument capable of instantaneous 5 GHz bandwidth with sub 100 kHz resolution, complimentary to experimental setups already existing in synchrotron facilities.

Chapter 6

Conclusion

Successful astrochemistry requires the cooperation of experimentalists, chemical modelers, and astronomical observers. This dissertation has described work performed experimentally to provide support to both chemical models, and astronomical observations aimed specifically to accomplish:

1. Construction of an instrument to measure rate constants and branching ratios for radical-neutral reactions to inform chemical models.
2. Measurement of high quality IR and mm-wave transition frequencies and spectroscopic constants to facilitate astronomical searches.
3. Construction of a new instrument to perform measurements in the THz gap with unprecedented broadband/resolution for studying molecules between 0.3–6 THz.

The main results of each project are summarized here, along with a brief discussion of potential future directions.

6.1 Low temperature rate coefficients and branching ratios

The instrument described in Chapters 2 and 3 has been developed with the ultimate goal of providing high quality rate coefficient and branching ratio data for reactions of hydrogen-bonding hydrocarbons with OH radicals between 10–200 K, which have previously been measured to occur much faster than assumed. Chapter 3 describes the production of three Laval nozzles whose flows range from 19-55 K with argon and helium as carrier gases, and describes the procedure for calculating more nozzles. A dual LIF/CP-FTMW spectroscopy detection scheme has been constructed to pair with the CRESU reaction environment. CP-FTMW also enables detection of molecules that are not good fluorophores, and can simultaneously detect multiple reactants and products in the flow. Due to the ability of CP-FTMW to spectroscopically resolve complex gas mixtures, it also detects unexpected species in the reaction, such as clusters, other products, and secondary chemistry.

Future directions

The next steps for the kinetics instrument are follow-up tests with LIF and CP-FTMW. The LIF has been tested and verified through the detection of acetone in a static cell, but has not been verified with the flow, as acetone seeded through the molecular beam persists in the chamber between gas pulses, which makes it difficult to determine if the fluorescent signal is from the ambient gas in the chamber, or from the flow. OH radical will be produced in the flow through pulsed laser photolysis, and detected using LIF in the beam. Because OH radical is highly reactive, it is expected to have a short lifetime outside of the beam and any light detected will be a result of fluorescence in the flow. OH radical should be measured using CP-FTMW. However, the rotational transitions in the Ka band are high J (between J = 11/2–15/2, E = 2544.91–3074.39 cm^{-1}), and may not be sufficiently populated to be detectable in the temperatures of the flow. CP-FTMW will also be used to verify the impact pressure temperatures measured in the beam profile experiments described in Chapter 3 using molecules produced in the beam by photolysis.

Similar instruments employing CP-FTMW[36] require of order of 6×10^6 averaged scans to get adequate signal to noise ratios for their measurements in the uniform flow. At a repetition rate of 10 reaction pulses per second, it requires approximately 166 hours of signal averaging to extract rate coefficients and branching ratios for a single temperature and density. This is due to the high collision rate inside the uniform beam, which causes the coherence times to shorten, making FIDs difficult to detect. To circumvent this issue, a proposed change to the instrument adds a skimmer and a secondary expansion chamber operating at much lower pressures than the uniform beam (See Figure 6.1).

The secondary expansion should be adiabatic, and the rapid drop in density should dramatically slow the reaction, leaving the relative abundances almost identical to their values at the end of the uniform flow. Work has begun on construction of this new chamber, and computational fluid dynamics calculations are being performed to ensure the flow will continue to be uniform through the reaction region.

Section 3.3 showed results of nozzles operating at 61.3 K, 19.8 K and 34.6 K. A larger set of nozzles will need to be produced to adequately cover the desired 10–200 K temperature range. Additionally, the 20 K argon and 35 K helium nozzles were only measured for low

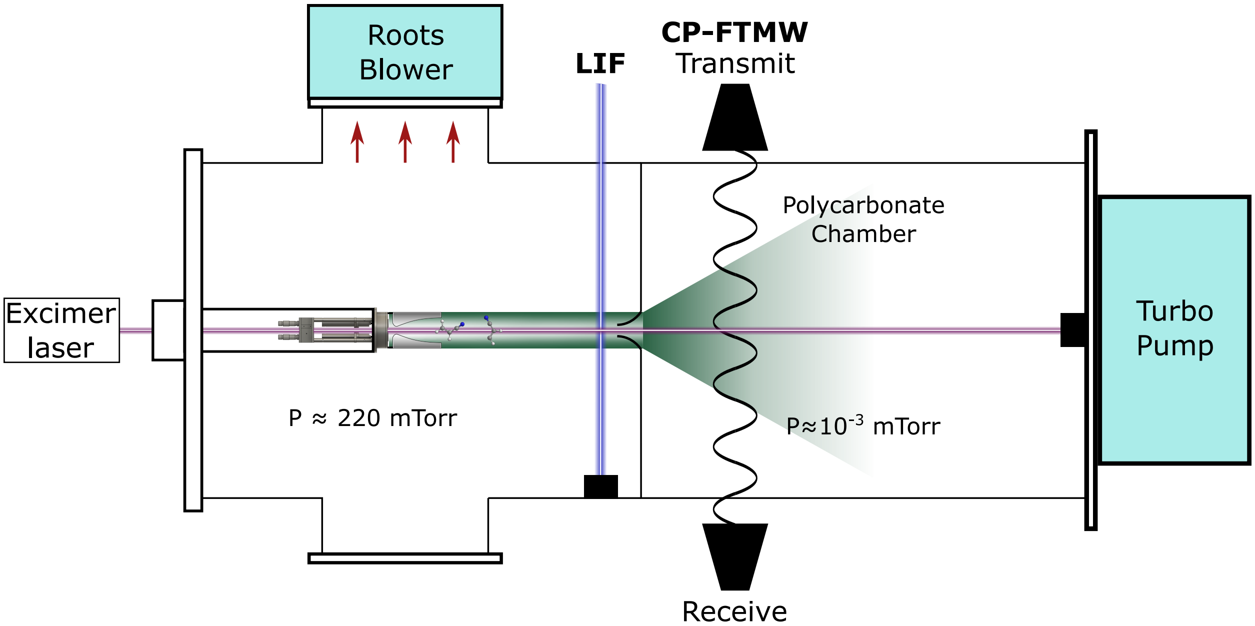

Figure 6.1: Proposed new chamber setup CRESU-CHIRP experiment. A skimmer will sample the center of the uniform beam, and adiabatically expand it into a polycarbonate secondary expansion chamber, pausing the chemistry. The secondary chamber is transparent to microwave radiation, and antenna horns can be aligned outside the chamber. LIF measurements still take place inside the uniform beam, where the density of reactants is high.

density/pressure conditions, which lead to short beams and short reaction lengths. The planned redesign of the kinetics experiment eliminates the need to minimize the density in the uniform beam, so it is logical to revisit these nozzles with higher backing pressures to produce longer, more stable beams.

6.2 Rotational and vibrational spectroscopy of nitrile labeled ring molecules

Chapter 4 shows the spectroscopic characterization in the mm-wave for phenylpropiolonitrile (PhC_3N), 1-cyanoadamantane (CNAda), 1-isocyanoadamantane (NCAda), *o*-dicyanobenzene (*o*-DCB) and *m*-dicyanobenzene (*m*-DCB). The mid- and far-IR regions of the electromagnetic spectrum were also explored for PhC_3N, CNAda, and NCAda.

Work performed to measure the spectra of five molecules at resolutions useful for astronomical detection ($f/\delta f > 10^6$) was described. These measurements were motivated by the increasing detection of nitrile containing species and aromatic molecules in space.[4,20,44,45,132] Astronomical observers require high resolution rotational spectra to identify new molecules in space.

The rotational spectra for each species are reported between 8–220 GHz with a resolution of 25 kHz in the cm-band and 50 kHz in the mm-band. Infrared measurements were performed for PhC_3N, CNAda and NCAda between 100–3600 cm^{-1} with a resolution of 0.5 cm^{-1}. The geometries for each molecule were optimized and density functional theory (DFT) harmonic calculation were performed for each molecule to aid in assignment of the spectra using Gaussian09,[110] and anharmonic calculations were performed for PhC_3N.

The rovibrational structure of PhC_3N could not be resolved with the instrument at SOLEIL, which had a maximum resolution of 0.0009 cm^{-1}, and only the fundamental vibrational bands were reported. Quantum numbers were assigned to 6256 pure rotational transitions, and the spectrum was fit to a rms value of 0.049 kHz. Spectroscopic constants are reported in Table 4.5. A total of 14 vibrational bands were assigned and are reported in Table 4.3. Follow up measurements for the vibrational spectrum at a higher pressure are needed to further assign vibrational bands with inadequate signal to noise ratios. Collaborators searched the GOTHAM survey[120] for PhC_3N, but it was not detected.

For CNAda, 17 vibrational bands, 24 vibrational bands of NCAda, 4929 rotational transitions for the ground state of CNAda, and 3968 rotational transitions for the ground state of NCAda were assigned. Additionally, 4375 rotational transitions for CNAda and 3703 transitions of NCAda were assigned for the $\nu_{50} = 1$ hot bands. The uncertainty in the vibrational assignments is several cm^{-1}, while the RMS values for the fits of CNAda/NCAda were 0.033/0.048 kHz. Rotational constants for these molecules can be found in Table 4.7.

For *o*-DCB, 5767 transitions were assigned to 4071 frequencies in the spectrum, and fit to rotational constants with a rms value of 0.041 kHz. Included in the fit were hyperfine splitting constants, which will aid in astronomical searches for this molecule, as *o*-DCB has its strongest frequencies in the cm-band under the conditions of the ISM. *m*-DCB had 7561 transitions assigned to 5695 frequencies, with a rms of 0.045 kHz. Collaborators at MIT searched the GOTHAM survey for both *o*-DCB and *m*-DCB; neither was detected towards TMC-1.

6.3 Broadband high resolution THz heterodyne spectrometer

Chapter 5 describes a new instrument that is capable of performing 5 GHz bandwidth, <100 kHz resolution measurements at frequencies between 0.3-6 THz.

Chapter 5 outlines work performed constructing a broadband high resolution THz heterodyne spectrometer at the synchrotron SOLEIL. A prototype instrument called THz-SOLEIL has been constructed by mixing synchrotron radiation from the AILES beamline at SOLEIL with radiation from a THz molecular laser that was built for the instrument. These two light sources were mixed using a hot electron bolometer heterodyne receiver, which measured a 5 GHz window of the synchrotron radiation centered at the laser output frequency. THzSOLEIL was used to measure 4 known transitions for CH_3OH and H_2S to a resolution of 88.5 kHz.

Also described in this chapter is the work building and testing a database of pump and lasing frequencies for a THz laser using molecular gas as a gain medium. The goal of this database is to provide coverage across the whole THz gap to couple with THzSOLEIL. Relative lasing intensities were predicted using a figure of merit dubbed the "gain factor" with some success. 39 of the 610 predicted lasing lines from the database built using the HITRAN[130] database were measured for NH_3.

6.3.1 Future directions

THzSOLEIL has proven to be capable of measuring high resolution THz spectra in 5 GHz windows. Chapter 5 shows evidence of jittering, most likely a result of instabilities in the molecular laser, which will need to be addressed before this spectrometer can be used for molecular characterization. A future project for this spectrometer is to design an active stabilization scheme to lock the laser cavity to a specific wavelength. By shifting the frequency of the molecular laser with this device, it will also be possible to separate the positive and negative side bands from the mixer. Monitoring the output from the THz laser to normalize the power output will also aid in reducing baseline shift due to the fluctuating laser power.

The next steps for the molecular laser are to continue to measure more lines from the database, and extend the laser into molecules other than NH_3, such as H_2O. The figure of merit for the laser database needs further refinement. Currently, Figure 5.2 shows G_m to be a poor predictor of the strongest laser lines. One area to investigate further is how the relaxation of the molecules from the excited state post excitation can affect this gain factor.

Appendix A

THz molecular laser lines

Table A.1: List of $^{14}NH_3$ lines reported in the literature that were resonantly pumped by CW gas lasers (CO_2 or N_2O)[133]. The THz lines occur inside the $\upsilon_2 = 1$ vibrational band. The MIR pumping lines occur between the ground state and the $\upsilon_2 = 1$ band. Lines having a possible competing laser line are labelled with an asterisk. Assuming that the pump laser is perfectly tuned to the centre of the ammonia line, the associated molecular gain factor is reported. Seq. stands for sequence bands.

HITRAN THz frequency / GHz	THz QN	G_m / μg	Pump laser line	MIR QN	Ref.
1030.5299	sQ(4,3)*	2.4E-18	CO_2, Seq. 9P(17)	sR(3,3)	[134]
2669.4110	aR(5,1)	1.6E-18	CO_2, Seq. 9P(7)	aR(5,1)	[135]
3442.2588	sR(3,3)*	1.1E-18	CO_2, Seq. 9P(17)	sR(3,3)	[134]
3679.5915	aR(7,7)*	2.9E-19	N_2O, P(13)	aQ(8,7)	[136]
7036.9995	aR(13,13)	3.9E-21	N_2O, P(29)	aQ(14,13)	[137]

Table A.2: List of $^{15}NH_3$ lines reported in the literature that were resonantly pumped by a CO_2 CW laser or a QCL[133,138]. The THz lines occur within the υ_2 = 1 vibrational band. The MIR pumping lines occur between the ground and the υ_2 = 1 states. Lines having a possible competing laser line are labelled with an asterisk. We have added our G_m factor. Calculations are performed assuming that the pump laser is perfectly tuned to the centre of the ammonia line. Seq. stands for sequence bands.

HITRAN THz frequency / GHz	THz QN	G_m / μg	Pump laser line	MIR QN	Ref.
571.1	sQ(13,7)	2.1E-21 [a)]	CO_2, Seq. 10P(5)	sQ(13,7)	[135]
802.9860	aR(2,0)	5.7E-18	CO_2, 10R(42)	aR(2,0)	[135,139]
1096.5	sQ(12,11)	1.8E-19 [a)]	CO_2, Seq. 10P(7)	sQ(12,11)	[135]
1371.4	aR(3,3)	2.2E-18 [a)]	CO_2, Seq. 10P(35)	aQ(4,3)	[135,139]
1962.7496	aR(4,4)	9.4E-19	$^{13}CO_2$, 10R(18)	aQ(5,4)	[140]
2679.8574	aR(5,2)	2.2E-19	CO_2, Seq. 10P(31)	aQ(6,2)	[135,139]
3201.8854	aR(6,5)	4.4E-19	CO_2, Seq. 9R(7)	aR(6,5)	[135]
4416.6765	sR(5,0)	3.3E-18	QCL	sR(5,0)	[138]
4423.6044	sR(5,1)*	1.6E-18	QCL	sR(5,1)	[138]
4444.5206	sR(5,2)*	1.4E-18	QCL	sR(5,2)	[138]
4480.2496	sR(5,3)*	2.2E-18	QCL	sR(5,3)	[138]
4532.1389	sR(5,4)*	6.7E-19	QCL	sR(5,4)	[138]

[a)] (Lines absent from our catalogues because they are not reported in HITRAN database. For these lines, the THz frequencies correspond to the conversion of the wavelengths reported in the corresponding reference. The G_m value was calculated by scaling the G_m value of the corresponding pair of pump/probe transitions of $^{14}NH_3$ by the ratio of molar masses of the two species.)

Table A.3: Table of possible THz laser lines within the $\upsilon_2 = 1$ vibrational band of $^{14}\mathrm{NH}_3$. An asterisk indicates a competition between possible emissions.

THz laser		IR pump											
		P				Q				R			
Freq. / GHz	QN	Freq. / cm^{-1}	QN	Pola.	G_m / μg	Freq. / cm^{-1}	QN	Pola.	G_m / μg	Freq. / cm^{-1}	QN	Pola.	G_m / μg
140.1419	aR(1,1)	872.5671	aP(3,1)	∥	1.5e-18	932.1362	aQ(2,1)	⊥	5.7e-19	971.8820	aR(1,1)	∥	1.2e-18
446.5256	sQ(13,3)*	-	-	-	-	-	-	-	-	1212.8633	sR(12,3)	⊥	1.6e-21
466.2458	sP(1,0)	948.2320	sP(1,0)	∥	4.8e-18	-	-	-	-	-	-	-	-
472.7172	sQ(13,4)*	-	-	-	-	-	-	-	-	1212.8300	sR(12,4)	⊥	1.6e-21
473.3056	sQ(14,6)*	-	-	-	-	-	-	-	-	1230.2321	sR(13,6)	⊥	2.4e-21
496.3563	sQ(12,2)*	-	-	-	-	-	-	-	-	1195.1930	sR(11,2)	⊥	1.2e-21
504.8735	sQ(13,5)*	-	-	-	-	-	-	-	-	1212.7480	sR(12,5)	⊥	2.7e-21
515.3808	sQ(12,3)*	-	-	-	-	-	-	-	-	1195.1336	sR(11,3)	⊥	5.6e-21
520.2789	sQ(14,7)*	-	-	-	-	-	-	-	-	1230.1397	sR(13,7)	⊥	1.9e-21
540.7765	sQ(12,4)*	-	-	-	-	-	-	-	-	1195.0464	sR(11,4)	⊥	5.3e-21
546.9373	sQ(13,6)*	688.4970	sP(14,6)	⊥	1.4e-21	959.7394	sQ(13,6)	∥	1.7e-21	1212.6649	sR(12,6)	⊥	8.6e-21
561.4592	sQ(11,2)*	-	-	-	-	-	-	-	-	1177.1978	sR(10,2)	⊥	3.6e-21
561.9381	sQ(15,9)*	-	-	-	-	-	-	-	-	1247.3303	sR(14,9)	⊥	2.2e-21
577.3480	sQ(12,5)*	708.4153	sP(13,5)	⊥	1.6e-21	960.9520	sQ(12,5)	∥	1.5e-21	1194.9762	sR(11,5)	⊥	8.9e-21
579.8942	sQ(14,8)*	-	-	-	-	-	-	-	-	1230.0694	sR(13,8)	⊥	2.8e-21
580.4775	sQ(11,3)*	728.8132	sP(12,3)	⊥	3.6e-21	962.2798	sQ(11,3)	∥	1.2e-21	1177.1108	sR(10,3)	⊥	1.7e-20
600.8666	sQ(13,7)*	687.4722	sP(14,7)	⊥	1.1e-21	959.2030	sQ(13,7)	∥	2.0e-21	1212.5951	sR(12,7)	⊥	6.6e-21
611.9772	sQ(11,4)*	728.3232	sP(12,4)	⊥	3.4e-21	962.0497	sQ(11,4)	∥	2.1e-21	1177.0776	sR(10,4)	⊥	1.6e-20
615.0456	sQ(10,1)*	-	-	-	-	-	-	-	-	1159.0473	sR(9,1)	⊥	2.6e-21
625.1605	sQ(12,6)*	707.5927	sP(13,6)	⊥	5.2e-21	960.5182	sQ(12,6)	∥	7.3e-21	1194.9111	sR(11,6)	⊥	2.8e-20
628.5864	sQ(10,2)*	748.5698	sP(11,2)	⊥	2.5e-21	-	-	-	-	1159.0258	sR(9,2)	⊥	1.0e-20
643.9029	sQ(15,10)*	-	-	-	-	-	-	-	-	1247.3221	sR(14,10)	⊥	1.7e-21
651.9892	sQ(10,3)*	748.2265	sP(11,3)	⊥	1.2e-20	963.0575	sQ(10,3)	∥	4.3e-21	1158.9850	sR(9,3)	⊥	4.9e-20
653.1278	sQ(11,5)*	727.6892	sP(12,5)	⊥	5.7e-21	961.7134	sQ(11,5)	∥	5.9e-21	1177.0212	sR(10,5)	⊥	2.7e-20
655.1437	sQ(14,9)*	665.9482	sP(15,9)	⊥	1.2e-21	957.0761	sQ(14,9)	∥	4.0e-21	1230.0439	sR(13,9)	⊥	8.4e-21
669.2437	sQ(13,8)*	686.3134	sP(14,8)	⊥	1.6e-21	958.6177	sQ(13,8)	∥	4.3e-21	1212.5581	sR(12,8)	⊥	9.8e-21
681.5026	sQ(9,1)*	768.3114	sP(10,1)	⊥	1.9e-21	-	-	-	-	1140.6997	sR(8,1)	⊥	6.8e-21
685.1681	sQ(10,4)*	747.7627	sP(11,4)	⊥	1.1e-20	962.7907	sQ(10,4)	∥	7.7e-21	1158.9289	sR(9,4)	⊥	4.5e-20
686.4131	sQ(12,7)*	706.6404	sP(13,7)	⊥	4.0e-21	960.0325	sQ(12,7)	∥	8.5e-21	1194.8679	sR(11,7)	⊥	2.1e-20

Continued on next page

Table A.3 – continued from previous page

THz laser		IR pump											
		P				Q				R			
Freq. / GHz	QN	Freq. / cm^{-1}	QN	Pola.	G_m / µg	Freq. / cm^{-1}	QN	Pola.	G_m / µg	Freq. / cm^{-1}	QN	Pola.	G_m / µg
696.4339	sQ(9,2)*	768.1283	sP(10,2)	⊥	7.6e-21	963.9242	sQ(9,2)	||	1.4e-21	1140.6792	sR(8,2)	⊥	2.7e-20
706.8979	sQ(11,6)*	726.9295	sP(12,6)	⊥	1.8e-20	961.3224	sQ(11,6)	||	3.6e-20	1176.9767	sR(10,6)	⊥	8.4e-20
721.2642	sQ(9,3)*	767.8090	sP(10,3)	⊥	3.5e-20	963.7365	sQ(9,3)	||	1.5e-20	1140.6274	sR(8,3)	⊥	1.3e-19
730.9841	sQ(10,5)*	747.1812	sP(11,5)	⊥	1.8e-20	962.4890	sQ(10,5)	||	2.2e-20	1158.8875	sR(9,5)	⊥	7.3e-20
741.7881	aR(2,2)	852.7247	aP(4,2)	||	9.6e-19	932.0940	aQ(3,2)	⊥	1.0e-18	991.6905	aR(2,2)	||	9.0e-19
747.2868	sQ(8,1)*	788.0214	sP(9,1)	⊥	5.0e-21	-	-	-	-	1122.1784	sR(7,1)	⊥	1.6e-20
747.3440	sQ(15,11)*	-	-	-	-	954.5983	sQ(15,11)	||	1.7e-21	1247.4088	sR(14,11)	⊥	2.4e-21
747.5883	sQ(16,12)*	-	-	-	-	952.6967	sQ(16,12)	||	1.3e-21	1264.5198	sR(15,12)	⊥	1.8e-21
749.9338	sQ(14,10)*	-	-	-	-	956.3676	sQ(14,10)	||	4.2e-21	1230.0949	sR(13,10)	⊥	6.0e-21
755.4456	sQ(13,9)*	685.0379	sP(14,9)	⊥	4.8e-21	958.0058	sQ(13,9)	||	1.9e-20	1212.5810	sR(12,9)	⊥	2.8e-20
759.0008	sQ(9,4)*	767.3960	sP(10,4)	⊥	3.3e-20	963.5342	sQ(9,4)	||	2.7e-20	1140.6037	sR(8,4)	⊥	1.1e-19
762.8525	aR(2,1)	853.5482	aP(4,1)	||	1.8e-18	932.8812	aQ(3,1)	⊥	3.8e-19	992.4503	aR(2,1)	||	2.2e-18
763.5831	sQ(8,2)*	787.8547	sP(9,2)	⊥	2.2e-20	964.6096	sQ(8,2)	||	4.5e-21	1122.1600	sR(7,2)	⊥	6.6e-20
763.9947	sQ(12,8)*	705.5734	sP(13,8)	⊥	5.9e-21	959.5139	sQ(12,8)	||	1.9e-20	1194.8697	sR(11,8)	⊥	3.0e-20
769.7102	aR(2,0)	853.8178	aP(4,0)	||	4.1e-18	-	-	-	-	992.6987	aR(2,0)	||	5.2e-18
775.7261	sQ(11,7)*	726.0576	sP(12,7)	⊥	1.4e-20	960.8930	sQ(11,7)	||	3.6e-20	1176.9636	sR(10,7)	⊥	6.0e-20
790.8172	sQ(10,6)*	746.4900	sP(11,6)	⊥	5.7e-20	962.1444	sQ(10,6)	||	1.1e-19	1158.8655	sR(9,6)	⊥	2.2e-19
791.5310	sQ(8,3)*	787.5761	sP(9,3)	⊥	9.6e-20	964.4670	sQ(8,3)	||	5.0e-20	1122.1329	sR(7,3)	⊥	3.0e-19
809.4812	sQ(9,5)*	766.8705	sP(10,5)	⊥	5.4e-20	963.2691	sQ(9,5)	||	7.7e-20	1140.5780	sR(8,5)	⊥	1.8e-19
810.9190	sQ(7,1)*	807.8716	sP(8,1)	⊥	1.3e-20	-	-	-	-	1103.4858	sR(6,1)	⊥	3.7e-20
828.5256	sQ(7,2)*	807.7223	sP(8,2)	⊥	5.3e-20	965.2727	sQ(7,2)	||	1.4e-20	1103.4698	sR(6,2)	⊥	1.4e-19
831.9689	sQ(8,4)*	787.1989	sP(9,4)	⊥	8.8e-20	964.2685	sQ(8,4)	||	8.9e-20	1122.1040	sR(7,4)	⊥	2.6e-19
858.3951	sQ(7,3)*	807.4718	sP(8,3)	⊥	2.4e-19	965.1377	sQ(7,3)	||	1.6e-19	1103.4412	sR(6,3)	⊥	6.3e-19
861.6717	sQ(12,9)*	704.4141	sP(13,9)	⊥	1.7e-20	958.9893	sQ(12,9)	||	7.7e-20	1194.9479	sR(11,9)	⊥	8.1e-20
862.8099	sQ(11,8)*	725.0925	sP(12,8)	⊥	1.9e-20	960.4482	sQ(11,8)	||	7.0e-20	1177.0084	sR(10,8)	⊥	8.1e-20
863.8601	sQ(13,10)*	683.6716	sP(14,10)	⊥	3.4e-21	957.3989	sQ(13,10)	||	2.0e-20	1212.7013	sR(12,10)	⊥	1.9e-20
867.3425	sQ(10,7)*	745.7056	sP(11,7)	⊥	4.1e-20	961.7762	sQ(10,7)	||	1.3e-19	1158.8848	sR(9,7)	⊥	1.5e-19
869.3362	sQ(14,11)*	662.8663	sP(15,11)	⊥	1.3e-21	955.6767	sQ(14,11)	||	8.8e-21	1230.2667	sR(13,11)	⊥	8.2e-21
870.8782	sQ(6,1)*	827.8334	sP(7,1)	⊥	3.4e-20	965.9677	sQ(6,1)	||	2.5e-21	1084.6237	sR(5,1)	⊥	7.5e-20
875.3682	sQ(9,6)*	766.2525	sP(10,6)	⊥	1.6e-19	962.9736	sQ(9,6)	||	3.9e-19	1140.5792	sR(8,6)	⊥	5.0e-19
878.0883	sQ(15,12)*	-	-	-	-	953.8223	sQ(15,12)	||	7.3e-21	1247.6422	sR(14,12)	⊥	6.6e-21
887.0183	sQ(8,5)*	786.7323	sP(9,5)	⊥	1.4e-19	964.0412	sQ(8,5)	||	2.6e-19	1122.0937	sR(7,5)	⊥	3.9e-19

Continued on next page

Table A.3 – continued from previous page

THz laser		IR pump											
		P				Q				R			
Freq. / GHz	QN	Freq. / cm^{-1}	QN	Pola.	G_m / µg	Freq. / cm^{-1}	QN	Pola.	G_m / µg	Freq. / cm^{-1}	QN	Pola.	G_m / µg
889.7112	sQ(6,2)*	827.7021	sP(7,2)	⊥	1.3e-19	965.8991	sQ(6,2)	∥	4.3e-20	1084.6098	sR(5,2)	⊥	2.9e-19
890.1306	sQ(16,13)*	-	-	-	-	951.8355	sQ(16,13)	∥	1.4e-21	1264.8260	sR(15,13)	⊥	1.3e-21
902.4589	sQ(7,4)*	807.1441	sP(8,4)	⊥	2.2e-19	964.9796	sQ(7,4)	∥	2.8e-19	1103.4305	sR(6,4)	⊥	5.2e-19
921.9405	sQ(6,3)*	827.4878	sP(7,3)	⊥	5.8e-19	965.7913	sQ(6,3)	∥	4.7e-19	1084.5931	sR(5,3)	⊥	1.2e-18
925.6582	sQ(5,1)*	847.8763	sP(6,1)	⊥	7.7e-20	966.5324	sQ(5,1)	∥	7.5e-21	1065.5943	sR(4,1)	⊥	1.4e-19
945.6048	sQ(5,2)*	847.7629	sP(6,2)	⊥	3.0e-19	966.4736	sQ(5,2)	∥	1.3e-19	1065.5817	sR(4,2)	⊥	5.3e-19
958.8279	sQ(8,6)*	786.1906	sP(9,6)	⊥	4.0e-19	963.7962	sQ(8,6)	∥	1.3e-18	1122.1177	sR(7,6)	⊥	9.7e-19
959.5663	sQ(9,7)*	765.5612	sP(10,7)	⊥	1.1e-19	962.6698	sQ(9,7)	∥	4.5e-19	1140.6320	sR(8,7)	⊥	3.1e-19
961.8846	sQ(7,5)*	806.7377	sP(8,5)	⊥	1.3e-19	964.7902	sQ(7,5)	∥	8.0e-19	1103.4343	sR(6,5)	⊥	7.0e-19
964.0600	sQ(10,8)*	744.8509	sP(11,8)	⊥	5.5e-20	961.4110	sQ(10,8)	∥	2.8e-19	1158.9758	sR(9,8)	⊥	1.8e-19
968.8093	sQ(6,4)*	827.2011	sP(7,4)	⊥	4.7e-19	965.6520	sQ(6,4)	∥	8.5e-19	1084.5836	sR(5,4)	⊥	9.0e-19
972.3013	sQ(11,9)*	724.0613	sP(12,9)	⊥	5.2e-20	960.0199	sQ(11,9)	∥	3.3e-19	1177.1477	sR(10,9)	⊥	1.9e-19
973.8268	sQ(4,1)*	867.9689	sP(5,1)	⊥	1.7e-19	967.0308	sQ(4,1)	∥	2.2e-20	1046.4006	sR(3,1)	⊥	2.5e-19
979.6498	sQ(5,3)*	847.5781	sP(6,3)	⊥	1.2e-18	966.3799	sQ(5,3)	∥	1.4e-18	1065.5654	sR(4,3)	⊥	2.0e-18
984.3138	sQ(12,10)*	703.1943	sP(13,10)	⊥	1.1e-20	958.4967	sQ(12,10)	∥	7.9e-20	1195.1464	sR(11,10)	⊥	4.9e-20
994.7477	sQ(4,2)*	867.8729	sP(5,2)	⊥	6.1e-19	966.9810	sQ(4,2)	∥	3.8e-19	1046.3880	sR(3,2)	⊥	8.5e-19
1000.1505	sQ(13,11)*	682.2518	sP(14,11)	⊥	4.6e-21	956.8418	sQ(13,11)	∥	4.2e-20	1212.9709	sR(12,11)	⊥	2.3e-20
1014.0847	sQ(3,1)*	888.0794	sP(4,1)	⊥	3.4e-19	967.4491	sQ(3,1)	∥	7.1e-20	1027.0470	sR(2,1)	⊥	4.1e-19
1019.8937	sQ(14,12)*	661.2358	sP(15,12)	⊥	3.6e-21	955.0557	sQ(14,12)	∥	3.7e-20	1230.6204	sR(13,12)	⊥	2.0e-20
1029.3749	sQ(5,4)*	847.3376	sP(6,4)	⊥	9.1e-19	966.2692	sQ(5,4)	∥	2.5e-18	1065.5638	sR(4,4)	⊥	1.1e-18
1030.5299	sQ(4,3)*	867.7196	sP(5,3)	⊥	2.3e-18	966.9051	sQ(4,3)	∥	4.2e-18	1046.3746	sR(3,3)	⊥	2.4e-18
1032.3214	sQ(6,5)*	826.8553	sP(7,5)	⊥	6.5e-19	965.4994	sQ(6,5)	∥	2.4e-18	1084.5992	sR(5,5)	⊥	9.1e-19
1035.8161	sQ(3,2)*	887.9998	sP(4,2)	⊥	1.1e-18	967.4068	sQ(3,2)	∥	1.2e-18	1027.0329	sR(2,2)	⊥	1.1e-18
1039.3598	sQ(7,6)*	806.2742	sP(8,6)	⊥	8.0e-19	964.5957	sQ(7,6)	∥	4.0e-18	1103.4795	sR(6,6)	⊥	1.3e-18
1043.6537	sQ(15,13)*	-	-	-	-	953.1392	sQ(15,13)	∥	7.8e-21	1248.0943	sR(14,13)	⊥	4.2e-21
1045.3191	sQ(2,1)*	908.1768	sP(3,1)	⊥	6.9e-19	967.7747	sQ(2,1)	∥	2.7e-19	1007.5405	sR(1,1)	⊥	5.7e-19
1050.5203	sQ(8,7)*	785.5963	sP(9,7)	⊥	2.4e-19	963.5585	sQ(8,7)	∥	1.5e-18	1122.2036	sR(7,7)	⊥	4.5e-19
1065.8671	sQ(9,8)*	764.8236	sP(10,8)	⊥	1.3e-19	962.3884	sQ(9,8)	∥	1.0e-18	1140.7706	sR(8,8)	⊥	2.8e-19
1066.6510	sQ(1,1)	928.2320	sP(2,1)	⊥	1.5e-18	967.9978	sQ(1,1)	∥	1.8e-18	-	-	-	-
1067.6770	sQ(2,2)	908.1123	sP(3,2)	⊥	1.8e-18	967.7384	sQ(2,2)	∥	4.6e-18	-	-	-	-
1071.5686	sQ(16,14)*	-	-	-	-	951.0932	sQ(16,14)	∥	3.0e-21	1265.3922	sR(15,14)	⊥	1.6e-21
1073.0499	sQ(3,3)	887.8768	sP(4,3)	⊥	3.2e-18	967.3463	sQ(3,3)	∥	1.3e-17	-	-	-	-

Continued on next page

Table A.3 – continued from previous page

THz laser		IR pump											
		P				Q				R			
Freq. / GHz	QN	Freq. / cm^{-1}	QN	Pola.	G_m / μg	Freq. / cm^{-1}	QN	Pola.	G_m / μg	Freq. / cm^{-1}	QN	Pola.	G_m / μg
1082.5928	sQ(4,4)	867.5201	sP(5,4)	⊥	1.3e-18	966.8147	sQ(4,4)	∥	7.5e-18	-	-	-	-
1085.4985	sQ(10,9)*	743.9582	sP(11,9)	⊥	1.3e-19	961.0860	sQ(10,9)	∥	1.2e-18	1159.1800	sR(9,9)	⊥	3.2e-19
1096.5904	sQ(5,5)	847.0513	sP(6,5)	⊥	9.4e-19	966.1511	sQ(5,5)	∥	7.2e-18	-	-	-	-
1103.8040	sQ(17,15)*	-	-	-	-	948.9188	sQ(17,15)	∥	2.2e-21	1282.5140	sR(16,15)	⊥	1.2e-21
1109.5454	sQ(11,10)*	723.0027	sP(12,10)	⊥	3.1e-20	959.6524	sQ(11,10)	∥	3.3e-19	1177.4315	sR(10,10)	⊥	8.7e-20
1115.0810	sQ(6,6)	826.4701	sP(7,6)	⊥	1.2e-18	965.3539	sQ(6,6)	∥	1.2e-17	-	-	-	-
1138.1722	sQ(12,11)*	701.9597	sP(13,11)	⊥	1.4e-20	958.0888	sQ(12,11)	∥	1.7e-19	1195.5251	sR(11,11)	⊥	4.5e-20
1138.2110	sQ(7,7)	805.7790	sP(8,7)	⊥	3.9e-19	964.4240	sQ(7,7)	∥	4.7e-18	-	-	-	-
1166.1643	sQ(8,8)	784.9805	sP(9,8)	⊥	2.2e-19	963.3627	sQ(8,8)	∥	3.3e-18	-	-	-	-
1171.5755	sQ(13,12)*	680.8321	sP(14,12)	⊥	1.1e-20	956.3968	sQ(13,12)	∥	1.7e-19	1213.4613	sR(12,12)	⊥	4.3e-20
1199.1625	sQ(9,9)	764.0774	sP(10,9)	⊥	2.4e-19	962.1714	sQ(9,9)	∥	4.4e-18	-	-	-	-
1209.9839	sQ(14,13)*	659.6231	sP(15,13)	⊥	2.2e-21	954.5783	sQ(14,13)	∥	4.4e-20	1231.2408	sR(13,13)	⊥	9.6e-21
1237.4652	sQ(10,10)	743.0731	sP(11,10)	⊥	6.0e-20	960.8522	sQ(10,10)	∥	1.3e-18	-	-	-	-
1253.6581	sQ(15,14)*	-	-	-	-	952.6354	sQ(15,14)	∥	1.7e-20	1248.8648	sR(14,14)	⊥	4.0e-21
1281.3702	sQ(11,11)	721.9708	sP(12,11)	⊥	2.8e-20	959.4071	sQ(11,11)	∥	7.2e-19	-	-	-	-
1302.8895	sQ(16,15)*	-	-	-	-	950.5708	sQ(16,15)	∥	1.3e-20	1266.3350	sR(15,15)	⊥	3.2e-21
1331.2132	sQ(12,12)	700.7745	sP(13,12)	⊥	2.6e-20	957.8390	sQ(12,12)	∥	7.5e-19	-	-	-	-
1338.6790	aR(3,3)	832.6348	aP(5,3)	∥	1.1e-18	931.7736	aQ(4,3)	⊥	2.1e-18	1011.2036	aR(3,3)	∥	1.2e-18
1358.0002	sQ(17,16)*	-	-	-	-	948.3876	sQ(17,16)	∥	2.5e-21	-	-	-	-
1373.0488	aR(3,2)	834.0122	aP(5,2)	∥	1.2e-18	933.0758	aQ(4,2)	⊥	7.3e-19	1012.4451	aR(3,2)	∥	1.7e-18
1387.3677	sQ(13,13)	679.4885	sP(14,13)	⊥	5.4e-21	956.1510	sQ(13,13)	∥	1.8e-19	-	-	-	-
1393.0785	aR(3,1)	834.8238	aP(5,1)	∥	1.6e-18	933.8425	aQ(4,1)	⊥	2.1e-19	1013.1755	aR(3,1)	∥	2.4e-18
1450.2437	sQ(14,14)	658.1175	sP(15,14)	⊥	2.2e-21	954.3469	sQ(14,14)	∥	8.4e-20	-	-	-	-
1520.2868	sQ(15,15)	636.6669	sP(16,15)	⊥	1.6e-21	952.4311	sQ(15,15)	∥	7.2e-20	-	-	-	-
1597.9758	sQ(16,16)	-	-	-	-	950.4086	sQ(16,16)	∥	1.5e-20	-	-	-	-
1683.8197	sQ(17,17)	-	-	-	-	948.2853	sQ(17,17)	∥	5.6e-21	-	-	-	-
1778.3533	sQ(18,18)	-	-	-	-	946.0679	sQ(18,18)	∥	4.0e-21	-	-	-	-
1931.0487	aR(4,4)	812.3011	aP(6,4)	∥	3.3e-19	931.1773	aQ(5,4)	⊥	9.0e-19	1030.4224	aR(4,4)	∥	4.0e-19
1978.1120	aR(4,3)	814.2415	aP(6,3)	∥	1.4e-18	932.9923	aQ(5,3)	⊥	1.6e-18	1032.1310	aR(4,3)	∥	2.2e-18
2010.3707	aR(4,2)	815.5910	aP(6,2)	∥	9.9e-19	934.2521	aQ(5,2)	⊥	4.4e-19	1033.3158	aR(4,2)	∥	1.8e-18
2029.2006	aR(4,1)	816.3862	aP(6,1)	∥	1.2e-18	934.9940	aQ(5,1)	⊥	1.2e-19	1034.0127	aR(4,1)	∥	2.2e-18
2035.4532	aR(4,0)	816.6510	aP(6,0)	∥	2.5e-18	-	-	-	-	1034.2448	aR(4,0)	∥	4.6e-18

Continued on next page

Table A.3 – continued from previous page

THz laser		IR pump											
		P				Q				R			
Freq. / GHz	QN	Freq. / cm^{-1}	QN	Pola.	G_m / µg	Freq. / cm^{-1}	QN	Pola.	G_m / µg	Freq. / cm^{-1}	QN	Pola.	G_m / µg
2244.4659	sR(1,0)	908.1991	sP(3,0)	∥	3.7e-18	-	-	-	-	1007.5471	sR(1,0)	∥	3.6e-18
2252.1120	sR(1,1)*	908.1768	sP(3,1)	∥	1.3e-18	967.7747	sQ(2,1)	⊥	4.9e-19	1007.5405	sR(1,1)	∥	1.0e-18
2518.6637	aR(5,5)	791.7268	aP(7,5)	∥	1.7e-19	930.3066	aQ(6,5)	⊥	6.7e-19	1049.3464	aR(5,5)	∥	2.5e-19
2578.1665	aR(5,4)	794.2441	aP(7,4)	∥	3.7e-19	932.6357	aQ(6,4)	⊥	6.6e-19	1051.5120	aR(5,4)	∥	7.0e-19
2622.0015	aR(5,3)	796.1341	aP(7,3)	∥	1.1e-18	934.3796	aQ(6,3)	⊥	8.9e-19	1053.1305	aR(5,3)	∥	2.3e-18
2651.9227	aR(5,2)	797.4477	aP(7,2)	∥	6.1e-19	935.5916	aQ(6,2)	⊥	2.2e-19	1054.2527	aR(5,2)	∥	1.4e-18
2669.4110	aR(5,1)	798.2222	aP(7,1)	∥	7.4e-19	936.3048	aQ(6,1)	⊥	5.6e-20	1054.9126	aR(5,1)	∥	1.6e-18
2822.2564	sR(2,1)*	888.0794	sP(4,1)	∥	1.6e-18	967.4491	sQ(3,1)	⊥	3.3e-19	1027.0470	sR(2,1)	∥	1.9e-18
2845.2812	sR(2,2)*	887.9998	sP(4,2)	∥	8.2e-19	967.4068	sQ(3,2)	⊥	8.6e-19	1027.0329	sR(2,2)	∥	7.7e-19
3101.5415	aR(6,6)	770.9138	aP(8,6)	∥	1.8e-19	929.1617	aQ(7,6)	⊥	9.1e-19	1067.9744	aR(6,6)	∥	3.0e-19
3173.2998	aR(6,5)	774.0253	aP(8,5)	∥	1.9e-19	932.0112	aQ(7,5)	⊥	4.8e-19	1070.5910	aR(6,5)	∥	4.1e-19
3228.0358	aR(6,4)	776.4616	aP(8,4)	∥	2.6e-19	934.2357	aQ(7,4)	⊥	3.4e-19	1072.6274	aR(6,4)	∥	6.6e-19
3268.2465	aR(6,3)	778.2899	aP(8,3)	∥	6.2e-19	935.9037	aQ(7,3)	⊥	4.2e-19	1074.1492	aR(6,3)	∥	1.7e-18
3295.7384	aR(6,2)	779.5640	aP(8,2)	∥	3.5e-19	937.0593	aQ(7,2)	⊥	9.9e-20	1075.2032	aR(6,2)	∥	9.8e-19
3311.7699	aR(6,1)	780.3141	aP(8,1)	∥	3.9e-19	937.7404	aQ(7,1)	⊥	2.5e-20	1075.8229	aR(6,1)	∥	1.1e-18
3317.2050	aR(6,0)	780.5677	aP(8,0)	∥	7.2e-19	-	-	-	-	1076.0331	aR(6,0)	∥	2.2e-18
3373.6128	sR(3,0)	868.0015	sP(5,0)	∥	2.9e-18	-	-	-	-	1046.4055	sR(3,0)	∥	4.6e-18
3380.9901	sR(3,1)*	867.9689	sP(5,1)	∥	1.4e-18	967.0308	sQ(4,1)	⊥	1.9e-19	1046.4006	sR(3,1)	∥	2.1e-18
3403.6125	sR(3,2)*	867.8729	sP(5,2)	∥	1.0e-18	966.9810	sQ(4,2)	⊥	6.3e-19	1046.3880	sR(3,2)	∥	1.4e-18
3442.2588	sR(3,3)*	867.7196	sP(5,3)	∥	9.9e-19	966.9051	sQ(4,3)	⊥	1.8e-18	1046.3746	sR(3,3)	∥	1.1e-18
3679.5915	aR(7,7)	749.8631	aP(9,7)	∥	4.6e-20	927.7420	aQ(8,7)	⊥	2.9e-19	1086.3042	aR(7,7)	∥	8.5e-20
3763.5615	aR(7,6)	753.5905	aP(9,6)	∥	1.9e-19	931.1220	aQ(8,6)	⊥	6.2e-19	1089.3699	aR(7,6)	∥	4.7e-19
3828.8208	aR(7,5)	756.5842	aP(9,5)	∥	1.3e-19	933.8260	aQ(8,5)	⊥	2.4e-19	1091.8119	aR(7,5)	∥	3.6e-19
3878.5013	aR(7,4)	758.9296	aP(9,4)	∥	1.6e-19	935.9373	aQ(8,4)	⊥	1.6e-19	1093.7114	aR(7,4)	∥	4.7e-19
3915.0670	aR(7,3)	760.6939	aP(9,3)	∥	3.7e-19	937.5155	aQ(8,3)	⊥	1.8e-19	1095.1293	aR(7,3)	∥	1.1e-18
3928.6856	sR(4,1)*	847.8763	sP(6,1)	∥	1.0e-18	966.5324	sQ(5,1)	⊥	9.8e-20	1065.5943	sR(4,1)	∥	1.9e-18
3939.7792	aR(7,2)	761.9181	aP(9,2)	∥	2.0e-19	938.6175	aQ(8,2)	⊥	4.1e-20	1096.1128	aR(7,2)	∥	5.9e-19
3950.7233	sR(4,2)*	847.7629	sP(6,2)	∥	8.5e-19	966.4736	sQ(5,2)	⊥	3.6e-19	1065.5817	sR(4,2)	∥	1.5e-18
3954.2658	aR(7,1)	762.6406	aP(9,1)	∥	2.0e-19	939.2636	aQ(8,1)	⊥	1.0e-20	1096.6898	aR(7,1)	∥	6.0e-19
3988.2917	sR(4,3)*	847.5781	sP(6,3)	∥	1.2e-18	966.3799	sQ(5,3)	⊥	1.4e-18	1065.5654	sR(4,3)	∥	1.9e-18
4043.0164	sR(4,4)*	847.3376	sP(6,4)	∥	2.8e-19	966.2692	sQ(5,4)	⊥	7.7e-19	1065.5638	sR(4,4)	∥	3.5e-19
4252.6877	aR(8,8)	728.5745	aP(10,8)	∥	2.2e-20	926.0457	aQ(9,8)	⊥	1.6e-19	1104.3325	aR(8,8)	∥	4.6e-20

Continued on next page

Table A.3 – continued from previous page

THz laser		IR pump											
		P				Q				R			
Freq. / GHz	QN	Freq. / cm^{-1}	QN	Pola.	G_m / µg	Freq. / cm^{-1}	QN	Pola.	G_m / µg	Freq. / cm^{-1}	QN	Pola.	G_m / µg
4348.9638	aR(8,7)	732.9436	aP(10,7)	∥	4.4e-20	929.9705	aQ(9,7)	⊥	1.8e-19	1107.8494	aR(8,7)	∥	1.2e-19
4424.4522	aR(8,6)	736.5090	aP(10,6)	∥	1.2e-19	933.1574	aQ(9,6)	⊥	2.9e-19	1110.6889	aR(8,6)	∥	3.9e-19
4458.8750	sR(5,0)	827.8777	sP(7,0)	∥	1.3e-18	-	-	-	-	1084.6290	sR(5,0)	∥	3.0e-18
4465.9475	sR(5,1)*	827.8334	sP(7,1)	∥	6.4e-19	965.9677	sQ(6,1)	⊥	4.8e-20	1084.6237	sR(5,1)	∥	1.4e-18
4482.9601	aR(8,5)	739.3747	aP(10,5)	∥	7.3e-20	935.7074	aQ(9,5)	⊥	1.0e-19	1112.9492	aR(8,5)	∥	2.4e-19
4487.2388	sR(5,2)*	827.7021	sP(7,2)	∥	5.6e-19	965.8991	sQ(6,2)	⊥	1.9e-19	1084.6098	sR(5,2)	∥	1.3e-18
4523.5918	sR(5,3)*	827.4878	sP(7,3)	∥	9.5e-19	965.7913	sQ(6,3)	⊥	7.7e-19	1084.5931	sR(5,3)	∥	2.0e-18
4527.3979	aR(8,4)	741.6214	aP(10,4)	∥	8.1e-20	937.6988	aQ(9,4)	⊥	6.4e-20	1114.7065	aR(8,4)	∥	2.7e-19
4559.8907	aR(8,3)	743.3067	aP(10,3)	∥	1.7e-19	939.1981	aQ(9,3)	⊥	7.2e-20	1116.0197	aR(8,3)	∥	6.1e-19
4576.3508	sR(5,4)*	827.2011	sP(7,4)	∥	3.2e-19	965.6520	sQ(6,4)	⊥	5.7e-19	1084.5836	sR(5,4)	∥	6.1e-19
4581.9994	aR(8,2)	744.4863	aP(10,2)	∥	8.8e-20	940.2276	aQ(9,2)	⊥	1.6e-20	1116.9269	aR(8,2)	∥	3.0e-19
4594.8800	aR(8,1)	745.1781	aP(10,1)	∥	8.9e-20	940.8361	aQ(9,1)	⊥	3.9e-21	1117.4591	aR(8,1)	∥	3.0e-19
4599.4936	aR(8,0)	745.4199	aP(10,0)	∥	1.8e-19	-	-	-	-	1117.6478	aR(8,0)	∥	6.4e-19
4647.5756	sR(5,5)*	826.8553	sP(7,5)	∥	1.5e-19	965.4994	sQ(6,5)	⊥	5.8e-19	1084.5992	sR(5,5)	∥	2.2e-19
4820.6691	aR(9,9)	707.0470	aP(11,9)	∥	1.9e-20	924.0703	aQ(10,9)	⊥	1.7e-19	1122.0551	aR(9,9)	∥	4.7e-20
4929.4840	aR(9,8)	712.0875	aP(11,8)	∥	1.9e-20	928.5579	aQ(10,8)	⊥	9.3e-20	1126.0291	aR(9,8)	∥	6.0e-20
4993.5672	sR(6,1)*	807.8716	sP(8,1)	∥	3.4e-19	965.3515	sQ(7,1)	⊥	2.2e-20	1103.4858	sR(6,1)	∥	9.4e-19
5013.9753	sR(6,2)*	807.7223	sP(8,2)	∥	3.2e-19	965.2727	sQ(7,2)	⊥	8.6e-20	1103.4698	sR(6,2)	∥	8.7e-19
5015.0349	aR(9,7)	716.2427	aP(11,7)	∥	2.6e-20	932.2348	aQ(10,7)	⊥	8.0e-20	1129.2617	aR(9,7)	∥	9.2e-20
5048.5821	sR(6,3)*	807.4718	sP(8,3)	∥	5.6e-19	965.1377	sQ(7,3)	⊥	3.7e-19	1103.4412	sR(6,3)	∥	1.5e-18
5081.8731	aR(9,6)	719.6367	aP(11,6)	∥	6.1e-20	935.2212	aQ(10,6)	⊥	1.2e-19	1131.8696	aR(9,6)	∥	2.2e-19
5099.3040	sR(6,4)*	807.1441	sP(8,4)	∥	2.5e-19	964.9796	sQ(7,4)	⊥	3.1e-19	1103.4305	sR(6,4)	∥	5.8e-19
5133.5090	aR(9,5)	722.3671	aP(11,5)	∥	3.3e-20	937.6115	aQ(10,5)	⊥	3.9e-20	1133.9442	aR(9,5)	∥	1.3e-19
5167.5058	sR(6,5)*	806.7377	sP(8,5)	∥	6.9e-20	964.7902	sQ(7,5)	⊥	4.1e-19	1103.4343	sR(6,5)	∥	3.6e-19
5172.6190	aR(9,4)	724.5095	aP(11,4)	∥	3.4e-20	939.4790	aQ(10,4)	⊥	2.4e-20	1135.5564	aR(9,4)	∥	1.4e-19
5201.4139	aR(9,3)	726.1270	aP(11,3)	∥	7.0e-20	940.8659	aQ(10,3)	⊥	2.6e-20	1136.7574	aR(9,3)	∥	2.7e-19
5220.4105	aR(9,2)	727.2435	aP(11,2)	∥	3.6e-20	941.8509	aQ(10,2)	⊥	5.5e-21	1137.5922	aR(9,2)	∥	1.4e-19
5231.6477	aR(9,1)	727.9019	aP(11,1)	∥	3.6e-20	942.4195	aQ(10,1)	⊥	1.3e-21	1138.0776	aR(9,1)	∥	1.4e-19
5255.9823	sR(6,6)*	806.2742	sP(8,6)	∥	1.6e-19	964.5957	sQ(7,6)	⊥	7.8e-19	1103.4795	sR(6,6)	∥	2.6e-19
5383.3395	aR(10,10)	685.2787	aP(12,10)	∥	4.1e-21	921.8120	aQ(11,10)	⊥	4.5e-20	1139.4669	aR(10,10)	∥	1.2e-20
5505.0656	aR(10,9)	691.0242	aP(12,9)	∥	1.6e-20	926.8846	aQ(11,9)	⊥	9.4e-20	1143.9078	aR(10,9)	∥	5.7e-20
5505.9143	sR(7,0)	788.0777	sP(9,0)	∥	3.3e-19	-	-	-	-	1122.1853	sR(7,0)	∥	1.1e-18

Continued on next page

Table A.3 – continued from previous page

THz laser		IR pump											
		P				Q				R			
Freq. / GHz	QN	Freq. / cm^{-1}	QN	Pola.	G_m / μg	Freq. / cm^{-1}	QN	Pola.	G_m / μg	Freq. / cm^{-1}	QN	Pola.	G_m / μg
5512.4717	sR(7,1)*	788.0214	sP(9,1)	∥	1.7e-19	964.6985	sQ(8,1)	⊥	9.0e-21	1122.1784	sR(7,1)	∥	5.5e-19
5531.8880	sR(7,2)*	787.8547	sP(9,2)	∥	1.7e-19	964.6096	sQ(8,2)	⊥	3.6e-20	1122.1600	sR(7,2)	∥	5.2e-19
5564.9930	sR(7,3)*	787.5761	sP(9,3)	∥	3.1e-19	964.4670	sQ(8,3)	⊥	1.6e-19	1122.1329	sR(7,3)	∥	9.6e-19
5600.6372	aR(10,8)	695.7908	aP(12,8)	∥	1.0e-20	931.0622	aQ(11,8)	⊥	4.1e-20	1147.5326	aR(10,8)	∥	4.3e-20
5612.9291	sR(7,4)*	787.1989	sP(9,4)	∥	1.4e-19	964.2685	sQ(8,4)	⊥	1.4e-19	1122.1040	sR(7,4)	∥	4.1e-19
5675.4304	aR(10,7)	699.7245	aP(12,7)	∥	1.2e-20	934.4861	aQ(11,7)	⊥	2.9e-20	1150.4782	aR(10,7)	∥	5.2e-20
5677.7236	sR(7,5)*	786.7323	sP(9,5)	∥	1.1e-19	964.0412	sQ(8,5)	⊥	2.1e-19	1122.0937	sR(7,5)	∥	3.2e-19
5733.6126	aR(10,6)	702.9413	aP(12,6)	∥	2.5e-20	937.2683	aQ(11,6)	⊥	3.9e-20	1152.8527	aR(10,6)	∥	1.1e-19
5761.7491	sR(7,6)*	786.1906	sP(9,6)	∥	1.6e-19	963.7962	sQ(8,6)	⊥	5.3e-19	1122.1177	sR(7,6)	∥	4.0e-19
5778.3853	aR(10,5)	705.5318	aP(12,5)	∥	1.3e-20	939.4963	aQ(11,5)	⊥	1.3e-20	1154.7407	aR(10,5)	∥	6.0e-20
5812.1831	aR(10,4)	707.5665	aP(12,4)	∥	1.3e-20	941.2378	aQ(11,4)	⊥	7.9e-21	1156.2073	aR(10,4)	∥	6.0e-20
5836.6795	aR(10,3)	709.0891	aP(12,3)	∥	2.6e-20	942.5657	aQ(11,3)	⊥	8.4e-21	1157.3046	aR(10,3)	∥	1.2e-19
5853.1391	aR(10,2)	710.1655	aP(12,2)	∥	1.3e-20	943.4506	aQ(11,2)	⊥	1.8e-21	1158.0580	aR(10,2)	∥	6.0e-20
5862.7103	aR(10,1)	710.7871	aP(12,1)	∥	1.3e-20	-	-	-	-	1158.4942	aR(10,1)	∥	6.1e-20
5866.6796	aR(10,0)	711.0215	aP(12,0)	∥	2.6e-20	-	-	-	-	1158.6670	aR(10,0)	∥	1.2e-19
5868.3228	sR(7,7)*	785.5963	sP(9,7)	∥	3.8e-20	963.5585	sQ(8,7)	⊥	2.4e-19	1122.2036	sR(7,7)	∥	7.3e-20
5940.4679	aR(11,11)	663.2666	aP(13,11)	∥	1.6e-21	919.2664	aQ(12,11)	⊥	2.1e-20	1156.5620	aR(11,11)	∥	5.2e-21
6023.6695	sR(8,1)*	768.3114	sP(10,1)	∥	7.9e-20	964.0226	sQ(9,1)	⊥	3.4e-21	1140.6997	sR(8,1)	∥	2.9e-19
6042.0165	sR(8,2)*	768.1283	sP(10,2)	∥	7.8e-20	963.9242	sQ(9,2)	⊥	1.4e-20	1140.6792	sR(8,2)	∥	2.8e-19
6072.6859	sR(8,3)*	767.8090	sP(10,3)	∥	1.5e-19	963.7365	sQ(9,3)	⊥	6.4e-20	1140.6274	sR(8,3)	∥	5.3e-19
6075.6190	aR(11,10)	669.7548	aP(13,10)	∥	3.0e-21	924.9500	aQ(12,10)	⊥	2.2e-20	1161.4833	aR(11,10)	∥	1.3e-20
6118.3675	sR(8,4)*	767.3960	sP(10,4)	∥	7.1e-20	963.5342	sQ(9,4)	⊥	5.8e-20	1140.6037	sR(8,4)	∥	2.4e-19
6179.4596	sR(8,5)*	766.8705	sP(10,5)	∥	6.4e-20	963.2691	sQ(9,5)	⊥	9.1e-20	1140.5780	sR(8,5)	∥	2.1e-19
6181.2928	aR(11,9)	675.1577	aP(13,9)	∥	7.9e-21	929.6424	aQ(12,9)	⊥	3.8e-20	1165.5028	aR(11,9)	∥	3.7e-20
6258.6483	sR(8,6)*	766.2525	sP(10,6)	∥	1.1e-19	962.9736	sQ(9,6)	⊥	2.6e-19	1140.5792	sR(8,6)	∥	3.3e-19
6263.7823	aR(11,8)	679.6458	aP(13,8)	∥	4.4e-21	933.5083	aQ(12,8)	⊥	1.4e-20	1168.7797	aR(11,8)	∥	2.1e-20
6327.9786	aR(11,7)	683.3547	aP(13,7)	∥	4.6e-21	936.6786	aQ(12,7)	⊥	9.7e-21	1171.4402	aR(11,7)	∥	2.3e-20
6359.0503	sR(8,7)*	765.5612	sP(10,7)	∥	3.8e-20	962.6698	sQ(9,7)	⊥	1.6e-19	1140.6320	sR(8,7)	∥	1.1e-19
6377.6542	aR(11,6)	686.3918	aP(13,6)	∥	9.2e-21	939.2565	aQ(12,6)	⊥	1.3e-20	1173.5835	aR(11,6)	∥	4.7e-20
6415.6953	aR(11,5)	688.8409	aP(13,5)	∥	4.5e-21	941.3224	aQ(12,5)	⊥	4.1e-21	1175.2869	aR(11,5)	∥	2.4e-20
6444.2900	aR(11,4)	690.7667	aP(13,4)	∥	4.4e-21	942.9382	aQ(12,4)	⊥	2.4e-21	1176.6095	aR(11,4)	∥	2.4e-20
6465.3995	aR(11,3)	692.2313	aP(13,3)	∥	8.7e-21	944.1142	aQ(12,3)	⊥	2.5e-21	1177.5909	aR(11,3)	∥	4.6e-20

Continued on next page

Table A.3 – continued from previous page

THz laser		IR pump											
		P				Q				R			
Freq. / GHz	QN	Freq. / cm^{-1}	QN	Pola.	G_m / μg	Freq. / cm^{-1}	QN	Pola.	G_m / μg	Freq. / cm^{-1}	QN	Pola.	G_m / μg
6478.4720	aR(11,2)	693.2290	aP(13,2)	||	4.3e-21	-	-	-	-	1178.2775	aR(11,2)	||	2.2e-20
6484.7191	sR(8,8)*	764.8236	sP(10,8)	||	1.8e-20	962.3884	sQ(9,8)	⊥	1.4e-19	1140.7706	sR(8,8)	||	3.9e-20
6486.3456	aR(11,1)	693.8091	aP(13,1)	||	4.2e-21	-	-	-	-	1178.6606	aR(11,1)	||	2.2e-20
6491.7883	aR(12,12)	641.0069	aP(14,12)	||	1.2e-21	916.4282	aQ(13,12)	⊥	1.8e-20	1173.3335	aR(12,12)	||	4.5e-21
6522.1586	sR(9,0)	748.8344	sP(11,0)	||	6.4e-20	-	-	-	-	1159.0561	sR(9,0)	||	2.7e-19
6528.1959	sR(9,1)*	748.7672	sP(11,1)	||	3.2e-20	963.3361	sQ(10,1)	⊥	1.2e-21	1159.0473	sR(9,1)	||	1.3e-19
6545.4309	sR(9,2)*	748.5698	sP(11,2)	||	3.2e-20	963.2298	sQ(10,2)	⊥	4.9e-21	1159.0258	sR(9,2)	||	1.3e-19
6574.6673	sR(9,3)*	748.2265	sP(11,3)	||	6.3e-20	963.0575	sQ(10,3)	⊥	2.3e-20	1158.9850	sR(9,3)	||	2.6e-19
6616.7879	sR(9,4)*	747.7627	sP(11,4)	||	3.1e-20	962.7907	sQ(10,4)	⊥	2.1e-20	1158.9289	sR(9,4)	||	1.2e-19
6641.0229	aR(12,11)	648.2795	aP(14,11)	||	1.1e-21	922.7526	aQ(13,11)	⊥	1.0e-20	1178.7524	aR(12,11)	||	5.4e-21
6673.9742	sR(9,5)*	747.1812	sP(11,5)	||	2.9e-20	962.4890	sQ(10,5)	⊥	3.5e-20	1158.8875	sR(9,5)	||	1.2e-19
6748.0585	sR(9,6)*	746.4900	sP(11,6)	||	5.3e-20	962.1444	sQ(10,6)	⊥	1.0e-19	1158.8655	sR(9,6)	||	2.0e-19
6757.0027	aR(12,10)	654.3471	aP(14,10)	||	1.4e-21	927.9773	aQ(13,10)	⊥	8.1e-21	1183.1725	aR(12,10)	||	7.8e-21
6841.9437	sR(9,7)*	745.7056	sP(11,7)	||	2.2e-20	961.7762	sQ(10,7)	⊥	6.9e-20	1158.8848	sR(9,7)	||	8.2e-20
6847.0416	aR(12,9)	659.4070	aP(14,9)	||	3.1e-21	932.2927	aQ(13,9)	⊥	1.2e-20	1186.7774	aR(12,9)	||	1.8e-20
6916.8315	aR(12,8)	663.6170	aP(14,8)	||	1.6e-21	935.8505	aQ(13,8)	⊥	4.2e-21	1189.7131	aR(12,8)	||	9.3e-21
6959.4111	sR(9,8)*	744.8509	sP(11,8)	||	1.6e-20	961.4110	sQ(10,8)	⊥	8.2e-20	1158.9758	sR(9,8)	||	5.3e-20
6970.7699	aR(12,7)	667.1021	aP(14,7)	||	1.5e-21	938.7708	aQ(13,7)	⊥	2.8e-21	1192.0947	aR(12,7)	||	9.5e-21
7012.2303	aR(12,6)	669.9607	aP(14,6)	||	3.0e-21	941.1477	aQ(13,6)	⊥	3.6e-21	1194.0124	aR(12,6)	||	1.8e-20
7027.0623	sR(10,1)*	729.4113	sP(12,1)	||	1.2e-20	-	-	-	-	1177.2180	sR(10,1)	||	5.5e-20
7036.9995	aR(13,13)	-	-	-	-	913.2912	aQ(14,13)	⊥	3.9e-21	-	-	-	-
7043.1848	sR(10,2)*	729.2030	sP(12,2)	||	1.2e-20	962.5378	sQ(11,2)	⊥	1.6e-21	1177.1978	sR(10,2)	||	5.5e-20
7043.7816	aR(12,5)	672.2694	aP(14,5)	||	1.4e-21	943.0544	aQ(13,5)	⊥	1.1e-21	1195.5359	aR(12,5)	||	9.0e-21
7067.3660	aR(12,4)	674.0872	aP(14,4)	||	1.4e-21	-	-	-	-	1196.7185	aR(12,4)	||	8.3e-21
7069.1462	sR(10,3)*	728.8132	sP(12,3)	||	2.3e-20	962.2798	sQ(11,3)	⊥	7.6e-21	1177.1108	sR(10,3)	||	1.1e-19
7084.1507	aR(12,3)	675.4389	aP(14,3)	||	2.6e-21	-	-	-	-	1197.6073	aR(12,3)	||	1.6e-20
7094.8740	aR(12,2)	676.4138	aP(14,2)	||	1.3e-21	-	-	-	-	1198.2085	aR(12,2)	||	7.7e-21
7100.9245	aR(12,1)	676.9419	aP(14,1)	||	1.2e-21	-	-	-	-	1198.5292	aR(12,1)	||	7.3e-21
7104.9681	aR(12,0)	677.1906	aP(14,0)	||	2.5e-21	-	-	-	-	1198.7089	aR(12,0)	||	1.4e-20
7105.3300	sR(9,9)*	743.9582	sP(11,9)	||	1.6e-20	961.0860	sQ(10,9)	⊥	1.5e-19	1159.1800	sR(9,9)	||	4.0e-20
7109.3284	sR(10,4)*	728.3232	sP(12,4)	||	1.2e-20	962.0497	sQ(11,4)	⊥	7.1e-21	1177.0776	sR(10,4)	||	5.6e-20
7162.4972	sR(10,5)*	727.6892	sP(12,5)	||	1.2e-20	961.7134	sQ(11,5)	⊥	1.2e-20	1177.0212	sR(10,5)	||	5.4e-20

Continued on next page

Table A.3 – continued from previous page

THz laser		IR pump											
		P				Q				R			
Freq. / GHz	QN	Freq. / cm^{-1}	QN	Pola.	G_m / μg	Freq. / cm^{-1}	QN	Pola.	G_m / μg	Freq. / cm^{-1}	QN	Pola.	G_m / μg
7201.1238	aR(13,12)	-	-	-	-	920.2901	aQ(14,12)	⊥	8.2e-21	1195.7113	aR(13,12)	∥	4.4e-21
7231.3277	sR(10,6)*	726.9295	sP(12,6)	∥	2.2e-20	961.3224	sQ(11,6)	⊥	4.5e-20	1176.9767	sR(10,6)	∥	1.0e-19
7318.4990	sR(10,7)*	726.0576	sP(12,7)	∥	1.0e-20	960.8930	sQ(11,7)	⊥	2.7e-20	1176.9636	sR(10,7)	∥	4.6e-20
7327.7365	aR(13,11)	-	-	-	-	926.0679	aQ(14,11)	⊥	3.3e-21	1200.5410	aR(13,11)	∥	3.0e-21
7425.2864	aR(13,10)	-	-	-	-	930.8432	aQ(14,10)	⊥	2.4e-21	1204.4735	aR(13,10)	∥	3.4e-21
7427.5070	sR(10,8)*	725.0925	sP(12,8)	∥	9.0e-21	960.4482	sQ(11,8)	⊥	3.3e-20	1177.0084	sR(10,8)	∥	3.8e-20
7500.3542	aR(13,9)	643.7362	aP(15,9)	∥	1.0e-21	934.7908	aQ(14,9)	⊥	3.3e-21	1207.6766	aR(13,9)	∥	7.0e-21
7515.5306	sR(11,0)	710.3386	sP(13,0)	∥	7.6e-21	-	-	-	-	1195.2169	sR(11,0)	∥	4.2e-20
7521.2162	sR(11,1)*	710.2623	sP(13,1)	∥	3.8e-21	-	-	-	-	1195.2069	sR(11,1)	∥	2.1e-20
7536.2875	sR(11,2)*	710.0490	sP(13,2)	∥	3.8e-21	-	-	-	-	1195.1930	sR(11,2)	∥	2.1e-20
7558.0250	aR(13,8)	-	-	-	-	938.0491	aQ(14,8)	⊥	1.1e-21	1210.2827	aR(13,8)	∥	3.4e-21
7561.2578	sR(11,3)*	709.6374	sP(13,3)	∥	7.8e-21	961.6669	sQ(12,3)	⊥	2.3e-21	1195.1336	sR(11,3)	∥	4.4e-20
7562.8654	sR(10,9)*	724.0613	sP(12,9)	∥	1.3e-20	960.0199	sQ(11,9)	⊥	8.4e-20	1177.1477	sR(10,9)	∥	5.0e-20
7575.7651	aR(14,14)	-	-	-	-	909.8484	aQ(15,14)	⊥	1.5e-21	-	-	-	-
7597.0436	sR(11,4)*	709.0973	sP(13,4)	∥	4.0e-21	961.3199	sQ(12,4)	⊥	2.2e-21	1195.0464	sR(11,4)	∥	2.2e-20
7602.2015	aR(13,7)	-	-	-	-	-	-	-	-	1212.3957	aR(13,7)	∥	3.2e-21
7635.8598	aR(13,6)	-	-	-	-	-	-	-	-	1214.0965	aR(13,6)	∥	6.2e-21
7646.1710	sR(11,5)*	708.4153	sP(13,5)	∥	4.1e-21	960.9520	sQ(12,5)	⊥	3.6e-21	1194.9762	sR(11,5)	∥	2.2e-20
7661.2562	aR(13,5)	-	-	-	-	-	-	-	-	1215.4472	aR(13,5)	∥	2.9e-21
7680.0916	aR(13,4)	-	-	-	-	-	-	-	-	1216.4954	aR(13,4)	∥	2.8e-21
7694.0989	aR(13,3)	-	-	-	-	-	-	-	-	1217.2664	aR(13,3)	∥	5.3e-21
7700.9284	aR(13,2)	-	-	-	-	-	-	-	-	1217.8144	aR(13,2)	∥	2.5e-21
7704.4656	aR(13,1)	-	-	-	-	-	-	-	-	1218.0381	aR(13,1)	∥	2.3e-21
7709.7126	sR(11,6)*	707.5927	sP(13,6)	∥	8.2e-21	960.5182	sQ(12,6)	⊥	1.1e-20	1194.9111	sR(11,6)	∥	4.4e-20
7730.3501	sR(10,10)*	723.0027	sP(12,10)	∥	3.4e-21	959.6524	sQ(11,10)	⊥	3.7e-20	1177.4315	sR(10,10)	∥	9.6e-21
7755.7370	aR(14,13)	-	-	-	-	917.5593	aQ(15,13)	⊥	1.6e-21	-	-	-	-
7790.1177	sR(11,7)*	706.6404	sP(13,7)	∥	4.1e-21	960.0325	sQ(12,7)	⊥	8.6e-21	1194.8679	sR(11,7)	∥	2.1e-20
7890.5869	sR(11,8)*	705.5734	sP(13,8)	∥	3.9e-21	959.5139	sQ(12,8)	⊥	1.2e-20	1194.8697	sR(11,8)	∥	2.0e-20
7893.4338	aR(14,12)	-	-	-	-	923.9142	aQ(15,12)	⊥	2.5e-21	1217.6067	aR(14,12)	∥	2.2e-21
7998.5631	aR(14,11)	-	-	-	-	-	-	-	-	1221.8692	aR(14,11)	∥	1.2e-21
8011.5226	sR(12,1)*	691.3353	sP(14,1)	∥	1.1e-21	-	-	-	-	1213.0081	sR(12,1)	∥	7.3e-21
8015.2658	sR(11,9)*	704.4141	sP(13,9)	∥	6.8e-21	958.9893	sQ(12,9)	⊥	3.1e-20	1194.9479	sR(11,9)	∥	3.3e-20

Continued on next page

Table A.3 – continued from previous page

THz laser		IR pump											
		P				Q				R			
Freq. / GHz	QN	Freq. / cm^{-1}	QN	Pola.	G_m / µg	Freq. / cm^{-1}	QN	Pola.	G_m / µg	Freq. / cm^{-1}	QN	Pola.	G_m / µg
8025.7455	sR(12,2)*	691.1292	sP(14,2)	‖	1.1e-21	-	-	-	-	1213.0116	sR(12,2)	‖	7.3e-21
8046.0571	sR(12,3)*	690.6559	sP(14,3)	‖	2.4e-21	-	-	-	-	1212.8633	sR(12,3)	‖	1.5e-20
8078.6916	aR(14,10)	-	-	-	-	-	-	-	-	1225.3345	aR(14,10)	‖	1.2e-21
8080.8596	sR(12,4)*	690.1011	sP(14,4)	‖	1.2e-21	-	-	-	-	1212.8300	sR(12,4)	‖	7.8e-21
8107.7133	aR(15,15)	-	-	-	-	906.0924	aQ(16,15)	⊥	1.1e-21	-	-	-	-
8126.0032	sR(12,5)*	689.3760	sP(14,5)	‖	1.3e-21	960.2113	sQ(13,5)	⊥	1.0e-21	1212.7480	sR(12,5)	‖	8.1e-21
8139.6645	aR(14,9)	-	-	-	-	-	-	-	-	1228.1541	aR(14,9)	‖	2.3e-21
8169.4783	sR(11,10)*	703.1943	sP(13,10)	‖	2.6e-21	958.4967	sQ(12,10)	⊥	1.8e-20	1195.1464	sR(11,10)	‖	1.1e-20
8184.3282	sR(12,6)*	688.4970	sP(14,6)	‖	2.7e-21	959.7394	sQ(13,6)	⊥	3.3e-21	1212.6649	sR(12,6)	‖	1.7e-20
8185.9627	aR(14,8)	-	-	-	-	-	-	-	-	1230.4466	aR(14,8)	‖	1.1e-21
8247.3648	aR(14,6)	-	-	-	-	-	-	-	-	1233.7997	aR(14,6)	‖	1.8e-21
8258.0496	sR(12,7)*	687.4722	sP(14,7)	‖	1.4e-21	959.2030	sQ(13,7)	⊥	2.5e-21	1212.5951	sR(12,7)	‖	8.5e-21
8291.2086	aR(14,3)	-	-	-	-	-	-	-	-	1236.6066	aR(14,3)	‖	1.5e-21
8303.7559	aR(14,0)	-	-	-	-	-	-	-	-	1237.4630	aR(14,0)	‖	1.4e-21
8350.0699	sR(12,8)*	686.3134	sP(14,8)	‖	1.4e-21	958.6177	sQ(13,8)	⊥	3.7e-21	1212.5581	sR(12,8)	‖	8.4e-21
8360.0103	sR(11,11)*	701.9597	sP(13,11)	‖	1.4e-21	958.0888	sQ(12,11)	⊥	1.7e-20	1195.5251	sR(11,11)	‖	4.4e-21
8464.1588	sR(12,9)*	685.0379	sP(14,9)	‖	2.7e-21	958.0058	sQ(13,9)	⊥	1.1e-20	1212.5810	sR(12,9)	‖	1.6e-20
8492.7876	sR(13,0)	-	-	-	-	-	-	-	-	1230.6237	sR(13,0)	‖	4.6e-21
8498.8176	sR(13,1)*	-	-	-	-	-	-	-	-	1230.6137	sR(13,1)	‖	2.3e-21
8512.9978	sR(13,2)*	-	-	-	-	-	-	-	-	1230.6716	sR(13,2)	‖	2.1e-21
8532.1772	sR(13,3)*	-	-	-	-	-	-	-	-	1230.5420	sR(13,3)	‖	4.8e-21
8561.5401	sR(13,4)*	-	-	-	-	-	-	-	-	1230.4215	sR(13,4)	‖	2.5e-21
8602.8291	sR(13,5)*	-	-	-	-	-	-	-	-	1230.3300	sR(13,5)	‖	2.6e-21
8605.1766	sR(12,10)*	683.6716	sP(14,10)	‖	1.2e-21	957.3989	sQ(13,10)	⊥	7.1e-21	1212.7013	sR(12,10)	‖	6.8e-21
8656.1027	sR(13,6)*	-	-	-	-	-	-	-	-	1230.2321	sR(13,6)	‖	5.6e-21
8723.3469	sR(13,7)*	-	-	-	-	-	-	-	-	1230.1397	sR(13,7)	‖	2.9e-21
8779.3456	sR(12,11)*	-	-	-	-	956.8418	sQ(13,11)	⊥	8.6e-21	1212.9709	sR(12,11)	‖	4.7e-21
8807.1629	sR(13,8)*	-	-	-	-	-	-	-	-	1230.0694	sR(13,8)	‖	3.0e-21
8910.9435	sR(13,9)*	-	-	-	-	957.0761	sQ(14,9)	⊥	2.9e-21	1230.0439	sR(13,9)	‖	6.2e-21
8994.5770	sR(12,12)*	680.8321	sP(14,12)	‖	1.0e-21	956.3968	sQ(13,12)	⊥	1.6e-20	1213.4613	sR(12,12)	‖	3.9e-21
9009.6303	sR(14,3)*	-	-	-	-	-	-	-	-	1247.8324	sR(14,3)	‖	1.4e-21
9039.0803	sR(13,10)*	-	-	-	-	956.3676	sQ(14,10)	⊥	2.1e-21	1230.0949	sR(13,10)	‖	3.0e-21

Continued on next page

Table A.3 – continued from previous page

THz laser		IR pump											
		P				Q				R			
Freq. / GHz	QN	Freq. / cm^{-1}	QN	Pola.	G_m / µg	Freq. / cm^{-1}	QN	Pola.	G_m / µg	Freq. / cm^{-1}	QN	Pola.	G_m / µg
9125.7588	sR(14,6)*	-	-	-	-	-	-	-	-	1247.6044	sR(14,6)	$\parallel$	1.7e-21
9197.2232	sR(13,11)*	-	-	-	-	955.6767	sQ(14,11)	$\perp$	2.8e-21	1230.2667	sR(13,11)	$\parallel$	2.6e-21
9356.7463	sR(14,9)*	-	-	-	-	-	-	-	-	1247.3303	sR(14,9)	$\parallel$	2.1e-21
9392.5929	sR(13,12)*	-	-	-	-	955.0557	sQ(14,12)	$\perp$	7.0e-21	1230.6204	sR(13,12)	$\parallel$	3.8e-21
9472.5283	sR(14,10)*	-	-	-	-	-	-	-	-	1247.3221	sR(14,10)	$\parallel$	1.1e-21
9615.2434	sR(14,11)*	-	-	-	-	-	-	-	-	1247.4088	sR(14,11)	$\parallel$	1.1e-21
9634.3511	sR(13,13)*	-	-	-	-	954.5783	sQ(14,13)	$\perp$	3.6e-21	-	-	-	-
9791.4158	sR(14,12)*	-	-	-	-	953.8223	sQ(15,12)	$\perp$	2.1e-21	1247.6422	sR(14,12)	$\parallel$	1.9e-21
10009.3750	sR(14,13)*	-	-	-	-	953.1392	sQ(15,13)	$\perp$	1.3e-21	-	-	-	-

Table A.4: Table of possible THz laser lines within the υ_2 vibrational band of $^{15}NH_3$. An asterisk indicates a competition between possible emissions.

THz laser		**IR pump**											
		P				Q				R			
Freq. / GHz	QN	Freq. / cm^{-1}	QN	Pola.	G_m / µg	Freq. / cm^{-1}	QN	Pola.	G_m / µg	Freq. / cm^{-1}	QN	Pola.	G_m / µg
175.0545	aR(1,1)	868.7867	aP(3,1)	∥	1.5e-18	928.2105	aQ(2,1)	⊥	6.0e-19	967.8597	aR(1,1)	∥	1.3e-18
430.0409	sP(1,0)	943.0531	sP(1,0)	∥	5.3e-18	-	-	-	-	-	-	-	-
548.7980	sQ(12,5)*	704.4714	sP(13,5)	⊥	1.8e-21	956.3615	sQ(12,5)	∥	1.6e-21	1189.7912	sR(11,5)	⊥	1.0e-20
550.6156	sQ(14,8)*	-	-	-	-	953.2363	sQ(14,8)	∥	1.0e-21	1224.8482	sR(13,8)	⊥	3.2e-21
552.1314	sQ(11,3)*	724.7878	sP(12,3)	⊥	4.0e-21	957.6577	sQ(11,3)	∥	1.3e-21	1171.9433	sR(10,3)	⊥	1.9e-20
582.6811	sQ(11,4)*	724.2631	sP(12,4)	⊥	3.8e-21	957.3935	sQ(11,4)	∥	2.3e-21	1171.8773	sR(10,4)	⊥	1.8e-20
585.9483	sQ(10,1)*	-	-	-	-	-	-	-	-	1153.8665	sR(9,1)	⊥	2.9e-21
595.1696	sQ(12,6)*	703.5964	sP(13,6)	⊥	5.8e-21	955.8772	sQ(12,6)	∥	8.2e-21	1189.6771	sR(11,6)	⊥	3.2e-20
599.0989	sQ(10,2)*	744.4163	sP(11,2)	⊥	2.8e-21	-	-	-	-	1153.8316	sR(9,2)	⊥	1.2e-20
621.8448	sQ(10,3)*	744.0483	sP(11,3)	⊥	1.3e-20	958.3339	sQ(10,3)	∥	4.9e-21	1153.7675	sR(9,3)	⊥	5.5e-20
622.6471	sQ(11,5)*	723.5852	sP(12,5)	⊥	6.4e-21	957.0148	sQ(11,5)	∥	6.6e-21	1171.7796	sR(10,5)	⊥	3.0e-20
623.5677	sQ(14,9)*	662.0831	sP(15,9)	⊥	1.3e-21	952.4689	sQ(14,9)	∥	4.5e-21	1224.7474	sR(13,9)	⊥	9.5e-21
637.6352	sQ(13,8)*	682.3510	sP(14,8)	⊥	1.8e-21	953.9629	sQ(13,8)	∥	4.9e-21	1207.2632	sR(12,8)	⊥	1.1e-20
650.8201	sQ(9,1)*	764.0287	sP(10,1)	⊥	2.1e-21	-	-	-	-	1135.4778	sR(8,1)	⊥	7.6e-21
654.1073	sQ(10,4)*	743.5499	sP(11,4)	⊥	1.2e-20	958.0336	sQ(10,4)	∥	8.6e-21	1153.6788	sR(9,4)	⊥	5.1e-20
654.6790	sQ(12,7)*	702.5800	sP(13,7)	⊥	4.5e-21	955.3295	sQ(12,7)	∥	9.5e-21	1189.5741	sR(11,7)	⊥	2.4e-20
665.3558	sQ(9,2)*	763.8306	sP(10,2)	⊥	8.5e-21	959.1319	sQ(9,2)	∥	1.5e-21	1135.4431	sR(8,2)	⊥	3.1e-20
674.9452	sQ(11,6)*	722.7704	sP(12,6)	⊥	2.0e-20	956.5704	sQ(11,6)	∥	3.3e-20	1171.6833	sR(10,6)	⊥	9.4e-20
689.5634	sQ(9,3)*	763.4871	sP(10,3)	⊥	4.0e-20	958.9207	sQ(9,3)	∥	1.7e-20	1135.3684	sR(8,3)	⊥	1.4e-19
698.7197	sQ(10,5)*	742.9225	sP(11,5)	⊥	2.0e-20	957.6872	sQ(10,5)	∥	2.5e-20	1153.5940	sR(9,5)	⊥	8.3e-20
712.5116	sQ(16,12)*	-	-	-	-	948.0738	sQ(16,12)	∥	1.5e-21	1259.1141	sR(15,12)	⊥	2.1e-21
715.1759	sQ(8,1)*	783.6022	sP(9,1)	⊥	5.9e-21	-	-	-	-	1116.9215	sR(7,1)	⊥	1.8e-20
715.7032	sQ(14,10)*	660.4908	sP(15,10)	⊥	1.0e-21	951.6684	sQ(14,10)	∥	4.7e-21	1224.7097	sR(13,10)	⊥	6.8e-21
721.4841	sQ(13,9)*	680.9893	sP(14,9)	⊥	5.3e-21	953.2677	sQ(13,9)	∥	2.1e-20	1207.2057	sR(12,9)	⊥	3.2e-20
726.3306	sQ(9,4)*	763.0366	sP(10,4)	⊥	3.6e-20	958.6817	sQ(9,4)	∥	3.0e-20	1135.3090	sR(8,4)	⊥	1.3e-19
730.2018	sQ(12,8)*	701.4363	sP(13,8)	⊥	6.6e-21	954.7365	sQ(12,8)	∥	2.1e-20	1189.5039	sR(11,8)	⊥	3.4e-20
731.0736	sQ(8,2)*	783.4198	sP(9,2)	⊥	2.4e-20	959.7310	sQ(8,2)	∥	5.0e-21	1116.8881	sR(7,2)	⊥	7.4e-20
742.0019	sQ(11,7)*	721.8312	sP(12,7)	⊥	1.5e-20	956.0758	sQ(11,7)	∥	3.8e-20	1171.6070	sR(10,7)	⊥	6.8e-20
757.0629	sQ(10,6)*	742.1737	sP(11,6)	⊥	6.3e-20	957.2866	sQ(10,6)	∥	1.2e-19	1153.5174	sR(9,6)	⊥	2.5e-19

Continued on next page

Table A.4 – continued from previous page

THz laser		IR pump											
		P				Q				R			
Freq. / GHz	QN	Freq. / cm^{-1}	QN	Pola.	G_m / µg	Freq. / cm^{-1}	QN	Pola.	G_m / µg	Freq. / cm^{-1}	QN	Pola.	G_m / µg
758.3559	sQ(8,3)*	783.1148	sP(9,3)	⊥	1.1e-19	959.5625	sQ(8,3)	||	5.6e-20	1116.8358	sR(7,3)	⊥	3.3e-19
775.5175	aR(2,2)	849.0059	aP(4,2)	||	1.0e-18	928.1815	aQ(3,2)	⊥	1.0e-18	987.6329	aR(2,2)	||	9.4e-19
775.5979	sQ(9,5)*	762.4634	sP(10,5)	⊥	6.0e-20	958.3701	sQ(9,5)	||	8.6e-20	1135.2379	sR(8,5)	⊥	2.0e-19
777.5447	sQ(7,1)*	803.3234	sP(8,1)	⊥	1.5e-20	-	-	-	-	1098.2006	sR(6,1)	⊥	4.1e-20
794.7519	sQ(7,2)*	803.1579	sP(8,2)	⊥	6.2e-20	960.3151	sQ(7,2)	||	1.6e-20	1098.1691	sR(6,2)	⊥	1.6e-19
796.1837	aR(2,1)	849.8334	aP(4,1)	||	1.9e-18	928.9725	aQ(3,1)	⊥	4.0e-19	988.3964	aR(2,1)	||	2.3e-18
797.8583	sQ(8,4)*	782.7001	sP(9,4)	⊥	9.9e-20	959.3273	sQ(8,4)	||	1.0e-19	1116.7710	sR(7,4)	⊥	2.9e-19
802.9860	aR(2,0)	850.1069	aP(4,0)	||	4.5e-18	-	-	-	-	988.6486	aR(2,0)	||	5.7e-18
823.9835	sQ(7,3)*	802.8811	sP(8,3)	⊥	2.8e-19	960.1544	sQ(7,3)	||	1.7e-19	1098.1154	sR(6,3)	⊥	7.0e-19
825.4977	sQ(12,9)*	700.1859	sP(13,9)	⊥	1.9e-20	954.1239	sQ(12,9)	||	9.0e-20	1189.4969	sR(11,9)	⊥	9.1e-20
827.0081	sQ(11,8)*	720.7853	sP(12,8)	⊥	2.1e-20	955.5527	sQ(11,8)	||	8.5e-20	1171.5758	sR(10,8)	⊥	9.1e-20
827.2044	sQ(13,10)*	679.5216	sP(14,10)	⊥	3.8e-21	952.5630	sQ(13,10)	||	2.2e-20	1207.2315	sR(12,10)	⊥	2.1e-20
831.8057	sQ(10,7)*	741.3189	sP(11,7)	⊥	4.5e-20	956.8500	sQ(10,7)	||	1.4e-19	1153.4702	sR(9,7)	⊥	1.7e-19
832.0875	sQ(14,11)*	658.7938	sP(15,11)	⊥	1.4e-21	950.8697	sQ(14,11)	||	9.9e-21	1224.7778	sR(13,11)	⊥	9.3e-21
836.4102	sQ(6,1)*	823.1646	sP(7,1)	⊥	3.7e-20	960.9555	sQ(6,1)	||	2.8e-21	1079.3180	sR(5,1)	⊥	8.4e-20
839.9900	sQ(9,6)*	761.7853	sP(10,6)	⊥	1.8e-19	958.0161	sQ(9,6)	||	4.3e-19	1135.1821	sR(8,6)	⊥	5.7e-19
851.3500	sQ(16,13)*	-	-	-	-	947.0851	sQ(16,13)	||	1.6e-21	1259.2981	sR(15,13)	⊥	1.4e-21
851.6939	sQ(8,5)*	782.1839	sP(9,5)	⊥	1.6e-19	959.0517	sQ(8,5)	||	2.8e-19	1116.7134	sR(7,5)	⊥	4.3e-19
854.8450	sQ(6,2)*	823.0167	sP(7,2)	⊥	1.5e-19	960.8707	sQ(6,2)	||	4.8e-20	1079.2881	sR(5,2)	⊥	3.2e-19
867.0846	sQ(7,4)*	802.5137	sP(8,4)	⊥	2.4e-19	959.9574	sQ(7,4)	||	3.1e-19	1098.0664	sR(6,4)	⊥	5.9e-19
886.4111	sQ(6,3)*	822.7744	sP(7,3)	⊥	6.5e-19	960.7353	sQ(6,3)	||	5.3e-19	1079.2443	sR(5,3)	⊥	1.3e-18
890.2670	sQ(5,1)*	843.0961	sP(6,1)	⊥	8.5e-20	961.4586	sQ(5,1)	||	8.3e-21	1060.2765	sR(4,1)	⊥	1.6e-19
909.8183	sQ(5,2)*	842.9657	sP(6,2)	⊥	3.3e-19	961.3831	sQ(5,2)	||	1.4e-19	1060.2474	sR(4,2)	⊥	5.9e-19
922.0162	sQ(8,6)*	781.5802	sP(9,6)	⊥	4.4e-19	958.7461	sQ(8,6)	||	1.4e-18	1116.6781	sR(7,6)	⊥	1.1e-18
922.4116	sQ(9,7)*	761.0208	sP(10,7)	⊥	1.2e-19	957.6410	sQ(9,7)	||	5.0e-19	1135.1653	sR(8,7)	⊥	3.4e-19
925.3043	sQ(7,5)*	802.0563	sP(8,5)	⊥	3.6e-19	959.7180	sQ(7,5)	||	8.9e-19	1098.0212	sR(6,5)	⊥	7.8e-19
926.4495	sQ(10,8)*	740.3798	sP(11,8)	⊥	6.1e-20	956.4029	sQ(10,8)	||	3.2e-19	1153.4815	sR(9,8)	⊥	2.0e-19
932.3515	sQ(6,4)*	822.4479	sP(7,4)	⊥	5.4e-19	960.5570	sQ(6,4)	||	9.4e-19	1079.1963	sR(5,4)	⊥	1.0e-18
934.1200	sQ(11,9)*	719.6587	sP(12,9)	⊥	5.7e-20	955.0317	sQ(11,9)	||	3.6e-19	1171.6251	sR(10,9)	⊥	2.2e-19
937.6801	sQ(4,1)*	863.0868	sP(5,1)	⊥	1.8e-19	961.9047	sQ(4,1)	||	2.5e-20	1041.0795	sR(3,1)	⊥	2.8e-19
943.2247	sQ(5,3)*	842.7529	sP(6,3)	⊥	1.4e-18	961.2619	sQ(5,3)	||	1.6e-18	1060.2039	sR(4,3)	⊥	2.2e-18
945.4435	sQ(12,10)*	698.8593	sP(13,10)	⊥	1.3e-20	953.5278	sQ(12,10)	||	9.6e-20	1189.5952	sR(11,10)	⊥	5.5e-20

Continued on next page

Table A.4 – continued from previous page

THz laser		IR pump											
		P				Q				R			
Freq. / GHz	QN	Freq. / cm^{-1}	QN	Pola.	G_m / µg	Freq. / cm^{-1}	QN	Pola.	G_m / µg	Freq. / cm^{-1}	QN	Pola.	G_m / µg
958.2089	sQ(4,2)*	862.9735	sP(5,2)	⊥	6.7e-19	961.8378	sQ(4,2)	||	4.2e-19	1041.0501	sR(3,2)	⊥	9.4e-19
960.4703	sQ(13,11)*	677.9835	sP(14,11)	⊥	5.2e-21	951.8915	sQ(13,11)	||	4.7e-20	1207.3906	sR(12,11)	⊥	2.6e-20
977.3450	sQ(3,1)*	883.1056	sP(4,1)	⊥	3.8e-19	962.2805	sQ(3,1)	||	7.9e-20	1021.7324	sR(2,1)	⊥	4.5e-19
992.0120	sQ(5,4)*	842.4710	sP(6,4)	⊥	1.0e-18	961.1104	sQ(5,4)	||	2.8e-18	1060.1621	sR(4,4)	⊥	1.2e-18
993.3404	sQ(4,3)*	862.7911	sP(5,3)	⊥	2.5e-18	961.7332	sQ(4,3)	||	4.6e-18	1041.0083	sR(3,3)	⊥	2.7e-18
994.6724	sQ(6,5)*	822.0498	sP(7,5)	⊥	7.1e-19	960.3530	sQ(6,5)	||	2.7e-18	1079.1614	sR(5,5)	⊥	1.0e-18
998.6884	sQ(3,2)*	883.0085	sP(4,2)	⊥	1.3e-18	962.2208	sQ(3,2)	||	1.3e-18	1021.7011	sR(2,2)	⊥	1.2e-18
1001.3107	sQ(7,6)*	801.5289	sP(8,6)	⊥	9.1e-19	959.4609	sQ(7,6)	||	4.5e-18	1098.0049	sR(6,6)	⊥	1.5e-18
1008.1427	sQ(2,1)*	903.1219	sP(3,1)	⊥	7.7e-19	962.5738	sQ(2,1)	||	3.0e-19	1002.2424	sR(1,1)	⊥	6.3e-19
1011.9545	sQ(8,7)*	780.9101	sP(9,7)	⊥	2.7e-19	958.4344	sQ(8,7)	||	1.7e-18	1116.6915	sR(7,7)	⊥	5.0e-19
1026.6663	sQ(9,8)*	760.1956	sP(10,8)	⊥	1.4e-19	957.2742	sQ(9,8)	||	1.1e-18	1135.2204	sR(8,8)	⊥	3.1e-19
1029.1878	sQ(1,1)	923.1066	sP(2,1)	⊥	1.7e-18	962.7752	sQ(1,1)	||	2.0e-18	-	-	-	-
1030.1163	sQ(2,2)	903.0397	sP(3,2)	⊥	2.0e-18	962.5199	sQ(2,2)	||	5.0e-18	-	-	-	-
1035.2013	sQ(3,3)	882.8534	sP(4,3)	⊥	3.6e-18	962.1285	sQ(3,3)	||	1.5e-17	-	-	-	-
1044.4973	sQ(4,4)	862.5502	sP(5,4)	⊥	1.4e-18	961.6018	sQ(4,4)	||	8.3e-18	-	-	-	-
1058.0557	sQ(5,5)	842.1313	sP(6,5)	⊥	1.0e-18	960.9397	sQ(5,5)	||	8.0e-18	-	-	-	-
1962.7496	aR(4,4)	808.7145	aP(6,4)	||	3.4e-19	927.3000	aQ(5,4)	⊥	9.4e-19	1026.3034	aR(4,4)	||	4.2e-19
2008.8550	aR(4,3)	810.6636	aP(6,3)	||	1.5e-18	929.1231	aQ(5,3)	⊥	1.7e-18	1028.0196	aR(4,3)	||	2.4e-18
2040.4267	aR(4,2)	812.0189	aP(6,2)	||	1.0e-18	930.3882	aQ(5,2)	⊥	4.4e-19	1029.2092	aR(4,2)	||	1.8e-18
2058.8442	aR(4,1)	812.8174	aP(6,1)	||	1.2e-18	931.1330	aQ(5,1)	⊥	1.2e-19	1029.9089	aR(4,1)	||	2.3e-18
2064.9399	aR(4,0)	813.0825	aP(6,0)	||	2.6e-18	-	-	-	-	1030.1412	aR(4,0)	||	4.9e-18
2204.8641	sR(1,0)	903.1500	sP(3,0)	||	4.1e-18	-	-	-	-	1002.2548	sR(1,0)	||	3.9e-18
2212.3850	sR(1,1)*	903.1219	sP(3,1)	||	1.4e-18	962.5738	sQ(2,1)	⊥	5.4e-19	1002.2424	sR(1,1)	||	1.1e-18
2549.5250	aR(5,5)	788.2108	aP(7,5)	||	1.9e-19	926.4515	aQ(6,5)	⊥	7.1e-19	1045.2014	aR(5,5)	||	2.6e-19
2607.7753	aR(5,4)	790.7390	aP(7,4)	||	4.0e-19	928.7905	aQ(6,4)	⊥	7.0e-19	1047.3760	aR(5,4)	||	7.4e-19
2650.6138	aR(5,3)	792.6366	aP(7,3)	||	1.1e-18	930.5412	aQ(6,3)	⊥	9.3e-19	1049.0006	aR(5,3)	||	2.4e-18
2679.8574	aR(5,2)	793.9551	aP(7,2)	||	7.0e-19	931.7576	aQ(6,2)	⊥	2.2e-19	1050.1269	aR(5,2)	||	1.5e-18
2696.9273	aR(5,1)	794.7325	aP(7,1)	||	7.7e-19	932.4733	aQ(6,1)	⊥	5.8e-20	1050.7889	aR(5,1)	||	1.7e-18
2781.6717	sR(2,1)*	883.1056	sP(4,1)	||	1.7e-18	962.2805	sQ(3,1)	⊥	3.6e-19	1021.7324	sR(2,1)	||	2.0e-18
2804.3225	sR(2,2)*	883.0085	sP(4,2)	||	9.0e-19	962.2208	sQ(3,2)	⊥	9.4e-19	1021.7011	sR(2,2)	||	8.5e-19
3131.6836	aR(6,6)	767.4715	aP(8,6)	||	1.9e-19	925.3320	aQ(7,6)	⊥	9.6e-19	1063.8068	aR(6,6)	||	3.2e-19
3201.8854	aR(6,5)	770.5959	aP(8,5)	||	2.0e-19	928.1929	aQ(7,5)	⊥	5.0e-19	1066.4336	aR(6,5)	||	4.4e-19

Continued on next page

Table A.4 – continued from previous page

THz laser		IR pump											
		P				Q				R			
Freq. / GHz	QN	Freq. / cm^{-1}	QN	Pola.	G_m / µg	Freq. / cm^{-1}	QN	Pola.	G_m / µg	Freq. / cm^{-1}	QN	Pola.	G_m / µg
3255.3447	aR(6,4)	773.0413	aP(8,4)	∥	2.9e-19	930.4255	aQ(7,4)	⊥	3.8e-19	1068.4770	aR(6,4)	∥	7.0e-19
3294.5656	aR(6,3)	774.8760	aP(8,3)	∥	7.2e-19	932.0990	aQ(7,3)	⊥	4.5e-19	1070.0035	aR(6,3)	∥	1.8e-18
3321.3515	aR(6,2)	776.1542	aP(8,2)	∥	4.0e-19	933.2581	aQ(7,2)	⊥	1.0e-19	1071.0605	aR(6,2)	∥	1.0e-18
3332.3527	sR(3,0)	863.1252	sP(5,0)	∥	3.3e-18	-	-	-	-	1041.0901	sR(3,0)	∥	5.2e-18
3336.9599	aR(6,1)	776.9067	aP(8,1)	∥	4.3e-19	933.9411	aQ(7,1)	⊥	2.6e-20	1071.6819	aR(6,1)	∥	1.1e-18
3339.6823	sR(3,1)*	863.0868	sP(5,1)	∥	1.5e-18	961.9047	sQ(4,1)	⊥	2.1e-19	1041.0795	sR(3,1)	∥	2.3e-18
3342.2269	aR(6,0)	777.1601	aP(8,0)	∥	8.7e-19	-	-	-	-	1071.8917	aR(6,0)	∥	2.3e-18
3361.9305	sR(3,2)*	862.9735	sP(5,2)	∥	1.1e-18	961.8378	sQ(4,2)	⊥	6.9e-19	1041.0501	sR(3,2)	∥	1.6e-18
3399.9562	sR(3,3)*	862.7911	sP(5,3)	∥	1.1e-18	961.7332	sQ(4,3)	⊥	2.0e-18	1041.0083	sR(3,3)	∥	1.2e-18
3709.1387	aR(7,7)	746.4976	aP(9,7)	∥	4.8e-20	923.9409	aQ(8,7)	⊥	3.0e-19	1082.1173	aR(7,7)	∥	9.0e-20
3791.2375	aR(7,6)	750.2397	aP(9,6)	∥	2.0e-19	927.3337	aQ(8,6)	⊥	6.5e-19	1085.1942	aR(7,6)	∥	4.9e-19
3854.9101	aR(7,5)	753.2438	aP(9,5)	∥	1.4e-19	930.0467	aQ(8,5)	⊥	2.6e-19	1087.6437	aR(7,5)	∥	3.9e-19
3886.7909	sR(4,1)*	843.0961	sP(6,1)	∥	1.1e-18	961.4586	sQ(5,1)	⊥	1.1e-19	1060.2765	sR(4,1)	∥	2.1e-18
3903.2969	aR(7,4)	755.5967	aP(9,4)	∥	1.7e-19	932.1641	aQ(8,4)	⊥	1.7e-19	1089.5483	aR(7,4)	∥	5.0e-19
3908.4539	sR(4,2)*	842.9657	sP(6,2)	∥	9.3e-19	961.3831	sQ(5,2)	⊥	4.0e-19	1060.2474	sR(4,2)	∥	1.7e-18
3938.8343	aR(7,3)	757.3661	aP(9,3)	∥	3.8e-19	933.7465	aQ(8,3)	⊥	1.9e-19	1090.9695	aR(7,3)	∥	1.2e-18
3945.4198	sR(4,3)*	842.7529	sP(6,3)	∥	1.3e-18	961.2619	sQ(5,3)	⊥	1.5e-18	1060.2039	sR(4,3)	∥	2.1e-18
3962.8672	aR(7,2)	758.5938	aP(9,2)	∥	2.0e-19	934.8513	aQ(8,2)	⊥	4.3e-20	1091.9552	aR(7,2)	∥	6.3e-19
3976.9280	aR(7,1)	759.3181	aP(9,1)	∥	2.1e-19	935.4988	aQ(8,1)	⊥	1.1e-20	1092.5333	aR(7,1)	∥	6.6e-19
3999.2593	sR(4,4)*	842.4710	sP(6,4)	∥	3.1e-19	961.1104	sQ(5,4)	⊥	8.4e-19	1060.1621	sR(4,4)	∥	3.8e-19
4281.7687	aR(8,8)	725.2889	aP(10,8)	∥	2.2e-20	922.2766	aQ(9,8)	⊥	1.7e-19	1100.1298	aR(8,8)	∥	4.8e-20
4375.8472	aR(8,7)	729.6743	aP(10,7)	∥	4.5e-20	926.2153	aQ(9,7)	⊥	1.9e-19	1103.6586	aR(8,7)	∥	1.3e-19
4416.6765	sR(5,0)	823.2145	sP(7,0)	∥	1.4e-18	-	-	-	-	1079.3287	sR(5,0)	∥	3.3e-18
4423.6044	sR(5,1)*	823.1646	sP(7,1)	∥	7.0e-19	960.9555	sQ(6,1)	⊥	5.3e-20	1079.3180	sR(5,1)	∥	1.6e-18
4444.5206	sR(5,2)*	823.0167	sP(7,2)	∥	6.3e-19	960.8707	sQ(6,2)	⊥	2.0e-19	1079.2881	sR(5,2)	∥	1.4e-18
4449.4279	aR(8,6)	733.2513	aP(10,6)	∥	1.3e-19	929.4117	aQ(9,6)	⊥	3.1e-19	1106.5058	aR(8,6)	∥	4.0e-19
4480.2496	sR(5,3)*	822.7744	sP(7,3)	∥	1.0e-18	960.7353	sQ(6,3)	⊥	8.4e-19	1079.2443	sR(5,3)	∥	2.2e-18
4506.3312	aR(8,5)	736.1253	aP(10,5)	∥	7.6e-20	931.9683	aQ(9,5)	⊥	1.1e-19	1108.7712	aR(8,5)	∥	2.6e-19
4532.1389	sR(5,4)*	822.4479	sP(7,4)	∥	3.6e-19	960.5570	sQ(6,4)	⊥	6.3e-19	1079.1963	sR(5,4)	∥	6.7e-19
4549.4675	aR(8,4)	738.3778	aP(10,4)	∥	8.4e-20	933.9642	aQ(9,4)	⊥	6.9e-20	1110.5317	aR(8,4)	∥	2.9e-19
4580.9637	aR(8,3)	740.0670	aP(10,3)	∥	1.8e-19	935.4667	aQ(9,3)	⊥	7.6e-20	1111.8470	aR(8,3)	∥	6.3e-19
4602.2531	sR(5,5)*	822.0498	sP(7,5)	∥	1.7e-19	960.3530	sQ(6,5)	⊥	6.3e-19	1079.1614	sR(5,5)	∥	2.4e-19

Continued on next page

Table A.4 – continued from previous page

THz laser		IR pump											
		P				Q				R			
Freq. / GHz	QN	Freq. / cm^{-1}	QN	Pola.	G_m / µg	Freq. / cm^{-1}	QN	Pola.	G_m / µg	Freq. / cm^{-1}	QN	Pola.	G_m / µg
4602.3611	aR(8,2)	741.2493	aP(10,2)	∥	9.2e-20	936.4980	aQ(9,2)	⊥	1.7e-20	1112.7555	aR(8,2)	∥	3.3e-19
4614.8150	aR(8,1)	741.9425	aP(10,1)	∥	9.3e-20	937.1074	aQ(9,1)	⊥	4.0e-21	1113.2882	aR(8,1)	∥	3.4e-19
4619.2529	aR(8,0)	742.1836	aP(10,0)	∥	1.9e-19	-	-	-	-	1113.4759	aR(8,0)	∥	6.9e-19
4849.4170	aR(9,9)	703.8446	aP(11,9)	∥	2.0e-20	920.3364	aQ(10,9)	⊥	1.9e-19	1117.8403	aR(9,9)	∥	5.0e-20
4950.9148	sR(6,1)*	803.3234	sP(8,1)	∥	3.9e-19	960.4097	sQ(7,1)	⊥	2.4e-20	1098.2006	sR(6,1)	∥	1.0e-18
4955.6958	aR(9,8)	708.9029	aP(11,8)	∥	2.0e-20	924.8390	aQ(10,8)	⊥	1.0e-19	1121.8267	aR(9,8)	∥	6.5e-20
4970.9484	sR(6,2)*	803.1579	sP(8,2)	∥	3.7e-19	960.3151	sQ(7,2)	⊥	9.4e-20	1098.1691	sR(6,2)	∥	9.6e-19
5004.9604	sR(6,3)*	802.8811	sP(8,3)	∥	6.5e-19	960.1544	sQ(7,3)	⊥	4.1e-19	1098.1154	sR(6,3)	∥	1.7e-18
5039.0055	aR(9,7)	713.0715	aP(11,7)	∥	2.7e-20	928.5258	aQ(10,7)	⊥	8.5e-20	1125.0668	aR(9,7)	∥	9.9e-20
5054.7805	sR(6,4)*	802.5137	sP(8,4)	∥	2.7e-19	959.9574	sQ(7,4)	⊥	3.4e-19	1098.0664	sR(6,4)	∥	6.4e-19
5103.9180	aR(9,6)	716.4733	aP(11,6)	∥	6.3e-20	931.5188	aQ(10,6)	⊥	1.2e-19	1127.6792	aR(9,6)	∥	2.5e-19
5121.8624	sR(6,5)*	802.0563	sP(8,5)	∥	1.8e-19	959.7180	sQ(7,5)	⊥	4.5e-19	1098.0212	sR(6,5)	∥	3.9e-19
5153.9450	aR(9,5)	719.2098	aP(11,5)	∥	3.4e-20	933.9135	aQ(10,5)	⊥	4.1e-20	1129.7566	aR(9,5)	∥	1.4e-19
5191.7560	aR(9,4)	721.3565	aP(11,4)	∥	3.6e-20	935.7839	aQ(10,4)	⊥	2.5e-20	1131.3704	aR(9,4)	∥	1.5e-19
5208.9842	sR(6,6)*	801.5289	sP(8,6)	∥	1.7e-19	959.4609	sQ(7,6)	⊥	8.6e-19	1098.0049	sR(6,6)	∥	2.8e-19
5219.5156	aR(9,3)	722.9772	aP(11,3)	∥	7.3e-20	937.1727	aQ(10,3)	⊥	2.7e-20	1132.5723	aR(9,3)	∥	3.1e-19
5237.8509	aR(9,2)	724.0956	aP(11,2)	∥	3.7e-20	938.1591	aQ(10,2)	⊥	5.8e-21	1133.4078	aR(9,2)	∥	1.6e-19
5248.6614	aR(9,1)	724.7547	aP(11,1)	∥	3.7e-20	938.7280	aQ(10,1)	⊥	1.4e-21	1133.8930	aR(9,1)	∥	1.6e-19
5411.8921	aR(10,10)	682.1626	aP(12,10)	∥	4.2e-21	918.1169	aQ(11,10)	⊥	4.7e-20	1135.2437	aR(10,10)	∥	1.2e-20
5463.2430	sR(7,0)	783.6637	sP(9,0)	∥	3.9e-19	-	-	-	-	1116.9334	sR(7,0)	∥	1.2e-18
5469.6489	sR(7,1)*	783.6022	sP(9,1)	∥	1.9e-19	959.8352	sQ(8,1)	⊥	9.9e-21	1116.9215	sR(7,1)	∥	6.1e-19
5488.6927	sR(7,2)*	783.4198	sP(9,2)	∥	1.9e-19	959.7310	sQ(8,2)	⊥	4.0e-20	1116.8881	sR(7,2)	∥	5.8e-19
5521.1737	sR(7,3)*	783.1148	sP(9,3)	∥	3.5e-19	959.5625	sQ(8,3)	⊥	1.8e-19	1116.8358	sR(7,3)	∥	1.1e-18
5530.7308	aR(10,9)	687.9275	aP(12,9)	∥	1.6e-20	923.2054	aQ(11,9)	⊥	1.0e-19	1139.6972	aR(10,9)	∥	6.2e-20
5568.2399	sR(7,4)*	782.7001	sP(9,4)	∥	1.6e-19	959.3273	sQ(8,4)	⊥	1.6e-19	1116.7710	sR(7,4)	∥	4.6e-19
5623.7144	aR(10,8)	692.7070	aP(12,8)	∥	1.1e-20	927.3929	aQ(11,8)	⊥	4.3e-20	1143.3290	aR(10,8)	∥	4.6e-20
5631.9086	sR(7,5)*	782.1839	sP(9,5)	∥	1.3e-19	959.0517	sQ(8,5)	⊥	2.3e-19	1116.7134	sR(7,5)	∥	3.5e-19
5696.2492	aR(10,7)	696.6496	aP(12,7)	∥	1.2e-20	930.8230	aQ(11,7)	⊥	3.1e-20	1146.2783	aR(10,7)	∥	5.6e-20
5714.5641	sR(7,6)*	781.5802	sP(9,6)	∥	1.8e-19	958.7461	sQ(8,6)	⊥	5.8e-19	1116.6781	sR(7,6)	∥	4.4e-19
5752.5067	aR(10,6)	699.8725	aP(12,6)	∥	2.6e-20	933.6091	aQ(11,6)	⊥	4.3e-20	1148.6546	aR(10,6)	∥	1.2e-19
5795.6804	aR(10,5)	702.4674	aP(12,5)	∥	1.4e-20	935.8397	aQ(11,5)	⊥	1.4e-20	1150.5434	aR(10,5)	∥	6.4e-20
5819.5382	sR(7,7)*	780.9101	sP(9,7)	∥	4.3e-20	958.4344	sQ(8,7)	⊥	2.7e-19	1116.6915	sR(7,7)	∥	8.0e-20

Continued on next page

Table A.4 – continued from previous page

THz laser		IR pump											
		P				Q				R			
Freq. / GHz	QN	Freq. / cm^{-1}	QN	Pola.	G_m / µg	Freq. / cm^{-1}	QN	Pola.	G_m / µg	Freq. / cm^{-1}	QN	Pola.	G_m / µg
5828.1920	aR(10,4)	704.5051	aP(12,4)	∥	1.4e-20	937.5827	aQ(11,4)	⊥	8.3e-21	1152.0101	aR(10,4)	∥	6.6e-20
5851.7164	aR(10,3)	706.0298	aP(12,3)	∥	2.7e-20	938.9119	aQ(11,3)	⊥	8.8e-21	1153.1075	aR(10,3)	∥	1.3e-19
5867.4735	aR(10,2)	707.1077	aP(12,2)	∥	1.3e-20	939.7973	aQ(11,2)	⊥	1.9e-21	1153.8608	aR(10,2)	∥	6.6e-20
5876.6166	aR(10,1)	707.7293	aP(12,1)	∥	1.3e-20	-	-	-	-	1154.2960	aR(10,1)	∥	6.6e-20
5880.4210	aR(10,0)	707.9631	aP(12,0)	∥	2.7e-20	-	-	-	-	1154.4678	aR(10,0)	∥	1.3e-19
5968.9680	aR(11,11)	660.2402	aP(13,11)	∥	1.7e-21	915.6137	aQ(12,11)	⊥	2.2e-20	1152.3342	aR(11,11)	∥	5.6e-21
5980.8113	sR(8,1)*	764.0287	sP(10,1)	∥	8.7e-20	959.2449	sQ(9,1)	⊥	3.8e-21	1135.4778	sR(8,1)	∥	3.2e-19
5998.7901	sR(8,2)*	763.8306	sP(10,2)	∥	8.5e-20	959.1319	sQ(9,2)	⊥	1.5e-20	1135.4431	sR(8,2)	∥	3.1e-19
6028.8830	sR(8,3)*	763.4871	sP(10,3)	∥	1.6e-19	958.9207	sQ(9,3)	⊥	7.0e-20	1135.3684	sR(8,3)	∥	5.9e-19
6073.6564	sR(8,4)*	763.0366	sP(10,4)	∥	7.7e-20	958.6817	sQ(9,4)	⊥	6.3e-20	1135.3090	sR(8,4)	∥	2.7e-19
6100.8668	aR(11,10)	666.7491	aP(13,10)	∥	3.2e-21	921.3138	aQ(12,10)	⊥	2.4e-20	1157.2682	aR(11,10)	∥	1.4e-20
6133.6230	sR(8,5)*	762.4634	sP(10,5)	∥	6.9e-20	958.3701	sQ(9,5)	⊥	1.0e-19	1135.2379	sR(8,5)	∥	2.3e-19
6203.5918	aR(11,9)	672.1653	aP(13,9)	∥	8.2e-21	926.0159	aQ(12,9)	⊥	4.0e-20	1161.2938	aR(11,9)	∥	4.0e-20
6211.4341	sR(8,6)*	761.7853	sP(10,6)	∥	1.1e-19	958.0161	sQ(9,6)	⊥	2.8e-19	1135.1821	sR(8,6)	∥	3.7e-19
6283.4778	aR(11,8)	676.6621	aP(13,8)	∥	4.6e-21	929.8873	aQ(12,8)	⊥	1.5e-20	1164.5731	aR(11,8)	∥	2.4e-20
6310.2136	sR(8,7)*	761.0208	sP(10,7)	∥	4.1e-20	957.6410	sQ(9,7)	⊥	1.7e-19	1135.1653	sR(8,7)	∥	1.2e-19
6345.4240	aR(11,7)	680.3768	aP(13,7)	∥	4.8e-21	933.0607	aQ(12,7)	⊥	1.0e-20	1167.2341	aR(11,7)	∥	2.5e-20
6393.1947	aR(11,6)	683.4179	aP(13,6)	∥	9.6e-21	935.6403	aQ(12,6)	⊥	1.3e-20	1169.3769	aR(11,6)	∥	5.2e-20
6429.6608	aR(11,5)	685.8698	aP(13,5)	∥	4.7e-21	937.7070	aQ(12,5)	⊥	4.3e-21	1171.0793	aR(11,5)	∥	2.6e-20
6434.0366	sR(8,8)*	760.1956	sP(10,8)	∥	2.0e-20	957.2742	sQ(9,8)	⊥	1.5e-19	1135.2204	sR(8,8)	∥	4.3e-20
6456.9926	aR(11,4)	687.7976	aP(13,4)	∥	4.6e-21	939.3234	aQ(12,4)	⊥	2.5e-21	1172.4010	aR(11,4)	∥	2.6e-20
6477.0889	aR(11,3)	689.2638	aP(13,3)	∥	9.0e-21	940.4994	aQ(12,3)	⊥	2.6e-21	1173.3815	aR(11,3)	∥	5.1e-20
6479.5484	sR(9,0)	744.6999	sP(11,0)	∥	6.9e-20	-	-	-	-	1153.8798	sR(9,0)	∥	2.9e-19
6485.4297	sR(9,1)*	744.6278	sP(11,1)	∥	3.5e-20	958.6504	sQ(10,1)	⊥	1.3e-21	1153.8665	sR(9,1)	∥	1.5e-19
6489.5294	aR(11,2)	690.2625	aP(13,2)	∥	4.4e-21	-	-	-	-	1174.0674	aR(11,2)	∥	2.5e-20
6496.9603	aR(11,1)	690.8410	aP(13,1)	∥	4.3e-21	-	-	-	-	1174.4480	aR(11,1)	∥	2.5e-20
6502.3053	sR(9,2)*	744.4163	sP(11,2)	∥	3.4e-20	958.5303	sQ(10,2)	⊥	5.4e-21	1153.8316	sR(9,2)	∥	1.5e-19
6520.3828	aR(12,12)	638.0736	aP(14,12)	∥	1.3e-21	912.8215	aQ(13,12)	⊥	2.0e-20	1169.1052	aR(12,12)	∥	4.9e-21
6530.9238	sR(9,3)*	744.0483	sP(11,3)	∥	6.8e-20	958.3339	sQ(10,3)	⊥	2.5e-20	1153.7675	sR(9,3)	∥	2.9e-19
6572.1939	sR(9,4)*	743.5499	sP(11,4)	∥	3.3e-20	958.0336	sQ(10,4)	⊥	2.3e-20	1153.6788	sR(9,4)	∥	1.4e-19
6628.2622	sR(9,5)*	742.9225	sP(11,5)	∥	3.2e-20	957.6872	sQ(10,5)	⊥	3.8e-20	1153.5940	sR(9,5)	∥	1.3e-19
6665.9869	aR(12,11)	645.3681	aP(14,11)	∥	1.2e-21	919.1630	aQ(13,11)	⊥	1.1e-20	1174.5366	aR(12,11)	∥	5.9e-21

Continued on next page

Table A.4 – continued from previous page

THz laser		IR pump											
		P				Q				R			
Freq. / GHz	QN	Freq. / cm^{-1}	QN	Pola.	G_m / µg	Freq. / cm^{-1}	QN	Pola.	G_m / µg	Freq. / cm^{-1}	QN	Pola.	G_m / µg
6700.9706	sR(9,6)*	742.1737	sP(11,6)	∥	5.8e-20	957.2866	sQ(10,6)	⊥	1.1e-19	1153.5174	sR(9,6)	∥	2.3e-19
6778.6414	aR(12,10)	651.4491	aP(14,10)	∥	1.5e-21	924.3968	aQ(13,10)	⊥	8.5e-21	1178.9616	aR(12,10)	∥	8.2e-21
6793.2227	sR(9,7)*	741.3189	sP(11,7)	∥	2.4e-20	956.8500	sQ(10,7)	⊥	7.7e-20	1153.4702	sR(9,7)	∥	9.0e-20
6865.7183	aR(12,9)	656.5173	aP(14,9)	∥	3.2e-21	928.7167	aQ(13,9)	⊥	1.3e-20	1182.5672	aR(12,9)	∥	1.9e-20
6908.8116	sR(9,8)*	740.3798	sP(11,8)	∥	1.8e-20	956.4029	sQ(10,8)	⊥	9.2e-20	1153.4815	sR(9,8)	∥	5.9e-20
6932.9227	aR(12,8)	660.7324	aP(14,8)	∥	1.6e-21	932.2764	aQ(13,8)	⊥	4.4e-21	1185.5016	aR(12,8)	∥	1.0e-20
6984.5059	sR(10,1)*	725.4212	sP(12,1)	∥	1.3e-20	-	-	-	-	1172.0833	sR(10,1)	∥	6.2e-20
6984.6435	aR(12,7)	664.2208	aP(14,7)	∥	1.6e-21	935.1972	aQ(13,7)	⊥	2.9e-21	1187.8811	aR(12,7)	∥	1.0e-20
7000.2852	sR(10,2)*	725.1998	sP(12,2)	∥	1.3e-20	957.9369	sQ(11,2)	⊥	1.7e-21	1172.0509	sR(10,2)	∥	6.2e-20
7024.2368	aR(12,6)	667.0816	aP(14,6)	∥	3.1e-21	937.5739	aQ(13,6)	⊥	3.8e-21	1189.7963	aR(12,6)	∥	1.9e-20
7025.6923	sR(10,3)*	724.7878	sP(12,3)	∥	2.5e-20	957.6577	sQ(11,3)	⊥	8.3e-21	1171.9433	sR(10,3)	∥	1.2e-19
7052.6371	sR(9,9)*	739.3875	sP(11,9)	∥	1.8e-20	955.9809	sQ(10,9)	⊥	1.7e-19	1153.5912	sR(9,9)	∥	4.4e-20
7054.2505	aR(12,5)	669.3919	aP(14,5)	∥	1.5e-21	939.4802	aQ(13,5)	⊥	1.2e-21	1191.3175	aR(12,5)	∥	9.5e-21
7064.9804	sR(10,4)*	724.2631	sP(12,4)	∥	1.3e-20	957.3935	sQ(11,4)	⊥	7.8e-21	1171.8773	sR(10,4)	∥	6.1e-20
7065.8405	aR(13,13)	-	-	-	-	909.7343	aQ(14,13)	⊥	4.1e-21	1185.5492	aR(13,13)	∥	1.0e-21
7076.6067	aR(12,4)	671.2109	aP(14,4)	∥	1.4e-21	-	-	-	-	1192.4981	aR(12,4)	∥	9.1e-21
7092.4858	aR(12,3)	672.5636	aP(14,3)	∥	2.7e-21	-	-	-	-	1193.3855	aR(12,3)	∥	1.8e-20
7102.4913	aR(12,2)	673.5394	aP(14,2)	∥	1.3e-21	-	-	-	-	1193.9855	aR(12,2)	∥	8.6e-21
7108.0129	aR(12,1)	674.0612	aP(14,1)	∥	1.3e-21	-	-	-	-	1194.2988	aR(12,1)	∥	8.1e-21
7112.0577	aR(12,0)	674.3144	aP(14,0)	∥	2.6e-21	-	-	-	-	1194.4827	aR(12,0)	∥	1.7e-20
7117.0472	sR(10,5)*	723.5852	sP(12,5)	∥	1.3e-20	957.0148	sQ(11,5)	⊥	1.3e-20	1171.7796	sR(10,5)	∥	6.0e-20
7184.5146	sR(10,6)*	722.7704	sP(12,6)	∥	2.4e-20	956.5704	sQ(11,6)	⊥	4.0e-20	1171.6833	sR(10,6)	∥	1.1e-19
7225.9432	aR(13,12)	-	-	-	-	916.7508	aQ(14,12)	⊥	8.6e-21	1191.4987	aR(13,12)	∥	4.7e-21
7270.0567	sR(10,7)*	721.8312	sP(12,7)	∥	1.1e-20	956.0758	sQ(11,7)	⊥	2.9e-20	1171.6070	sR(10,7)	∥	5.1e-20
7348.8371	aR(13,11)	-	-	-	-	922.5368	aQ(14,11)	⊥	3.4e-21	1196.3317	aR(13,11)	∥	3.2e-21
7377.1723	sR(10,8)*	720.7853	sP(12,8)	∥	9.8e-21	955.5527	sQ(11,8)	⊥	3.9e-20	1171.5758	sR(10,8)	∥	4.2e-20
7443.0517	aR(13,10)	-	-	-	-	927.3152	aQ(14,10)	⊥	2.5e-21	1200.2629	aR(13,10)	∥	3.6e-21
7473.4309	sR(11,0)	706.5071	sP(13,0)	∥	8.2e-21	-	-	-	-	1190.1364	sR(11,0)	∥	4.7e-20
7478.9737	sR(11,1)*	706.4264	sP(13,1)	∥	4.1e-21	-	-	-	-	1190.1224	sR(11,1)	∥	2.3e-20
7493.7373	sR(11,2)*	706.2020	sP(13,2)	∥	4.1e-21	-	-	-	-	1190.0983	sR(11,2)	∥	2.3e-20
7510.3917	sR(10,9)*	719.6587	sP(12,9)	∥	1.4e-20	955.0317	sQ(11,9)	⊥	9.2e-20	1171.6251	sR(10,9)	∥	5.5e-20
7515.1871	aR(13,9)	640.9475	aP(15,9)	∥	1.0e-21	931.2631	aQ(14,9)	⊥	3.5e-21	1203.4625	aR(13,9)	∥	7.4e-21

Continued on next page

Table A.4 – continued from previous page

THz laser		IR pump											
		P				Q				R			
Freq. / GHz	QN	Freq. / cm^{-1}	QN	Pola.	G_m / µg	Freq. / cm^{-1}	QN	Pola.	G_m / µg	Freq. / cm^{-1}	QN	Pola.	G_m / µg
7518.0699	sR(11,3)*	705.7663	sP(13,3)	‖	8.5e-21	957.1465	sQ(12,3)	⊥	2.5e-21	1190.0164	sR(11,3)	‖	4.8e-20
7553.0551	sR(11,4)*	705.1952	sP(13,4)	‖	4.3e-21	956.7697	sQ(12,4)	⊥	2.4e-21	1189.9003	sR(11,4)	‖	2.4e-20
7570.3202	aR(13,8)	-	-	-	-	934.5203	aQ(14,8)	⊥	1.2e-21	1206.0643	aR(13,8)	‖	3.6e-21
7601.1059	sR(11,5)*	704.4714	sP(13,5)	‖	4.4e-21	956.3615	sQ(12,5)	⊥	4.0e-21	1189.7912	sR(11,5)	‖	2.5e-20
7605.0104	aR(14,14)	-	-	-	-	906.3451	aQ(15,14)	⊥	1.6e-21	-	-	-	-
7612.3331	aR(13,7)	-	-	-	-	-	-	-	-	1208.1730	aR(13,7)	‖	3.4e-21
7644.1785	aR(13,6)	-	-	-	-	-	-	-	-	1209.8698	aR(13,6)	‖	6.5e-21
7663.3095	sR(11,6)*	703.5964	sP(13,6)	‖	8.9e-21	955.8772	sQ(12,6)	⊥	1.3e-20	1189.6771	sR(11,6)	‖	4.9e-20
7668.0897	aR(13,5)	-	-	-	-	-	-	-	-	1211.2171	aR(13,5)	‖	3.1e-21
7675.5329	sR(10,10)*	718.4882	sP(12,10)	‖	3.7e-21	954.5556	sQ(11,10)	⊥	4.2e-20	1171.8033	sR(10,10)	‖	1.1e-20
7685.7436	aR(13,4)	-	-	-	-	-	-	-	-	1212.2627	aR(13,4)	‖	2.9e-21
7698.7740	aR(13,3)	-	-	-	-	-	-	-	-	1213.0313	aR(13,3)	‖	5.5e-21
7704.9018	aR(13,2)	-	-	-	-	-	-	-	-	1213.5786	aR(13,2)	‖	2.6e-21
7707.1865	aR(13,1)	-	-	-	-	-	-	-	-	1213.7653	aR(13,1)	‖	2.2e-21
7742.1049	sR(11,7)*	702.5800	sP(13,7)	‖	4.4e-21	955.3295	sQ(12,7)	⊥	9.4e-21	1189.5741	sR(11,7)	‖	2.4e-20
7780.5556	aR(14,13)	-	-	-	-	914.0740	aQ(15,13)	⊥	1.6e-21	-	-	-	-
7840.6877	sR(11,8)*	701.4363	sP(13,8)	‖	4.2e-21	954.7365	sQ(12,8)	⊥	1.3e-20	1189.5039	sR(11,8)	‖	2.2e-20
7914.1222	aR(14,12)	-	-	-	-	920.4360	aQ(15,12)	⊥	2.6e-21	1213.4027	aR(14,12)	‖	2.4e-21
7963.2093	sR(11,9)*	700.1859	sP(13,9)	‖	7.4e-21	954.1239	sQ(12,9)	⊥	3.6e-20	1189.4969	sR(11,9)	‖	3.6e-20
7969.6902	sR(12,1)*	687.6576	sP(14,1)	‖	1.2e-21	-	-	-	-	1207.9767	sR(12,1)	‖	8.0e-21
7983.7205	sR(12,2)*	687.4456	sP(14,2)	‖	1.2e-21	-	-	-	-	1207.9754	sR(12,2)	‖	7.9e-21
8003.3788	sR(12,3)*	686.9478	sP(14,3)	‖	2.6e-21	-	-	-	-	1207.8042	sR(12,3)	‖	1.7e-20
8015.5261	aR(14,11)	-	-	-	-	-	-	-	-	1217.6614	aR(14,11)	‖	1.3e-21
8037.3234	sR(12,4)*	686.3611	sP(14,4)	‖	1.3e-21	-	-	-	-	1207.7414	sR(12,4)	‖	8.6e-21
8081.4261	sR(12,5)*	685.5965	sP(14,5)	‖	1.4e-21	955.7328	sQ(13,5)	⊥	1.1e-21	1207.6229	sR(12,5)	‖	8.9e-21
8092.3629	aR(14,10)	-	-	-	-	-	-	-	-	1221.1206	aR(14,10)	‖	1.3e-21
8115.0170	sR(11,10)*	698.8593	sP(13,10)	‖	2.8e-21	953.5278	sQ(12,10)	⊥	2.2e-20	1189.5952	sR(11,10)	‖	1.2e-20
8137.5257	aR(15,15)	-	-	-	-	902.6464	aQ(16,15)	⊥	1.2e-21	-	-	-	-
8138.4506	sR(12,6)*	684.6680	sP(14,6)	‖	2.9e-21	955.2132	sQ(13,6)	⊥	3.6e-21	1207.4939	sR(12,6)	‖	1.8e-20
8150.4695	aR(14,9)	-	-	-	-	-	-	-	-	1223.9334	aR(14,9)	‖	2.4e-21
8194.3034	aR(14,8)	-	-	-	-	-	-	-	-	1226.2194	aR(14,8)	‖	1.1e-21
8210.5983	sR(12,7)*	683.5826	sP(14,7)	‖	1.5e-21	954.6184	sQ(13,7)	⊥	2.7e-21	1207.3679	sR(12,7)	‖	9.4e-21

Continued on next page

Table A.4 – continued from previous page

THz laser		IR pump											
		P				Q				R			
Freq. / GHz	QN	Freq. / cm^{-1}	QN	Pola.	G_m / µg	Freq. / cm^{-1}	QN	Pola.	G_m / µg	Freq. / cm^{-1}	QN	Pola.	G_m / µg
8227.2521	aR(14,7)	-	-	-	-	-	-	-	-	1228.0715	aR(14,7)	‖	1.0e-21
8251.8767	aR(14,6)	-	-	-	-	-	-	-	-	1229.5614	aR(14,6)	‖	1.9e-21
8292.4468	aR(14,3)	-	-	-	-	-	-	-	-	1232.3611	aR(14,3)	‖	1.6e-21
8300.7597	sR(12,8)*	682.3510	sP(14,8)	‖	1.5e-21	953.9629	sQ(13,8)	⊥	4.1e-21	1207.2632	sR(12,8)	‖	9.3e-21
8302.9536	sR(11,11)*	697.5003	sP(13,11)	‖	1.5e-21	952.9994	sQ(12,11)	⊥	2.0e-20	1189.8570	sR(11,11)	‖	4.9e-21
8303.8143	aR(14,0)	-	-	-	-	-	-	-	-	1233.2108	aR(14,0)	‖	1.5e-21
8412.7001	sR(12,9)*	680.9893	sP(14,9)	‖	2.9e-21	953.2677	sQ(13,9)	⊥	1.2e-20	1207.2057	sR(12,9)	‖	1.8e-20
8451.4789	sR(13,0)	-	-	-	-	-	-	-	-	1225.6508	sR(13,0)	‖	5.0e-21
8457.5344	sR(13,1)*	-	-	-	-	-	-	-	-	1225.6372	sR(13,1)	‖	2.5e-21
8472.2848	sR(13,2)*	-	-	-	-	-	-	-	-	1225.7206	sR(13,2)	‖	2.1e-21
8489.8595	sR(13,3)*	-	-	-	-	-	-	-	-	1225.5374	sR(13,3)	‖	5.3e-21
8518.5220	sR(13,4)*	-	-	-	-	-	-	-	-	1225.3927	sR(13,4)	‖	2.8e-21
8551.2894	sR(12,10)*	679.5216	sP(14,10)	‖	1.3e-21	952.5630	sQ(13,10)	⊥	7.8e-21	1207.2315	sR(12,10)	‖	7.5e-21
8558.8184	sR(13,5)*	-	-	-	-	-	-	-	-	1225.2673	sR(13,5)	‖	2.9e-21
8610.8440	sR(13,6)*	-	-	-	-	-	-	-	-	1225.1266	sR(13,6)	‖	6.1e-21
8676.5663	sR(13,7)*	-	-	-	-	-	-	-	-	1224.9818	sR(13,7)	‖	3.2e-21
8722.7820	sR(12,11)*	677.9835	sP(14,11)	‖	1.0e-21	951.8915	sQ(13,11)	⊥	9.4e-21	1207.3906	sR(12,11)	‖	5.2e-21
8758.5710	sR(13,8)*	-	-	-	-	953.2363	sQ(14,8)	⊥	1.1e-21	1224.8482	sR(13,8)	‖	3.4e-21
8860.2390	sR(13,9)*	-	-	-	-	952.4689	sQ(14,9)	⊥	3.2e-21	1224.7474	sR(13,9)	‖	6.9e-21
8935.1640	sR(12,12)*	676.4266	sP(14,12)	‖	1.1e-21	951.3138	sQ(13,12)	⊥	1.7e-20	1207.7525	sR(12,12)	‖	4.2e-21
8967.9670	sR(14,3)*	-	-	-	-	-	-	-	-	1242.8904	sR(14,3)	‖	1.5e-21
8985.9593	sR(13,10)*	-	-	-	-	951.6684	sQ(14,10)	⊥	2.3e-21	1224.7097	sR(13,10)	‖	3.3e-21
9081.1782	sR(14,6)*	-	-	-	-	-	-	-	-	1242.5658	sR(14,6)	‖	1.8e-21
9141.3948	sR(13,11)*	-	-	-	-	950.8697	sQ(14,11)	⊥	3.1e-21	1224.7778	sR(13,11)	‖	2.9e-21
9215.0497	sR(14,8)*	-	-	-	-	-	-	-	-	1242.2507	sR(14,8)	‖	1.1e-21
9306.9223	sR(14,9)*	-	-	-	-	-	-	-	-	1242.1145	sR(14,9)	‖	2.3e-21
9333.8109	sR(13,12)*	-	-	-	-	950.1234	sQ(14,12)	⊥	7.7e-21	1225.0106	sR(13,12)	‖	4.2e-21
9420.3328	sR(14,10)*	-	-	-	-	-	-	-	-	1242.0236	sR(14,10)	‖	1.2e-21
9560.3560	sR(14,11)*	-	-	-	-	-	-	-	-	1242.0134	sR(14,11)	‖	1.2e-21
9572.4649	sR(13,13)*	-	-	-	-	949.5007	sQ(14,13)	⊥	3.6e-21	-	-	-	-
9733.5344	sR(14,12)*	-	-	-	-	949.0439	sQ(15,12)	⊥	2.3e-21	1242.1339	sR(14,12)	‖	2.1e-21
9948.2560	sR(14,13)*	-	-	-	-	948.2242	sQ(15,13)	⊥	1.5e-21	-	-	-	-

Table A.5: Laser lines of $^{14}NH_3$ in competition for a given MIR pumping of the ν_2 band. These lines are reported with asterisk in the rest of the article.

IR pump	**THz freq.**					
Freq. / cm^{-1}	Freq. / GHz	Pola.	G$_m$ / µg	Freq. / GHz	Pola.	G$_m$ / µg
680.8321	1171.5755	⊥	1.1e-20	8994.5770	∥	1.0e-21
683.6716	863.8601	⊥	3.4e-21	8605.1766	∥	1.2e-21
685.0379	755.4456	⊥	4.8e-21	8464.1588	∥	2.7e-21
686.3134	669.2437	⊥	1.6e-21	8350.0699	∥	1.4e-21
687.4722	600.8666	⊥	1.1e-21	8258.0496	∥	1.4e-21
688.4970	546.9373	⊥	1.4e-21	8184.3282	∥	2.7e-21
701.9597	1138.1722	⊥	1.4e-20	8360.0103	∥	1.4e-21
703.1943	984.3138	⊥	1.1e-20	8169.4783	∥	2.6e-21
704.4141	861.6717	⊥	1.7e-20	8015.2658	∥	6.8e-21
705.5734	763.9947	⊥	5.9e-21	7890.5869	∥	3.9e-21
706.6404	686.4131	⊥	4.0e-21	7790.1177	∥	4.1e-21
707.5927	625.1605	⊥	5.2e-21	7709.7126	∥	8.2e-21
708.4153	577.3480	⊥	1.6e-21	7646.1710	∥	4.1e-21
723.0027	1109.5454	⊥	3.1e-20	7730.3501	∥	3.4e-21
724.0613	972.3013	⊥	5.2e-20	7562.8654	∥	1.3e-20
725.0925	862.8099	⊥	1.9e-20	7427.5070	∥	9.0e-21
726.0576	775.7261	⊥	1.4e-20	7318.4990	∥	1.0e-20
726.9295	706.8979	⊥	1.8e-20	7231.3277	∥	2.2e-20
727.6892	653.1278	⊥	5.7e-21	7162.4972	∥	1.2e-20
728.3232	611.9772	⊥	3.4e-21	7109.3284	∥	1.2e-20
728.8132	580.4775	⊥	3.6e-21	7069.1462	∥	2.3e-20
743.9582	1085.4985	⊥	1.3e-19	7105.3300	∥	1.6e-20
744.8509	964.0600	⊥	5.5e-20	6959.4111	∥	1.6e-20
745.7056	867.3425	⊥	4.1e-20	6841.9437	∥	2.2e-20
746.4900	790.8172	⊥	5.7e-20	6748.0585	∥	5.3e-20
747.1812	730.9841	⊥	1.8e-20	6673.9742	∥	2.9e-20
747.7627	685.1681	⊥	1.1e-20	6616.7879	∥	3.1e-20
748.2265	651.9892	⊥	1.2e-20	6574.6673	∥	6.3e-20
748.5698	628.5864	⊥	2.5e-21	6545.4309	∥	3.2e-20
764.8236	1065.8671	⊥	1.3e-19	6484.7191	∥	1.8e-20
765.5612	959.5663	⊥	1.1e-19	6359.0503	∥	3.8e-20
766.2525	875.3682	⊥	1.6e-19	6258.6483	∥	1.1e-19
766.8705	809.4812	⊥	5.4e-20	6179.4596	∥	6.4e-20
767.3960	759.0008	⊥	3.3e-20	6118.3675	∥	7.1e-20
767.8090	721.2642	⊥	3.5e-20	6072.6859	∥	1.5e-19
768.1283	696.4339	⊥	7.6e-21	6042.0165	∥	7.8e-20
768.3114	681.5026	⊥	1.9e-21	6023.6695	∥	7.9e-20
785.5963	1050.5203	⊥	2.4e-19	5868.3228	∥	3.8e-20
786.1906	958.8279	⊥	4.0e-19	5761.7491	∥	1.6e-19

Continued on next page

Table A.5 – continued from previous page

IR pump	THz freq.					
Freq. / cm^{-1}	Freq. / GHz	Pola.	G$_m$ / µg	Freq. / GHz	Pola.	G$_m$ / µg
786.7323	887.0183	⊥	1.4e-19	5677.7236	||	1.1e-19
787.1989	831.9689	⊥	8.8e-20	5612.9291	||	1.4e-19
787.5761	791.5310	⊥	9.6e-20	5564.9930	||	3.1e-19
787.8547	763.5831	⊥	2.2e-20	5531.8880	||	1.7e-19
788.0214	747.2868	⊥	5.0e-21	5512.4717	||	1.7e-19
806.2742	1039.3598	⊥	8.0e-19	5255.9823	||	1.6e-19
806.7377	961.8846	⊥	1.3e-19	5167.5058	||	6.9e-20
807.1441	902.4589	⊥	2.2e-19	5099.3040	||	2.5e-19
807.4718	858.3951	⊥	2.4e-19	5048.5821	||	5.6e-19
807.7223	828.5256	⊥	5.3e-20	5013.9753	||	3.2e-19
807.8716	810.9190	⊥	1.3e-20	4993.5672	||	3.4e-19
826.8553	1032.3214	⊥	6.5e-19	4647.5756	||	1.5e-19
827.2011	968.8093	⊥	4.7e-19	4576.3508	||	3.2e-19
827.4878	921.9405	⊥	5.8e-19	4523.5918	||	9.5e-19
827.7021	889.7112	⊥	1.3e-19	4487.2388	||	5.6e-19
827.8334	870.8782	⊥	3.4e-20	4465.9475	||	6.4e-19
847.3376	1029.3749	⊥	9.1e-19	4043.0164	||	2.8e-19
847.5781	979.6498	⊥	1.2e-18	3988.2917	||	1.2e-18
847.7629	945.6048	⊥	3.0e-19	3950.7233	||	8.5e-19
847.8763	925.6582	⊥	7.7e-20	3928.6856	||	1.0e-18
867.7196	1030.5299	⊥	2.3e-18	3442.2588	||	9.9e-19
867.8729	994.7477	⊥	6.1e-19	3403.6125	||	1.0e-18
867.9689	973.8268	⊥	1.7e-19	3380.9901	||	1.4e-18
887.9998	1035.8161	⊥	1.1e-18	2845.2812	||	8.2e-19
888.0794	1014.0847	⊥	3.4e-19	2822.2564	||	1.6e-18
908.1768	1045.3191	⊥	6.9e-19	2252.1120	||	1.3e-18
953.1392	1043.6537	||	7.8e-21	10009.3750	⊥	1.3e-21
953.8223	878.0883	||	7.3e-21	9791.4158	⊥	2.1e-21
954.5783	1209.9839	||	4.4e-20	9634.3511	⊥	3.6e-21
955.0557	1019.8937	||	3.7e-20	9392.5929	⊥	7.0e-21
955.6767	869.3362	||	8.8e-21	9197.2232	⊥	2.8e-21
956.3676	749.9338	||	4.2e-21	9039.0803	⊥	2.1e-21
956.3968	1171.5755	||	1.7e-19	8994.5770	⊥	1.6e-20
956.8418	1000.1505	||	4.2e-20	8779.3456	⊥	8.6e-21
957.0761	655.1437	||	4.0e-21	8910.9435	⊥	2.9e-21
957.3989	863.8601	||	2.0e-20	8605.1766	⊥	7.1e-21
958.0058	755.4456	||	1.9e-20	8464.1588	⊥	1.1e-20
958.0888	1138.1722	||	1.7e-19	8360.0103	⊥	1.7e-20
958.4967	984.3138	||	7.9e-20	8169.4783	⊥	1.8e-20
958.6177	669.2437	||	4.3e-21	8350.0699	⊥	3.7e-21
958.9893	861.6717	||	7.7e-20	8015.2658	⊥	3.1e-20

Continued on next page

Table A.5 – continued from previous page

IR pump	THz freq.					
Freq. / cm^{-1}	Freq. / GHz	Pola.	G$_m$ / μg	Freq. / GHz	Pola.	G$_m$ / μg
959.2030	600.8666	‖	2.0e-21	8258.0496	⊥	2.5e-21
959.5139	763.9947	‖	1.9e-20	7890.5869	⊥	1.2e-20
959.6524	1109.5454	‖	3.3e-19	7730.3501	⊥	3.7e-20
959.7394	546.9373	‖	1.7e-21	8184.3282	⊥	3.3e-21
960.0199	972.3013	‖	3.3e-19	7562.8654	⊥	8.4e-20
960.0325	686.4131	‖	8.5e-21	7790.1177	⊥	8.6e-21
960.4482	862.8099	‖	7.0e-20	7427.5070	⊥	3.3e-20
960.5182	625.1605	‖	7.3e-21	7709.7126	⊥	1.1e-20
960.8930	775.7261	‖	3.6e-20	7318.4990	⊥	2.7e-20
960.9520	577.3480	‖	1.5e-21	7646.1710	⊥	3.6e-21
961.0860	1085.4985	‖	1.2e-18	7105.3300	⊥	1.5e-19
961.3224	706.8979	‖	3.6e-20	7231.3277	⊥	4.5e-20
961.4110	964.0600	‖	2.8e-19	6959.4111	⊥	8.2e-20
961.7134	653.1278	‖	5.9e-21	7162.4972	⊥	1.2e-20
961.7762	867.3425	‖	1.3e-19	6841.9437	⊥	6.9e-20
962.0497	611.9772	‖	2.1e-21	7109.3284	⊥	7.1e-21
962.1444	790.8172	‖	1.1e-19	6748.0585	⊥	1.0e-19
962.2798	580.4775	‖	1.2e-21	7069.1462	⊥	7.6e-21
962.3884	1065.8671	‖	1.0e-18	6484.7191	⊥	1.4e-19
962.4890	730.9841	‖	2.2e-20	6673.9742	⊥	3.5e-20
962.6698	959.5663	‖	4.5e-19	6359.0503	⊥	1.6e-19
962.7907	685.1681	‖	7.7e-21	6616.7879	⊥	2.1e-20
962.9736	875.3682	‖	3.9e-19	6258.6483	⊥	2.6e-19
963.0575	651.9892	‖	4.3e-21	6574.6673	⊥	2.3e-20
963.2691	809.4812	‖	7.7e-20	6179.4596	⊥	9.1e-20
963.5342	759.0008	‖	2.7e-20	6118.3675	⊥	5.8e-20
963.5585	1050.5203	‖	1.5e-18	5868.3228	⊥	2.4e-19
963.7365	721.2642	‖	1.5e-20	6072.6859	⊥	6.4e-20
963.7962	958.8279	‖	1.3e-18	5761.7491	⊥	5.3e-19
963.9242	696.4339	‖	1.4e-21	6042.0165	⊥	1.4e-20
964.0412	887.0183	‖	2.6e-19	5677.7236	⊥	2.1e-19
964.2685	831.9689	‖	8.9e-20	5612.9291	⊥	1.4e-19
964.4670	791.5310	‖	5.0e-20	5564.9930	⊥	1.6e-19
964.5957	1039.3598	‖	4.0e-18	5255.9823	⊥	7.8e-19
964.6096	763.5831	‖	4.5e-21	5531.8880	⊥	3.6e-20
964.7902	961.8846	‖	8.0e-19	5167.5058	⊥	4.1e-19
964.9796	902.4589	‖	2.8e-19	5099.3040	⊥	3.1e-19
965.1377	858.3951	‖	1.6e-19	5048.5821	⊥	3.7e-19
965.2727	828.5256	‖	1.4e-20	5013.9753	⊥	8.6e-20
965.4994	1032.3214	‖	2.4e-18	4647.5756	⊥	5.8e-19
965.6520	968.8093	‖	8.5e-19	4576.3508	⊥	5.7e-19

Continued on next page

Table A.5 – continued from previous page

IR pump	THz freq.					
Freq. / cm^{-1}	Freq. / GHz	Pola.	G_m / µg	Freq. / GHz	Pola.	G_m / µg
965.7913	921.9405	‖	4.7e-19	4523.5918	⊥	7.7e-19
965.8991	889.7112	‖	4.3e-20	4487.2388	⊥	1.9e-19
965.9677	870.8782	‖	2.5e-21	4465.9475	⊥	4.8e-20
966.2692	1029.3749	‖	2.5e-18	4043.0164	⊥	7.7e-19
966.3799	979.6498	‖	1.4e-18	3988.2917	⊥	1.4e-18
966.4736	945.6048	‖	1.3e-19	3950.7233	⊥	3.6e-19
966.5324	925.6582	‖	7.5e-21	3928.6856	⊥	9.8e-20
966.9051	1030.5299	‖	4.2e-18	3442.2588	⊥	1.8e-18
966.9810	994.7477	‖	3.8e-19	3403.6125	⊥	6.3e-19
967.0308	973.8268	‖	2.2e-20	3380.9901	⊥	1.9e-19
967.4068	1035.8161	‖	1.2e-18	2845.2812	⊥	8.6e-19
967.4491	1014.0847	‖	7.1e-20	2822.2564	⊥	3.3e-19
967.7747	1045.3191	‖	2.7e-19	2252.1120	⊥	4.9e-19
1007.5405	1045.3191	⊥	5.7e-19	2252.1120	‖	1.0e-18
1027.0329	1035.8161	⊥	1.1e-18	2845.2812	‖	7.7e-19
1027.0470	1014.0847	⊥	4.1e-19	2822.2564	‖	1.9e-18
1046.3746	1030.5299	⊥	2.4e-18	3442.2588	‖	1.1e-18
1046.3880	994.7477	⊥	8.5e-19	3403.6125	‖	1.4e-18
1046.4006	973.8268	⊥	2.5e-19	3380.9901	‖	2.1e-18
1065.5638	1029.3749	⊥	1.1e-18	4043.0164	‖	3.5e-19
1065.5654	979.6498	⊥	2.0e-18	3988.2917	‖	1.9e-18
1065.5817	945.6048	⊥	5.3e-19	3950.7233	‖	1.5e-18
1065.5943	925.6582	⊥	1.4e-19	3928.6856	‖	1.9e-18
1084.5836	968.8093	⊥	9.0e-19	4576.3508	‖	6.1e-19
1084.5931	921.9405	⊥	1.2e-18	4523.5918	‖	2.0e-18
1084.5992	1032.3214	⊥	9.1e-19	4647.5756	‖	2.2e-19
1084.6098	889.7112	⊥	2.9e-19	4487.2388	‖	1.3e-18
1084.6237	870.8782	⊥	7.5e-20	4465.9475	‖	1.4e-18
1103.4305	902.4589	⊥	5.2e-19	5099.3040	‖	5.8e-19
1103.4343	961.8846	⊥	7.0e-19	5167.5058	‖	3.6e-19
1103.4412	858.3951	⊥	6.3e-19	5048.5821	‖	1.5e-18
1103.4698	828.5256	⊥	1.4e-19	5013.9753	‖	8.7e-19
1103.4795	1039.3598	⊥	1.3e-18	5255.9823	‖	2.6e-19
1103.4858	810.9190	⊥	3.7e-20	4993.5672	‖	9.4e-19
1122.0937	887.0183	⊥	3.9e-19	5677.7236	‖	3.2e-19
1122.1040	831.9689	⊥	2.6e-19	5612.9291	‖	4.1e-19
1122.1177	958.8279	⊥	9.7e-19	5761.7491	‖	4.0e-19
1122.1329	791.5310	⊥	3.0e-19	5564.9930	‖	9.6e-19
1122.1600	763.5831	⊥	6.6e-20	5531.8880	‖	5.2e-19
1122.1784	747.2868	⊥	1.6e-20	5512.4717	‖	5.5e-19
1122.2036	1050.5203	⊥	4.5e-19	5868.3228	‖	7.3e-20

Continued on next page

Table A.5 – continued from previous page

IR pump	THz freq.					
Freq. / cm^{-1}	Freq. / GHz	Pola.	G_m / μg	Freq. / GHz	Pola.	G_m / μg
1140.5780	809.4812	⊥	1.8e-19	6179.4596	||	2.1e-19
1140.5792	875.3682	⊥	5.0e-19	6258.6483	||	3.3e-19
1140.6037	759.0008	⊥	1.1e-19	6118.3675	||	2.4e-19
1140.6274	721.2642	⊥	1.3e-19	6072.6859	||	5.3e-19
1140.6320	959.5663	⊥	3.1e-19	6359.0503	||	1.1e-19
1140.6792	696.4339	⊥	2.7e-20	6042.0165	||	2.8e-19
1140.6997	681.5026	⊥	6.8e-21	6023.6695	||	2.9e-19
1140.7706	1065.8671	⊥	2.8e-19	6484.7191	||	3.9e-20
1158.8655	790.8172	⊥	2.2e-19	6748.0585	||	2.0e-19
1158.8848	867.3425	⊥	1.5e-19	6841.9437	||	8.2e-20
1158.8875	730.9841	⊥	7.3e-20	6673.9742	||	1.2e-19
1158.9289	685.1681	⊥	4.5e-20	6616.7879	||	1.2e-19
1158.9758	964.0600	⊥	1.8e-19	6959.4111	||	5.3e-20
1158.9850	651.9892	⊥	4.9e-20	6574.6673	||	2.6e-19
1159.0258	628.5864	⊥	1.0e-20	6545.4309	||	1.3e-19
1159.0473	615.0456	⊥	2.6e-21	6528.1959	||	1.3e-19
1159.1800	1085.4985	⊥	3.2e-19	7105.3300	||	4.0e-20
1176.9636	775.7261	⊥	6.0e-20	7318.4990	||	4.6e-20
1176.9767	706.8979	⊥	8.4e-20	7231.3277	||	1.0e-19
1177.0084	862.8099	⊥	8.1e-20	7427.5070	||	3.8e-20
1177.0212	653.1278	⊥	2.7e-20	7162.4972	||	5.4e-20
1177.0776	611.9772	⊥	1.6e-20	7109.3284	||	5.6e-20
1177.1108	580.4775	⊥	1.7e-20	7069.1462	||	1.1e-19
1177.1477	972.3013	⊥	1.9e-19	7562.8654	||	5.0e-20
1177.1978	561.4592	⊥	3.6e-21	7043.1848	||	5.5e-20
1177.4315	1109.5454	⊥	8.7e-20	7730.3501	||	9.6e-21
1194.8679	686.4131	⊥	2.1e-20	7790.1177	||	2.1e-20
1194.8697	763.9947	⊥	3.0e-20	7890.5869	||	2.0e-20
1194.9111	625.1605	⊥	2.8e-20	7709.7126	||	4.4e-20
1194.9479	861.6717	⊥	8.1e-20	8015.2658	||	3.3e-20
1194.9762	577.3480	⊥	8.9e-21	7646.1710	||	2.2e-20
1195.0464	540.7765	⊥	5.3e-21	7597.0436	||	2.2e-20
1195.1336	515.3808	⊥	5.6e-21	7561.2578	||	4.4e-20
1195.1464	984.3138	⊥	4.9e-20	8169.4783	||	1.1e-20
1195.1930	496.3563	⊥	1.2e-21	7536.2875	||	2.1e-20
1195.5251	1138.1722	⊥	4.5e-20	8360.0103	||	4.4e-21
1212.5581	669.2437	⊥	9.8e-21	8350.0699	||	8.4e-21
1212.5810	755.4456	⊥	2.8e-20	8464.1588	||	1.6e-20
1212.5951	600.8666	⊥	6.6e-21	8258.0496	||	8.5e-21
1212.6649	546.9373	⊥	8.6e-21	8184.3282	||	1.7e-20
1212.7013	863.8601	⊥	1.9e-20	8605.1766	||	6.8e-21

Continued on next page

Table A.5 – continued from previous page

IR pump	**THz freq.**					
Freq. / cm^{-1}	Freq. / GHz	Pola.	G_m / µg	Freq. / GHz	Pola.	G_m / µg
1212.7480	504.8735	⊥	2.7e-21	8126.0032	||	8.1e-21
1212.8300	472.7172	⊥	1.6e-21	8080.8596	||	7.8e-21
1212.8633	446.5256	⊥	1.6e-21	8046.0571	||	1.5e-20
1212.9709	1000.1505	⊥	2.3e-20	8779.3456	||	4.7e-21
1213.4613	1171.5755	⊥	4.3e-20	8994.5770	||	3.9e-21
1230.0439	655.1437	⊥	8.4e-21	8910.9435	||	6.2e-21
1230.0694	579.8942	⊥	2.8e-21	8807.1629	||	3.0e-21
1230.0949	749.9338	⊥	6.0e-21	9039.0803	||	3.0e-21
1230.1397	520.2789	⊥	1.9e-21	8723.3469	||	2.9e-21
1230.2321	473.3056	⊥	2.4e-21	8656.1027	||	5.6e-21
1230.2667	869.3362	⊥	8.2e-21	9197.2232	||	2.6e-21
1230.6204	1019.8937	⊥	2.0e-20	9392.5929	||	3.8e-21
1247.3221	643.9029	⊥	1.7e-21	9472.5283	||	1.1e-21
1247.3303	561.9381	⊥	2.2e-21	9356.7463	||	2.1e-21
1247.4088	747.3440	⊥	2.4e-21	9615.2434	||	1.1e-21
1247.6422	878.0883	⊥	6.6e-21	9791.4158	||	1.9e-21

Table A.6: Laser lines of $^{15}NH_3$ in competition for a given MIR pumping in the ν_2 band. These lines are reported with asterisk in the rest of the article.

IR pump	**THz freq.**					
Freq. / cm^{-1}	Freq. / GHz	Pola.	G_m / µg	Freq. / GHz	Pola.	G_m / µg
677.9835	960.4703	⊥	5.2e-21	8722.7820	||	1.0e-21
679.5216	827.2044	⊥	3.8e-21	8551.2894	||	1.3e-21
680.9893	721.4841	⊥	5.3e-21	8412.7001	||	2.9e-21
682.3510	637.6352	⊥	1.8e-21	8300.7597	||	1.5e-21
698.8593	945.4435	⊥	1.3e-20	8115.0170	||	2.8e-21
700.1859	825.4977	⊥	1.9e-20	7963.2093	||	7.4e-21
701.4363	730.2018	⊥	6.6e-21	7840.6877	||	4.2e-21
702.5800	654.6790	⊥	4.5e-21	7742.1049	||	4.4e-21
703.5964	595.1696	⊥	5.8e-21	7663.3095	||	8.9e-21
704.4714	548.7980	⊥	1.8e-21	7601.1059	||	4.4e-21
719.6587	934.1200	⊥	5.7e-20	7510.3917	||	1.4e-20
720.7853	827.0081	⊥	2.1e-20	7377.1723	||	9.8e-21
721.8312	742.0019	⊥	1.5e-20	7270.0567	||	1.1e-20
722.7704	674.9452	⊥	2.0e-20	7184.5146	||	2.4e-20
723.5852	622.6471	⊥	6.4e-21	7117.0472	||	1.3e-20
724.2631	582.6811	⊥	3.8e-21	7064.9804	||	1.3e-20

Continued on next page

Table A.6 – continued from previous page

IR pump	THz freq.					
Freq. / cm^{-1}	Freq. / GHz	Pola.	G_m / μg	Freq. / GHz	Pola.	G_m / μg
724.7878	552.1314	⊥	4.0e-21	7025.6923	||	2.5e-20
740.3798	926.4495	⊥	6.1e-20	6908.8116	||	1.8e-20
741.3189	831.8057	⊥	4.5e-20	6793.2227	||	2.4e-20
742.1737	757.0629	⊥	6.3e-20	6700.9706	||	5.8e-20
742.9225	698.7197	⊥	2.0e-20	6628.2622	||	3.2e-20
743.5499	654.1073	⊥	1.2e-20	6572.1939	||	3.3e-20
744.0483	621.8448	⊥	1.3e-20	6530.9238	||	6.8e-20
744.4163	599.0989	⊥	2.8e-21	6502.3053	||	3.4e-20
760.1956	1026.6663	⊥	1.4e-19	6434.0366	||	2.0e-20
761.0208	922.4116	⊥	1.2e-19	6310.2136	||	4.1e-20
761.7853	839.9900	⊥	1.8e-19	6211.4341	||	1.1e-19
762.4634	775.5979	⊥	6.0e-20	6133.6230	||	6.9e-20
763.0366	726.3306	⊥	3.6e-20	6073.6564	||	7.7e-20
763.4871	689.5634	⊥	4.0e-20	6028.8830	||	1.6e-19
763.8306	665.3558	⊥	8.5e-21	5998.7901	||	8.5e-20
764.0287	650.8201	⊥	2.1e-21	5980.8113	||	8.7e-20
780.9101	1011.9545	⊥	2.7e-19	5819.5382	||	4.3e-20
781.5802	922.0162	⊥	4.4e-19	5714.5641	||	1.8e-19
782.1839	851.6939	⊥	1.6e-19	5631.9086	||	1.3e-19
782.7001	797.8583	⊥	9.9e-20	5568.2399	||	1.6e-19
783.1148	758.3559	⊥	1.1e-19	5521.1737	||	3.5e-19
783.4198	731.0736	⊥	2.4e-20	5488.6927	||	1.9e-19
783.6022	715.1759	⊥	5.9e-21	5469.6489	||	1.9e-19
801.5289	1001.3107	⊥	9.1e-19	5208.9842	||	1.7e-19
802.0563	925.3043	⊥	3.6e-19	5121.8624	||	1.8e-19
802.5137	867.0846	⊥	2.4e-19	5054.7805	||	2.7e-19
802.8811	823.9835	⊥	2.8e-19	5004.9604	||	6.5e-19
803.1579	794.7519	⊥	6.2e-20	4970.9484	||	3.7e-19
803.3234	777.5447	⊥	1.5e-20	4950.9148	||	3.9e-19
822.0498	994.6724	⊥	7.1e-19	4602.2531	||	1.7e-19
822.4479	932.3515	⊥	5.4e-19	4532.1389	||	3.6e-19
822.7744	886.4111	⊥	6.5e-19	4480.2496	||	1.0e-18
823.0167	854.8450	⊥	1.5e-19	4444.5206	||	6.3e-19
823.1646	836.4102	⊥	3.7e-20	4423.6044	||	7.0e-19
842.4710	992.0120	⊥	1.0e-18	3999.2593	||	3.1e-19
842.7529	943.2247	⊥	1.4e-18	3945.4198	||	1.3e-18
842.9657	909.8183	⊥	3.3e-19	3908.4539	||	9.3e-19
843.0961	890.2670	⊥	8.5e-20	3886.7909	||	1.1e-18
862.7911	993.3404	⊥	2.5e-18	3399.9562	||	1.1e-18
862.9735	958.2089	⊥	6.7e-19	3361.9305	||	1.1e-18
863.0868	937.6801	⊥	1.8e-19	3339.6823	||	1.5e-18

Continued on next page

Table A.6 – continued from previous page

IR pump	THz freq.					
Freq. / cm^{-1}	Freq. / GHz	Pola.	G_m / μg	Freq. / GHz	Pola.	G_m / μg
883.0085	998.6884	⊥	1.3e-18	2804.3225	∥	9.0e-19
883.1056	977.3450	⊥	3.8e-19	2781.6717	∥	1.7e-18
903.1219	1008.1427	⊥	7.7e-19	2212.3850	∥	1.4e-18
950.8697	832.0875	∥	9.9e-21	9141.3948	⊥	3.1e-21
951.6684	715.7032	∥	4.7e-21	8985.9593	⊥	2.3e-21
951.8915	960.4703	∥	4.7e-20	8722.7820	⊥	9.4e-21
952.4689	623.5677	∥	4.5e-21	8860.2390	⊥	3.2e-21
952.5630	827.2044	∥	2.2e-20	8551.2894	⊥	7.8e-21
953.2363	550.6156	∥	1.0e-21	8758.5710	⊥	1.1e-21
953.2677	721.4841	∥	2.1e-20	8412.7001	⊥	1.2e-20
953.5278	945.4435	∥	9.6e-20	8115.0170	⊥	2.2e-20
953.9629	637.6352	∥	4.9e-21	8300.7597	⊥	4.1e-21
954.1239	825.4977	∥	9.0e-20	7963.2093	⊥	3.6e-20
954.7365	730.2018	∥	2.1e-20	7840.6877	⊥	1.3e-20
955.0317	934.1200	∥	3.6e-19	7510.3917	⊥	9.2e-20
955.3295	654.6790	∥	9.5e-21	7742.1049	⊥	9.4e-21
955.5527	827.0081	∥	8.5e-20	7377.1723	⊥	3.9e-20
955.8772	595.1696	∥	8.2e-21	7663.3095	⊥	1.3e-20
956.0758	742.0019	∥	3.8e-20	7270.0567	⊥	2.9e-20
956.3615	548.7980	∥	1.6e-21	7601.1059	⊥	4.0e-21
956.4029	926.4495	∥	3.2e-19	6908.8116	⊥	9.2e-20
956.5704	674.9452	∥	3.3e-20	7184.5146	⊥	4.0e-20
956.8500	831.8057	∥	1.4e-19	6793.2227	⊥	7.7e-20
957.0148	622.6471	∥	6.6e-21	7117.0472	⊥	1.3e-20
957.2742	1026.6663	∥	1.1e-18	6434.0366	⊥	1.5e-19
957.2866	757.0629	∥	1.2e-19	6700.9706	⊥	1.1e-19
957.3935	582.6811	∥	2.3e-21	7064.9804	⊥	7.8e-21
957.6410	922.4116	∥	5.0e-19	6310.2136	⊥	1.7e-19
957.6577	552.1314	∥	1.3e-21	7025.6923	⊥	8.3e-21
957.6872	698.7197	∥	2.5e-20	6628.2622	⊥	3.8e-20
958.0161	839.9900	∥	4.3e-19	6211.4341	⊥	2.8e-19
958.0336	654.1073	∥	8.6e-21	6572.1939	⊥	2.3e-20
958.3339	621.8448	∥	4.9e-21	6530.9238	⊥	2.5e-20
958.3701	775.5979	∥	8.6e-20	6133.6230	⊥	1.0e-19
958.4344	1011.9545	∥	1.7e-18	5819.5382	⊥	2.7e-19
958.6817	726.3306	∥	3.0e-20	6073.6564	⊥	6.3e-20
958.7461	922.0162	∥	1.4e-18	5714.5641	⊥	5.8e-19
958.9207	689.5634	∥	1.7e-20	6028.8830	⊥	7.0e-20
959.0517	851.6939	∥	2.8e-19	5631.9086	⊥	2.3e-19
959.1319	665.3558	∥	1.5e-21	5998.7901	⊥	1.5e-20
959.3273	797.8583	∥	1.0e-19	5568.2399	⊥	1.6e-19

Continued on next page

Table A.6 – continued from previous page

IR pump	THz freq.					
Freq. / cm^{-1}	Freq. / GHz	Pola.	G_m / μg	Freq. / GHz	Pola.	G_m / μg
959.4609	1001.3107	∥	4.5e-18	5208.9842	⊥	8.6e-19
959.5625	758.3559	∥	5.6e-20	5521.1737	⊥	1.8e-19
959.7180	925.3043	∥	8.9e-19	5121.8624	⊥	4.5e-19
959.7310	731.0736	∥	5.0e-21	5488.6927	⊥	4.0e-20
959.9574	867.0846	∥	3.1e-19	5054.7805	⊥	3.4e-19
960.1544	823.9835	∥	1.7e-19	5004.9604	⊥	4.1e-19
960.3151	794.7519	∥	1.6e-20	4970.9484	⊥	9.4e-20
960.3530	994.6724	∥	2.7e-18	4602.2531	⊥	6.3e-19
960.5570	932.3515	∥	9.4e-19	4532.1389	⊥	6.3e-19
960.7353	886.4111	∥	5.3e-19	4480.2496	⊥	8.4e-19
960.8707	854.8450	∥	4.8e-20	4444.5206	⊥	2.0e-19
960.9555	836.4102	∥	2.8e-21	4423.6044	⊥	5.3e-20
961.1104	992.0120	∥	2.8e-18	3999.2593	⊥	8.4e-19
961.2619	943.2247	∥	1.6e-18	3945.4198	⊥	1.5e-18
961.3831	909.8183	∥	1.4e-19	3908.4539	⊥	4.0e-19
961.4586	890.2670	∥	8.3e-21	3886.7909	⊥	1.1e-19
961.7332	993.3404	∥	4.6e-18	3399.9562	⊥	2.0e-18
961.8378	958.2089	∥	4.2e-19	3361.9305	⊥	6.9e-19
961.9047	937.6801	∥	2.5e-20	3339.6823	⊥	2.1e-19
962.2208	998.6884	∥	1.3e-18	2804.3225	⊥	9.4e-19
962.2805	977.3450	∥	7.9e-20	2781.6717	⊥	3.6e-19
962.5738	1008.1427	∥	3.0e-19	2212.3850	⊥	5.4e-19
1002.2424	1008.1427	⊥	6.3e-19	2212.3850	∥	1.1e-18
1021.7011	998.6884	⊥	1.2e-18	2804.3225	∥	8.5e-19
1021.7324	977.3450	⊥	4.5e-19	2781.6717	∥	2.0e-18
1041.0083	993.3404	⊥	2.7e-18	3399.9562	∥	1.2e-18
1041.0501	958.2089	⊥	9.4e-19	3361.9305	∥	1.6e-18
1041.0795	937.6801	⊥	2.8e-19	3339.6823	∥	2.3e-18
1060.1621	992.0120	⊥	1.2e-18	3999.2593	∥	3.8e-19
1060.2039	943.2247	⊥	2.2e-18	3945.4198	∥	2.1e-18
1060.2474	909.8183	⊥	5.9e-19	3908.4539	∥	1.7e-18
1060.2765	890.2670	⊥	1.6e-19	3886.7909	∥	2.1e-18
1079.1614	994.6724	⊥	1.0e-18	4602.2531	∥	2.4e-19
1079.1963	932.3515	⊥	1.0e-18	4532.1389	∥	6.7e-19
1079.2443	886.4111	⊥	1.3e-18	4480.2496	∥	2.2e-18
1079.2881	854.8450	⊥	3.2e-19	4444.5206	∥	1.4e-18
1079.3180	836.4102	⊥	8.4e-20	4423.6044	∥	1.6e-18
1098.0049	1001.3107	⊥	1.5e-18	5208.9842	∥	2.8e-19
1098.0212	925.3043	⊥	7.8e-19	5121.8624	∥	3.9e-19
1098.0664	867.0846	⊥	5.9e-19	5054.7805	∥	6.4e-19
1098.1154	823.9835	⊥	7.0e-19	5004.9604	∥	1.7e-18

Continued on next page

Table A.6 – continued from previous page

IR pump	THz freq.					
Freq. / cm^{-1}	Freq. / GHz	Pola.	G$_\mathrm{m}$ / µg	Freq. / GHz	Pola.	G$_\mathrm{m}$ / µg
1098.1691	794.7519	⊥	1.6e-19	4970.9484	∥	9.6e-19
1098.2006	777.5447	⊥	4.1e-20	4950.9148	∥	1.0e-18
1116.6781	922.0162	⊥	1.1e-18	5714.5641	∥	4.4e-19
1116.6915	1011.9545	⊥	5.0e-19	5819.5382	∥	8.0e-20
1116.7134	851.6939	⊥	4.3e-19	5631.9086	∥	3.5e-19
1116.7710	797.8583	⊥	2.9e-19	5568.2399	∥	4.6e-19
1116.8358	758.3559	⊥	3.3e-19	5521.1737	∥	1.1e-18
1116.8881	731.0736	⊥	7.4e-20	5488.6927	∥	5.8e-19
1116.9215	715.1759	⊥	1.8e-20	5469.6489	∥	6.1e-19
1135.1653	922.4116	⊥	3.4e-19	6310.2136	∥	1.2e-19
1135.1821	839.9900	⊥	5.7e-19	6211.4341	∥	3.7e-19
1135.2204	1026.6663	⊥	3.1e-19	6434.0366	∥	4.3e-20
1135.2379	775.5979	⊥	2.0e-19	6133.6230	∥	2.3e-19
1135.3090	726.3306	⊥	1.3e-19	6073.6564	∥	2.7e-19
1135.3684	689.5634	⊥	1.4e-19	6028.8830	∥	5.9e-19
1135.4431	665.3558	⊥	3.1e-20	5998.7901	∥	3.1e-19
1135.4778	650.8201	⊥	7.6e-21	5980.8113	∥	3.2e-19
1153.4702	831.8057	⊥	1.7e-19	6793.2227	∥	9.0e-20
1153.4815	926.4495	⊥	2.0e-19	6908.8116	∥	5.9e-20
1153.5174	757.0629	⊥	2.5e-19	6700.9706	∥	2.3e-19
1153.5940	698.7197	⊥	8.3e-20	6628.2622	∥	1.3e-19
1153.6788	654.1073	⊥	5.1e-20	6572.1939	∥	1.4e-19
1153.7675	621.8448	⊥	5.5e-20	6530.9238	∥	2.9e-19
1153.8316	599.0989	⊥	1.2e-20	6502.3053	∥	1.5e-19
1153.8665	585.9483	⊥	2.9e-21	6485.4297	∥	1.5e-19
1171.5758	827.0081	⊥	9.1e-20	7377.1723	∥	4.2e-20
1171.6070	742.0019	⊥	6.8e-20	7270.0567	∥	5.1e-20
1171.6251	934.1200	⊥	2.2e-19	7510.3917	∥	5.5e-20
1171.6833	674.9452	⊥	9.4e-20	7184.5146	∥	1.1e-19
1171.7796	622.6471	⊥	3.0e-20	7117.0472	∥	6.0e-20
1171.8773	582.6811	⊥	1.8e-20	7064.9804	∥	6.1e-20
1171.9433	552.1314	⊥	1.9e-20	7025.6923	∥	1.2e-19
1189.4969	825.4977	⊥	9.1e-20	7963.2093	∥	3.6e-20
1189.5039	730.2018	⊥	3.4e-20	7840.6877	∥	2.2e-20
1189.5741	654.6790	⊥	2.4e-20	7742.1049	∥	2.4e-20
1189.5952	945.4435	⊥	5.5e-20	8115.0170	∥	1.2e-20
1189.6771	595.1696	⊥	3.2e-20	7663.3095	∥	4.9e-20
1189.7912	548.7980	⊥	1.0e-20	7601.1059	∥	2.5e-20
1207.2057	721.4841	⊥	3.2e-20	8412.7001	∥	1.8e-20
1207.2315	827.2044	⊥	2.1e-20	8551.2894	∥	7.5e-21
1207.2632	637.6352	⊥	1.1e-20	8300.7597	∥	9.3e-21

Continued on next page

Table A.6 – continued from previous page

IR pump	THz freq.					
Freq. / cm^{-1}	Freq. / GHz	Pola.	G_m / μg	Freq. / GHz	Pola.	G_m / μg
1207.3906	960.4703	⊥	2.6e-20	8722.7820	‖	5.2e-21
1224.7097	715.7032	⊥	6.8e-21	8985.9593	‖	3.3e-21
1224.7474	623.5677	⊥	9.5e-21	8860.2390	‖	6.9e-21
1224.7778	832.0875	⊥	9.3e-21	9141.3948	‖	2.9e-21
1224.8482	550.6156	⊥	3.2e-21	8758.5710	‖	3.4e-21

Bibliography

[1] Cabezas, C.; Bermúdez, C.; Endo, Y.; Tercero, B.; Cernicharo, J. Rotational spectroscopy and astronomical search for glutaronitrile. *Astronomy and Astrophysics* **2020**, *636*, 4–9.

[2] Van Dishoeck, E. F. Astrochemistry of dust, ice and gas: Introduction and overview. *Faraday Discussions* **2014**, *168*, 9–47.

[3] Endres, C. P.; Schlemmer, S.; Schilke, P.; Stutzki, J.; Müller, H. S. The Cologne Database for Molecular Spectroscopy, CDMS, in the Virtual Atomic and Molecular Data Centre, VAMDC. *Journal of Molecular Spectroscopy* **2016**, *327*, 95–104.

[4] McGuire, B. A.; Burkhardt, A. M.; Kalenskii, S.; Shingledecker, C. N.; Remijan, A. J.; Herbst, E.; McCarthy, M. C. Detection of the aromatic molecule benzonitrile ($c{-}C_6H_5CN$) in the interstellar medium. *Science* **2018**, *359*, 202–205.

[5] Le Petit, F.; Nehme, C.; Le Bourlot, J.; Roueff, E. A Model for Atomic and Molecular Interstellar Gas: The Meudon PDR Code. *The Astrophysical Journal Supplement Series* **2006**, *164*, 506–529.

[6] Hollenbach, D.; Kaufman, M. J.; Neufeld, D.; Wolfire, M.; Goicoechea, J. R. The

chemistry of interstellar OH^+, H_2O^+, and H_3O^+: Inferring the cosmic-ray ionization rates from observations of molecular ions. *Astrophysical Journal* **2012**, *754*.

[7] Antiñolo, M.; Agúndez, M.; Jiménez, E.; Ballesteros, B.; Canosa, A.; Dib, G. E.; Albaladejo, J.; Cernicharo, J. Reactivity of OH and CH_3OH between 22 and 64 K: Modeling the gas phase production of CH_3O in Barnard 1b. *The Astrophysical Journal* **2016**, *823*, 25.

[8] Berteloite, C.; Le Picard, S. D.; Balucani, N.; Canosa, A.; Sims, I. R. Low temperature rate coefficients for reactions of the butadiynyl radical, C_4H, with various hydrocarbons. Part I: reactions with alkanes (CH_4, C_2H_6, C_3H_8, C_4H_{10}). *Physical Chemistry Chemical Physics* **2010**, *12*, 3666–76.

[9] Smith, I. W. M. Reactions at very low temperatures: gas kinetics at a new frontier. *Angewandte Chemie (International edition)* **2006**, *45*, 2842–61.

[10] Snow, T. P.; McCall, B. J. Diffuse atomic and molecular clouds. *Annual Review of Astronomy and Astrophysics* **2006**, *44*, 367–414.

[11] Jiménez-Serra, I.; Vasyunin, A. I.; Caselli, P.; Marcelino, N.; Billot, N.; Viti, S.; Testi, L.; Vastel, C.; Lefloch, B.; Bachiller, R. The spatial distribution of complex organic molecules in the L1544 pre-stellar core. *The Astrophysical Journal* **2016**, *830*, L6.

[12] Bacmann, A.; Faure, A.; Berteaud, J. Cold and Yet Complex: Detection of Ethylene Oxide in a Prestellar Core. *ACS Earth and Space Chemistry* **2019**, *3*, 1000–1013.

[13] Vastel, C.; Ceccarelli, C.; Lefloch, B.; Bachiller, R. The origin of complex organic molecules in prestellar cores. *The Astrophysical Journal* **2014**, *795*, L2.

[14] Lattanzi, V.; Bizzocchi, L.; Vasyunin, A. I.; Harju, J.; Giuliano, B. M.; Vastel, C.; Caselli, P. Molecular complexity in pre-stellar cores: A 3 mm-band study of L183 and L1544. *Astronomy and Astrophysics* **2020**, *633*, 1–17.

[15] Turner, B.; Apponi, A. Microwave detection of interstellar vinyl alcohol, CH_2=CHOH. *The Astrophysical Journal Letters* **2008**, *561*, L207.

[16] Bacmann, A.; García-García, E.; Faure, A. Detection of protonated formaldehyde in the prestellar core L1689B. *Astronomy and Astrophysics* **2016**, *588*, 8–11.

[17] Bacmann, A.; Taquet, V.; Faure, A.; Kahane, C.; Ceccarelli, C. Detection of complex organic molecules in a prestellar core: a new challenge for astrochemical models. *Astronomy & Astrophysics* **2012**, *541*, L12.

[18] Scibelli, S.; Shirley, Y. Prevalence of Complex Organic Molecules in Starless and Prestellar Cores within the Taurus Molecular Cloud. *The Astrophysical Journal* **2020**, *891*, 73.

[19] Jiménez, E.; Antiñolo, M.; Ballesteros, B.; Canosa, A.; Albaladejo, J. First evidence of the dramatic enhancement of the reactivity of methyl formate ($HC(O)OCH_3$) with OH at temperatures of the interstellar medium: A gas-phase kinetic study between 22 K and 64 K. *Physical Chemistry Chemical Physics* **2016**, *18*, 2183–2191.

[20] McCarthy, M. C.; McGuire, B. A. Aromatics and cyclic molecules in molecular clouds: A new dimension of interstellar organic chemistry. *Journal of Physical Chemistry A* **2021**, *125*, 3231–3243.

[21] Balucani, N.; Ceccarelli, C.; Taquet, V. Formation of complex organic molecules in cold objects: The role of gas-phase reactions. *Monthly Notices of the Royal Astronomical Society: Letters* **2015**, *449*, L16–L20.

[22] Smith, D.; Adams, N. G. A brief review of interstellar ion chemistry. *Journal of the Chemical Society, Faraday Transactions 2* **1989**, *85*, 1613–1630.

[23] Bohme, D.; Rakshit, A.; Schiff, H. Reactions of $^{12}C^+$ with hydrocarbons at 296 K: carbon-carbon bond formation. *Chemical Physics Letters* **1982**, *93*, 592–597.

[24] Cooke, I. R.; Sims, I. R. Experimental studies of gas-phase reactivity in relation to complex organic molecules in star-forming regions. *ACS Earth and Space Chemistry* **2019**, *3*, 1109–1134.

[25] Rowe, B. R.; Dupeyrat, G.; Marquette, J. B.; Gaucherel, P. Study of the reactions $N_2^+ + 2\,N_2 \rightarrow N_4^+ + N_2$ and $O_2^+ + 2\,O_2 \rightarrow O_4^+ + O_2$ from 20 to 160 K by the CRESU technique. *The Journal of Chemical Physics* **1984**, *80*, 4915.

[26] Rowe, B.; Marquette, J. CRESU studies of ion/molecule reactions. *International Journal of Mass Spectrometry and Ion Processes* **1987**, *80*, 239–254.

[27] Cooke, I. R.; Gupta, D.; Messinger, J. P.; Sims, I. R. Benzonitrile as a proxy for benzene in the cold ISM: Low-temperature rate coefficients for $CN + C_6H_6$. *The Astrophysical Journal* **2020**, *891*, L41.

[28] Dupeyrat, G.; Marquette, J. B.; Rowe, B. R. Design and testing of axisymmetric nozzles for ion-molecule reaction studies between 20 K and 160 K. *Physics of Fluids* **1985**, *28*, 1273.

[29] Ocaña, A. J.; Blázquez, S.; Potapov, A.; Ballesteros, B.; Canosa, A.; Antiñolo, M.; Vereecken, L.; Albaladejo, J.; Jiménez, E. Gas-phase reactivity of CH_3OH toward OH at interstellar temperatures (11.7–177.5 K): Experimental and theoretical study. *Physical Chemistry Chemical Physics* **2019**, *21*, 6942–6957.

[30] Shannon, R. J.; Blitz, M. a.; Goddard, A.; Heard, D. E. Accelerated chemistry in the reaction between the hydroxyl radical and methanol at interstellar temperatures facilitated by tunnelling. *Nature Chemistry* **2013**, *5*, 745–9.

[31] Shannon, R. J.; Caravan, R. L.; Blitz, M. A.; Heard, D. E. A combined experimental and theoretical study of reactions between the hydroxyl radical and oxygenated hydrocarbons relevant to astrochemical environments. *Physical Chemistry Chemical Physics* **2014**, *16*, 3466–3478.

[32] Gómez Martín, J. C.; Caravan, R. L.; Blitz, M. A.; Heard, D. E.; Plane, J. M. Low temperature kinetics of the CH_3OH + OH reaction. *Journal of Physical Chemistry A* **2014**, *118*, 2693–2701.

[33] Caravan, R. L.; Shannon, R. J.; Lewis, T.; Blitz, M. A.; Heard, D. E. Measurements of rate coefficients for reactions of OH with ethanol and propan-2-ol at very low temperatures. *Journal of Physical Chemistry A* **2015**, *119*, 7130–7137.

[34] Messinger, J. P.; Gupta, D.; Cooke, I. R.; Okumura, M.; Sims, I. R. Rate constants of the CN + toluene reaction from 15 to 294 K and interstellar implications. *The Journal of Physical Chemistry A* **2020**, *124*, 7950–7958.

[35] Taylor, S. E.; Goddard, A.; Blitz, M. A.; Cleary, P. A.; Heard, D. E. Pulsed Laval

nozzle study of the kinetics of OH with unsaturated hydrocarbons at very low temperatures. *Physical Chemistry Chemical Physics* **2008**, *10*, 422–437.

[36] Hearne, T. S.; Abdelkader Khedaoui, O.; Hays, B. M.; Guillaume, T.; Sims, I. R. A novel Ka-band chirped-pulse spectrometer used in the determination of pressure broadening coefficients of astrochemical molecules. *Journal of Chemical Physics* **2020**, *153*.

[37] Spangenberg, T.; Köhler, S.; Hansmann, B.; Wachsmuth, U.; Abel, B.; Smith, M. A. Low-temperature reactions of OH radicals with propene and isoprene in pulsed laval nozzle expansions. *Journal of Physical Chemistry A* **2004**, *108*, 7527–7534.

[38] Morales, S. B.; Le Picard, S. D.; Canosa, A.; Sims, I. R. Experimental measurements of low temperature rate coefficients for neutral–neutral reactions of interest for atmospheric chemistry of Titan, Pluto and Triton: Reactions of the CN radical. *Faraday Discussions* **2010**, *147*, 155.

[39] Abeysekera, C.; Zack, L. N.; Park, G. B.; Joalland, B.; Oldham, J. M.; Prozument, K.; Ariyasingha, N. M.; Sims, I. R.; Field, R. W.; Suits, A. G. A chirped-pulse Fourier-transform microwave/pulsed uniform flow spectrometer. II. Performance and applications for reaction dynamics. *The Journal of Chemical Physics* **2014**, *141*, 214203.

[40] Sims, I. R.; Queffelec, J. L.; Defrance, A.; Rebrion-Rowe, C.; Travers, D.; Rowe, B. R.; Smith, I. W. Ultra-low temperature kinetics of neutral-neutral reactions: The reaction of $CH^{+}O_2$ down to 26 K. *Journal of Chemical Physics* **1992**, *97*, 8798–8800.

[41] Schläppi, B.; Litman, J. H.; Ferreiro, J. J.; Stapfer, D.; Signorell, R. A pulsed uniform

Laval expansion coupled with single photon ionization and mass spectrometric detection for the study of large molecular aggregates. *Physical Chemistry Chemical Physics* **2015**, *17*, 25761–25771.

[42] Abeysekera, C.; Joalland, B.; Ariyasingha, N.; Zack, L. N.; Sims, I. R.; Field, R. W.; Suits, A. G. Product branching in the low temperature reaction of CN with propyne by chirped-pulse microwave spectroscopy in a uniform supersonic flow. *Journal of Physical Chemistry Letters* **2015**, *6*, 1599–1604.

[43] Brown, G. G.; Dian, B. C.; Douglass, K. O.; Geyer, S. M.; Shipman, S. T.; Pate, B. H. A broadband Fourier transform microwave spectrometer based on chirped pulse excitation. *The Review of Scientific Instruments* **2008**, *79*.

[44] McCarthy, M. C.; Lee, K. L. K.; Carroll, P. B.; Porterfield, J. P.; Changala, P. B.; Thorpe, J. H.; Stanton, J. F. Exhaustive product analysis of three benzene discharges by microwave spectroscopy. *Journal of Physical Chemistry A* **2020**, *124*, 5170–5181.

[45] Kelvin Lee, K. L.; Changala, P. B.; Loomis, R. A.; Burkhardt, A. M.; Xue, C.; Cordiner, M. A.; Charnley, S. B.; McCarthy, M. C.; McGuire, B. A. Interstellar detection of 2-cyanocyclopentadiene, C_5H_5CN, a second five-membered ring toward TMC-1 . *The Astrophysical Journal Letters* **2021**, *910*, L2.

[46] Tielens, A. G. Interstellar polycyclic aromatic hydrocarbon molecules. *Annual Review of Astronomy and Astrophysics* **2008**, *46*, 289–337.

[47] Saslaw, W. C.; Gaustad, J. E. Interstellar Dust and Diamonds. *Nature* **1969**, *221*, 160–162.

[48] Lewis, R. S.; Ming, T.; Wacker, J. F.; Anders, E.; Steel, E. Interstellar diamonds in meteorites. *Nature* **1987**, *326*, 160–162.

[49] Jones, A. P.; D'Hendecourt, L. B.; Sheu, S. Y.; Chang, H. C.; Cheng, C. L.; Hill, H. G. Surface C-H stretching features on meteoritic nanodiamonds. *Astronomy and Astrophysics* **2004**, *416*, 235–241.

[50] Dahl, J. E.; Liu, S. G.; Carlson, R. M. Isolation and structure of higher diamondoids, nanometer-sized diamond molecules. *Science* **2003**, *299*, 96–99.

[51] Pirali, O.; Boudon, V.; Oomens, J.; Vervloet, M. Rotationally resolved infrared spectroscopy of adamantane. *Journal of Chemical Physics* **2012**, *136*.

[52] Pirali, O.; Boudon, V.; Carrasco, N.; Dartois, E. Rotationally resolved IR spectroscopy of hexamethylenetetramine (HMT) $C_6N_4H_{12}$. *Astronomy and Astrophysics* **2014**, *561*, 4–9.

[53] Pirali, O.; Boudon, V. Synchrotron-based Fourier transform spectra of the ν_{23} and ν_{24} IR bands of hexamethylenetetramine $C_6N_4H_{12}$. *Journal of Molecular Spectroscopy* **2015**, *315*, 37–40.

[54] Spaun, B.; Changala, P. B.; Patterson, D.; Bjork, B. J.; Heckl, O. H.; Doyle, J. M.; Ye, J. Continuous probing of cold complex molecules with infrared frequency comb spectroscopy. *Nature* **2016**, *533*, 517–520.

[55] McNaughton, D.; Jahn, M. K.; Travers, M. J.; Wachsmuth, D.; Godfrey, P. D.; Grabow, J. U. Laboratory rotational spectroscopy of cyano substituted polycyclic

aromatic hydrocarbons. *Monthly Notices of the Royal Astronomical Society* **2018**, *476*, 5268–5273.

[56] Lee, K. L. K.; McGuire, B. A.; McCarthy, M. C. Gas-phase synthetic pathways to benzene and benzonitrile: A combined microwave and thermochemical investigation. *Physical Chemistry Chemical Physics* **2019**, *21*, 2946–2956.

[57] Schlemmer, S. *Frontiers and Advances in Molecular Spectroscopy*; Elsevier Inc., 2018; pp 471–525.

[58] Widicus Weaver, S. L. Astrochemistry in the terahertz gap. *Physics Today* **2022**, *75*, 28–33.

[59] Yu, S.; Pearson, J. C.; Drouin, B. J.; Crawford, T.; Daly, A. M.; Elliott, B.; Amano, T. Rotational spectroscopy of vibrationally excited N_2H^+ and N_2D^+ up to 2.7 THz. *Journal of Molecular Spectroscopy* **2015**, *314*, 19–25.

[60] Lewis, R. A. A review of terahertz sources. *Journal of Physics D: Applied Physics* **2014**, *47*.

[61] Bark, H. S.; Park, M.-W.; Baek, I. H.; Jang, K.-H.; Jeong, Y. U.; Lee, K.; Jeon, T.-I. Broadband terahertz guided-mode resonance filter using cyclic olefin copolymer. *Optics Express* **2022**, *30*, 7976.

[62] Tammaro, S.; Pirali, O.; Roy, P.; Lampin, J. F.; Ducournau, G.; Cuisset, A.; Hindle, F.; Mouret, G. High density terahertz frequency comb produced by coherent synchrotron radiation. *Nature Communications* **2015**, *6*, 1–6.

[63] Lampin, J.-F.; Pirali, O.; Buchanan, Z.; Eliet, S.; Martin-Drumel, M.-A.; Turut, J.; Roy, P.; Hindle, F.; Mouret, G. Broadband terahertz heterodyne spectrometer exploiting synchrotron radiation at megahertz resolution. *Optics Letters* **2019**, *44*, 4985.

[64] Bouwman, J.; Fournier, M.; Sims, I. R.; Leone, S. R.; Wilson, K. R. Reaction rate and isomer-specific product branching ratios of $C_2H + C_4H_8$: 1-butene, cis-2-butene, trans-2-butene, and isobutene at 79 K. *The journal of physical chemistry. A* **2013**,

[65] Atkinson, D. B.; Smith, M. A. Radical-molecule kinetics in pulsed uniform supersonic flows: termolecular association of OH + NO between 90 and 220 K. *The Journal of Physical Chemistry* **1994**, *98*, 5797–5800.

[66] Crabtree, K. N.; Martin-Drumel, M. A.; Brown, G. G.; Gaster, S. A.; Hall, T. M.; McCarthy, M. C. Microwave spectral taxonomy: A semi-automated combination of chirped-pulse and cavity Fourier-transform microwave spectroscopy. *Journal of Chemical Physics* **2016**, *144*.

[67] Coxon, J. A.; Sastry, K. V. L. N.; Austin, J. A.; Levy, D. H. The microwave spectrum of the OH $X^2\Pi$ radical in the ground and vibrationally-excited ($v \leq 6$) levels . *Canadian Journal of Physics* **1979**, *57*, 619–634.

[68] ter Meulen, J. J.; Majewski, W. A.; Meerts, W. L.; Dymanus, A. Determination of the spin-rotation and hyperfine structure in the $A^2\Sigma^+_{12}$, $v = 0$ and $v = 1$ states of OH. *Chemical Physics Letters* **1983**, *94*, 25–28.

[69] Sims, I. R.; Queffelec, J.-l.; Travers, D.; Rowe, B. R.; Herbert, L. B.; Karthäuser, J.;

Smith, I. W. Rate constants for the reactions of CN with hydrocarbons at low and ultra-low temperatures. *Chemical Physics Letters* **1993**, *211*, 461–468.

[70] Daranlot, J.; Jorfi, M.; Xie, C.; Bergeat, A.; Costes, M.; Caubet, P.; Xie, D.; Guo, H.; Honvault, P.; Hickson, K. M. Revealing atom-radical reactivity at low temperature through the N + OH reaction. *Science* **2011**, *334*, 1538–1541.

[71] Canosa, A.; Ocaña, A. J.; Antiñolo, M.; Ballesteros, B.; Jiménez, E.; Albaladejo, J. Design and testing of temperature tunable de Laval nozzles for applications in gas-phase reaction kinetics. *Experiments in Fluids* **2016**, *57*, 152.

[72] Atkinson, D. B.; Smith, M. a. Design and characterization of pulsed uniform supersonic expansions for chemical applications. *Review of Scientific Instruments* **1995**, *66*, 4434.

[73] Daugey, N.; Caubet, P.; Retail, B.; Costes, M.; Bergeat, A.; Dorthe, G. Kinetic measurements on methylidyne radical reactions with several hydrocarbons at low temperatures. *Physical Chemistry Chemical Physics* **2005**, *7*, 2921.

[74] Broderick, B. M.; Suas-David, N.; Dias, N.; Suits, A. G. Isomer-specific detection in the UV photodissociation of the propargyl radical by chirped-pulse mm-wave spectroscopy in a pulsed quasi-uniform flow. *Physical Chemistry Chemical Physics* **2018**, *20*, 5517–5529.

[75] James, P. L.; Sims, I. R.; Smith, I. W. Total and state-to-state rate coefficients for rotational energy transfer in collisions between NO($X^2\Pi$) and He at temperatures down to 15 K. *Chemical Physics Letters* **1997**, *272*, 412–418.

[76] Oldham, J. M.; Abeysekera, C.; Joalland, B.; Zack, L. N.; Prozument, K.; Sims, I. R.; Park, G. B.; Field, R. W.; Suits, A. G. A chirped-pulse Fourier-transform microwave/pulsed uniform flow spectrometer. I. the low-temperature flow system. *Journal of Chemical Physics* **2014**, *141*, 1–8.

[77] Jiménez, E.; Ballesteros, B.; Canosa, A.; Townsend, T. M.; Maigler, F. J.; Napal, V.; Rowe, B. R.; Albaladejo, J. Development of a pulsed uniform supersonic gas expansion system based on an aerodynamic chopper for gas phase reaction kinetic studies at ultra-low temperatures. *Review of Scientific Instruments* **2015**, *86*, 045108.

[78] Durif, O. et al. A new instrument for kinetics and branching ratio studies of gas phase collisional processes at very low temperatures. *Review of Scientific Instruments* **2021**, *92*.

[79] Suas-David, N.; Thawoos, S.; Suits, A. G. A uniform flow-cavity ring-down spectrometer (UF-CRDS): A new setup for spectroscopy and kinetics at low temperature. *Journal of Chemical Physics* **2019**, *151*.

[80] Jen, T.-C.; Pan, L.; Li, L.; Chen, Q.; Cui, W. The acceleration of charged nano-particles in gas stream of supersonic de-Laval-type nozzle coupled with static electric field. *Applied Thermal Engineering* **2006**, *26*, 613–621.

[81] Anderson, J. D. *Fundamentals of Aerodynamics*, sixth ed.; McGraw-Hill: New York, 2017.

[82] Atkinson, D. B. Radical-molecule reaction dynamics in the low temperature regime. Ph.D. thesis, University of Arizona, 1995.

[83] Hall, N. NASA Isentropic Flow. 2021; `https://www.grc.nasa.gov/www/k-12/airplane/isentrop.html`.

[84] Shapiro, A. H. *The Dynamics and Thermodynamics of Compressible Fluid Flow*; Ronald Press Company, 1954.

[85] Moger, W.; Ramsay, D.; Moger, Supersonic Axisymmetric Nozzle Design By Mass Flow Techniques Utilizing a Digital Computer. **1964**,

[86] Hall, N. Prandtl-Meyer Angle. 2021; `https://www.grc.nasa.gov/www/k-12/airplane/pranmyer.html`.

[87] Cohen, C. B.; Reshotko, E. *The compressible laminar boundary layer with heat transfer and arbitrary pressure gradient*; 1956.

[88] Cohen, C. B.; Reshotko, E. Similar solutions for the compressible laminar boundary layer with heat transfer and pressure gradient. *NACA Technical Note* **1956**,

[89] Lee, S.; Hoobler, R. J.; Leone, S. R. A pulsed Lavai nozzle apparatus with laser ionization mass spectroscopy for direct measurements of rate coefficients at low temperatures with condensable gases. *Review of Scientific Instruments* **2000**, *71*, 1816–1823.

[90] Martin-Drumel, M. A.; Pirali, O.; Falvo, C.; Parneix, P.; Gamboa, A.; Calvo, F.; Bréchignac, P. Low-energy vibrational spectra of flexible diphenyl molecules: Biphenyl, diphenylmethane, bibenzyl and 2-, 3- and 4-phenyltoluene. *Physical Chemistry Chemical Physics* **2014**, *16*, 22062–22072.

[91] Loomis, R. A.; Burkhardt, A. M.; Shingledecker, C. N.; Charnley, S. B.; Cordiner, M. A.; Herbst, E.; Kalenskii, S.; Lee, K. L. K.; Willis, E. R.; Xue, C.; Remijan, A. J.; McCarthy, M. C.; McGuire, B. A. An investigation of spectral line stacking techniques and application to the detection of $HC_{11}N$. *Nature Astronomy* **2021**, *5*, 188–196.

[92] Bennett, C. J.; Morales, S. B.; Le Picard, S. D.; Canosa, A.; Sims, I. R.; Shih, Y. H.; Chang, A. H.; Gu, X.; Zhang, F.; Kaiser, R. I. A chemical dynamics, kinetics, and theoretical study on the reaction of the cyano radical (CN; $X^2\Sigma^+$) with phenylacetylene (C_6H_5CCH; X^1A_1). *Physical Chemistry Chemical Physics* **2010**, *12*, 8737–8749.

[93] Jawad, K.; Viquez Rojas, C.; Slipchenko, L.; Zwier, T. The exotic excited state behavior of 3-phenyl-2-propynenitrile. International Symposium on Molecular Spectroscopy. 2017.

[94] Schultz, G.; Brunvoll, J.; Almenningen, A. On the molecular-structure of ortho-dicyanobenzene as studied by electron-diffraction. *Acta Chemica Scandinavica Series A-Physical and Inorganic Chemistry* **1986**, *40*, 77–82.

[95] Williamson, B. E.; VanCott, T. C.; Rose, J. L.; Schrimpf, A.; Koralewski, M.; Schatz, P. N. Electronic spectra of phthalonitrile isolated in an argon matrix. *Journal of Physical Chemistry* **1991**, *95*, 6835–6842.

[96] Higgins, J.; Zhou, X.; Liu, R. Density functional theory study of vibrational spectra: 9. Structures and vibrational assignments of dicyanobenzenes. *Spectrochimica Acta Part A: Molecular and Biomolecular Spectroscopy* **1997**, *53*, 721–731.

[97] Campanelli, A. R.; Domenicano, A.; Ramondo, F.; Hargittai, I. Molecular structure and benzene ring deformation of three cyanobenzenes from gas-phase electron diffraction and quantum chemical calculations. *Journal of Physical Chemistry A* **2008**, *112*, 10998–11008.

[98] Fujita, K.; Fujiwara, T.; Matsunaga, K.; Ono, F.; Nakajima, A.; Watanabe, H.; Koguchi, T.; Suzuka, I.; Matsuzawa, H. Electronic spectra of *p*-dicyanobenzene (*p*-DCNB), *p*-DCNB-H2O complex, and *p*-DCNB dimer in a supersonic jet. *The Journal of Physical Chemistry* **1992**, *96*, 10693–10697.

[99] Hadden, N.; Hamner, W. F. Infrared analysis of isomeric dicyanobenzene mixtures. *Analytical Chemistry* **1959**, *31*, 1052–1054.

[100] Melinger, J. S.; Laman, N.; Harsha, S. S.; Grischkowsky, D. Line narrowing of terahertz vibrational modes for organic thin polycrystalline films within a parallel plate waveguide. *Applied Physics Letters* **2006**, *89*, 251110.

[101] Oppenheim, K. C.; Korter, T. M.; Melinger, J. S.; Grischkowsky, D. Solid-state density functional theory investigation of the terahertz spectra of the structural isomers 1,2-dicyanobenzene and 1,3-dicyanobenzene. *The Journal of Physical Chemistry A* **2010**, *114*, 12513–12521.

[102] Chang, H. C.; Lin, J. C.; Wu, J. Y.; Chen, K. H. Infrared spectroscopy and vibrational relaxation of CH_x and CD_x stretches on synthetic diamond nanocrystal surfaces. *Journal of Physical Chemistry* **1995**, *99*, 11081–11088.

[103] Sheu, S.-Y.; Lee, I.-P.; Lee, Y. T.; Chang, H.-C. Laboratory investigation of hydro-

genated diamond surfaces: Implications for the formation and size of interstellar nanodiamonds. *The Astrophysical Journal* **2002**, *581*, L55–L58.

[104] Chadwick, D.; Legon, A. C.; Millen, D. J. Microwave spectra and structures of 1-cyano- and 1-iodo-adamantane. *Journal of the Chemical Society, Faraday Transactions 2: Molecular and Chemical Physics* **1972**, *68*, 2064–2069.

[105] Pirali, O.; Vervloet, M.; Dahl, J. E.; Carlson, R. M. K.; Tielens, A. G. G. M.; Oomens, J. Infrared spectroscopy of diamondoid molecules: New insights into the presence of nanodiamonds in the interstellar medium. *The Astrophysical Journal* **2007**, *661*, 919–925.

[106] Pirali, O.; Goubet, M.; Huet, T. R.; Georges, R.; Soulard, P.; Asselin, P.; Courbe, J.; Roy, P.; Vervloet, M. The far infrared spectrum of naphthalene characterized by high resolution synchrotron FTIR spectroscopy and anharmonic DFT calculations. *Physical Chemistry Chemical Physics* **2013**, *15*, 10141–10150.

[107] Frisch, M. J. et al. Gaussian 16 Revision C.01. 2016; Gaussian Inc. Wallingford CT.

[108] Chai, J.-D.; Head-Gordon, M. Long-range corrected hybrid density functionals with damped atom–atom dispersion corrections. *Physical Chemistry Chemical Physics* **2008**, *10*, 6615–6620.

[109] Dunning, T. H. Gaussian basis sets for use in correlated molecular calculations. I. The atoms boron through neon and hydrogen. *The Journal of Chemical Physics* **1989**, *90*, 1007–1023.

[110] Frisch, M. J. et al. Gaussian 09 Revision B.01. 2009; Gaussian Inc. Wallingford CT 2009.

[111] Western, C. M. PGOPHER: A program for simulating rotational, vibrational and electronic spectra. *Journal of Quantitative Spectroscopy and Radiative Transfer* **2017**, *186*, 221–242.

[112] Buchanan, Z.; Lee, K. L. K.; Chitarra, O.; McCarthy, M. C.; Pirali, O.; Martin-Drumel, M. A. A rotational and vibrational investigation of phenylpropiolonitrile ($C_6H_5C_3N$). *Journal of Molecular Spectroscopy* **2021**, *377*, 111425.

[113] King, G. W.; So, S. P. Ethynylbenzene; The vibrational spectra of some deuterated isomers. *Journal of Molecular Spectroscopy* **1970**, *36*, 468–487.

[114] Pirali, O.; Vervloet, M.; Mulas, G.; Malloci, G.; Joblin, C. High-resolution infrared absorption spectroscopy of thermally excited naphthalene. Measurements and calculations of anharmonic parameters and vibrational interactions. *Physical Chemistry Chemical Physics* **2009**, *11*, 3443–3454.

[115] Pickett, H. The Fitting and Prediction of Vibration-rotation Spectra with Spin Interactions. *Journal of Molecular Spectroscopy* **1991**, *148*, 371–377.

[116] Łodyga, W.; Kreglewski, M.; Pracna, P.; Urban, Š. Advanced graphical software for assignments of transitions in rovibrational spectra. *Journal of Molecular Spectroscopy* **2007**, *243*, 182–188.

[117] Cooke, S. A.; Ohring, P. Decoding pure rotational molecular spectra for asymmetric molecules. *Journal of Spectroscopy* **2013**, *2013*, 1–10.

[118] Lee, K. L. K.; McCarthy, M. Bayesian Analysis of Theoretical Rotational Constants from Low-Cost Electronic Structure Methods. *Journal of Physical Chemistry A* **2020**, *124*, 898–910.

[119] Wohlfart, K.; Schnell, M.; Grabow, J. U.; Küpper, J. Precise dipole moment and quadrupole coupling constants of benzonitrile. *Journal of Molecular Spectroscopy* **2008**, *247*, 119–121.

[120] McGuire, B. A.; Burkhardt, A. M.; Loomis, R. A.; Shingledecker, C. N.; Lee, K. L. K.; Charnley, S. B.; Cordiner, M. A.; Herbst, E.; Kalenskii, S. V.; Momjian, E.; Willis, E. R.; Xue, C.; Remijan, A. J.; McCarthy, M. C. Early science from GOTHAM: Project overview, methods, and the detection of interstellar propargyl cyanide ($HCCCH_2CN$) in TMC-1. *Astrophysical Journal Letters* **2020**, *900*, L10.

[121] Russell D. Johnson III, NIST Computational Chemistry Comparison and Benchmark Database. 2022; `http://cccbdb.nist.gov/`.

[122] Kassi, S.; Petitprez, D.; Wlodarczak, G. Microwave Fourier transform spectroscopy of t-butylchloride and t-butylbromide isotopic species. *Journal of Molecular Structure* **2000**, *517*, 375–386.

[123] Tudorie, M.; Coudert, L. H.; Huet, T. R.; Jegouso, D.; Sedes, G. Magnetic hyperfine coupling of a methyl group undergoing internal rotation: A case study of methyl formate. *Journal of Chemical Physics* **2011**, *134*.

[124] Pearson, J. C.; Drouin, B. J.; Yu, S. Instrumentation for THz spectroscopy in the laboratory and in space. *IEEE Journal of Microwaves* **2021**, *1*, 43–54.

[125] Pagies, A.; Ducournau, G.; Lampin, J. F. Low-threshold terahertz molecular laser optically pumped by a quantum cascade laser. *APL Photonics* **2016**, *1*.

[126] Danielewicz, E.; Weiss, C. Far infrared laser emission from $^{15}NH_3$ optically pumped by a CW sequence band CO_2 laser. *IEEE Journal of Quantum Electronics* **1978**, *14*, 222–223.

[127] Chang, T. Y.; Bridges, T. J. Laser action at 452, 496, and 541 μm in optically pumped CH_3F. *Optics Communications* **1970**, *1*, 423–426.

[128] Faist, J.; Capasso, F.; Sivco, D. L.; Sirtori, C.; Hutchinson, A. L.; Cho, A. Y. Quantum cascade laser. *Science* **1994**, *264*, 553–556.

[129] Mammez, M.-H.; Buchanan, Z.; Pirali, O.; Martin-Drumel, M.-A.; Turut, J.; Ducournau, G.; Eliet, S.; Hindle, F.; Barbieri, S.; Roy, P.; Mouret, G.; Lampin, J.-F. Optically pumped terahertz molecular laser: Gain factor and validation up to 5.5 THz. *Advanced Photonics Research* **2022**,

[130] Gordon, I. E. et al. The HITRAN2016 molecular spectroscopic database. *Journal of Quantitative Spectroscopy and Radiative Transfer* **2017**, *203*, 3–69.

[131] Tennyson, J.; Yurchenko, S. N. The ExoMol project: Software for computing large molecular line lists. *International Journal of Quantum Chemistry* **2017**, *117*, 92–103.

[132] McGuire, B. A.; Loomis, R. A.; Burkhardt, A. M.; Lee, K. L. K.; Shingledecker, C. N.; Charnley, S. B.; Cooke, I. R.; Cordiner, M. A.; Herbst, E.; Kalenskii, S.; Siebert, M. A.; Willis, E. R.; Xue, C.; Remijan, A. J.; McCarthy, M. C. Detection of two interstellar

polycyclic aromatic hydrocarbons via spectral matched filtering. *Science* **2021**, *371*, 1265–1269.

[133] Weiss, C. O.; Fourrier, M.; Gastaud, C.; Redon, M. *Reviews of Infrared and Millimeter Waves (Vol. 2): Optically Pumped Far-Infrared Laser*; Springer US, 1984; pp 277–335.

[134] Danielewicz, E. J.; Weiss, C. O. New CW far-infrared D_2O, $^{12}CH_3F$ and $^{14}NH_3$ laser lines. *Optics communications* **1978**, *27*, 98–100.

[135] Frank, E. M.; Weiss, C. O.; Siemsen, K.; Grinda, M.; Willenberg, G. D. Predictions of far-infrared laser lines from $^{14}NH_3$ and $^{15}NH_3$. *Optics letters* **1982**, *7*, 96–98.

[136] Chang, T. Y.; Bridges, T. J.; Burkhardt, E. G. CW laser action at 81.5 and 263.4 µm in optically pumped ammonia gas. *Applied Physics Letters* **1970**, *17*, 357–358.

[137] Willenberg, G. D. Continuous-wave far-infrared two-photon-pumped, single-photon-pumped, and Raman laser emission from $^{14}NH_3$. *Optics letters* **1981**, *6*, 372–373.

[138] Wienold, M.; Zubairova, A.; Hübers, H.-W. Laser emission at 4.5 THz from 15 NH_3 and a mid-infrared quantum-cascade laser as a pump source. *Optics Express* **2020**, *28*, 23114–23121.

[139] Danielewicz, E. J.; Weiss, C. O. Far Infrared Laser Emission From $^{15}NH_3$ Optically Pumped by a CW Sequence band CO_2 laser. *IEEE Journal of Quantum Electronics* **1978**, *14*, 222–223.

[140] Wood, R. A.; Davis, B. W.; Vass, A.; Pidgeon, C. R. Application of an isotopically

enriched $^{13}C^{16}O_2$ laser to an optically pumped far-infrared laser. *Optics Letters* **1980**, *5*, 153–154.